1-1-1998

A study of x-ray substructure in rich clusters of galaxies

Philip Leroy Rogers
University of Nevada, Las Vegas

INFORMATION TO USERS

This manuscript has been reproduced from the microfilm master. UMI films the text directly from the original or copy submitted. Thus, some thesis and dissertation copies are in typewriter face, while others may be from any type of computer printer.

The quality of this reproduction is dependent upon the quality of the copy submitted. Broken or indistinct print, colored or poor quality illustrations and photographs, print bleedthrough, substandard margins, and improper alignment can adversely affect reproduction.

In the unlikely event that the author did not send UMI a complete manuscript and there are missing pages, these will be noted. Also, if unauthorized copyright material had to be removed, a note will indicate the deletion.

Oversize materials (e.g., maps, drawings, charts) are reproduced by sectioning the original, beginning at the upper left-hand corner and continuing from left to right in equal sections with small overlaps. Each original is also photographed in one exposure and is included in reduced form at the back of the book.

Photographs included in the original manuscript have been reproduced xerographically in this copy. Higher quality 6" x 9" black and white photographic prints are available for any photographs or illustrations appearing in this copy for an additional charge. Contact UMI directly to order.

UMI

A Bell & Howell Information Company
300 North Zeeb Road, Ann Arbor MI 48106-1346 USA
313/761-4700 800/521-0600

A STUDY OF X-RAY SUBSTRUCTURE IN RICH CLUSTERS OF GALAXIES

by

Philip L. Rogers, Jr.

Bachelor of Science
University of Nevada, Reno
1993

A thesis submitted in partial fulfillment
of the requirements for the degree of

Master of Science

in

Physics

Department of Physics
University of Nevada, Las Vegas
August 1998

UNLV
UNLV

Thesis Approval
The Graduate College
University of Nevada, Las Vegas

July 24, 1998

The Thesis prepared by

Philip L. Rogers, Jr.

Entitled

A Study of X-Ray Substructure in Rich Clusters of Galaxies

is approved in partial fulfillment of the requirements for the degree of

Master of Science in Physics

Examination Committee Chair

Dean of the Graduate College

Examination Committee Member

Examination Committee Member

Graduate College Faculty Representative

ABSTRACT

A Study of X-ray Substructure in Rich Clusters of Galaxies

by

Philip L. Rogers, Jr.

Dr. George Rhee, Examination Committee Chair
Professor of Physics
University of Nevada, Las Vegas

A comparison of three tests to determine substructure in rich Abell clusters of galaxies was preformed and the results are presented in this paper. The data used are ROSAT PSPC X-ray images of a sample of 21 clusters drawn from the ACO catalog, and a subset of the ESO Nearby Abell Cluster Survey done by Katgert et. al. The three methods used are: the 'center shift' method developed by Mohr et al., the 'moment' method developed by Buote & Tsai, and a wavelet analysis developed by Starck et al.. Models were then created to check the significance of our findings. The conclusions reached were that substructure and cooling flows are present in at least 50% of our sample. In addition, although it is possible to get a generally accurate result using only one of the above methods, the use of a multi-pronged analysis approach to achieve maximum accuracy is desirable.

TABLE OF CONTENTS

LIST OF FIGURES

ACKNOWLEDGMENTS

I would like to thank NASA for partially supporting this research through the Nevada Space Grant Consortium.

I would like to thank Dr. George Rhee, whose guidance, knowledge and enthusiasm have made this project both educational and enjoyable. It is also a pleasure to thank S. Lepp, L. Spight, and D. Weistrop for their insightful suggestions and support during this project.

I would like to express my gratitude to my friends and compatriots S. Cruzen, D. Eggers, J. Kilburg, D. Carrol, T. Rennie, J. Opfer, K. Eddy, G. Budai, T. Colegrove, M. Rodrigue, and S. Mitchell. I have found their patience and sometimes not so subtle hints to be invaluable.

Lastly and most importantly, I want to thank my wife, Alison, and my parents, Philip Sr. and Bessie, to whom I dedicate this work. Without their love and guidance, I would be a much lesser person.

CHAPTER 1

INTRODUCTION

One of the greatest quests in cosmology is the search for the value of Ω, known as the cosmological density parameter. Ω is defined as the ratio of ρ_o, the observed or measured density of the universe, to ρ_c, the critical density of the universe, so called because it is the density needed to make the universe just closed. The knowledge of its value holds the key to the mystery of the ultimate fate of the cosmos. A value of Ω less than 1 would indicate that the observed density of the universe is less than the critical density, meaning that there is not enough matter in the universe to overcome the current acceleration. This would lead to an open universe, which would continue to expand forever. On the other hand, if the value of Ω were greater than 1 the observed density of universe would be more than the critical density. This would indicate that there is enough matter in the universe to overcome the its current acceleration, making the universe closed. In this case the universe would eventually begin to contract and continue to do so until it reached a singularity of infinite density. Many methods can be used to determine the limits of Ω. One of these is the study of substructure in rich clusters of galaxies. The reasoning is that we currently believe galaxy clusters form by a process known as "violent relaxation", a process that tends to erase substructure by dynamical evolution. If we take this as given, then the observation of substructure in galaxy clusters may indicate that the clusters are still in the early stages of virialization. This is an idea we can use to probe the value of Ω.

It has been held for many years that the frequency of substructure in galaxy clusters can lead to determining the lower limit of Ω (Richstone, Loeb & Turner 1992; Kauffmann & White 1993; Lacey & Cole 1993). To make sense of this statement we need to look a little closer at the scenario. Imagine the value of Ω is low. If this is so then large structures such as rich galaxy clusters must form early in time, before expansion could overcome the local gravitational attraction. This being the case we would expect to find most clusters in a virialized or relaxed state because the universe is sufficiently old for most of the matter on the cluster size scale to have smoothed out. On the other hand, if the value of Ω is high, than the density of the universe is sufficient to allow galaxy cluster formation into the present era. In other words, on the large scale there is still enough matter close together to interact and form clusters. If we accept the latter as the case, we would expect to see some substructure in at least a few still forming galaxy clusters. In fact, recent observations support the latter view, suggesting 30% - 50% of galaxy clusters show at least some evidence of substructure either optically or in their plasma distributions (Geller & Beers 1982; Dressler & Shectman 1988; Mohr, Frabricant & Geller 1993; Salvador-Sole, Sanroma & Gonzalez-Casado 1993; Bird 1994; Escalera et al. 1994; West et al. 1994).

Rich galaxy clusters are typically groups of hundreds or thousands of galaxies bound together by their mutual gravitation. On average they have a diameter of about 3 Mpc. Using the virial theorem and independent velocity dispersions it has been found that they can contain upwards of several times 10^{15} solar masses. Given the current interpretation of general relativity, each cluster contains three components of mass. Firstly, there is the mass associated with the emitted light we see from the individual galaxies, which amounts to less than 10% of the total mass. Secondly, there is the mass associated with the hot intracluster plasma, which

amounts to perhaps 20% of the total mass. Lastly, there is the component associated with the remaining bulk of the mass which is, non-luminous, and referred to as "Dark Matter".

In general, clusters are characterized by their redshifts, velocity dispersions and apparent morphologies. There is a wide range of accepted morphological classification schemes. However for brevity we shall adopt two for this work. The Bautz and Morgan(1970) system will be used for all the clusters, as well as the revised Rood-Sastry(1971) system from Struble and Rood(1982) for the southern clusters and those clusters far enough north to have been classified in this scheme.

The Bautz-Morgan system uses three main classifications or types and adds two other categories that are merely combinations of the three main types. The types are defined as follows:

Type I : Clusters dominated by a single bright central cD galaxy.

Type II: Clusters whose brightest galaxies are intermediate between cD and giant ellipticals.

Type III: Clusters that have no dominating cluster galaxies.

Type I – II and II – III: are clusters that are intermediates.

The Rood-Sastry system is defined as follows:

cD: the cluster is dominated by a central cD or cluster dominant galaxy.

B: binary – the cluster is dominated by a pair of luminous galaxies.

L: line - at least three of the brightest galaxies appear to be in a straight line.

C: core – four or more of the ten brightest galaxies form a cluster core, with comparable separations.

F: flat – the brightest galaxies form a flattened distribution on the sky.

I: irregular – the distribution of brightest galaxies is irregular with no obvious center or core.

Cluster Classifications

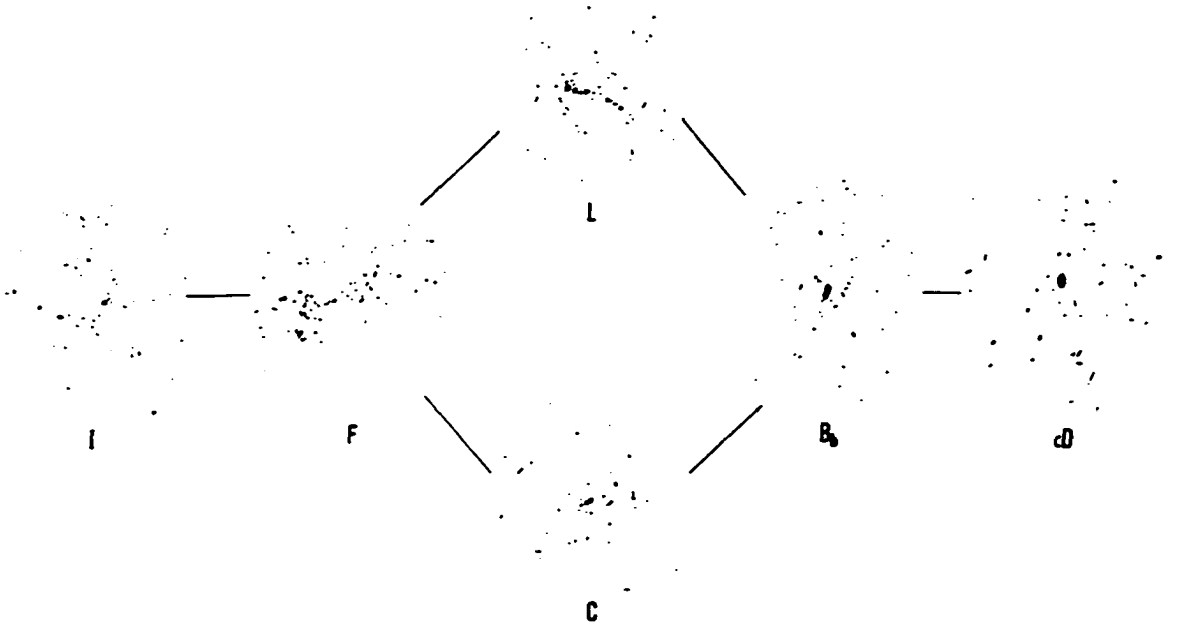

Figure 1. Revised R.S. Cluster classifications from Struble and Rood(1982).

The Rood-Sastry classifications are not the easiest to visualize so figure 1 is supplied for clarification.

For our purposes the intracluster plasma is the prime concern, so lets look at it in more detail. This plasma ranges in temperature from 10^7 K to about 10^8 K, with a density of $\approx 10^{-3}$ atoms/cm^3. It is comprised mostly of hydrogen and helium but also contains traces of iron and other heavy elements that have been stripped from the constituent galaxies by ram pressure due to dynamical friction. This hot gas gives off emissions in the X-ray spectrum due to bremsstrahlung. This is caused by relativistic electrons emitting "breaking radiation" due to changes in the magnitudes of their acceleration when they interact with other ions. Because a plasma consists of ions, its emission is proportional to the density squared. The free-free

emissivity of a plasma with an electron temperature T_g a frequency υ and an ion charge of Z can be expressed as follows

$$e_{\upsilon}^{ff} = \frac{2^5 \pi e^6}{3 m_e c^3}\left(\frac{2\pi}{3 m_e k}\right)^{1/2} Z^2 n_e n_i g_{ff}(Z, T_g, \upsilon) \times T_g^{-1/2} \exp\left(\frac{-h\upsilon}{kT_g}\right).$$

Here n_e and n_i are the number densities of electrons and ions, and g_{ff} (Z, T_g , υ) is the gaunt factor. This factor corrects for quantum mechanical effects and distant collisions. This reliance on the density squared makes the clusters stand out from the background radiation more prominently than clusters in the optical range. Thus it is possible to see the plasma distributions of many more clusters at greater distances using X-rays than it is to see the galaxy distributions of the same clusters in optical wavelengths. Obviously, this advantage can be used to produce a larger and more complete cluster sample, which is exactly the type of sample we want in order to give us a more accurate measure of substructure in the universe.

With the above in mind this project was taken on with the intent of answering three important questions.

1) How do the three analysis programs used in this survey compare?
2) What is the prevalence of substructure in rich clusters of galaxies?
3) What are the implications of this result concerning the value of Ω?

In chapter 2, I discuss the data selection and processing. In chapter 3, the three methods of analysis are covered. Chapter 4 contains the details of the models used to calculate errors and significance. Chapter 5 contains a detailed description of the results for 3 of the 21 clusters. Finally, in chapter 6, there is a discussion of the general results and their relevance to our search.

CHAPTER 2

THE DATA

The sample of clusters was drawn from the ESO Nearby Abell Cluster Survey, or ENACS for short, (Katgert et al 1994). This sample was chosen because the ENACS group's motivation was to compile a more complete redshift database for Abell clusters with richness greater than 1 out to a redshift of approximately 0.1 than was previously available. The Abell catalog was chosen because it uses a more stringent cluster definition than the other major catalogs. To be defined as a rich cluster in the Abell or ACO (Abell, Corwin & Olowin 1989) catalog, a cluster has to have ≥ 50 galaxies within 2 magnitudes of the 3rd brightest galaxy lying within 3 Mpc of the observed cluster center. The importance of using rich clusters of galaxies is that due to their size and mass they have long been known to be objects that can provide data on the physics of large-scale structure formation. The ESO survey was done for all clusters meeting the above criteria in a solid angle of 2.55 sr about the South Galactic Pole, resulting in a database containing 107 clusters. In short, this should provided us with a complete and unbiased database of rich Abell clusters from which to draw our sample.

It then had to be decided which X-ray satellite archive to use, ROSAT or the Einstein Observatory. The ROSAT PSPC (Position Sensitive Proportional Counter) has a field of view of 2° and an energy resolution of 43% at 0.93 KeV with an on-axis resolution of about 25" at 1Kev out to 20' from the center. This distance of 20' is sufficient to include the entire cluster X-ray morphology for all our data frames. The Einstein Observatory's

IPC (Image Proportional Counter) has a field of view of about 1° and a spatial resolution of only 1.7'at Full Width Half Maximum. It was concluded that for the purposes of observing subtle changes in the cluster plasma the ROSAT PSPC was the best instrument to use.

X-ray photons are of such high energy that they cannot be collected in the same fashion as are photons in optical wavelengths. These photons have a distinct tendency to be absorbed rather than reflected. In order to reflect target photons the X-ray telescope aboard ROSAT uses a method of collection called grazing incidence. At energies $\leq$ 2 KeV the incoming x-ray photons can be reflected off composite metal surfaces when their angle of incidence approaches unity. The X-ray telescope uses just such optics in an arrangement called a Wolter type I telescope, which uses a combination of annular sections of parabolic mirrors as grazing incidence reflectors. Several of these systems are arranged concentrically in a nested configuration to increase the sensitivity of the system. A position sensitive detector is then placed at the focal plane to produce high resolution images limited only by irregularities in the mirrors. The drawback of this type of apparatus is that it only allows observations of cluster plasmas with temperatures less than 2.4 keV. We know from cluster dynamics that cluster plasma temperatures can reach upwards of 30 keV in some cases. To convince ourselves that the 2.4 keV limit will still suit our needs let us look at the above figure 2. Taking into account that the Coma cluster is one of the better studied clusters and assuming it as an average cluster representative it can be clearly seen the predominant emissions are due to temperatures in the 2-5 keV range, with the 2-3 keV range making up most of the photon counts in this area of the curve. Thus for our purposes, the 2.4 keV limit is a sufficient range to detect substructure.

Energy Spectrum for the Coma Cluster

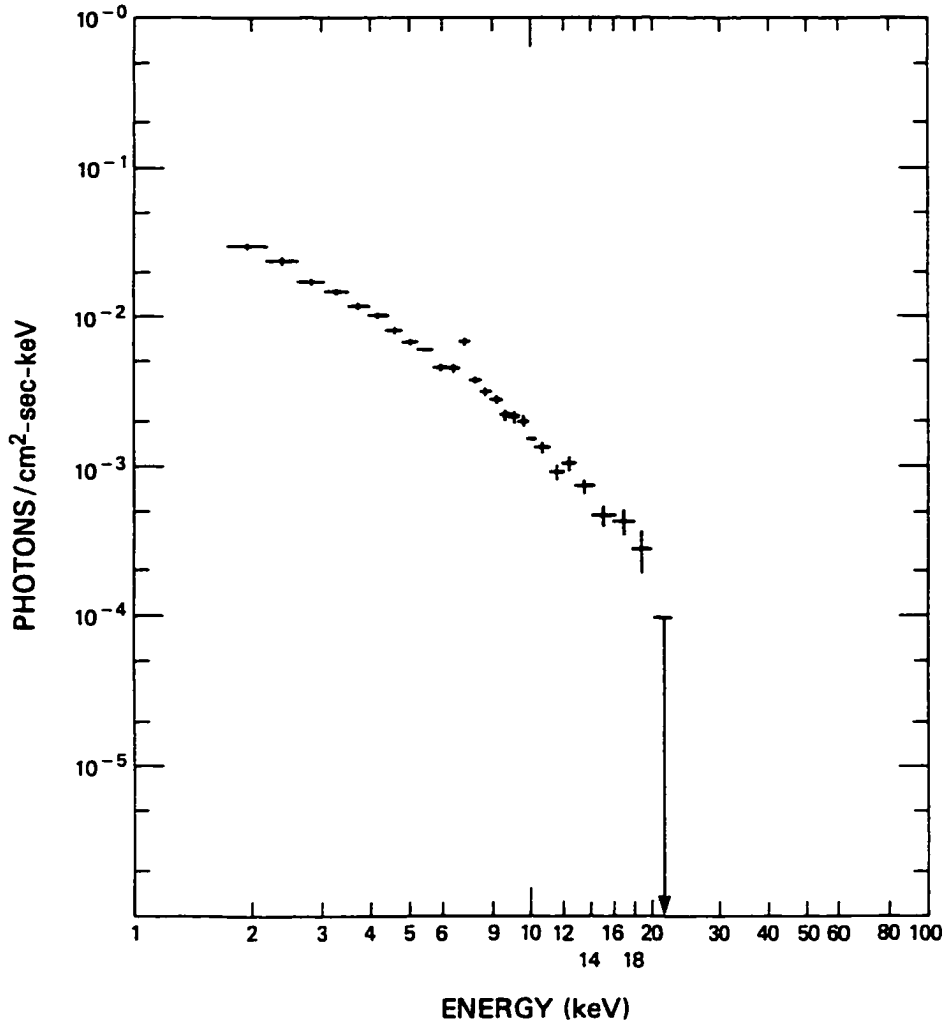

Figure 2. HEAO-1 A-2 low resolution X-ray spectrum of the Coma cluster. The plot gives the number flux of X-ray photons per cm^2-sec-keV versus photon energy in keV(Henriksen and Mushotzky, 1986).

The ROSAT archive was scanned for all the observed and archived Abell clusters that were common to both lists. In all, 44 clusters were found in the ROSAT archive that were also in the ENACS survey. For each cluster there are three data frames available. A soft

band image from 0.07 – 0.4 keV, a hard band image from 0.4 - 2.4 keV and a total band image which is comprised of both images together. It was decided to download only the hardband (0.4 – 2.4 KeV) images of the clusters because this energy range is high enough to minimize distortions due to the point spread function from the PSPC. It also reduces the contamination effects from the X-ray background known to occur in the lower end of the X-ray spectrum. After an initial examination of the data, 23 of the frames had to be discarded. Seven of the frames were discarded due to misalignment of the instrument. This misalignment either caused the clusters to appear at the edge of the frame, where the distortions of the detector are greatest, or under the support structure, where it was unobservable. The other sixteen frames were unusable because the exposure times were too short to show any subtle plasma structure, thus making it impossible to run our substructure analysis programs. This left us with a total of 21 usable cluster data frames (Table 1 page 39).

These remaining data frames were processed in the following manner. Firstly, they were divided by their exposure maps, which were also provided by the ROSAT archive. This was done to correct for exposure variations and instrument vignetting. Secondly, they were multiplied by their exposure times so that the final image was in the form of counts. Thirdly, they were filtered using a program supplied by Starck et al. that uses a bspline wavelet transform to reduce overall image noise, essentially smoothing the image. Lastly, they were cleaned of point sources. Each image was visually inspected for "obvious" point source contamination that occurred outside the central plasma source. The sources were checked to see if their FWHM was comparable to that of point sources imaged by the PSPC. Unresolved sources were removed using the imedit program in the TV package of IRAF. Briefly, what imedit does is replace what is in a user defined circle with the average

counts contained in an annulus placed at a specific radius which is also defined by the user. We identified point sources by eye because automated methods tended to identify and correct "point sources" inside the central plasma structure. Although this is a plausible place to find point source contamination, the automated corrections caused distortions in the portion of the plasma structure in which we hoped to find subtle changes. Point sources near or in the center of the cluster cores were deleted using the fixpix program in the PROTO package of IRAF. This gave substantially better results than the imedit program that was used for the outlying point sources.

CHAPTER 3

THE METHODS

In this section, I discuss the three methods that were used to analyze the data, the 'Center shift' method, the 'moment' method, and the wavelet transform method. These three very different methods were chosen in the hope that they would complement each other and give a more complete picture of the amount and type of substructure in Abell clusters.

3.1 Moment Method

The first method that will be discussed is what I refer to as the 'moment' method developed and supplied by Buote and Tsai (1995). The main idea of this method is to be able to quantitatively classify cluster morphologies in direct relation to their dynamical state as indicated by the gravitational potential (Buote and Tsai 1995). The most natural way to accomplish this is to use a two-dimensional multipole expansion of the projected gravitational potential. If we let $\Sigma(R,\phi)$ be the two dimensional projection of the mass density then we can write the two dimensional potential $\Psi(R,\phi)$, as:

$$\nabla^2\Psi(R,\phi) = 4\pi G\Sigma(R,\phi)$$

with G being the gravitational constant.. Using Green's functions it can be shown that the potential due to the material interior to R is given by:

$$\Psi(R,\phi) = -2Ga_0 \ln\left(\frac{1}{R}\right) - 2G\sum_{m=1}^{\infty}\frac{1}{m R^m}\left(a_m \cos m\phi + b_m \sin m\phi\right)$$

where a_m and b_m are the "Moments" of interest. They can be expressed in the following way:

$$a_m = \int_{R' \le R} \Sigma(\vec{x}')(R')^m \cos m\phi' \, d^2x'$$

$$b_m = \int_{R' \le R} \Sigma(\vec{x}')(R')^m \sin m\phi' \, d^2x'$$

with $\vec{x}' = (R', \phi')$. Ψ does not represent the total gravitational potential since the equation fails to account for the mass exterior to R. However we are only concerned with the gravitational effects of the mass interior to R.

It is clear from the above equations that we can consider as many moments as we like. For our purposes we only concern ourselves with m=1, 2, 3, and 4, as higher order terms reflect smaller scales which are dynamically less significant. It is also clear that R is as yet undefined. The fact that our clusters are centrally positioned on our data frames leaves very little distance between their apparent edge and the ROSAT support spider. For this reason we limited R to a single value of 1 Mpc referred to as R_{ap} our radius aperture. This places our boundary of interest just inside the support structure, leaving plenty of room to search for substructure but ignoring the area underneath and around the support structure where any source information can be either screened or distorted.

Another small problem to be dealt with is that the $m \geq 1$ terms of the equation for $\Psi(R, \phi)$ vanish when integrated over ϕ. This forces us to consider only the magnitude of the terms for each order integrated over ϕ. If we let Ψ_m be the m^{th} term of the multipole expansion for Ψ we can define the following quantity:

$$P_{m,m'}(R_{ap}) = \frac{1}{2\pi} \int_0^{2\pi} \Psi_{m'}(R_{ap}, \phi) \Psi_m(R_{ap}, \phi) d\phi \, .$$

Such that only terms for m=m' are non-vanishing. This means $P_m = P_{m,m}$ measures the 'power' interior to R_{ap} for the terms of order m. If we ignore the factors of 2G, these values are given by, $P_0 = [a_0 \ln(1/R_{ap})]^2$ for m=0 and $P_m = \frac{1}{2m^2 R_{ap}^{2m}}(a_m^2 + b_m^2)$ for values of m>0. The total 'power' of all the moments would then be given by $P = \sum_{m=0}^{\infty} P_m$. Therefore, the ratio of P_m to P reflects the contribution of the m^{th} moment to the 'power' of the total potential interior to R_{ap}. Knowing that the gravitational potential is precisely related to the dynamical state of the cluster, the P_m's are the substructure measures we are looking for.

This can be put in a graphical sense in the following way. Let's look at the 1st moment, which would look something like an 8 or ∞. If this pattern is placed over the center of the cluster and we add up the counts in each ear and subtract one from the other, any value greater than 0 indicates the presence of substructure. The higher the number, the greater the power of the substructure! This thought analysis can be extended to any of the moments by simply adding another figure 8 overlapped at the center for each additional moment.

3.2 Center Shift Method

The second method is the 'center shift' method developed and supplied by Mohr et al.(1993). This program is also based on measuring the low order moments of a cluster. However with this method we find the 1st moment $M_1(\bar{r})$, axial ratio $\eta(\bar{r})$, and ellipsoidal orientation angle $\theta_2(\bar{r})$ at several different radii for each cluster. To make the measurements we need to choose an initial radius and width for our annulus and find the proper place to locate it on our data frame. For our purposes, we chose an initial radius of

2 pixels and an annulus of 2 pixels with each pixel having a value of 15". We next Fourier expand the section of the image $I(\theta,\bar{r})$ that lies within the annulus so that we can determine the coefficient C_1, defined in the following expansion as

$$I(\theta,\bar{r}) = \sum_{m=0}^{m_{max}} C_m(\bar{r})\cos[m\theta - m\theta_m(\bar{r})]$$

with m_{max} being the highest calculated harmonic. Next the location of the annulus on the data frame is varied. This is repeated until we minimize C_1. By minimizing C_1 we can find the center of the image. However in order to save cpu time, the center values obtained from the 'moment' method were used as starting values. With this done, the Fourier expansion of the photon distribution, defined by the centered location of the annulus is now computed. We can use the expansion parameters to find the 1st moment $M_1 = (\bar{x},\bar{y})$, the ellipsoidal orientation angle θ_2, and the axial ratio η.

$$\eta(\bar{r}) \approx 1 - \frac{2C_2(\bar{r})}{\bar{r}(dC_0/dr)|_{\bar{r}}}$$

Where, $(dC_0/dr)|_{\bar{r}}$ is the radial gradient of the surface brightness evaluated at $\bar{r}$. Finally we increase the radius of the annulus by 2 pixels per iteration and repeat the above steps until the radius extends past the area of the X-ray image we are investigating.

Let us once again look at this in a graphical manner. Imagine a series of hula-hoops having different radii but possessing the same thickness. Now let us place our hula-hoops over the top of a symmetric anthill one at a time starting with the smallest one first. If we look down on our system from an overhead position, we notice that all the hoops share the same center. Now imagine our anthill has some inhomogeneous asymmetry. In other words, it may look symmetric at its apex but as we look farther down the base, it bulges to one side or the other. Now start again by placing the hoops on the anthill one at a time

with the smallest one first. As the radii of our hoops increase we notice that the centers of our hoops are moving in the direction of our conic distortions. This 'center shift' is caused by the asymmetry of the anthill! As we begin to place larger and larger hoops over the structure we begin to pick up the changes in the structure. In the case of X-ray clusters it is the substructure that will be picked up by these 'center shifts'.

3.3 Wavelet Transform Method

The third method is the wavelet transform method developed and supplied by Starck et al. (1995), also see Slezak et al. (1994). This method is considerably more visual than either of the previously described methods. First, it is necessary to think of the X-ray data as a superposition of different valued scales. Now let $f(x)$ be the complete data function. Its 1-dimensional wavelet transform can now be written as

$$C(a,b)=\frac{1}{\sqrt{a}}\int_{-\infty}^{\infty} f(x)g^{*}(\frac{x-b}{a})dx$$

where "a" is the scale, "b" is the location, and g* is the complex conjugate of the analyzing wavelet. Consider $C(a,b)$ which is the wavelet transform of $f(x)$. We can restore $f(x)$ with the following formula

$$f(x)=\frac{1}{C_g}\int_{0}^{\infty}\int_{-\infty}^{\infty}\frac{1}{\sqrt{a}}C(a,b)g\left(\frac{x-b}{a}\right)\frac{dadb}{a^2}$$

where:

$$C_g=\int_{0}^{\infty}\frac{|\hat{g}(v)|^2}{v}dv\ .$$

Of course, this is only true if C_g is defined. This is generally so as long as $\hat{g}(0)=0$. In other words the mean value of the interrogating wavelet must be zero. It is the ability to

vary the scale of the interrogating wavelet that makes this method a truly multi-resolution approach. In our case, the scale of the wavelets ranges from 1 to 8 pixels in order to provide a more complete range to look for substructure.

Once again, let us look at the graphical implications. Imagine that we are going to look for structure on an anthill. This time instead of using hoops or figure eights we are going to use calipers set to different sizes to measure the 2-D projected surface of the anthill. The object is to use the calipers, set at differing widths, to trace the projection in order to search for the different scale anomalies. First, let us assume that the anthill is on the order of 1 meter in size and contains several polymorphic anomalies. Let us then imagine that we start with the calipers set to a very small diameter, say 1 μm. Next, we slide the calipers along the outer surface or projection of the anthill in a tracing fashion. After doing this we see that we can only measure variations that happen to occur between the caliper edges, in this case on the order of 1 μm. As the diameter of the caliper setting is increased to larger sizes and the anthill is traced each time, larger variations in the structure can be measured with each pass. Of course, if we add up all the measured variations at all the different scales we can reconstruct our anthill in all its glory. It was hoped that the variability of this method could be used as a visual check to see at which resolution level or levels the other two methods were detecting substructure.

CHAPTER 4

THE MODELS

In order to calculate our errors and discern the significance of our results, cluster models were created.

We began by parameterizing the cluster plasma distribution using the standard King (1966) model, which appears as follows:

$$I(x,y) = I_0\left[1+\left[\frac{x}{r_c}\right]^2+\left[\frac{y}{\eta r_c}\right]^2\right]^{1/2-3\beta}$$

where I(x, y) is the x-ray intensity as a function of x and y, I_0 is the intensity at the center of the cluster, x and y are the cluster image coordinates, r_c is the radius of the core, η is the axial ratio, and β is the power-law index. Each cluster was inspected and a model was created using the 'best fit' method. During this process it was discovered that the central regions for nearly ½ of our clusters could not be fitted using the standard King model. This standard King model describes the central regions of clusters as being somewhat flattened, meaning that these areas are, for the most part, isothermal. To the contrary, we found that some of our clusters had central regions better characterized by sharp intensity spikes. We believe that this is due to cluster cooling flows.

A cluster cooling flow occurs when the gas at the center of a cluster, where the temperature and density are highest, cools through bremsstrahlung and line emission in a time less than the cluster lifetime. As the temperature drops due to cooling, the pressure in the cluster central

region also drops. In order to maintain the pressure the central density has to rise. This happens with an inward flow of gas, resulting in an excess of luminosity at the cluster centers. With the advent of newer X-ray satellites such as ASCA, better resolution is possible, which enables more accurate observations of cluster cooling flows. These more accurate observations in combination with the data presented in this paper and recent analysis of ROSAT PSPC observations (Sarazin, 1998), indicates that perhaps as many as 50% of clusters exhibit cooling flows.

As knowledge of cooling flows is still in its infancy, it was decided to ignore the cooling flow process in our models. This should not effect the results because the primary concern is substructure that resides in the areas surrounding the central regions which is adequately described by the King model. The 'best fit' models were then used to create 500 Monte Carlo simulations for each cluster in which a random amount (between 1 and 5 counts) of Poisson noise was added to each iteration. In order to fully emulate the real data fully, each simulation was divided by the appropriate exposure map and multiplied by the image live-time.

To save CPU time, the models were centered at 256, 256 of the 512, 512 image frame. The fact that only the total 'center shift' and 'moment' numbers are important in this paper and these values are independent of the models position on the image frame makes this short cut possible. Each analysis program was allowed to run on the 500 models for each cluster. The results for the 500 models for each cluster were sent to separate files and Fortran programs were used to extract the pertinent data from each file. Although it is possible to plot the results in a myriad of ways, it was decided that the results for the 'center shift' method would be in $\sigma_{model} / \sigma_{data}$ format. This process uses the actual significance of the changes in the model in respect to the data to create the plots. The 'moment' model results were plotted as histograms where the number of models having a particular moment value were binned. These plotting

criteria made it possible to compare the data to the models, find the significance of our results, and calculate our error bars. There was no reason to compare the models to the wavelet transform method for the following reason. If we know the type of noise in advance we can tailor the wavelet transform method to account for this. In our case we input Poisson noise into the program. The wavelet transform method calculates the mean and standard deviation for the noise in each resolution range and only the signal above a user defined clipping level, 3 sigma for this study, is sent to the output image. The result of this, in theory at least, is that all the structures we see in the wavelet transform images are considered significant.

CHAPTER 5

THE RESULTS

In all, 21 clusters were analyzed using all three data analysis programs the results of which are presented in figures 3-149. For each cluster we present the smoothed image and contour plot, the histogram plots for the moment model results for P_3 and P_4, and finally the $\sigma_{model}/\sigma_{data}$ and total shift plots for the 'center shift' method. Only three clusters Abell 133, Abell 514, and Abell 2052 will be discussed in detail here. I believe that these three clusters portray the variety of cluster morphologies that were encountered in our sample and thus are a good representation of the results that our analysis programs produced. In addition, the general results from all the 21 clusters will be used to compare and contrast the various methods.

5.1 Abell 133 Results

Abell 133 is a cD cluster by the Rood-Sastry designation system and has a redshift of .0566 (see Table 1). Visually this cluster appears to quite relaxed and symmetric (Figures 17 & 18). This is also how the cluster appears after inspection of the wavelet images (Figure 19). Each wavelet transformed image shows only a central regularly shaped circular image that seems to remain homogeneous as the wavelet scales get larger, which is exactly what one would expect for a relaxed cluster with little or no detectable substructure. The results for the 'moment' program run on this data frame for P_3 and P_4 (see Table 3 & Figures 20 & 21) are within 3 sigma of the model values, making them statistically insignificant, which also agrees with a

regular relaxed cluster. The total shift in RA and DEC (Figure 23) as reported by the 'center shift' method shows that there is variation in shift of less than 0.5 arc minutes over most of the 13 arc minute search radius. There appears to be a somewhat larger shift of about 1 arc minute in the outer 3 arc minutes of this radius. However, changes of even a single count can make the results seem much larger out here where the counts in general are very low. It can be seen from the graph of $\sigma_{model} / \sigma_{data}$ (Figure 22) that the mean value (see Table 2) is about .73 with a calculated standard deviation value of .21 placing many of the values near unity. This indicates that there is minimal difference between the two values and therefore little or no substructure detected by the 'center shift' method.

5.2 Abell 514 Results

Abell 514 has a R.S. designation of F, a Bautz-Morgan type of II-III, and a velocity dispersion of 874 km/sec with a red shift of 0.0713 (see Table 1). Abell 514 is perhaps the most visually interesting cluster of the sample. The cluster (Figures 38 & 39) appears as an irregular cloud that is surrounded by diffuse plasma forming an elongated kidney-shaped object. The wavelet transform images (Figure 40) show substructure on a progressive scale. In the 2 pixel scale several small knots of plasma can be seen with very little diffuse plasma present. In the 3 pixel scale more of the diffuse plasma can be seen. This diffuse plasma appears as an irregular and elongated foot-like extension that appears to be connecting several of the more prominent plasma knots. By the time the 4 pixel scale is reached virtually all the knots are no longer individually visible and in the 5 pixel scale the cluster looks like a single elongated blob of diffuse plasma with a brightened end. The 'moment' program (see Table 3 & Figures 41 & 42) run on the data yields a value of P_3 that is 37 sigma above the mean model values! The value for P_4 is surprisingly small given the extremely large P_3 value. A data value of

4.5 sigma above the mean model values indicates only a moderate significance. The 'center shift' analysis method (Table 2 & Figure 44) shows a shift of almost 6 arc minutes. This proves to be very significant when compared to the $\sigma_{model} / \sigma_{data}$ plot (Figure 43), which has a mean value of .11 with only a .03 standard deviation value. This indicates that only about 10% of the models have a center shift that is on the order of the center shift of the cluster.

5.3 Abell 2052 Results

The third cluster is Abell 2052 which has a R.S. designation of cD and a B.M. designation of I-II (see Table 1). It is known to possess a large cooling flow and has a redshift of .0348. By observing the contour plot (Figures 52 & 53) of this cluster it is possible to see that it appears slightly irregular, possessing a mostly off center oval shape. If the wavelet transforms (Figure 54) are observed it is possible to see only a small portion of this apparent offset. For the most part the wavelet data shows nothing particularly irregular on any scale. The significance observed when the 'moment' program is run on the data in the 2nd moment (see Table 3) which would pick up this apparent elongation cannot be computed because our models were made to emulate this type of feature. The value of P_3 (see Table 3 & Figure 55) appears to be marginally significant at best, possessing a value only 4.5 sigma above the mean model values. The cluster value for P_4 (Figure 56) is completely insignificant, on the order of 1.5 sigma above the average model value. The 'center shift' method (Figure 58) shows only a very small (<.5 arc min.) overall shift inside the first 9.75 arc minutes of a 15 arc minute search radius. Outside this radius, extending through to the outer edge, we see a total shift of about 1.5 arc minutes. This shift is relatively small but appears quite significant when the $\sigma_{model} / \sigma_{data}$ plot (Figure 57) is viewed. This plot has a mean value of .38 with a standard deviation of .11. (see Table 2).

This significance can best be explained if the off-center characteristics of the cluster plasma are taken into account.

The above three described clusters were picked to be representative of several types of cluster morphologies: a regular relaxed cluster with little or no substructure at any level, a cluster that is very irregular and shows substructure at many different levels, and finally a cluster that is somewhat regular on some scales but shows substructure at others. I believe that these clusters clearly show the sensitivity ranges of the three analysis programs. For instance, Abell 133 appears to be 'regular' on virtually all scales to all three programs. If the results of each program are inspected individually it would not be misleading to say that this cluster appears to be a regular relaxed system. For Abell 514 each program shows substructure on different levels. The wavelet transform program shows substructure in the intermediate and small levels while still showing the overall shape and form of the cluster. However, with no quantitative numbers it is difficult to classify the cluster or compare it to other clusters. The 'moment' method's large P_3 value indicates that the shape is somewhat triangular, which can be seen if one imagines a narrow elongated triangle lying on its side. The elevated P_4 value indicates that there is at least some amount of surrounding substructure. These structures are indeed observed in the cluster, and with the quantitative numbers it is possible compare it to other clusters. However the program doesn't present a very visual picture of the cluster. The 'center shift' results shown on the total shift plot for Abell 514 shows very strong indications for substructure. This method does not tell us exactly what kind of substructure there is, but it can indicate how "strong" the substructure is. It can also tell us how that substructure is oriented in relation to the main structure and image orientation. This method also provides the quantitative means necessary to compare one cluster to another directly. The results for Abell 2052 show the clear differences between the programs. The wavelet transform program shows

little or no irregularity. Due to the fact our models were made to emulate the clusters' overall oval shape, we are not able to tell the significance of the 'moment' method P_2 results. However, if the P_2 result is compared to the other clusters P_2 values, it does not appear very large at all. In fact it turns out to be one of the smallest! On the other hand the center shift method shows a clearly significant result, indicating that at least for this example it is capable of detecting very subtle changes.

CHAPTER 6

CONCLUSIONS

Great care was taken to find and collect a non-biased group of rich galaxy clusters, run three different types of analysis programs on each of them, and create cluster models in order to determine the significance of our results. We are now in a position to ask ourselves, what conclusions, if any can be drawn from this experience? In fact, there are several interesting conclusions that can be drawn from our research. Let us recall the three main questions proposed in the introduction and attempt to answer them one at a time.

1) How do the three analysis methods used in this survey compare?

It has already been seen from the detailed examples that the three methods appear to be in agreement for the most obvious substructure cases. In order to get a better picture of the overall agreement between the two analytical methods we can look at the comparison chart on Table 4. Before any comparisons can be made it must be stated that in order to stay on the conservative side a 6 sigma cut-off for the 'moment' method is used. For the 'center shift' method a value of (mean + sigma ≥ 0.7) is taken as the approximate cut-off. Using these criteria and taking marginal results as positive, it can be seen that there is agreement between the methods for all but 5 of the clusters. As can be seen from the comments section of the chart, one of the disagreements for the Abell 3111 can be attributed to the cluster observation having counts that are possibly too low to work with. Two clusters, Abell 2052 and 3112, have predominantly off-set oval structures not accounted for in the 'moment' values of P_3 and P_4.

As our models were made with this type of substructure we can ignore this apparent discrepancy. For Abell 3266 and 3562 it is possible that the substructure configurations are neither triangular nor cross like. These are the approximate shapes that the P_3 and P_4 moments would pick up. The type of substructure observed in these clusters might be more accurately detected in higher moments.

As far as individual program performance is concerned, there is a general trend observable. The wavelet transform method allows us to attain a strong visual sense for the cluster structure. However, this is attained without clear quantitative means of comparing one cluster to another. The 'moment' program supplies us with the quantitative means of comparison as well as giving us a general sense of the overall cluster morphology. The weakness of this program seems to be that it is fairly insensitive to small changes in intensity at or near the cluster centers or at their extremities. The 'center shift' method by its nature is more sensitive to small changes at any position on the image. It is possible to use the results of this program to produce RA and DEC shift plots (not shown in this paper) for each cluster, making it possible to get a rough picture of how substructure is placed throughout the cluster. This data, however, only indicates substructure placement, giving little or no idea what that the intricacies of the substructure actually look like.

Clearly, taking the above observations into account, it is possible using only one of the above methods to get a fairly clear picture of substructure, given a particular sample. If we were to ignore the clusters with low counts and the fact that our models were designed to account for elongated substructure, we would find only two major discrepancies between the methods. As has already been stated, the last two may be due to our use of only low moment values. Of course, it is always desirable to have the most complete picture attainable. This is true especially when attempting to expound on an issue as sensitive and controversial as the

value of Ω. It must also be taken into consideration the idea that all substructure may not be created equal! There may be many explanations for the presence of substructure in galaxy clusters. For instance, if we wished to know if clusters are still forming we would look for evidence of large amounts of substructure at or near the centers of a clusters, which might indicate that the clusters were still undergoing dynamic relaxation. Suppose all that was found were fairly spherical cluster cores with some small outlying substructure blobs. This finding might indicate that these clusters are mature relaxed systems that happen to have recently swallowed some nearby matter, indicating that they are not young at all. With this in mind it becomes quite clear that searches of this type must be conducted with great care.

2) What is the prevalence of substructure in rich clusters of galaxies?

Recall that we started with the most unbiased cluster sample possible. Unfortunately, because not all clusters in this sample were observed by ROSAT or some observations were miss-pointed, our data set is only a subset of the original sample. We do, however, believe that this data set is still an unbiased representation. To convince ourselves of this the abstract for each observation proposal was searched. It was found that only 1 (Abell 3266) of the 21 cluster observations was done for the express purpose of a substructure search. Three others (Abell 3111, 3112, 3158) were observed for evidence of cluster-cluster or cluster-supercluster interactions. Generally this interaction leads to cluster elongation, a shape we do not consider substructure in our survey. However, to be conservative we take this as possible evidence for substructure and therefore possible sample biasing. Seven clusters (Abell, 85, 119, 133, 754, 3562, 3667, and 3897) were observed to help probe their cluster mass functions and help determine binding mass and dark matter distributions. Four clusters (Abell 496, 2052, 4038, and 4059) were observed to investigate cooling flow clusters. The remaining six were observed

for a variety of reasons ranging from measuring the brightness gradients of clusters inside super clusters to measuring the X-ray emissions of clusters near WAT (Wide-Angle-Tailed) radio sources. With this in mind and again accepting marginal results as positives, the 'center shift' method found 13 of 21, or 62% of clusters showing evidence of substructure. The 'moment' method found that 11 of 21 clusters, or about 52% of the sample, exhibits definitive evidence for significant substructure. If our sample is indeed non-biased, then this is clear evidence that galaxy clusters are still forming.

3) What implications does this result have on the current accepted value of Ω?

Recall, that if galaxy clusters are still forming, this implies we must accept an increased value of Ω. At least larger than the currently held value of $\Omega \leq 0.2$.

4) Bonus Question: What is the percentage of rich galaxy clusters with cooling flows?

As frequently happens in scientific endeavors of this type, an unexpected but important observation was made. During the modeling phase of our research it was found that almost 50% of our sample exhibited very high counts at their cluster cores, indicating cooling flow activity. Until very recently it was unknown what the cooling flow percentage of galaxy clusters was or even if the phenomena was real. This was due to the inability to resolve the clusters central regions finely enough. In the last two years instruments such as A.S.C.A and others have given us the resolution necessary to begin a comprehensive search for cooling flows in galaxy clusters. The most recent information has led to the finding that as many as ½ of all galaxy clusters exhibit some cooling flow mechanics (Sarazin et al 1998). With these types of clusters occupying a greater percentage of the total it is imperative that our models become more sophisticated. We can only know the significance of our data if we properly and accurately model the physical phenomena we are probing.

It is hoped that our results, along with further research in this area, will lead to the construction of a more reliable database, one that can not only be used to help answer the questions of today but one that is also sufficiently detailed to answer the questions of tomorrow.

APPENDIX A

TABLES

Table 1: General Cluster Information

Abell Cluster	z	σ_V^c	R.A. (J2000)	DEC. (J2000)	Rood-Sastry Type	Bautz-Morgan Type
85	.0556	853	00 41 49	-09 17 51	CD	I
119	.0440	740	00 56 14	-01 15 58	C	II - III
133	.0566	—	01 02 38	-21 47 53	CD	–
496	.0327	682	04 22 38	-13 15 40	CD	I:
500	.0666	—	04 38 52	-22 06 38	I	III
514	.0731	874	04 47 40	-20 25 44	F	II – III:
754	.0534	—	09 08 35	-09 37 28	CD	I – II:
2052	.0348	—	13 33 31	-31 40 22	CD	I – II
2382	.0648	—	21 52 01	-15 39 53	L	II – III
2717	.0498	512	00 03 15	-35 57 18	–	I - II
2734	.0618	581	00 11 20	-28 52 18	–	III
3111	.0775	770	03 17 47	-45 44 05	–	I – II
3112	.0751	950	03 17 56	-44 14 06	–	I
3158	.0590	1005	03 44 35	-53 28 27	–	I – II
3266	.0594	1122	04 31 09	-61 26 39	–	I – II
3558	.0478	—	13 27 59	-31 30 31	–	I
3562	.0499	—	13 33 31	-31 40 22	–	I
3667	.0530	1059	20 12 29	-56 48 59	–	I – II
3897	.0733	548	22 39 17	-17 23 21	–	II
4038	.0283	839	23 47 53	-28 09 19	–	III
4059	.0478	536	23 57 01	-34 45 36	–	I

Table 2: Center shift data

Abell Cluster	$\sigma_{model}/\sigma_{data}$ Mean	σ	Number of values Greater than 1
85	.28	.07	0
119	.29	.07	0
133	.73	.21	54
496	.94	.26	175
500	.31	.12	0
514	.11	.03	0
754	.21	.06	0
2052	.38	.11	0
2382	.65	.20	24
2717	.41	.15	0
2734	.26	.10	0
3111	.30	.10	0
3112	.42	.17	0
3158	.54	.18	11
3266	.35	.09	0
3558	.15	.04	0
3562	.24	.06	0
3667	.10	.03	0
3897	.89	.33	184
4038	.57	.25	35
4059	.63	.23	30

Table 3: Moment data

ABELL CLUSTER	P_0	P_1 / P_0	P_2 / P_0	P_3 / P_0	Data distance from models in sigma	P_4 / P_0	Data distance from models in sigma
85	0.739E+11	0.330E+01	0.109E+02	0.578E+00	24	0.194E+00	14
119	0.500E+11	0.137E+01	0.165E+01	0.263E+01	50	0.273E+00	11
133	0.326E+11	0.297E+00	0.495E+01	0.166E+00	2.2	0.341E-01	.89
496	0.849E+11	0.120E+01	0.698E+00	0.109E+00	1.2	0.262E-01	.67
500	0.264E+10	0.311E+00	0.262E+00	0.288E+01	20	0.445E+00	6.9
514	0.242E+10	0.439E+01	0.147E+03	0.585E+01	37	0.485E+00	4.5
754	0.165E+11	0.503E+04	0.932E+02	0.588E+01	50.2	0.182E+01	8.2
2052	0.398E+11	0.832E+00	0.120E+01	0.165E+00	4.5	0.509E-01	1.5
2382	0.345E+10	0.252E+01	0.269E+02	0.112E+01	7.5	0.311E+00	4.6
2717	0.316E+10	0.160E+01	0.957E+01	0.127E+01	8.1	0.504E+00	7.5
2734	0.145E+10	0.108E+01	0.751E+01	0.121E+01	14	0.519E-01	1.4
3111	0.940E+08	0.144E+01	0.171E+02	0.500E+01	5.7	0.239E+01	5.8
3112	0.118E+10	0.495E+01	0.345E+01	0.804E-01	.44	0.273E-01	.20
3158	0.160E+10	0.459E+01	0.212E+02	0.621E+00	3.1	0.113E+00	.91
3266	0.217E+11	0.486E+01	0.170E+02	0.140E+00	2.1	0.169E-01	.62
3558	0.527E+13	0.772E+00	0.468E+02	0.250E+01	312	0.681E+00	32
3562	0.503E+11	0.196E+01	0.184E+02	0.133E+00	1.7	0.145E+00	3.8
3667	0.782E+11	0.218E+01	0.522E+02	0.184E+01	71	0.574E+00	22
3897	0.474E+08	0.654E+00	0.203E+01	0.242E+01	2.4	0.524E+00	1.0
4038	0.542E+10	0.306E+01	0.149E+02	0.570E-01	.05	0.172E+00	1.4
4059	0.577E+10	0.114E+01	0.305E+01	0.168E-01	.16	0.795E-01	1.4

Table 4: Comparison Table

Abell Cluster	Center Shift Detection	Moment P_3 Detection	Moment P_4 Detection	Agreement	Comments
85	yes	yes	yes	yes	——
119	yes	yes	yes	yes	——
133	no	no	no	yes	——
496	no	no	no	yes	——
500	yes	yes	yes	yes	——
514	yes	yes	no	yes	——
754	yes	yes	yes	yes	——
2052	yes	no	no	no	Offset oval shape not accounted for in P_3 or P_4 values
2382	no	yes	no	no	Possibly due to low counts.
2717	yes	yes	yes	yes	——
2734	yes	yes	no	yes	——
3111	yes	marginal	marginal	marginal	Possibly due to very low counts
3112	yes	no	no	no	Offset oval shape not accounted for in P_3 or P_4 values
3158	no	no	no	yes	——
3266	yes	no	no	no	Substructure doesn't fit P_3 or P_4 shapes.
3558	yes	yes	yes	yes	——
3562	yes	no	no	no	Substructure doesn't fit P_3 or P_4 shapes.
3667	yes	yes	yes	yes	——
3897	no	no	no	yes	——
4038	no	no	no	yes	——
4059	no	no	no	yes	——

APPENDIX B

FIGURES

ABELL 85

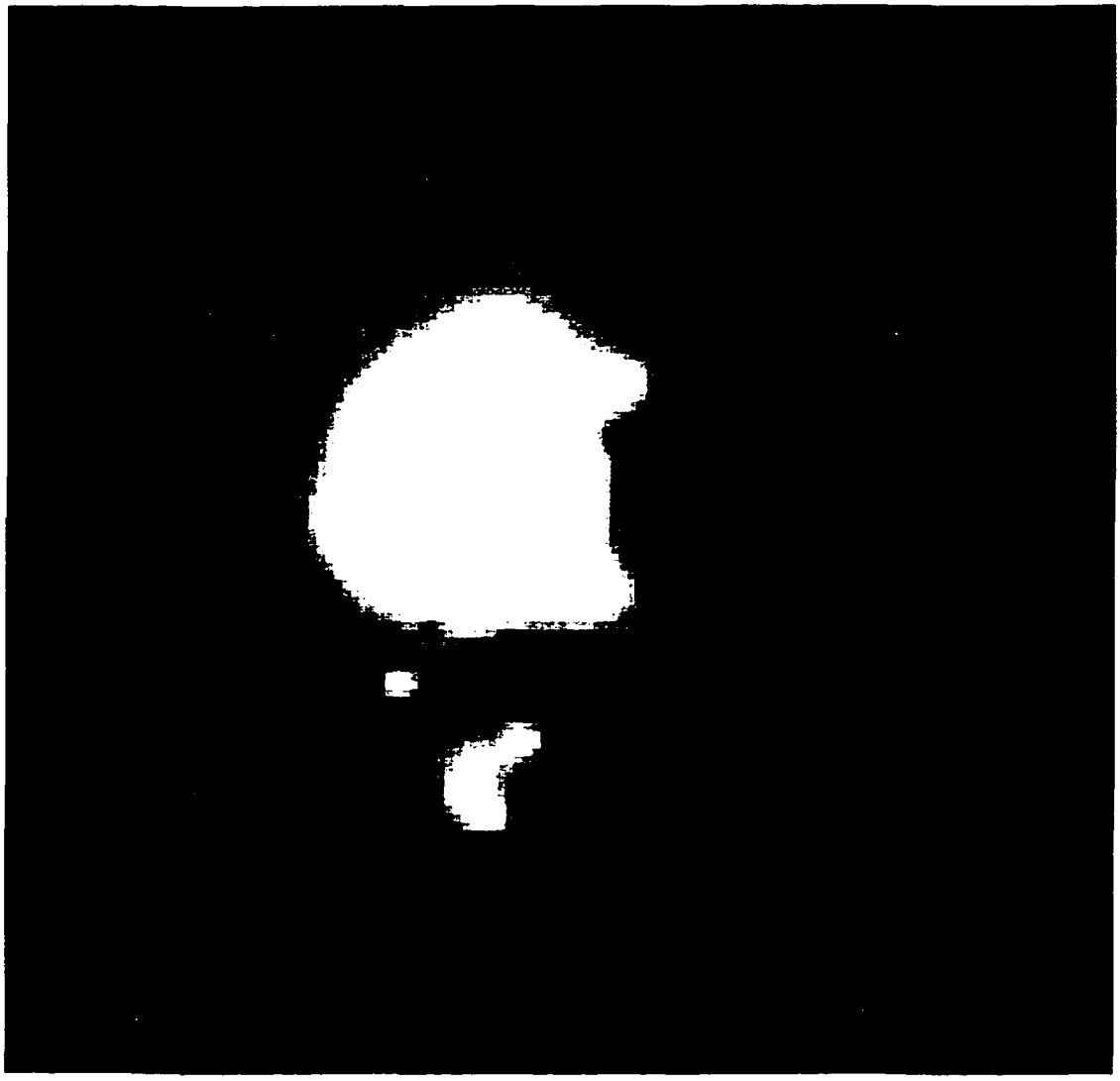

Figure 3. Cleaned and filtered image of Abell 85. Scale is approximately 2 Mpc per side.

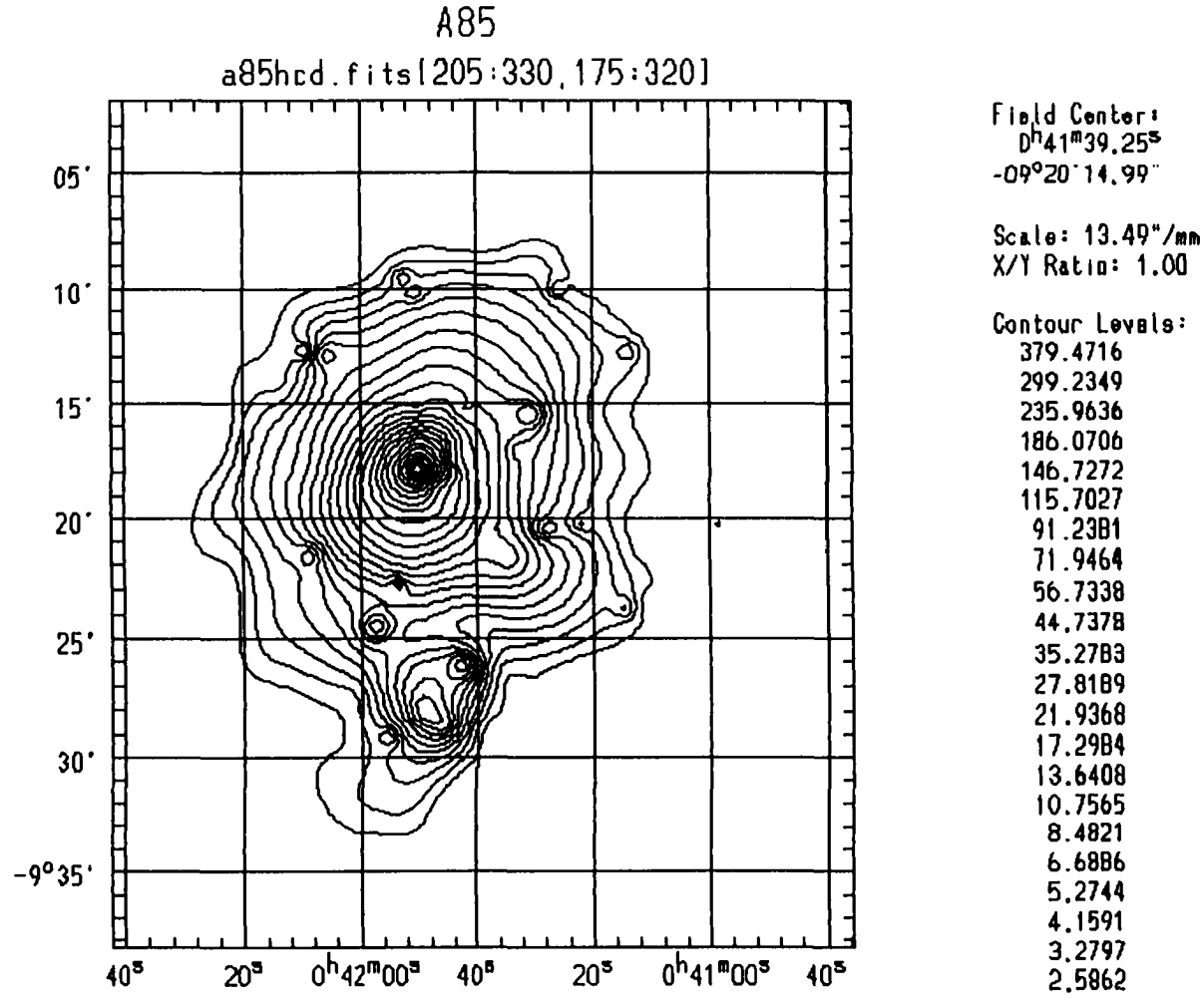

Figure 4. Contour plot for Abell 85. Contour lines are in counts. Scale is approximately 2 Mpc per side.

ABELL 85

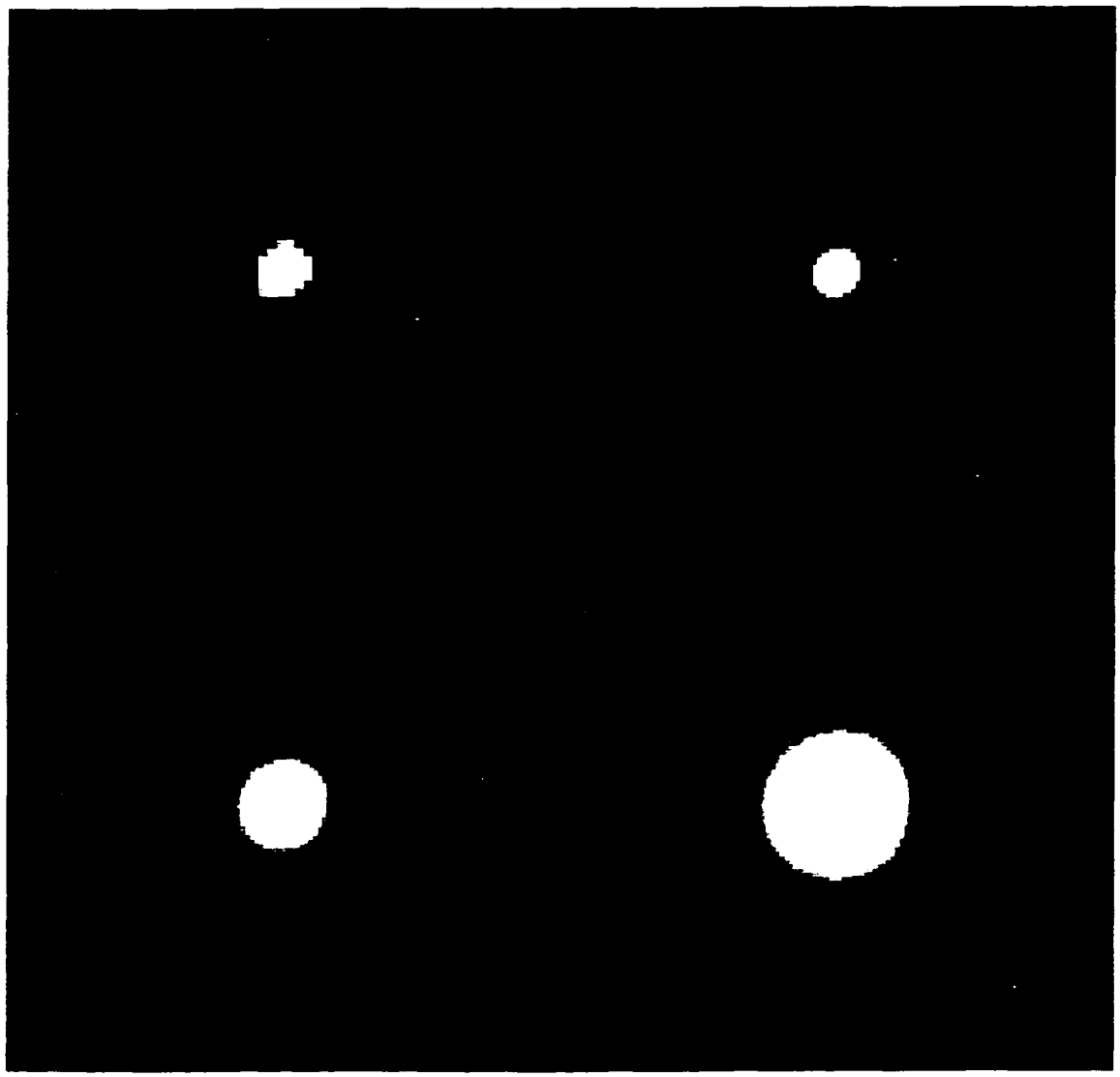

Figure 5. Wavelet transform images for Abell 85. Clockwise from upper left in 2, 3, 4, and 5 pixel scales.

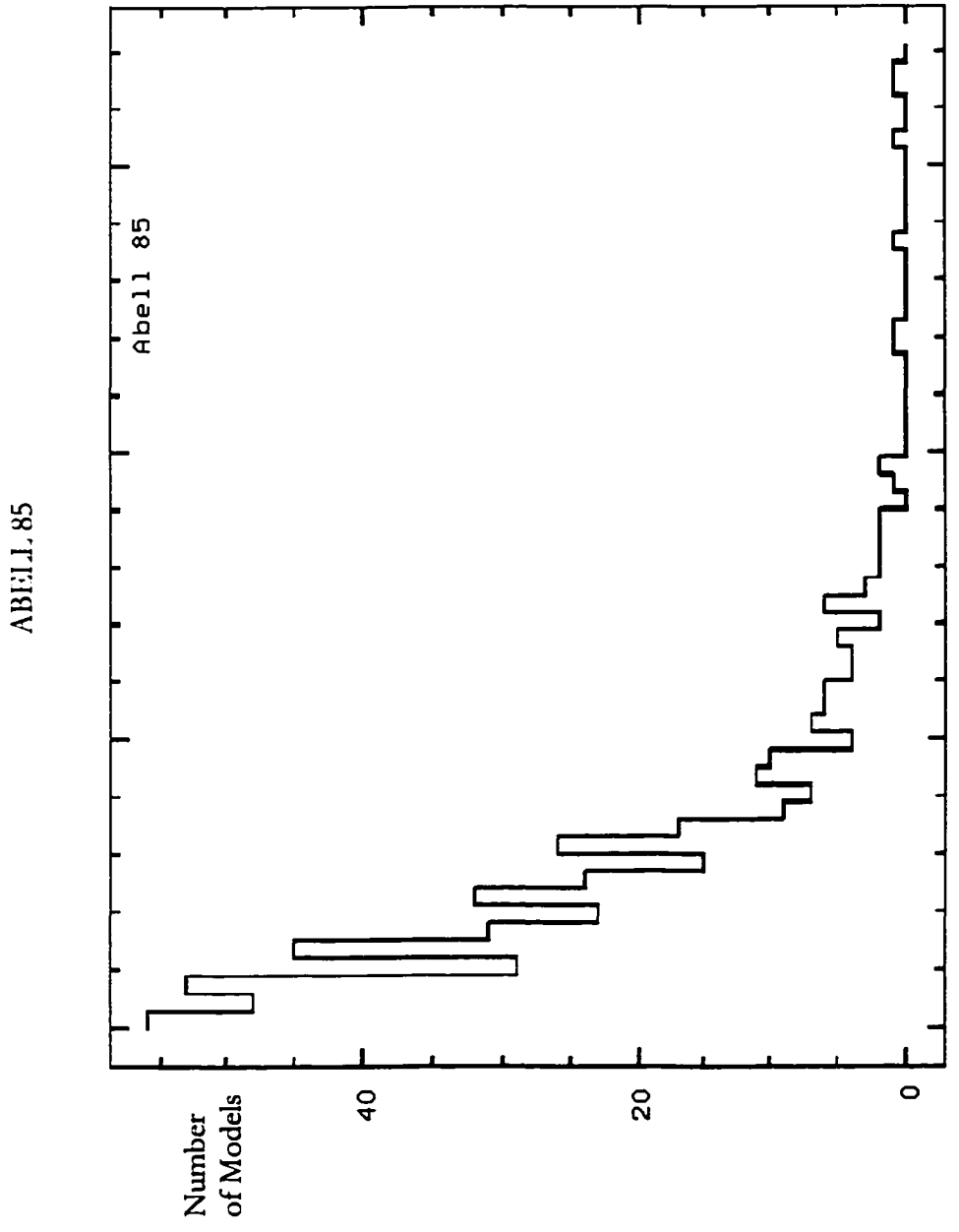

Figure 6. Histogram plot for P_3 moment for models of Abell 85.

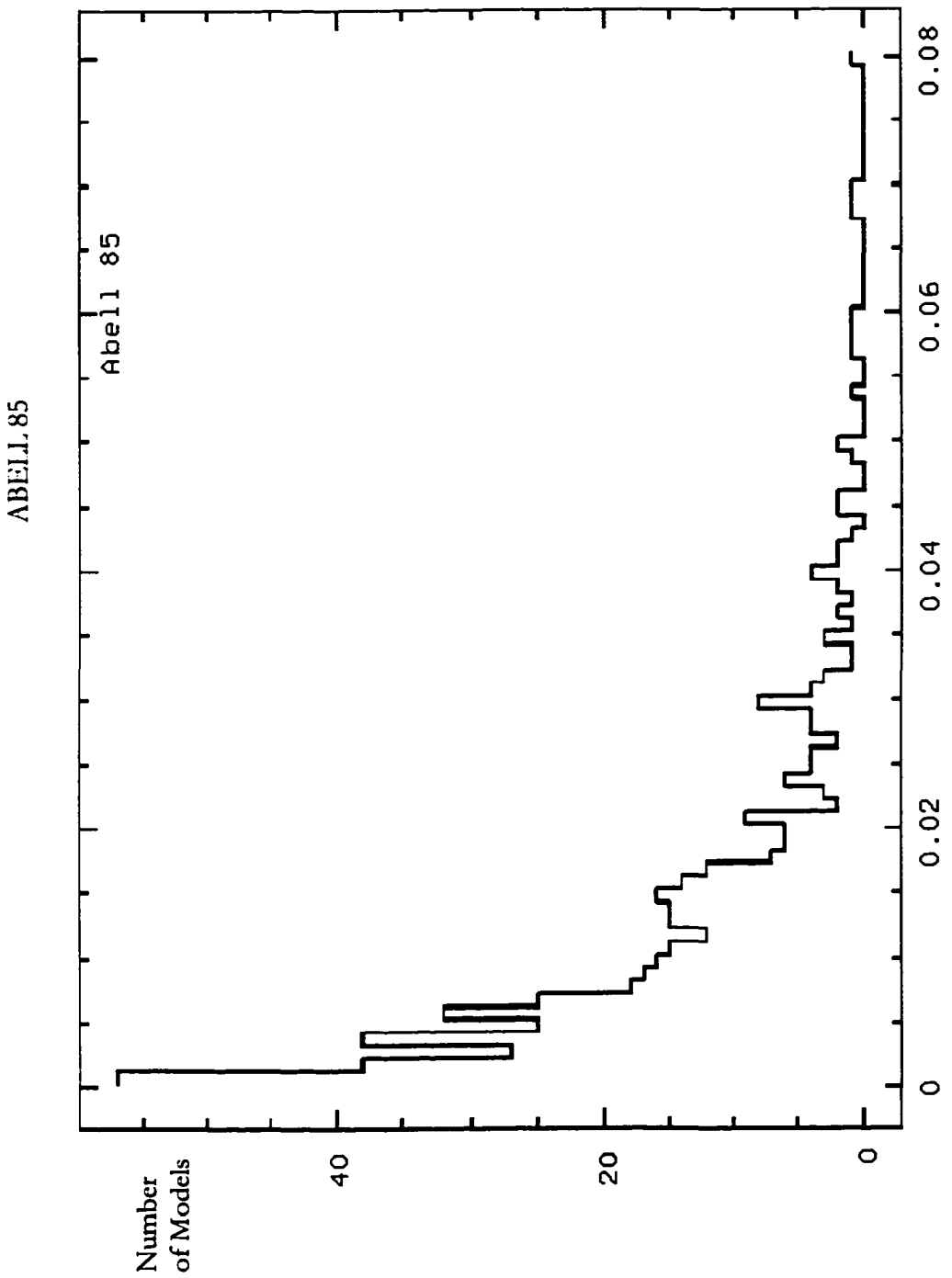

Figure 7. Histogram plot for P_4 moment for models of Abell 85.

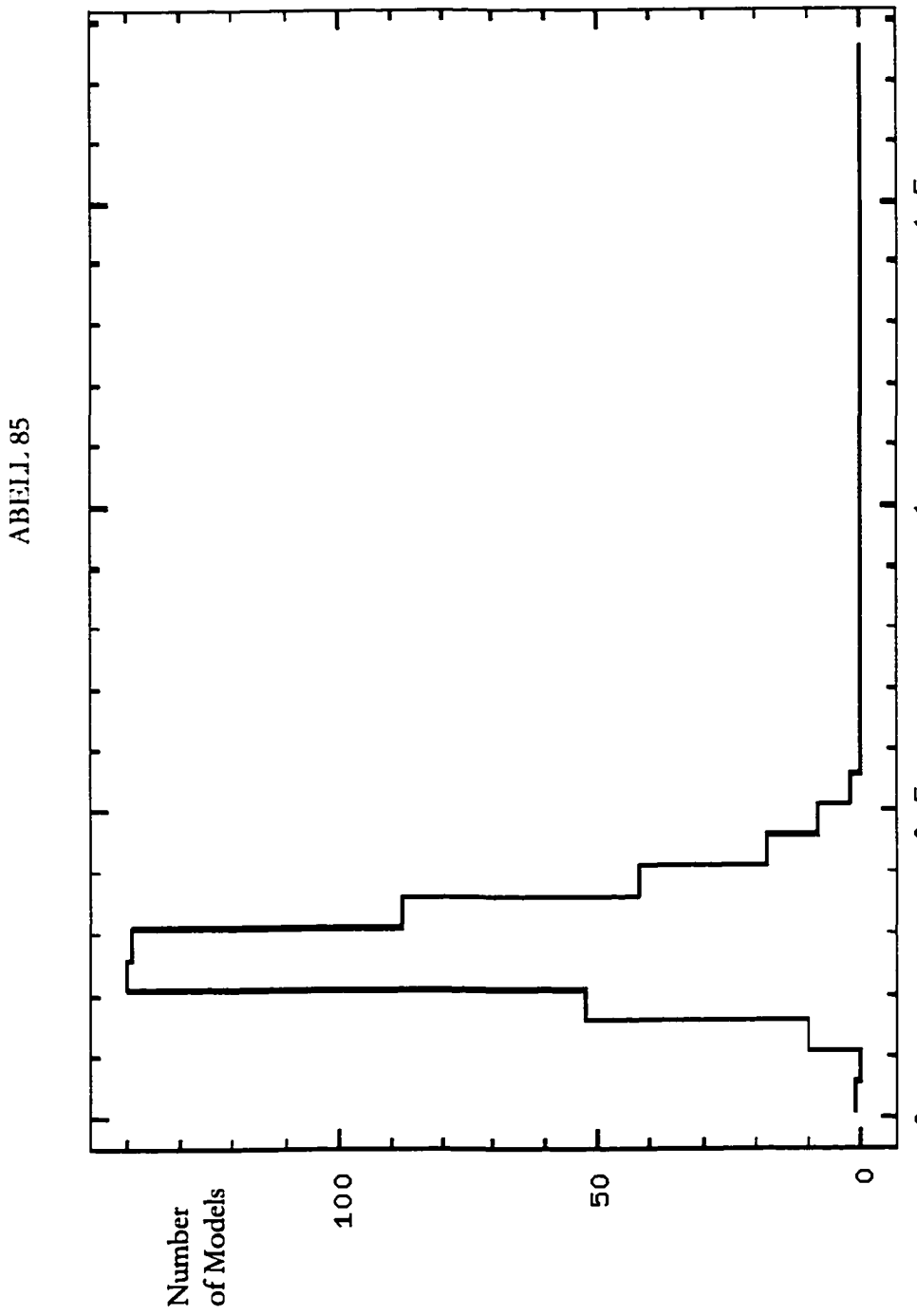

Figure 8. Sigma significance plot for Abell 85 for 'center shift' program.

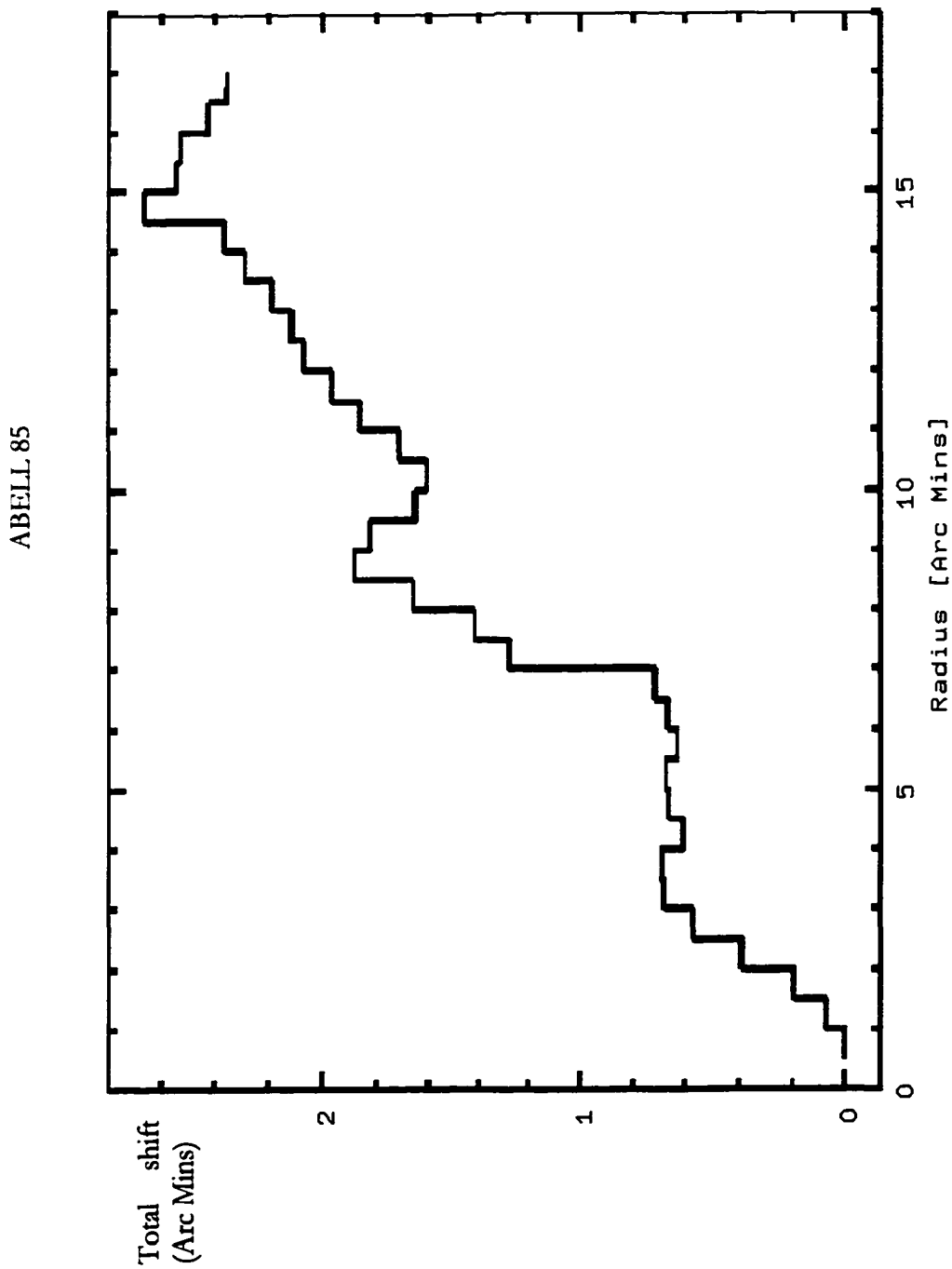

Figure 9. Total shift plots for Abell 85 for 'center shift' program.

ABELL 119

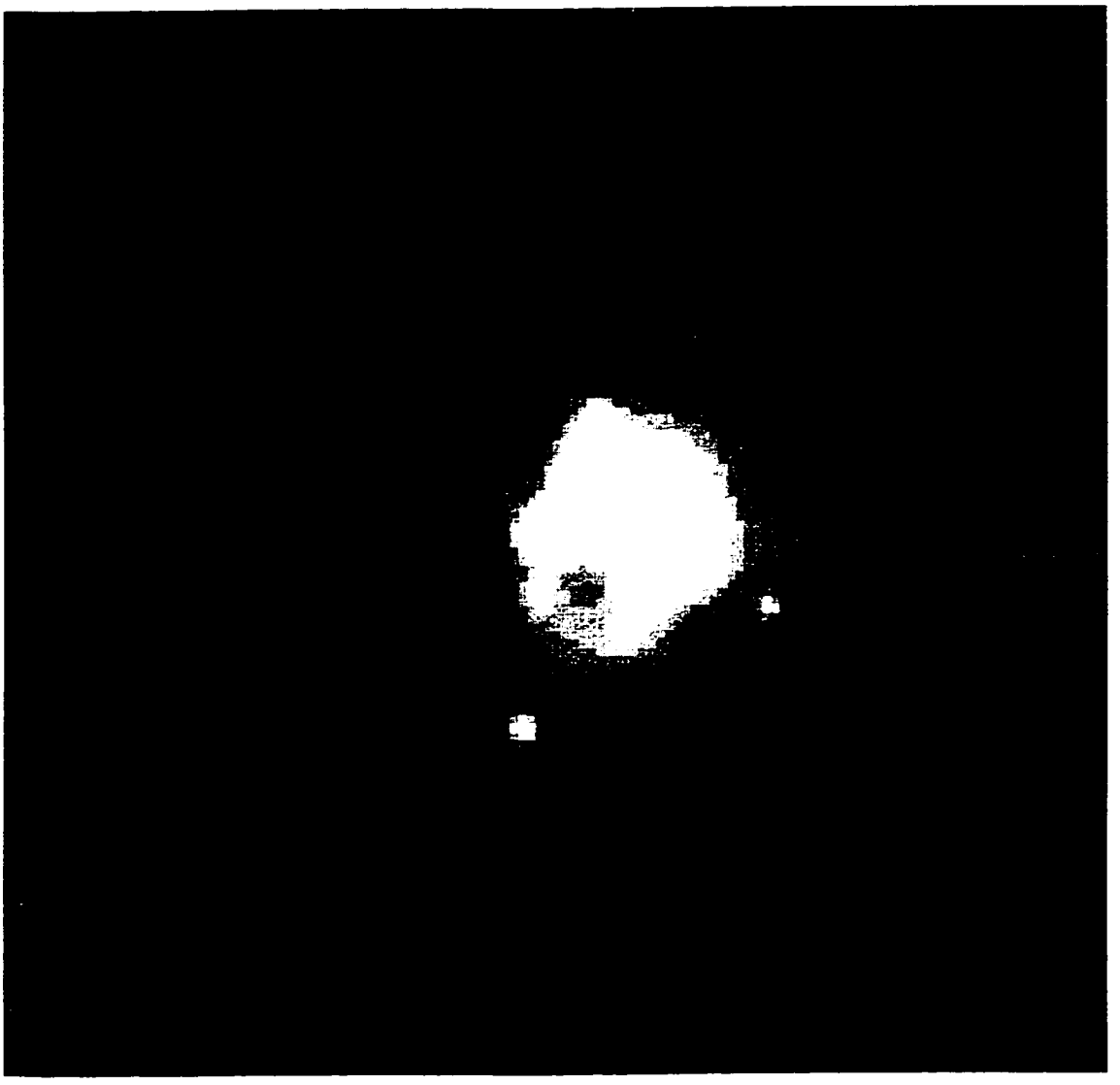

Figure 10. Cleaned and filtered image map of Abell 119. Scale is approximately 2 Mpc per side.

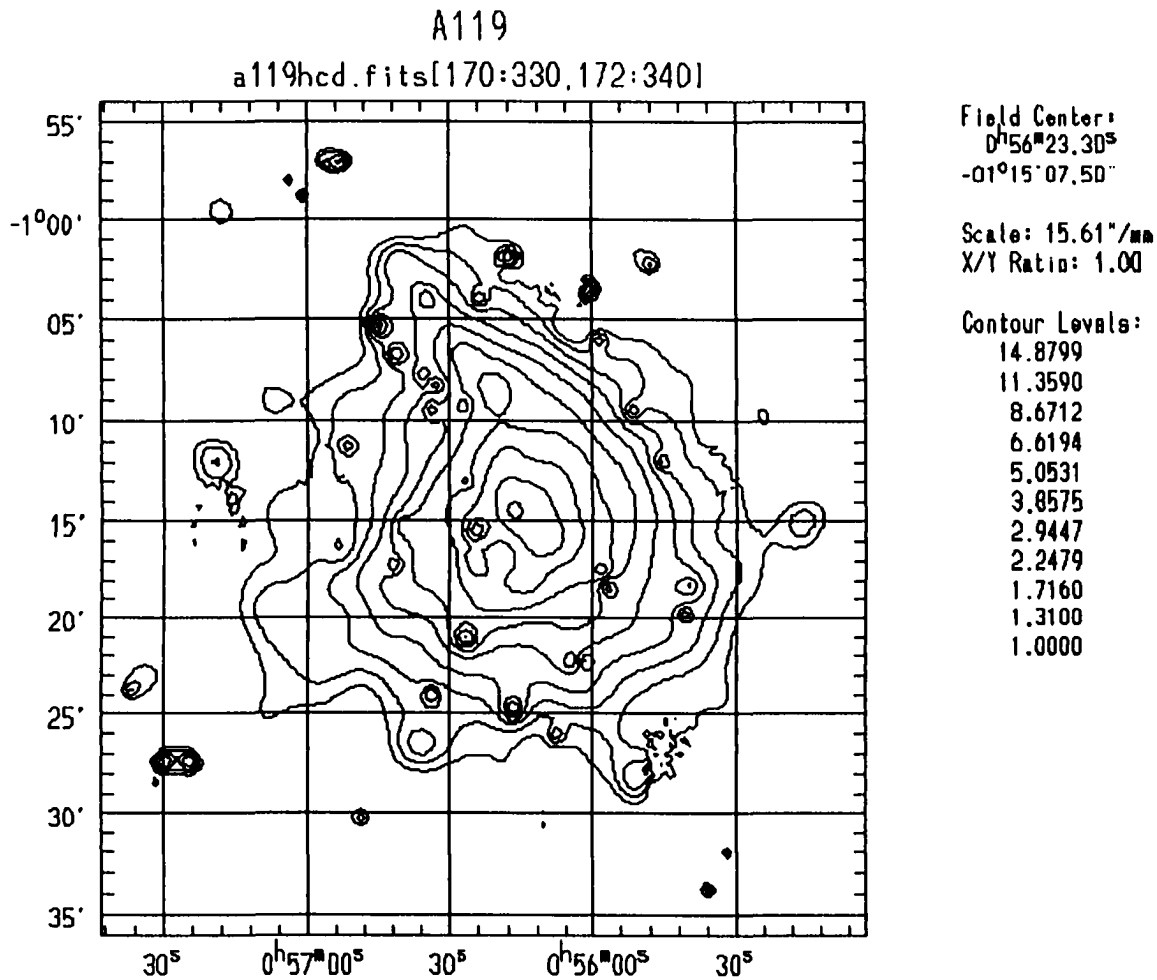

Figure 11. Contour map of Abell 119. Scale is approximately 2 Mpc per side. Contour levels given in counts.

ABELL 119

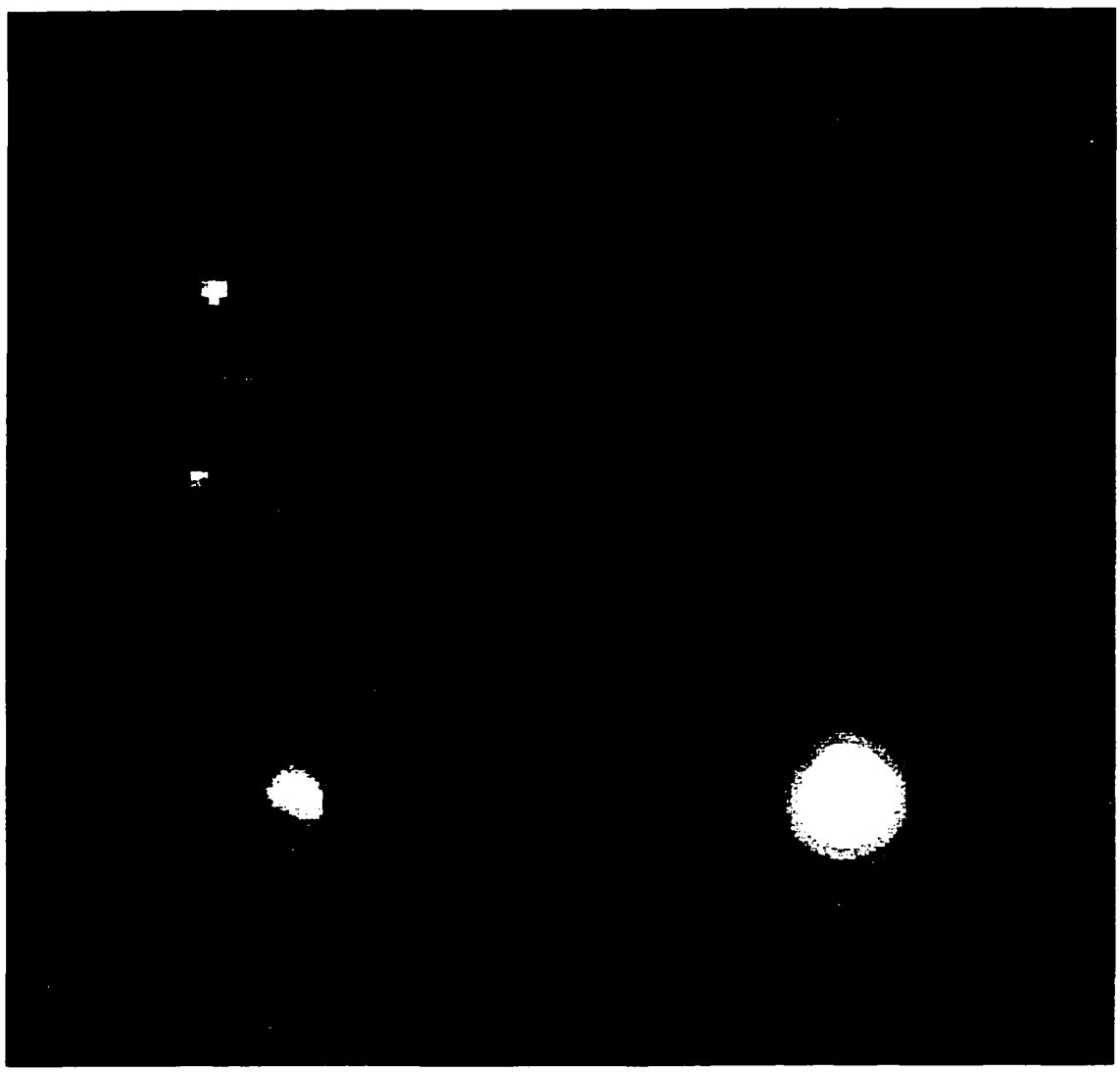

Figure 12. Wavelet transform images for Abell 119. Clockwise from upper left in 2, 3, 4, and 5 pixel scales.

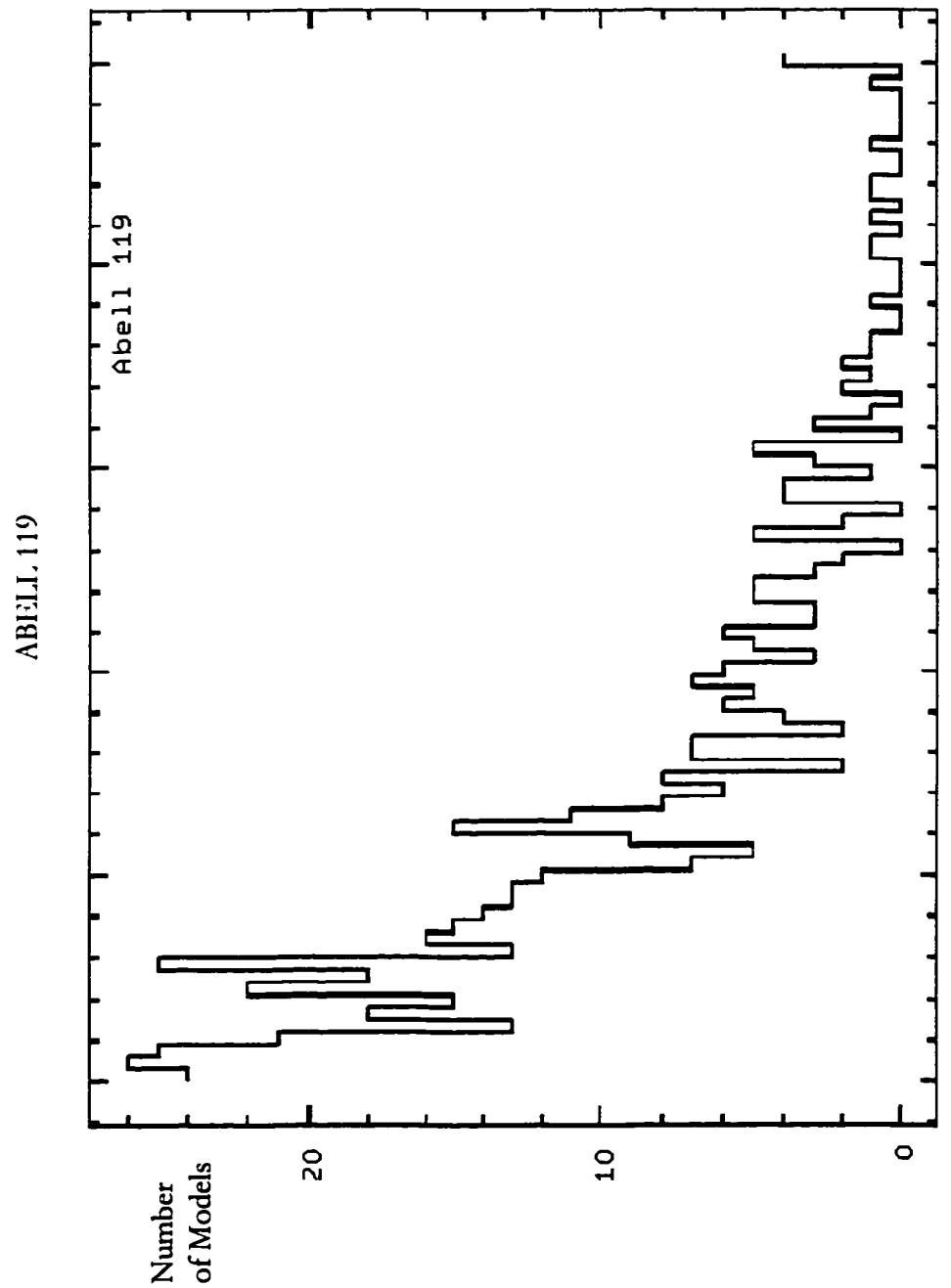

Figure 13. Histogram plot for P_3 moments for models of Abell 119.

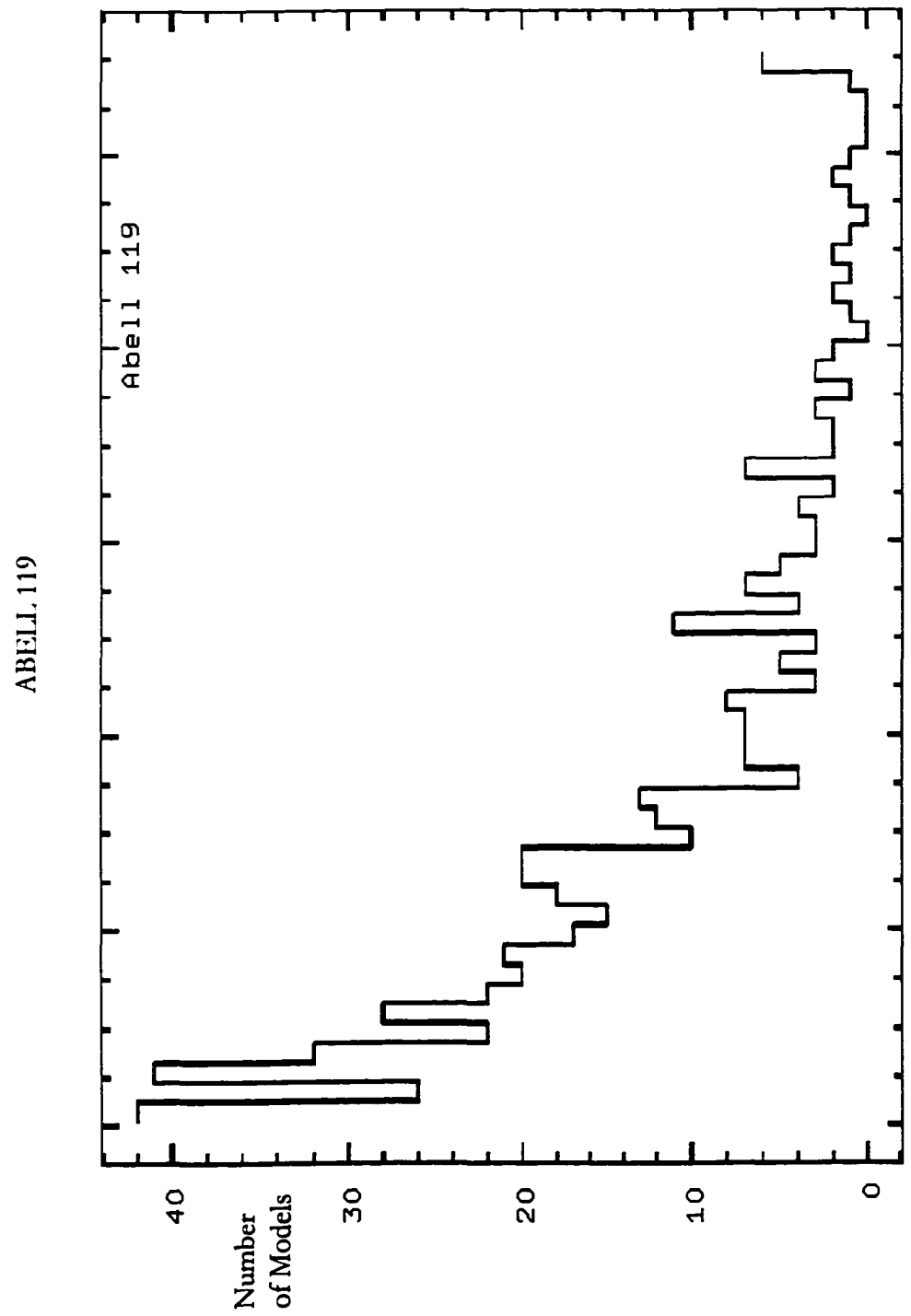

Figure 14. Histogram plot for P_4 moment for models of Abell 119.

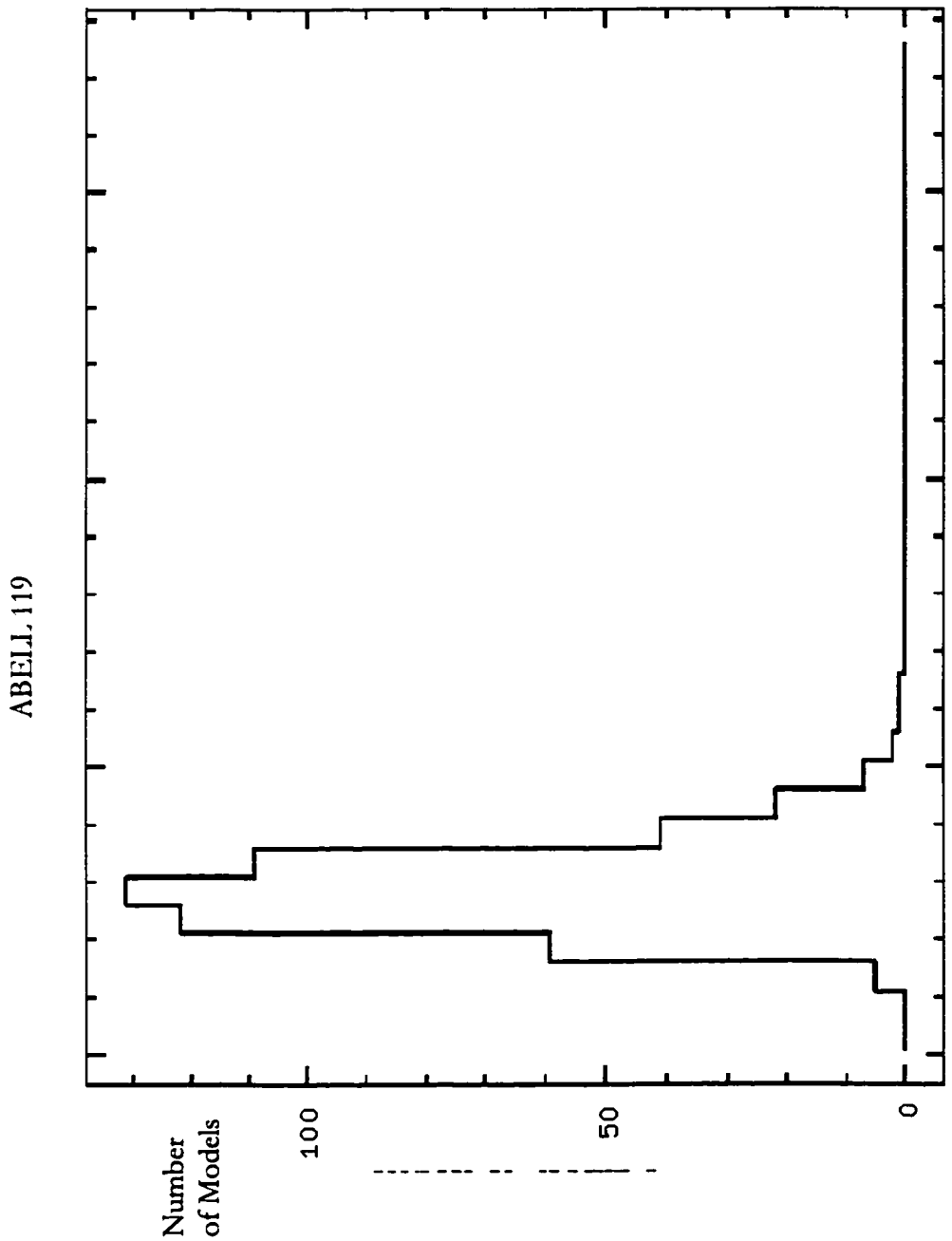

Figure 15. Sigma significance plot for Abell 119 for 'center shift' program

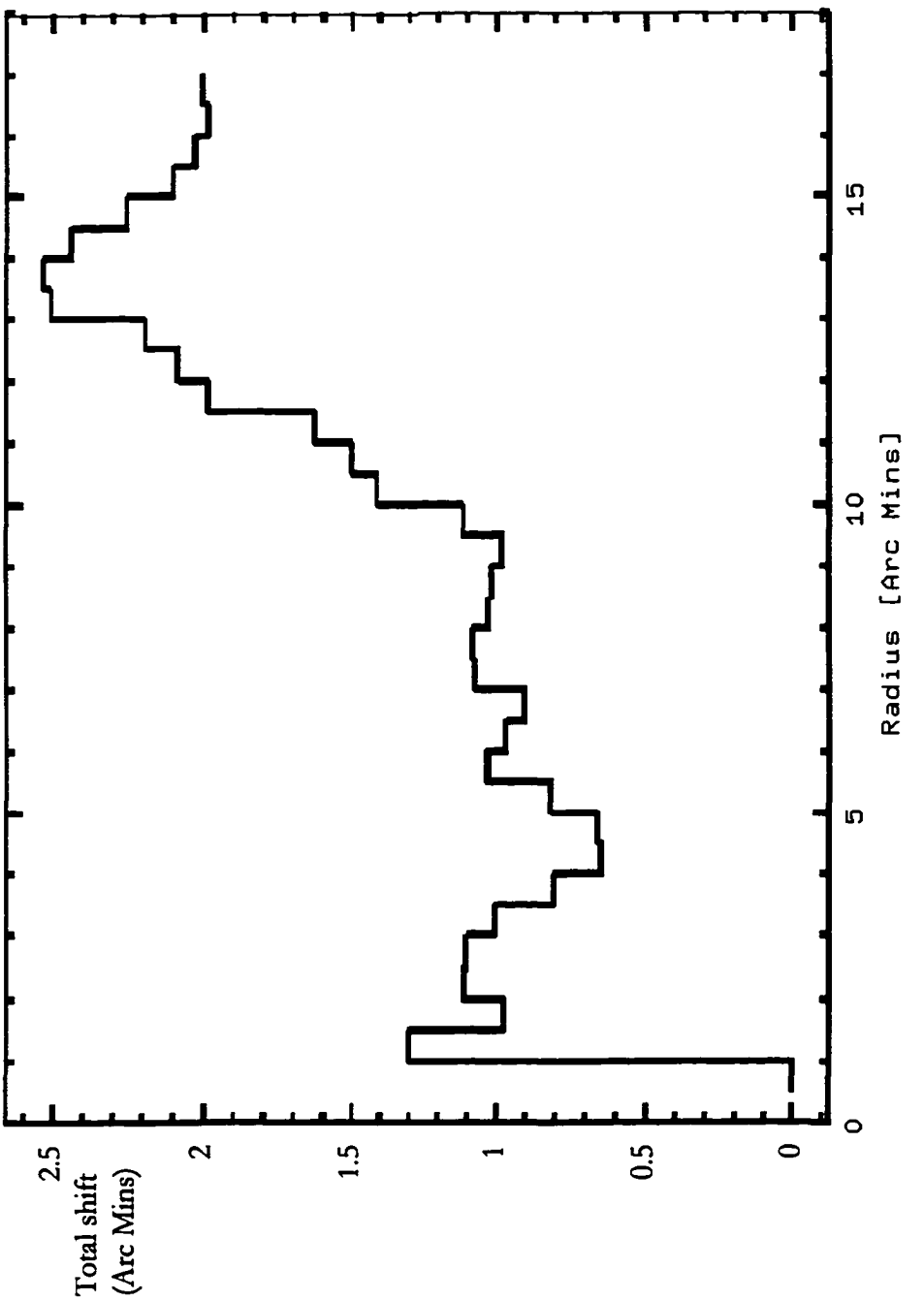

Figure 16. Total shift plot for Abell 119 for 'center shift' program

ABELL 133

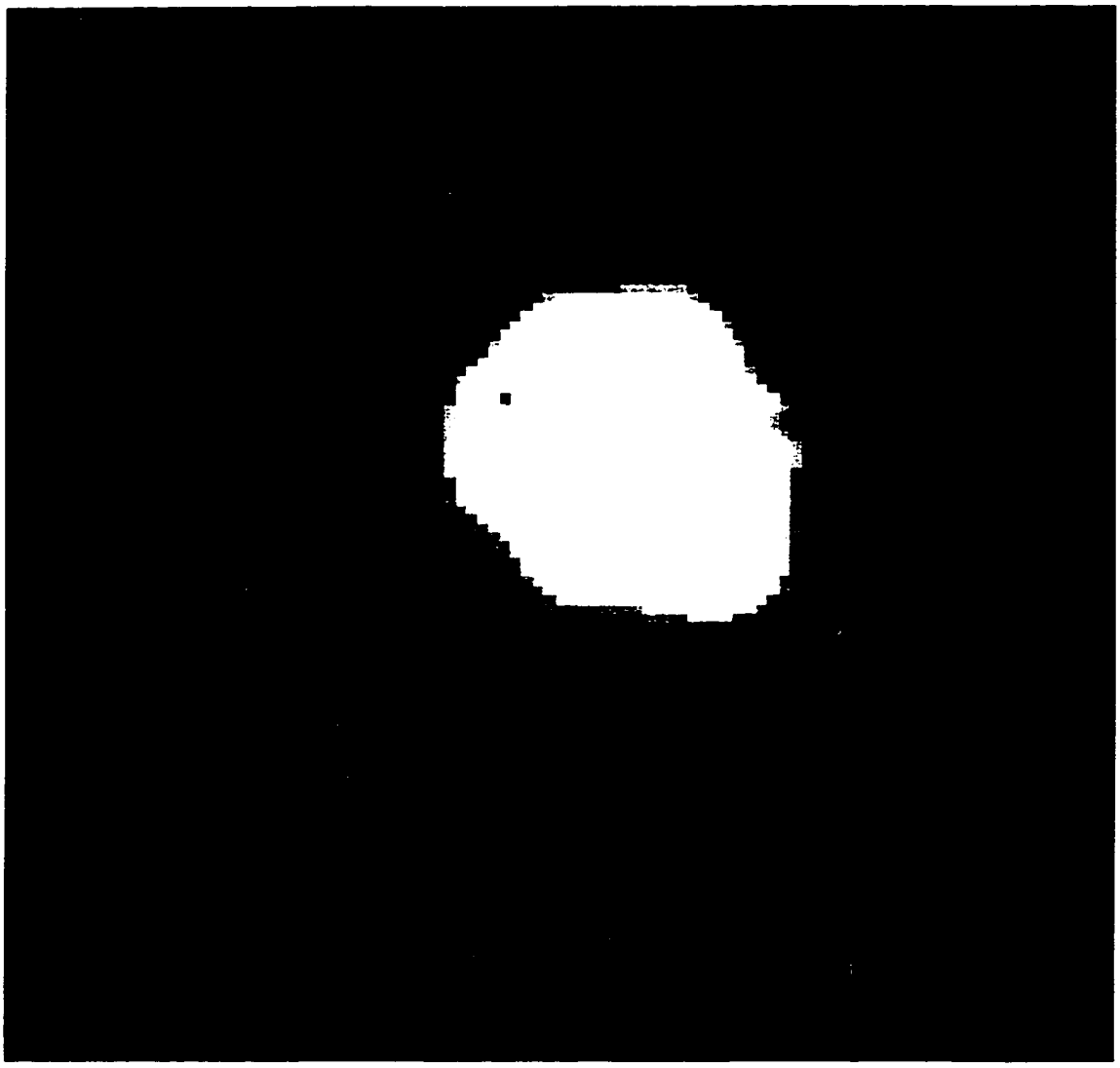

Figure 17. Cleaned and filtered image map of Abell 133. Scale is approximately 1.5 Mpc per side.

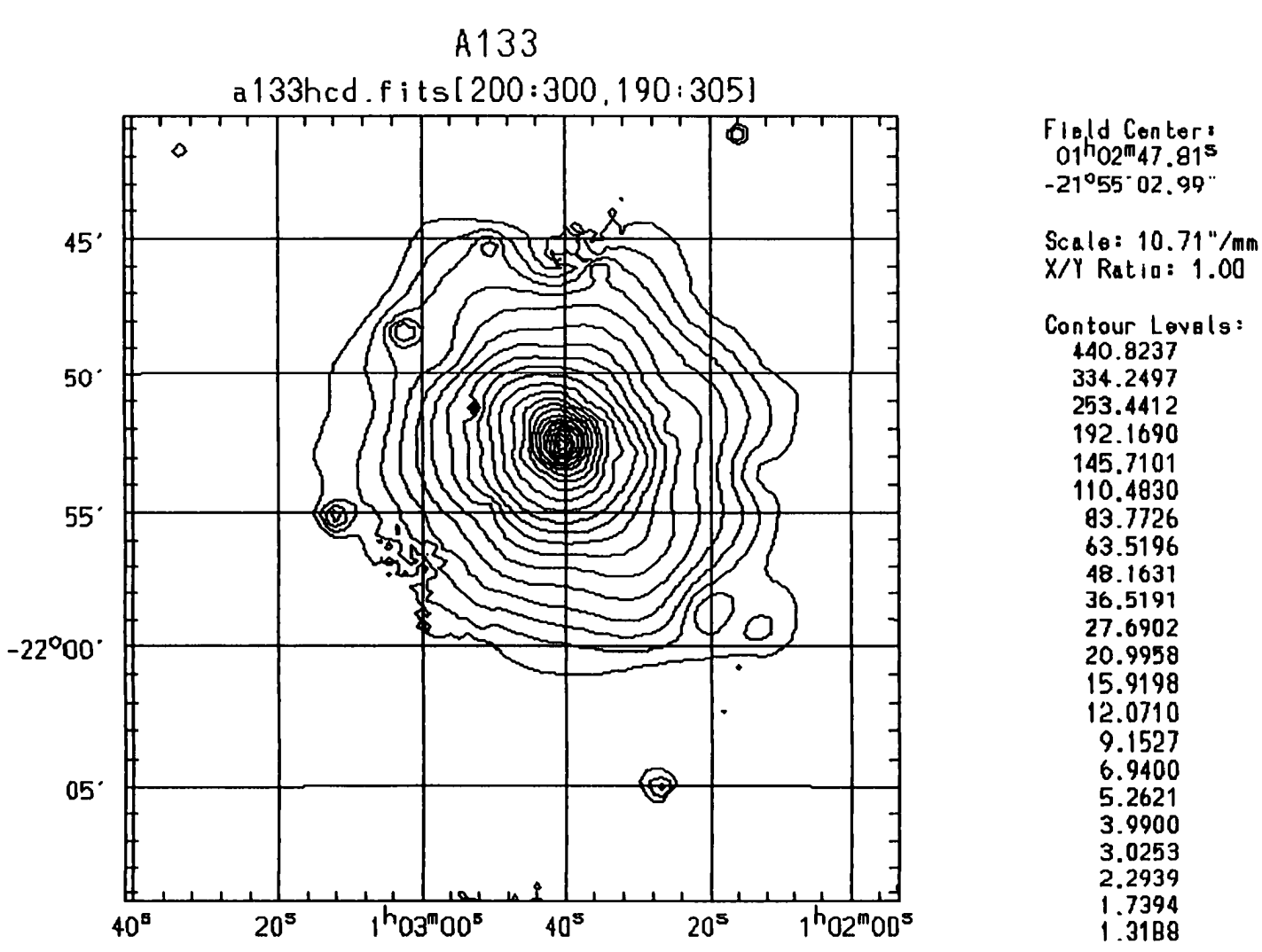

Figure 18. Contour map of Abell 133. Scale is approximately 1.5 Mpc per side. Contour levels are given in counts.

ABELL 133

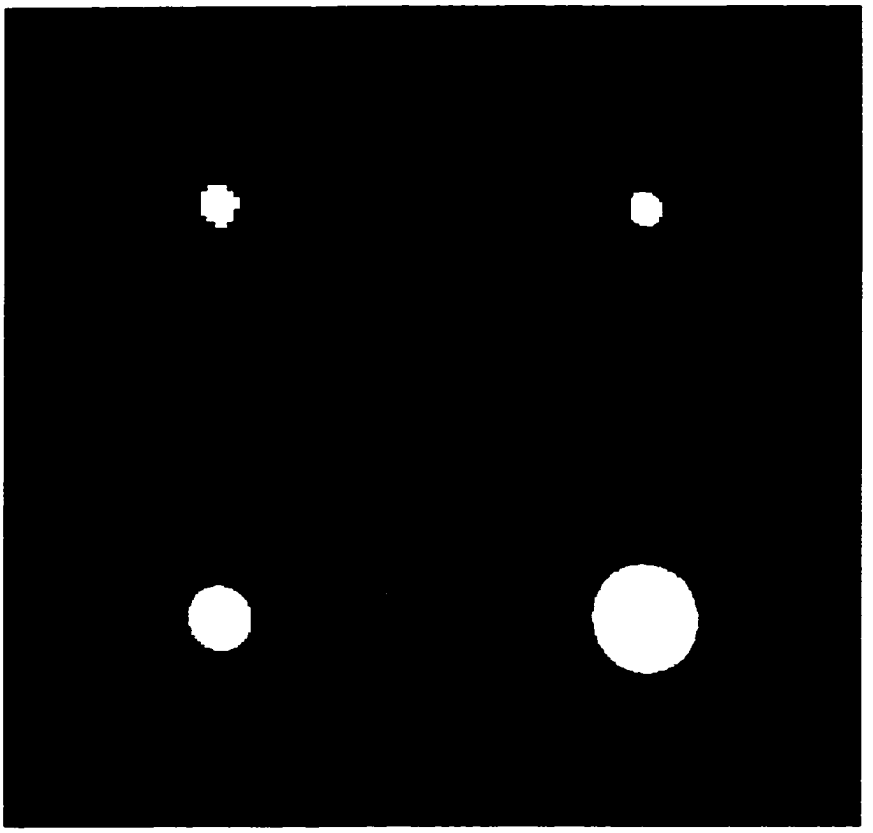

Figure 19. Wavelet transform images for Abell 133. Clockwise from upper left in 2, 3, 4, and 5 pixel scales.

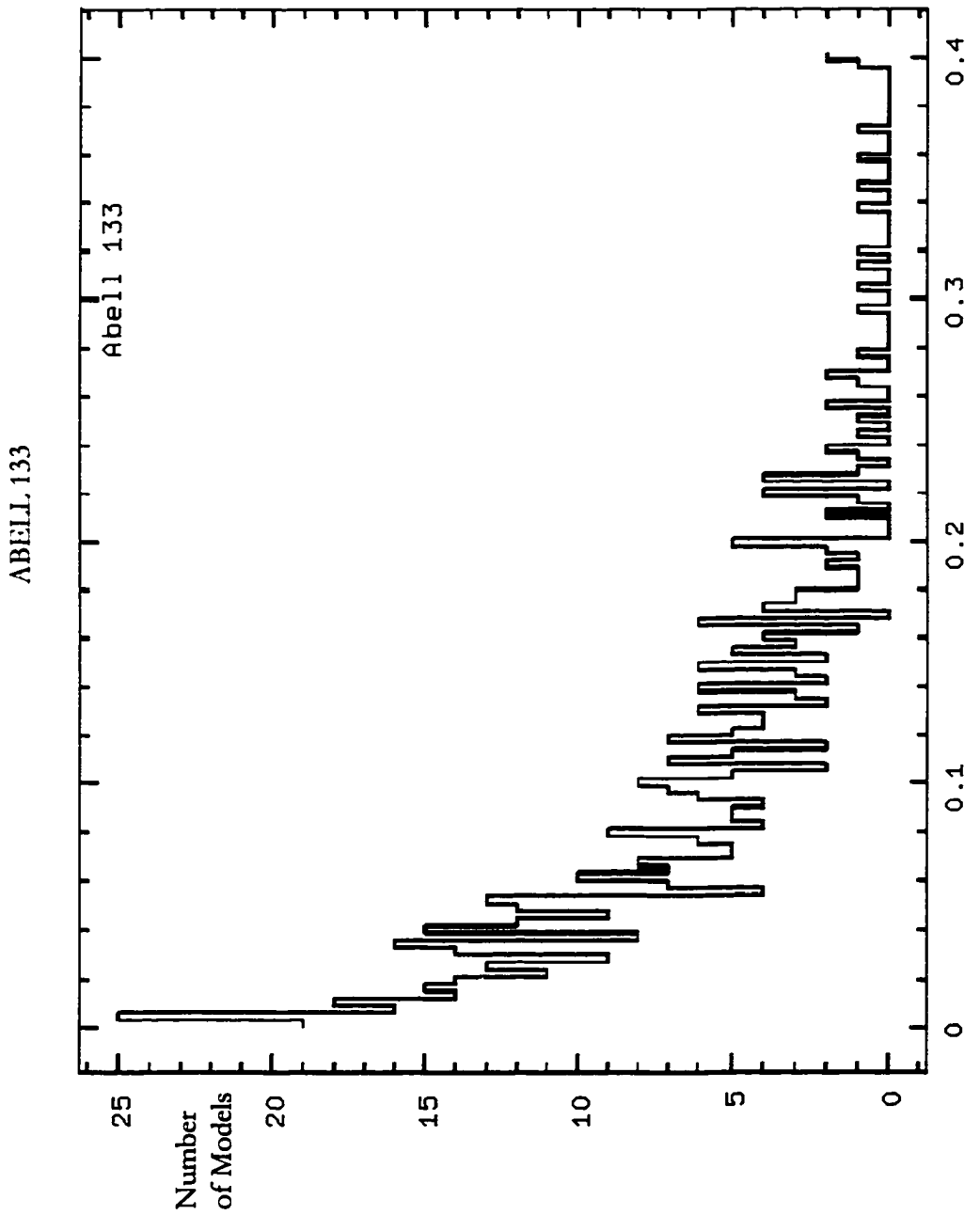

Figure 20. Histogram plot for P_3 moment for models of Abell 133

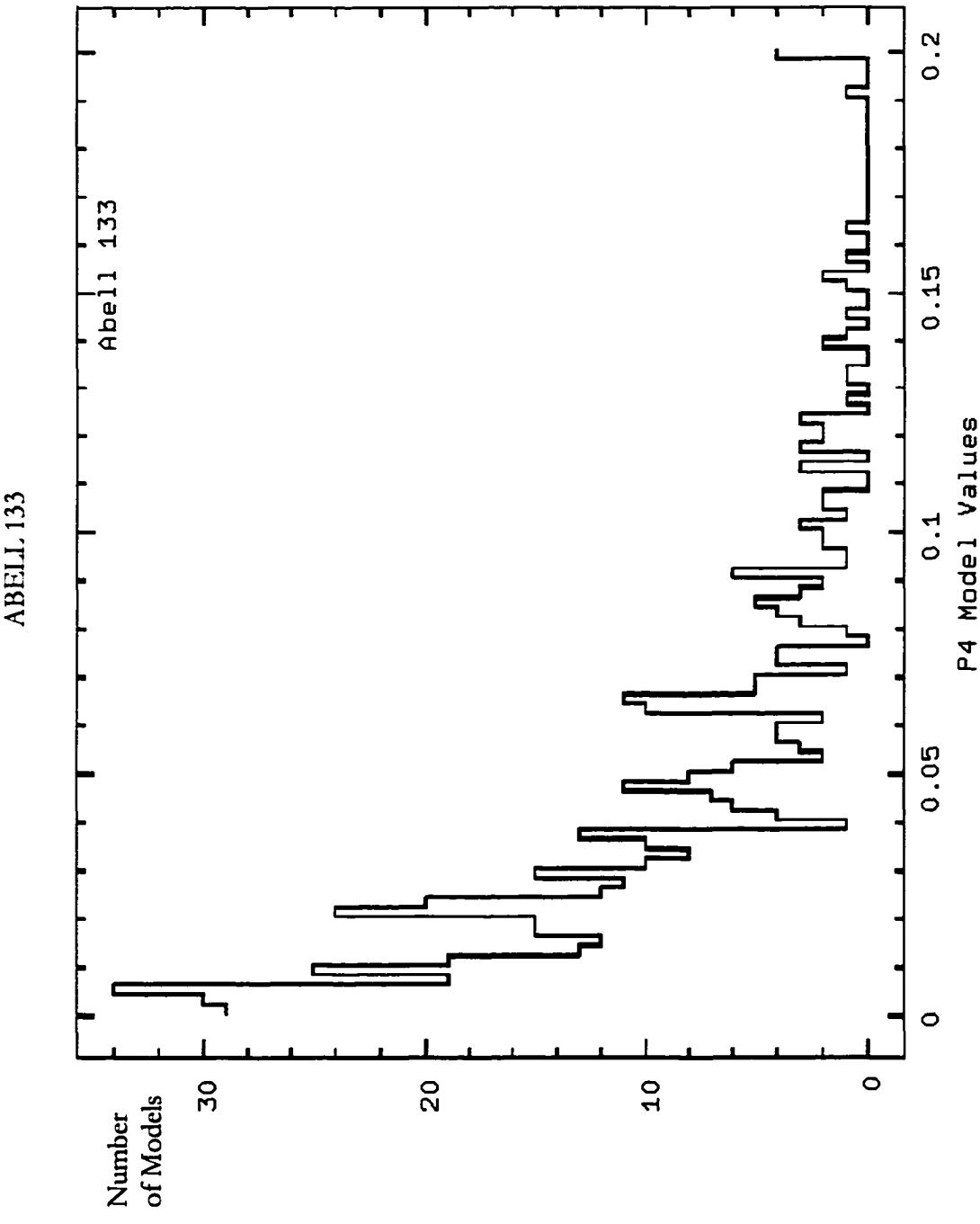

Figure 21. Histogram plot for P_4 moment for models of Abell 133

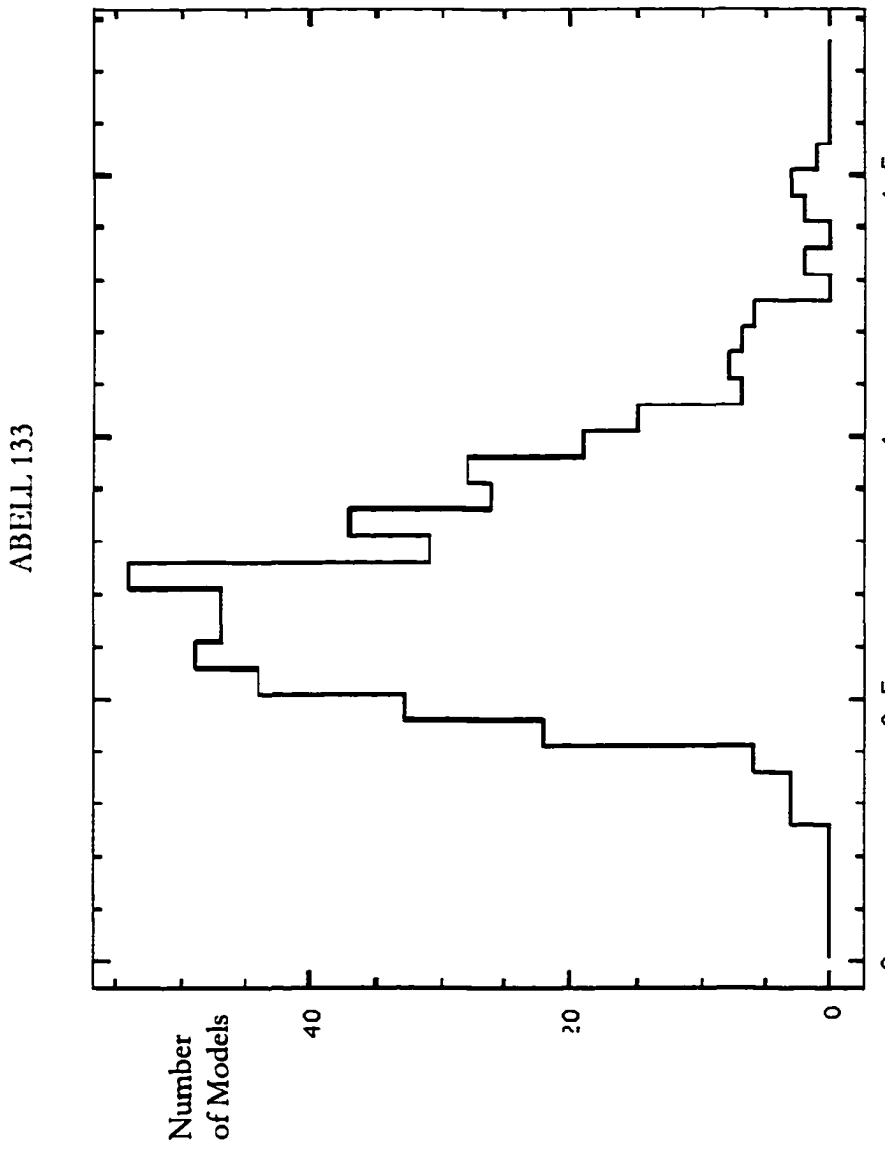

Figure 22. Sigma significance and total shift plots for Abell 133 for 'center shift' program.

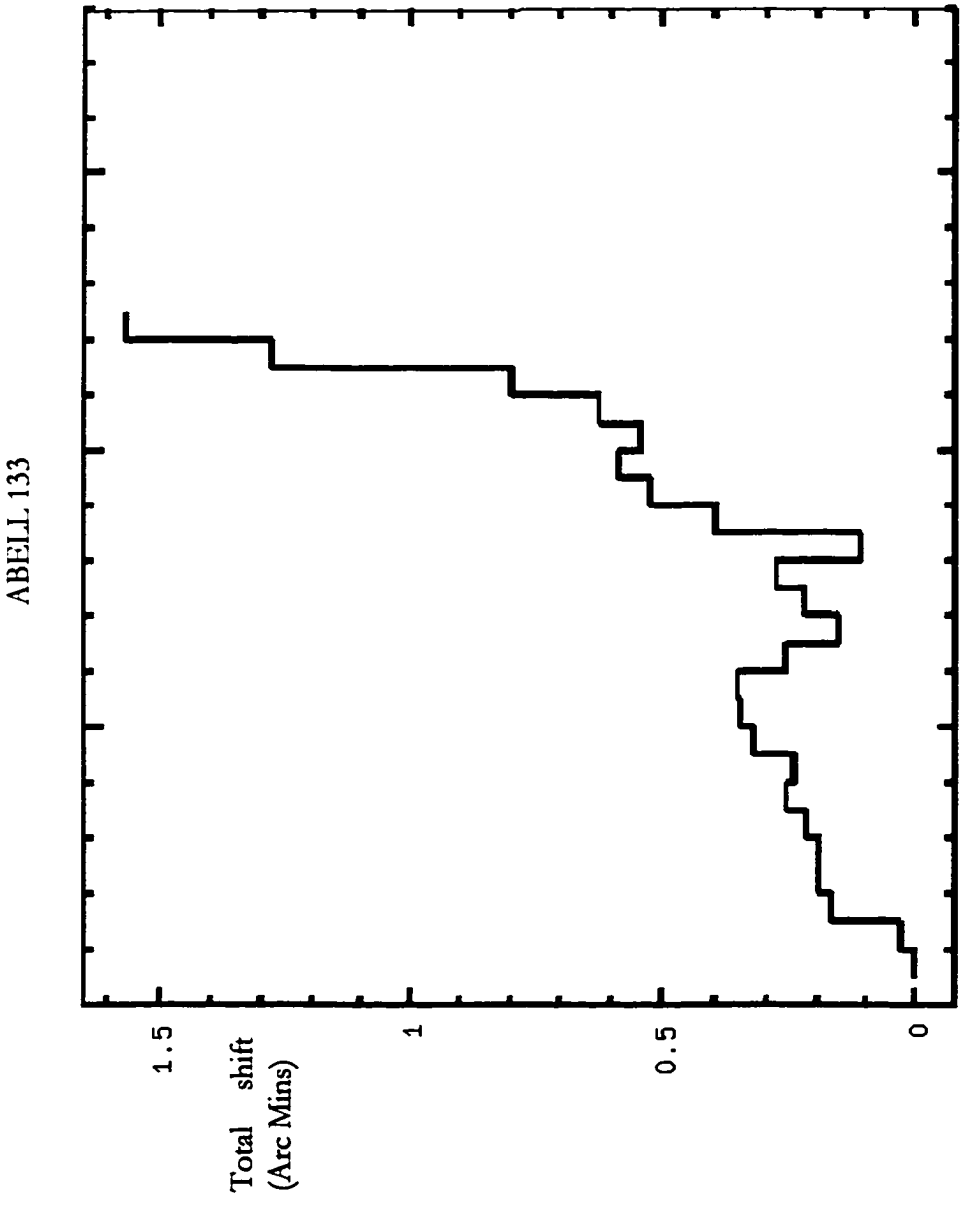

Figure 23. Sigma significance and total shift plots for Abell 133 for 'center shift' program.

ABELL 496

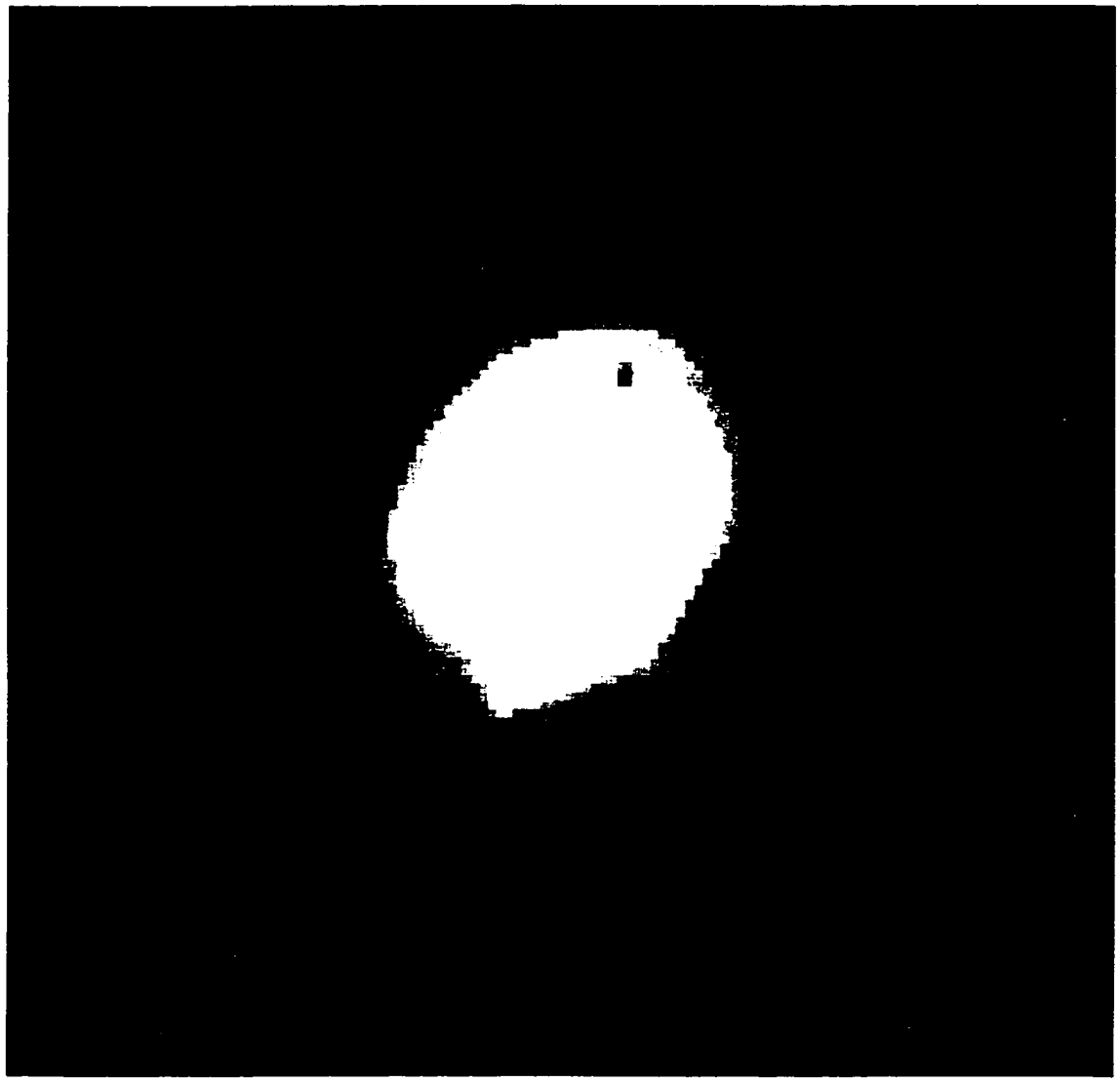

Figure 24. Cleaned and filtered image map of Abell 496. Scale is approximately 1.1 Mpc per side.

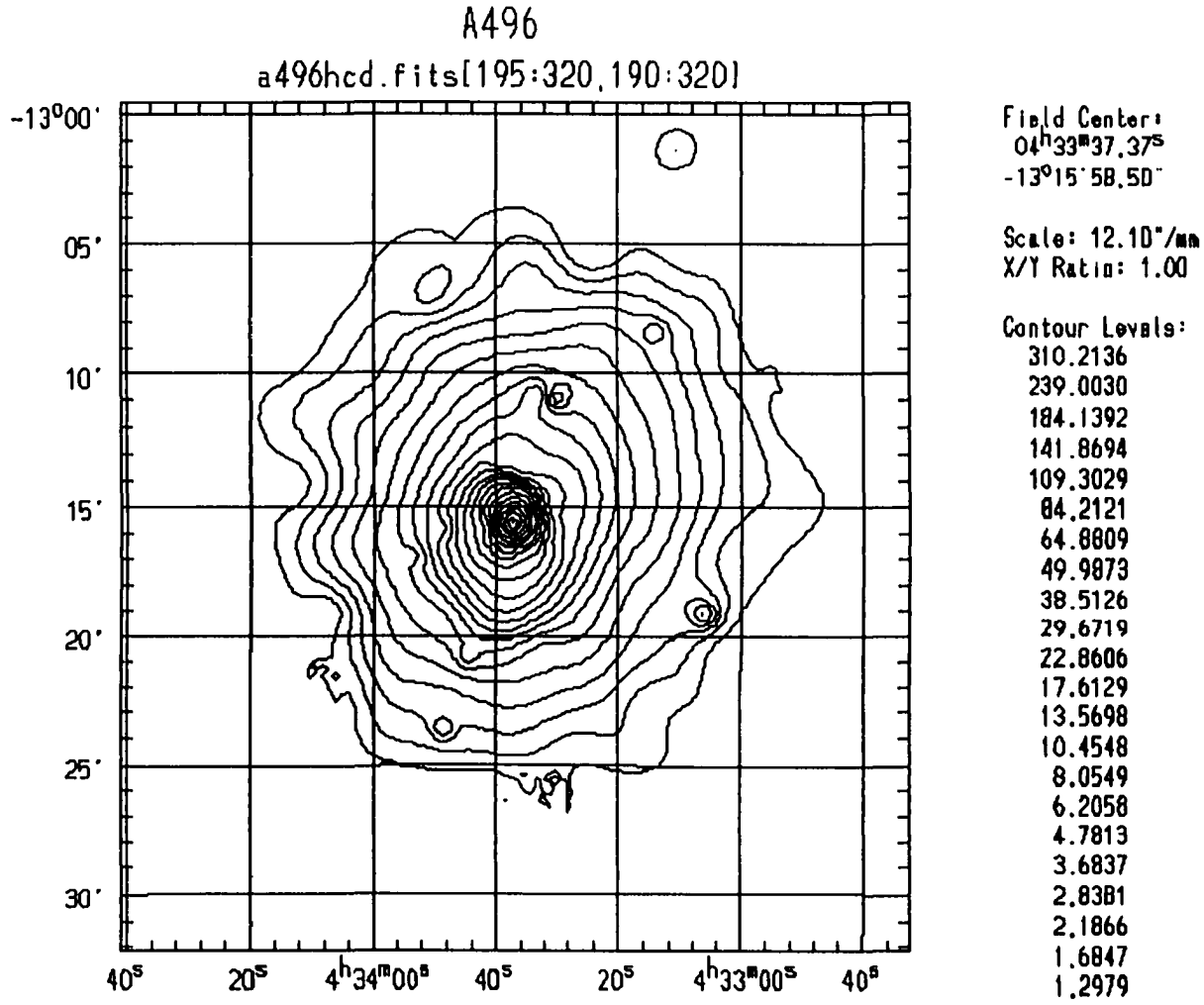

Figure 25. Contour map of Abell 496. Scale is approximately 1.1 Mpc per side. Contour levels are given in counts.

ABELL 496

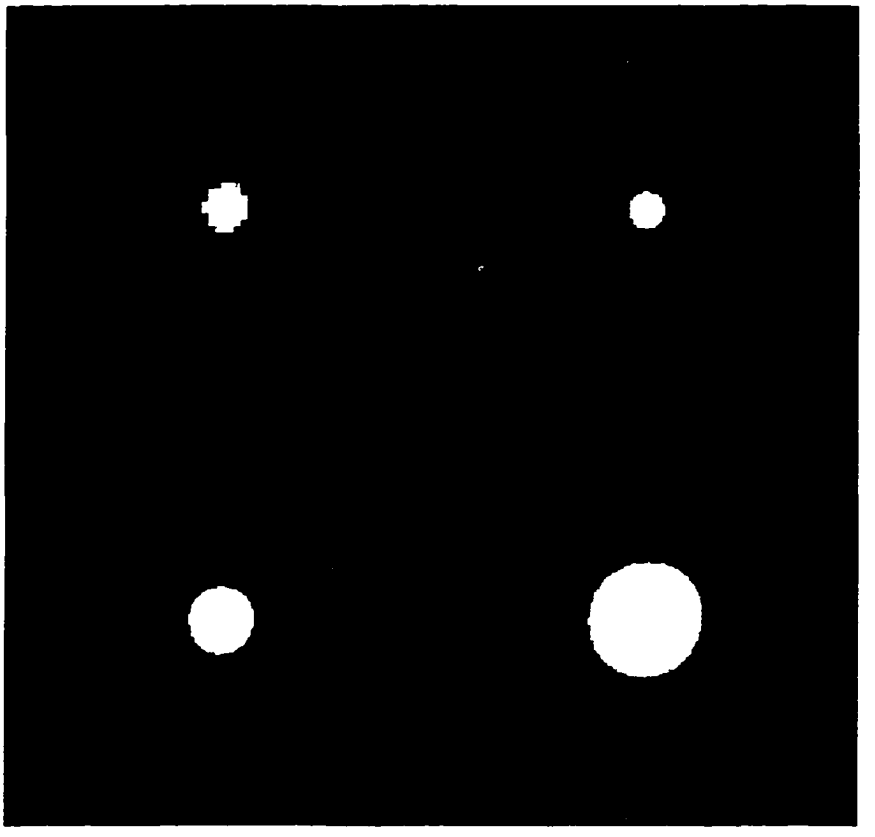

Figure 26. Wavelet transform images for Abell 496. Clockwise from upper left in 2, 3, 4, and 5 pixel scales.

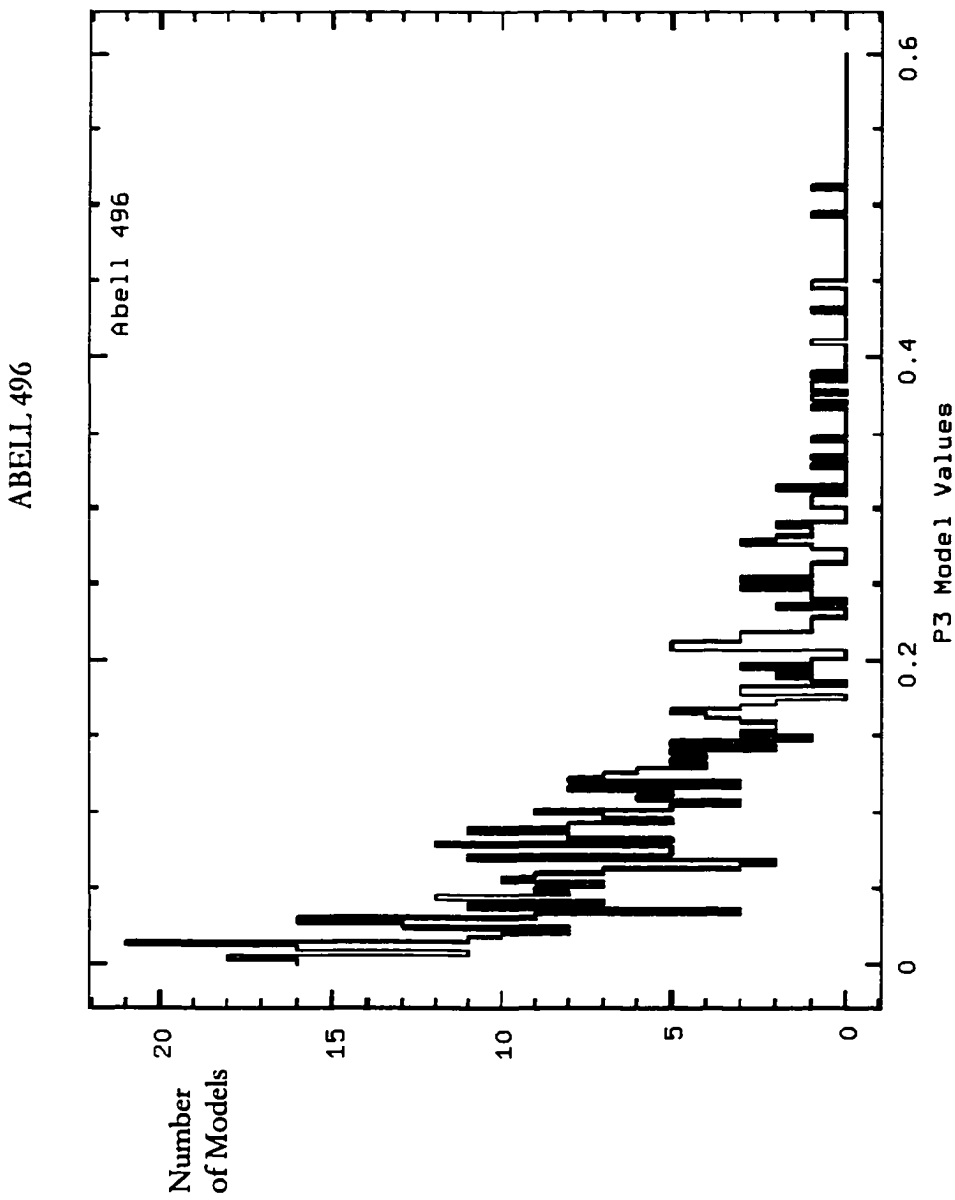

Figure 27. Histogram plots for P_3 moment for models of Abell 496.

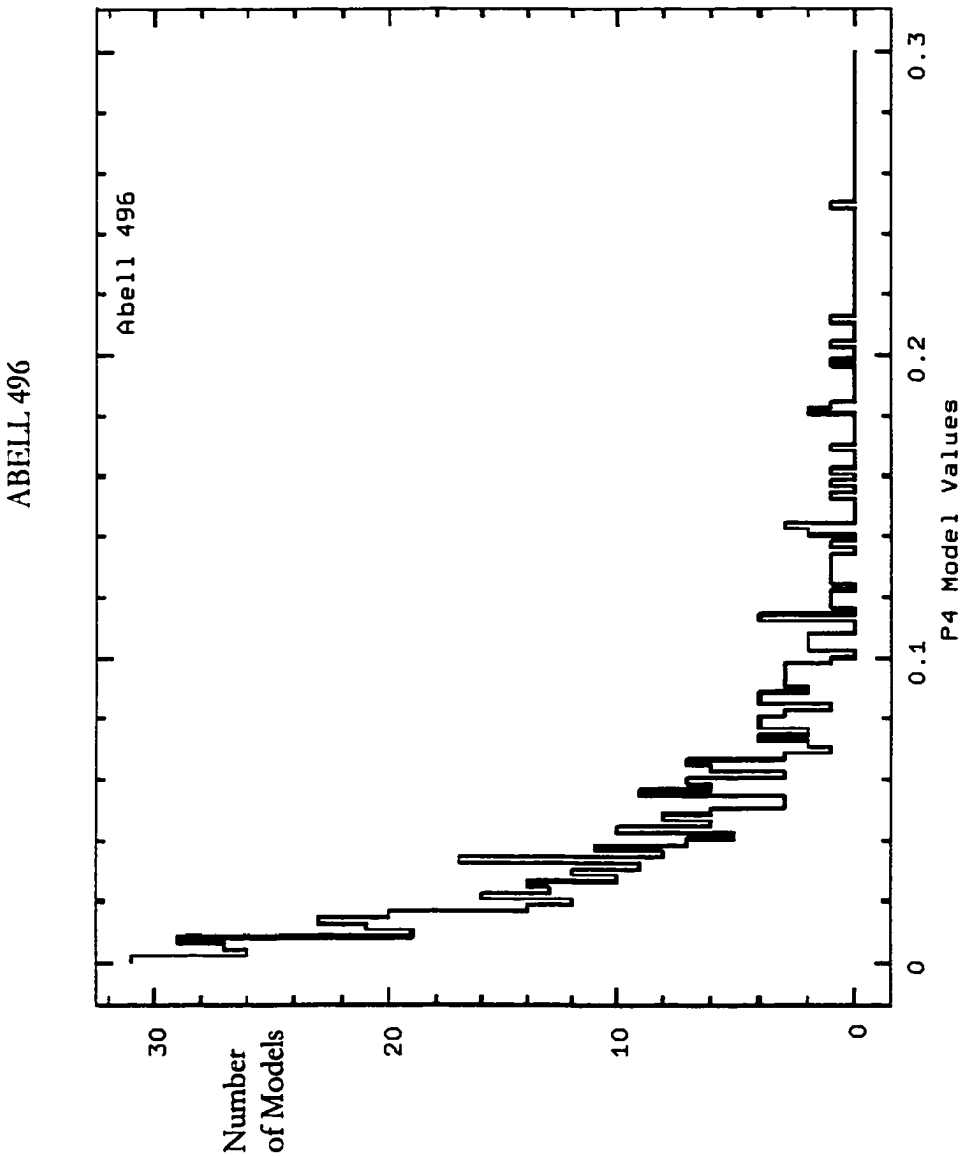

Figure 28. Histogram plots for P_4 moment for models of Abell 496.

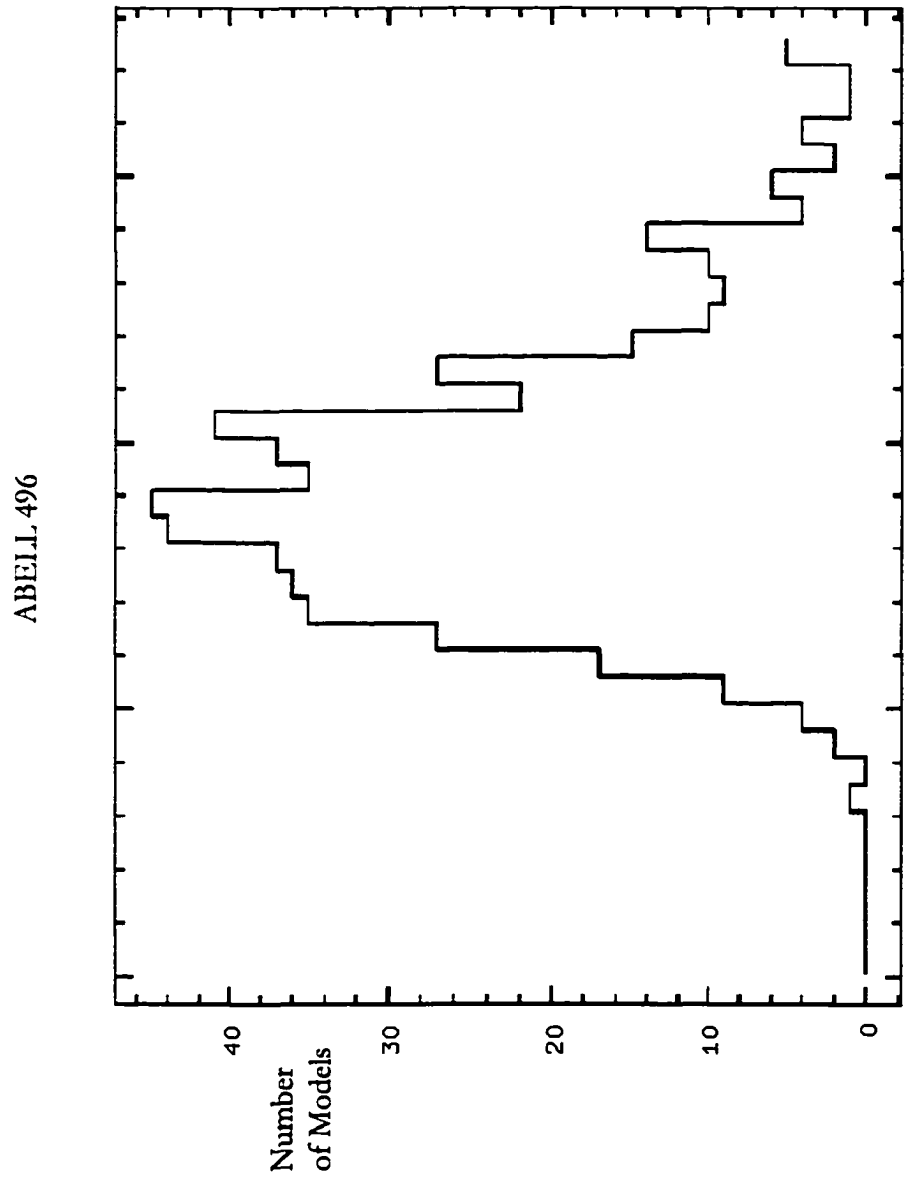

Figure 29. Sigma significance plot for Abell 496 for 'center shift' program.

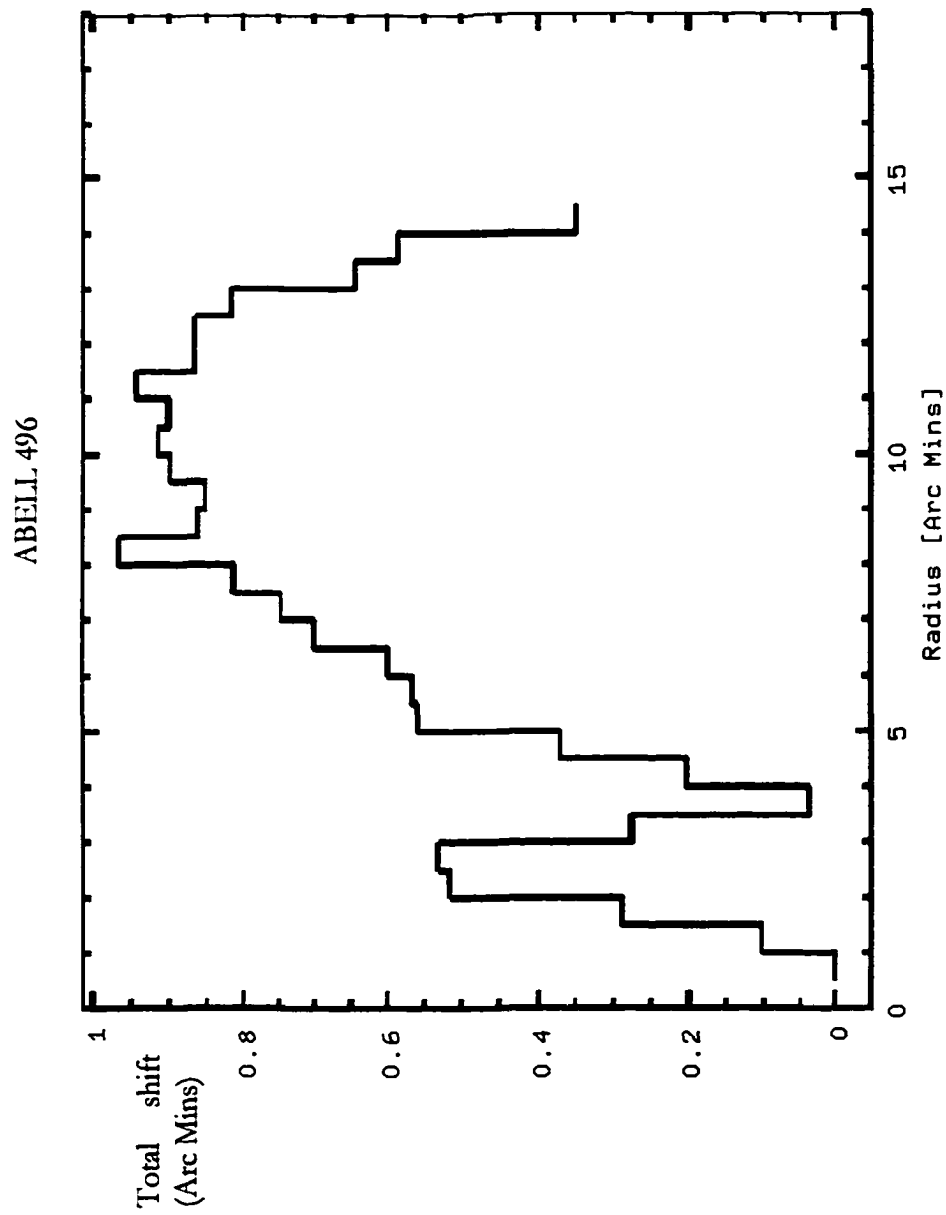

Figure 30. Total shift plot for Abell 496 for 'center shift' program.

ABELL 500

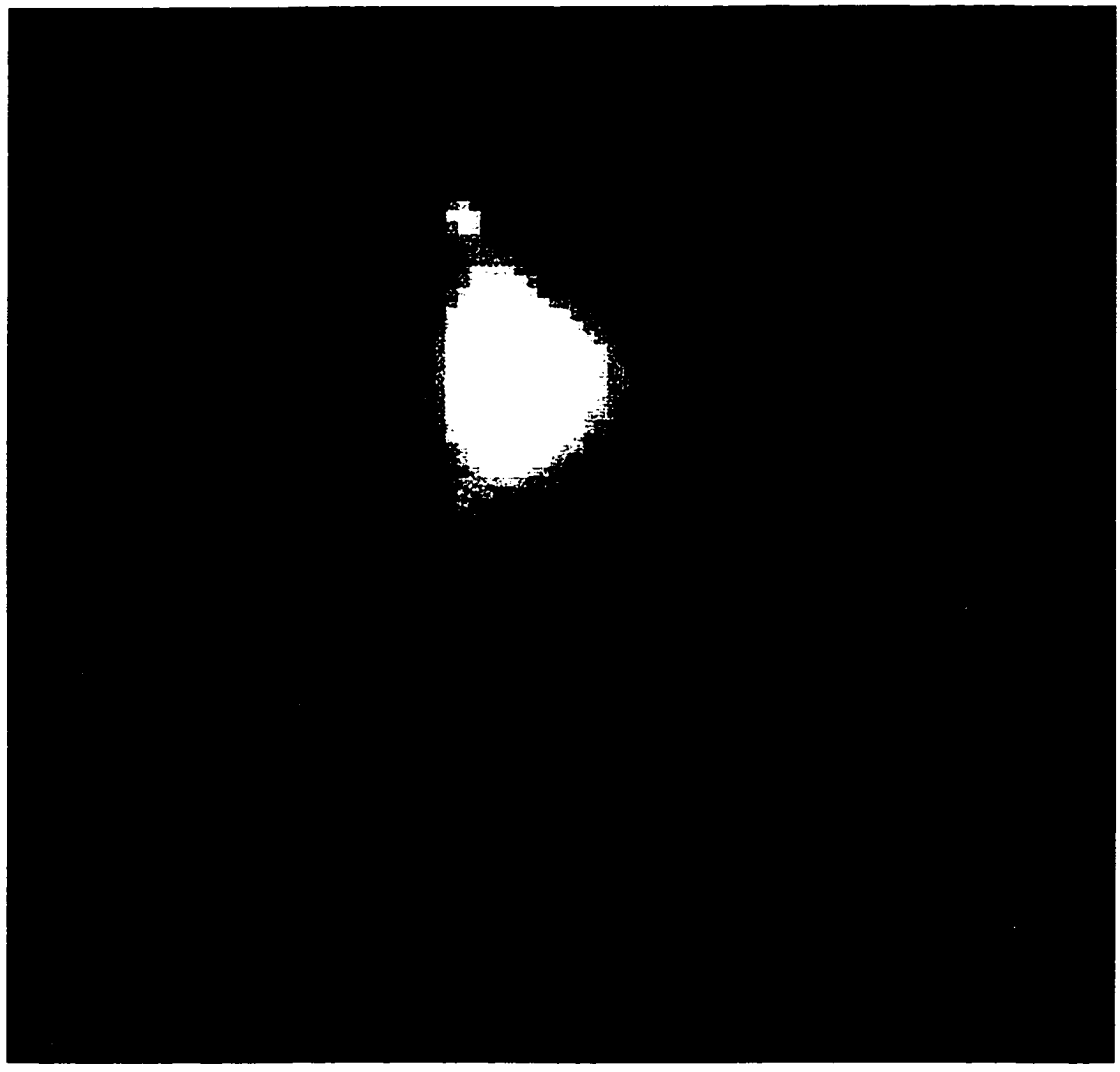

Figure 31. Cleaned and filtered image map of Abell 500. Scale is approximately 1.6 Mpc per side.

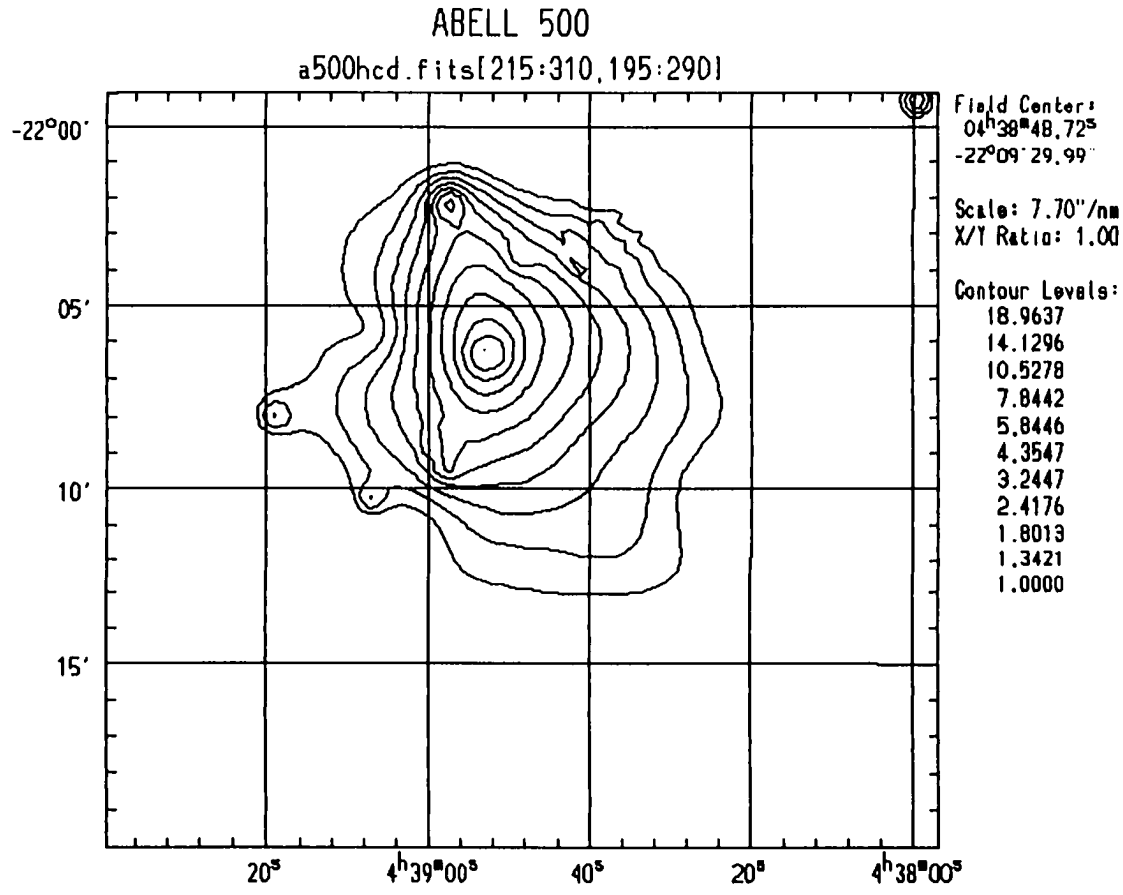

Figure 32. Contour map of Abell 500. Scale is approximately 1.6 Mpc per side. Contour levels are given in counts.

ABELL 500

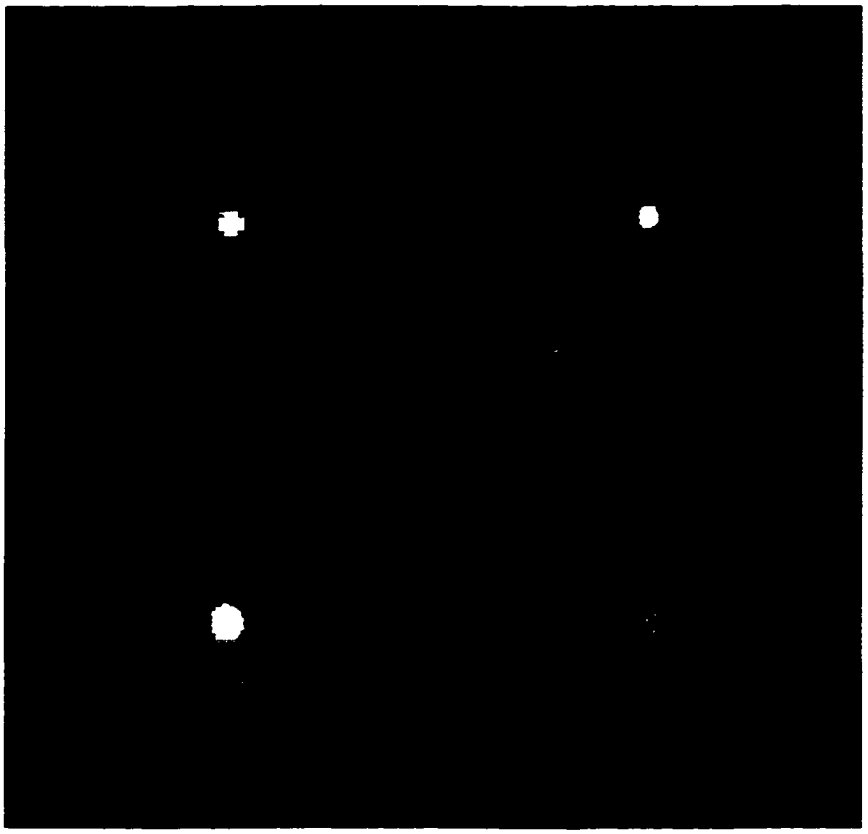

Figure 33. Wavelet transform images for Abell 500. Clockwise from upper left in 2, 3, 4, and 5 pixel scales.

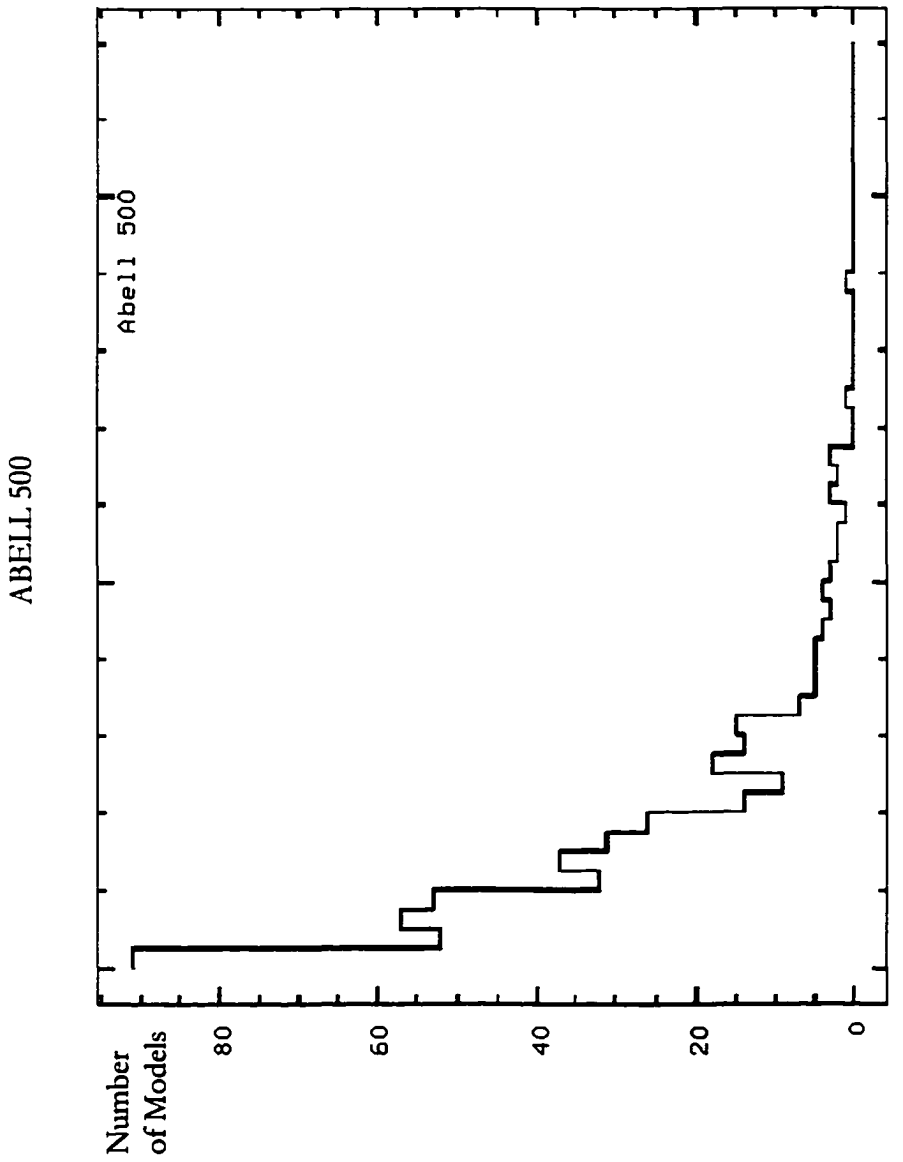

Figure 34. Histogram plots for P_3 moment for models of Abell 500.

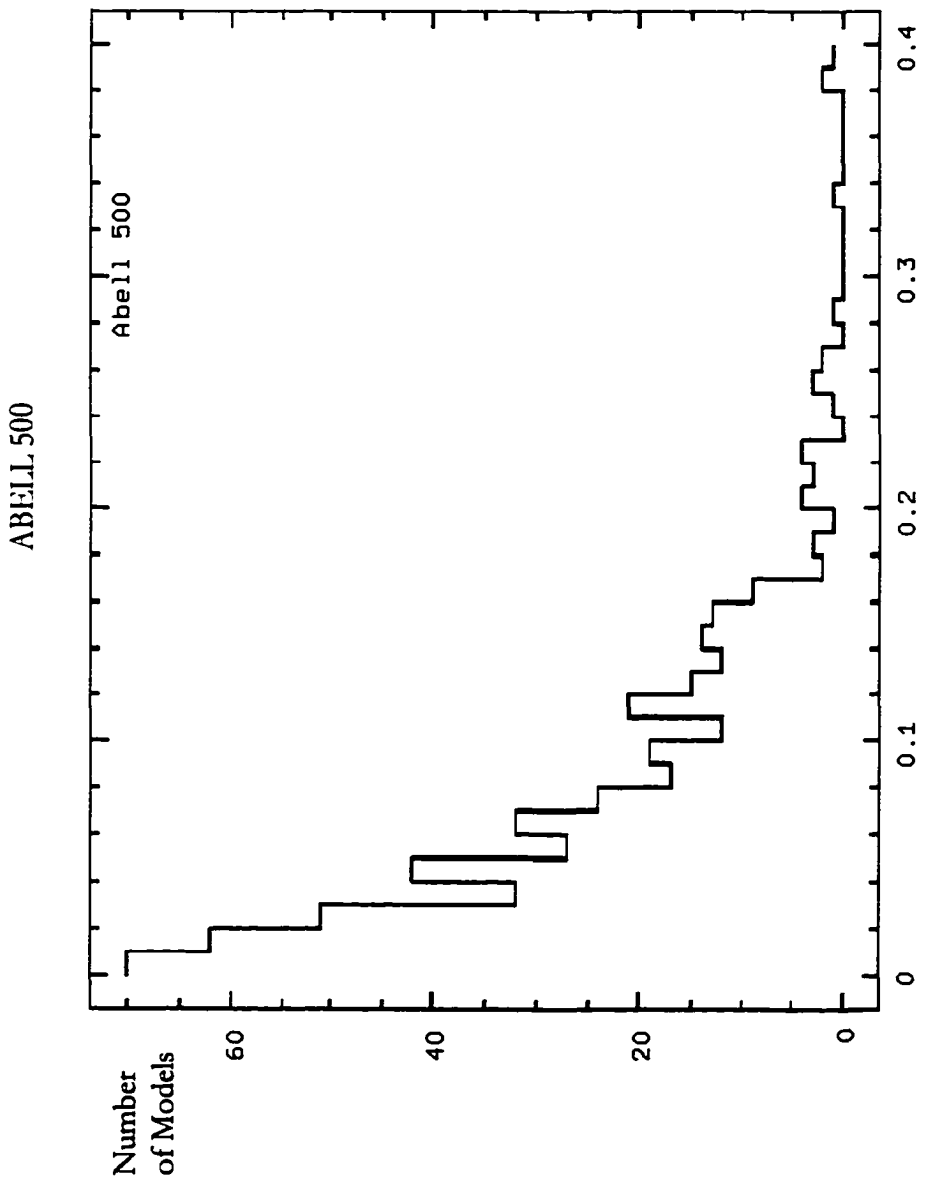

Figure 35. Histogram plots for P_4 moment for models of Abell 500.

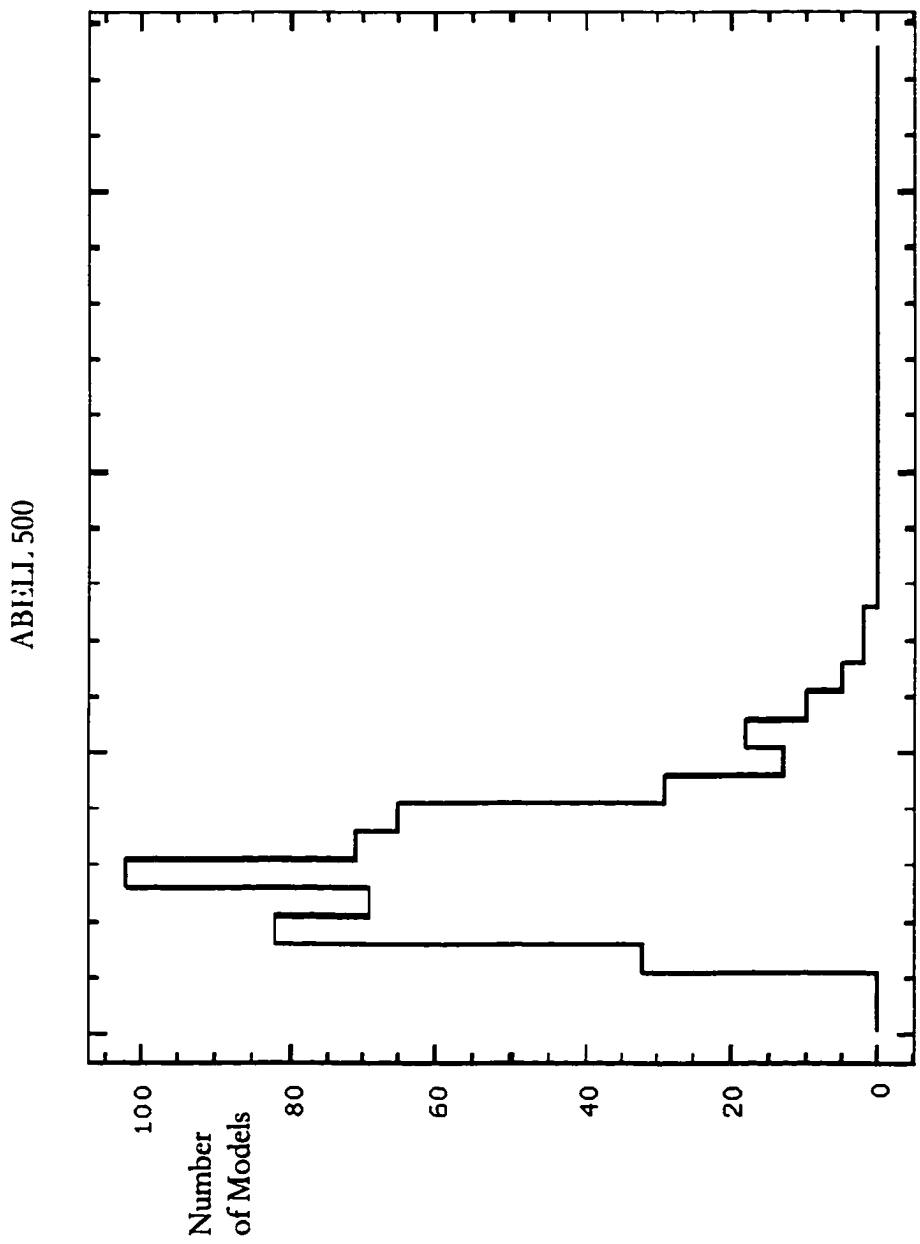

Figure 36. Sigma significance plot for Abell 500 for 'center shift' program.

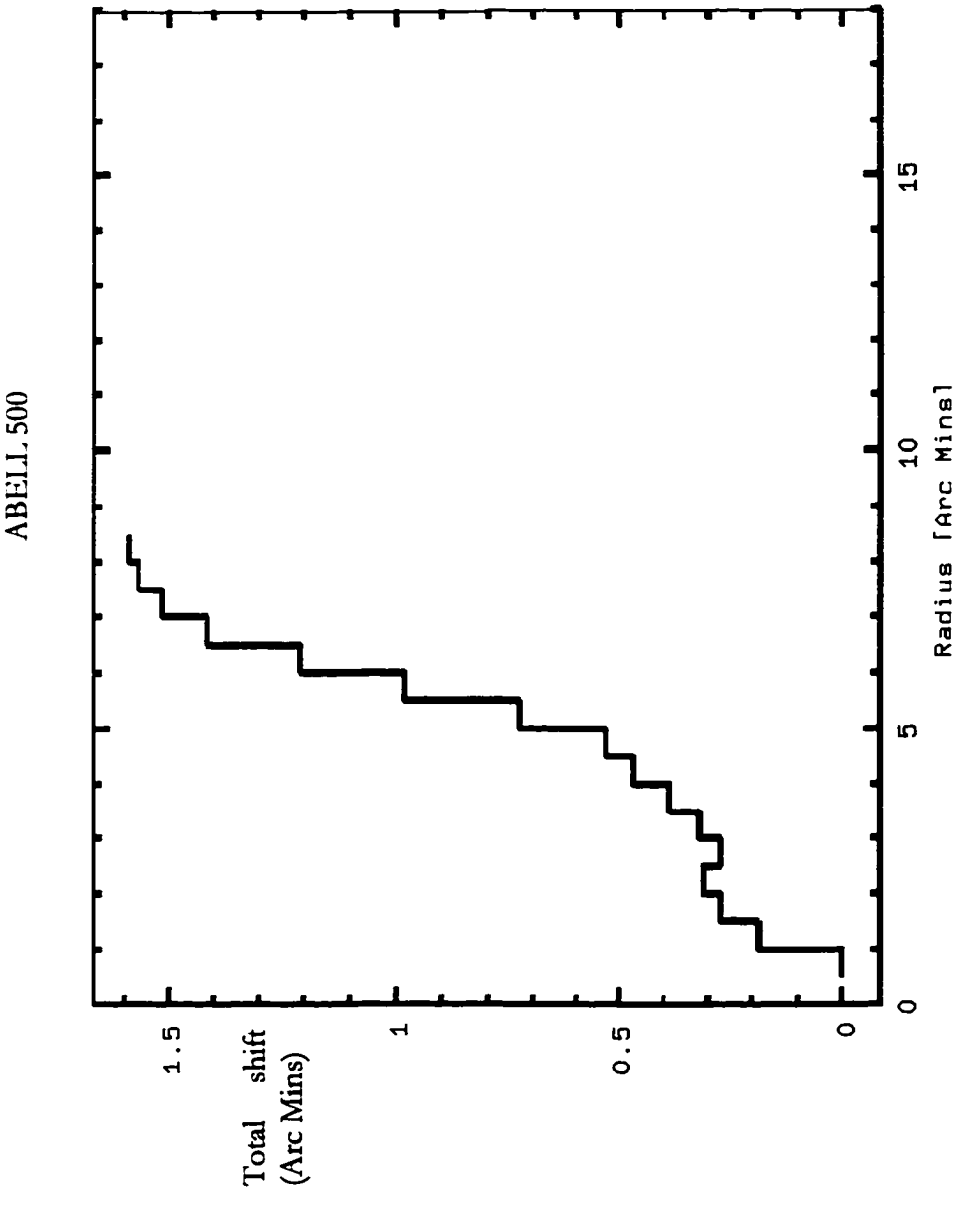

Figure 37. Total shift plot for Abell 500 for 'center shift' program.

ABELL 514

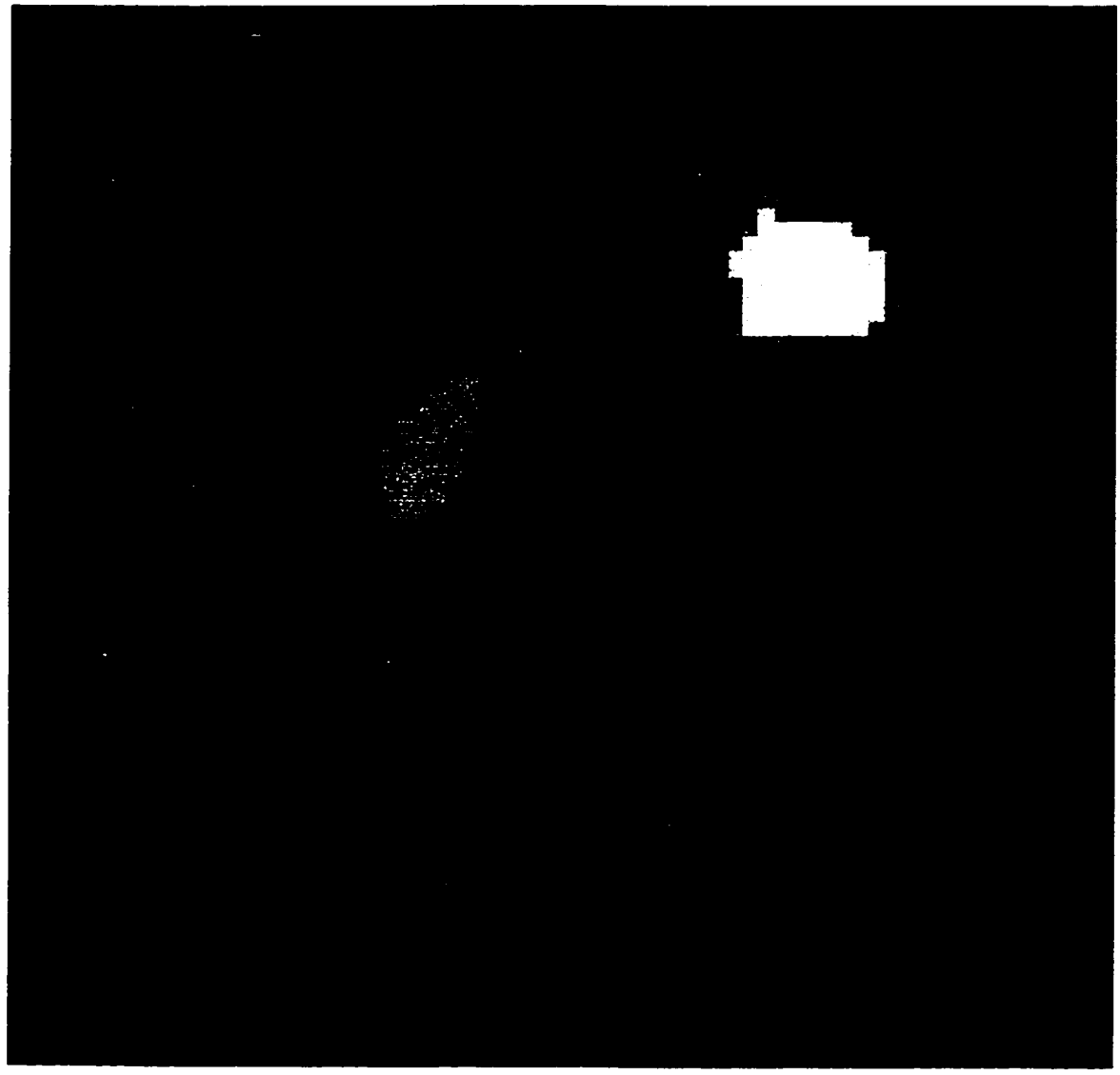

Figure 38. Cleaned and filtered image map of Abell 514. Scale is approximately 1.3 Mpc per side.

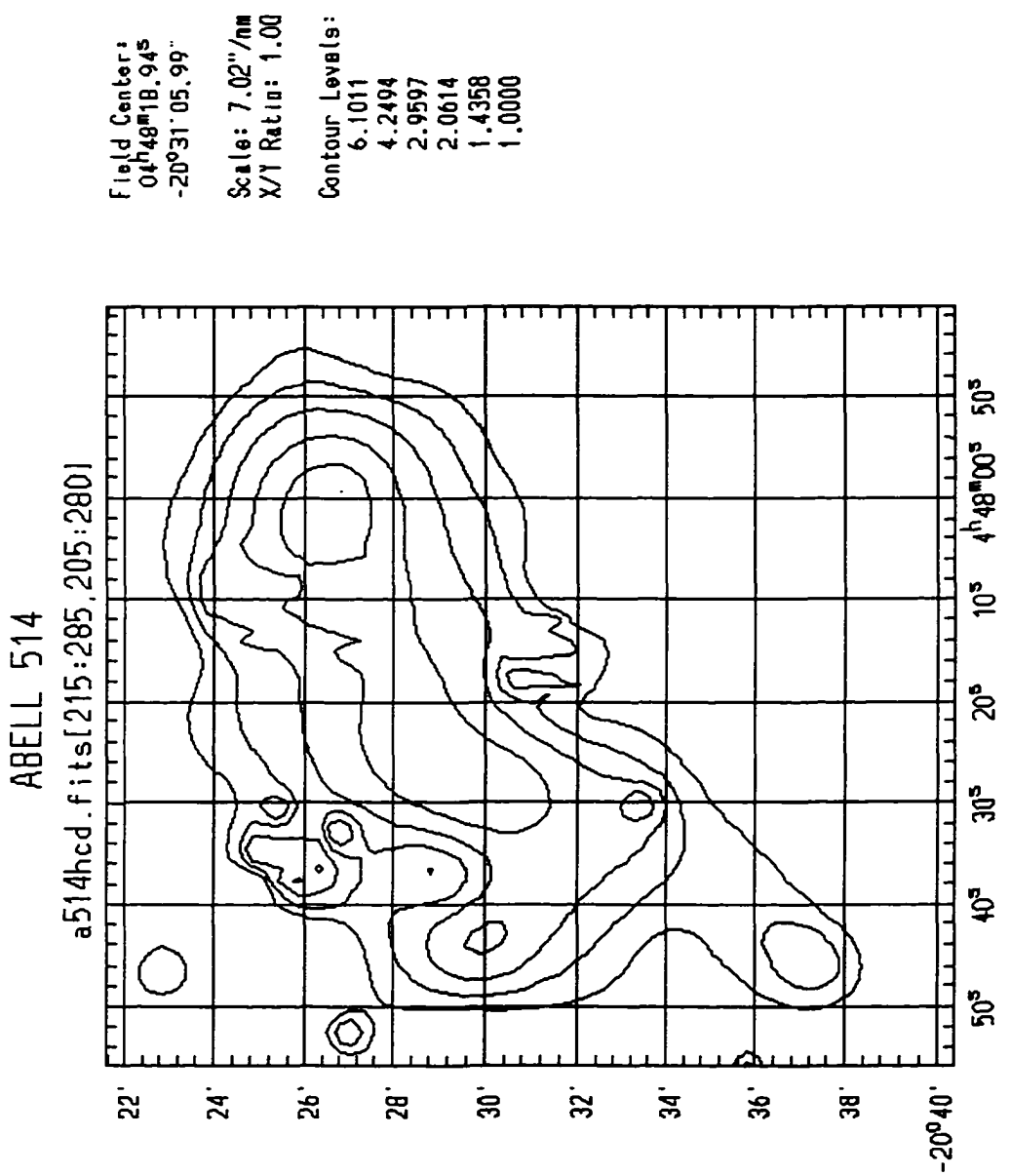

Figure 39. Contour map of Abell 514. Scale is approximately 1.3 Mpc per side. Contour levels are given in counts.

ABELL 514

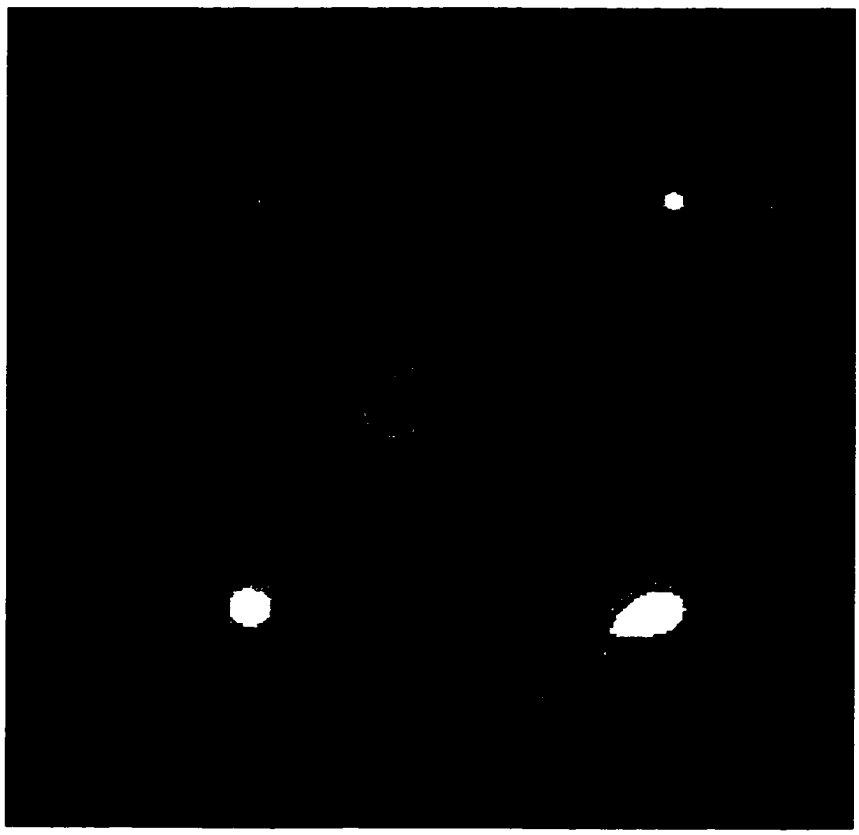

Figure 40. Wavelet transform images for Abell 514. Clockwise from upper left in 2, 3, 4, and 5 pixel scales.

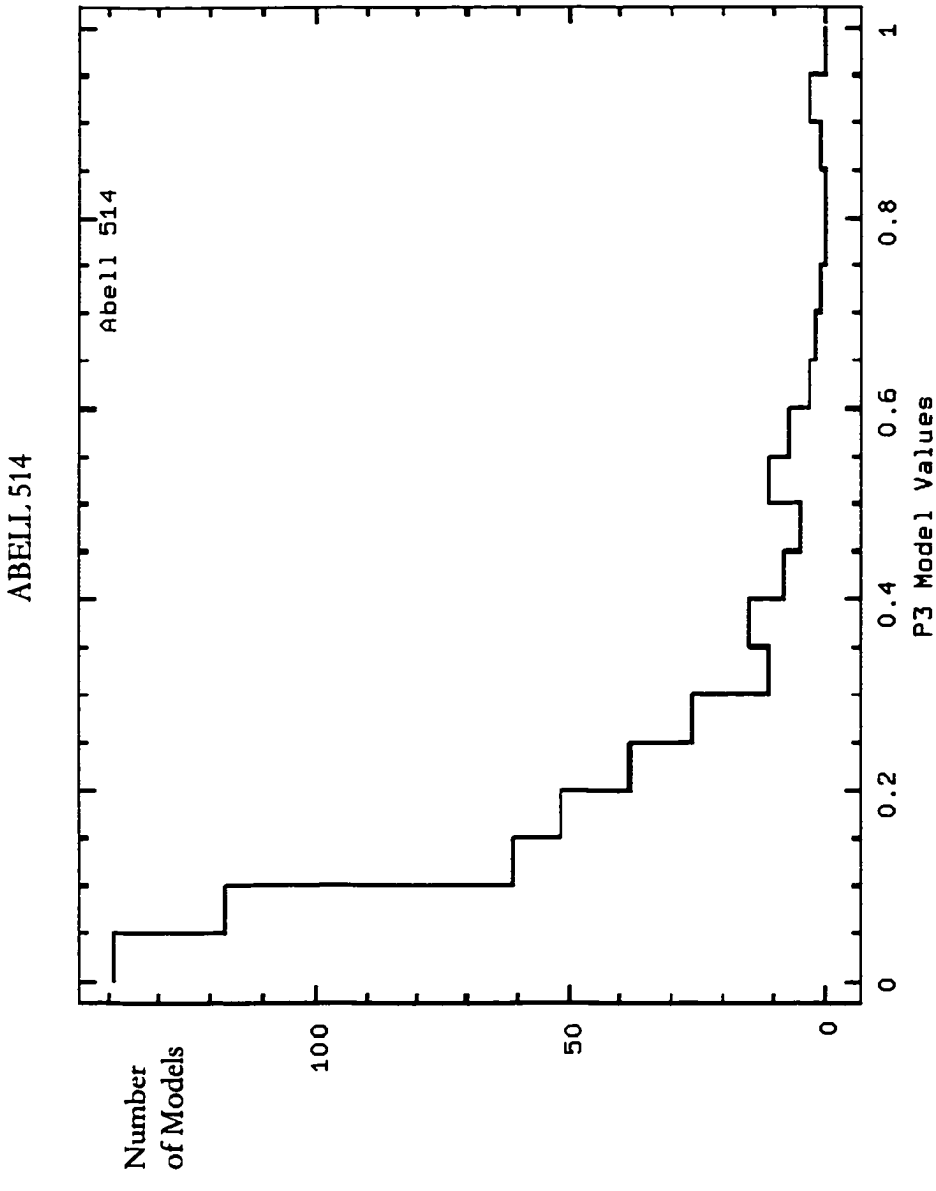

Figure 41. Histogram plots for P_3 moment for models of Abell 514.

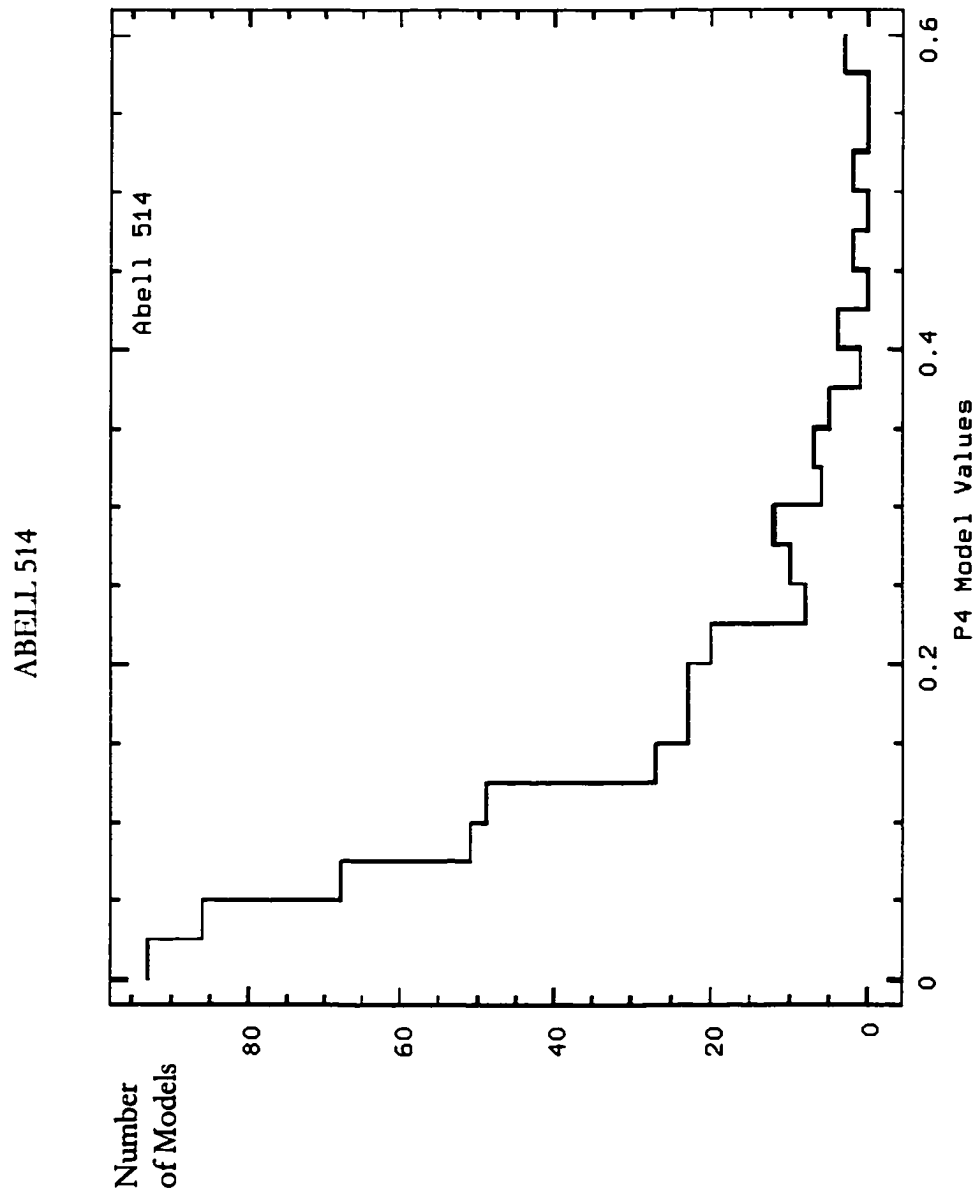

Figure 42. Histogram plots for P_4 moment for models of Abell 514.

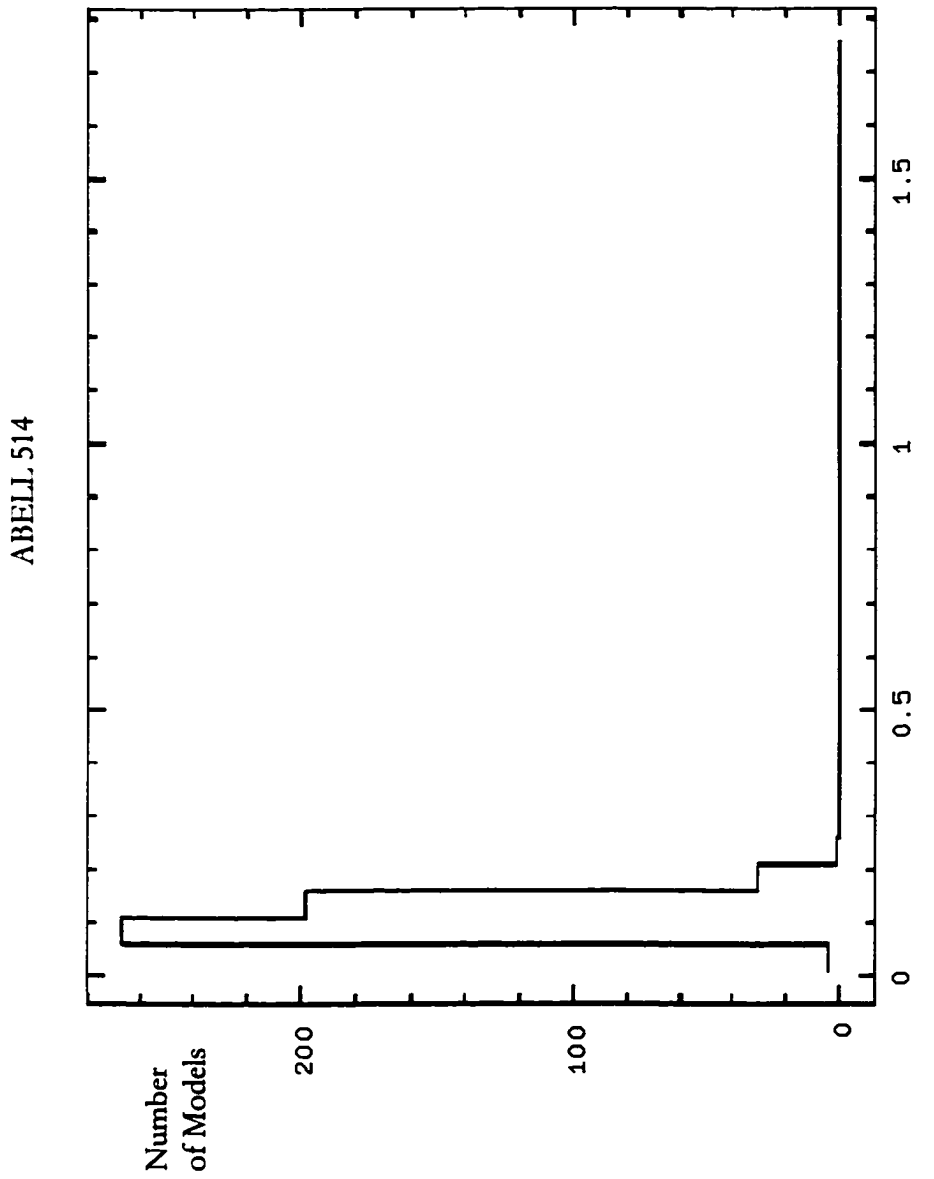

Figure 43. Sigma significance plot for Abell 514 for 'center shift' program.

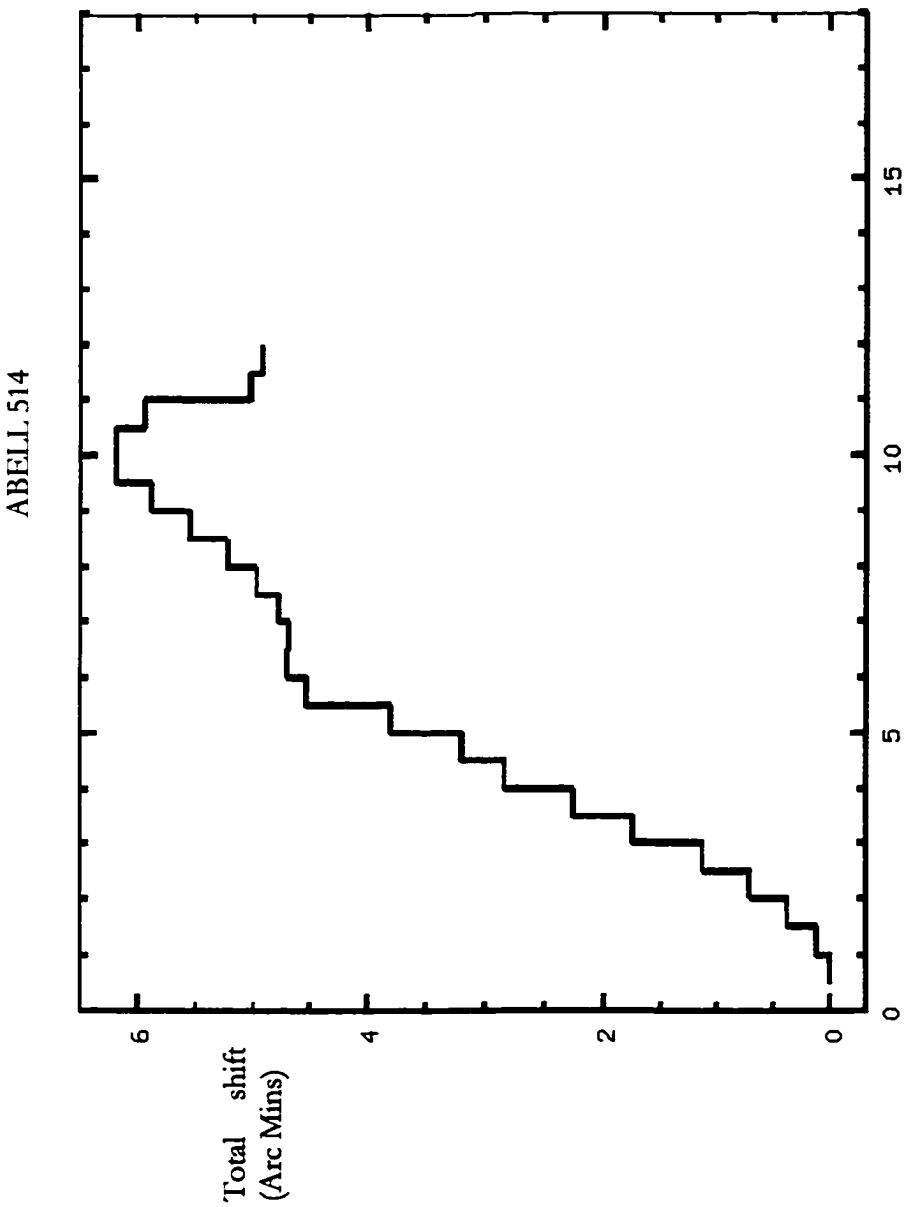

Figure 44. Total shift plot for Abell 514 for 'center shift' program.

ABELL 754

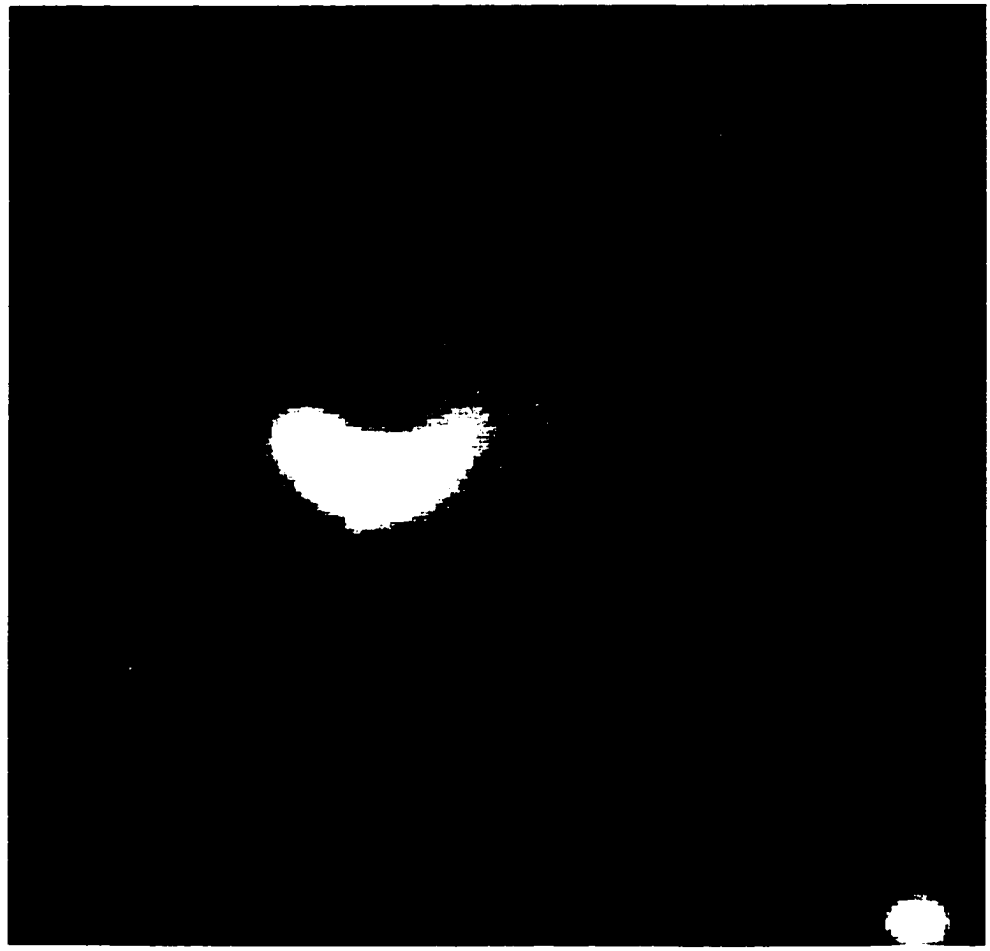

Figure 45. Cleaned and filtered image of Abell 754. Scale is approximately 1.9 Mpc per side.

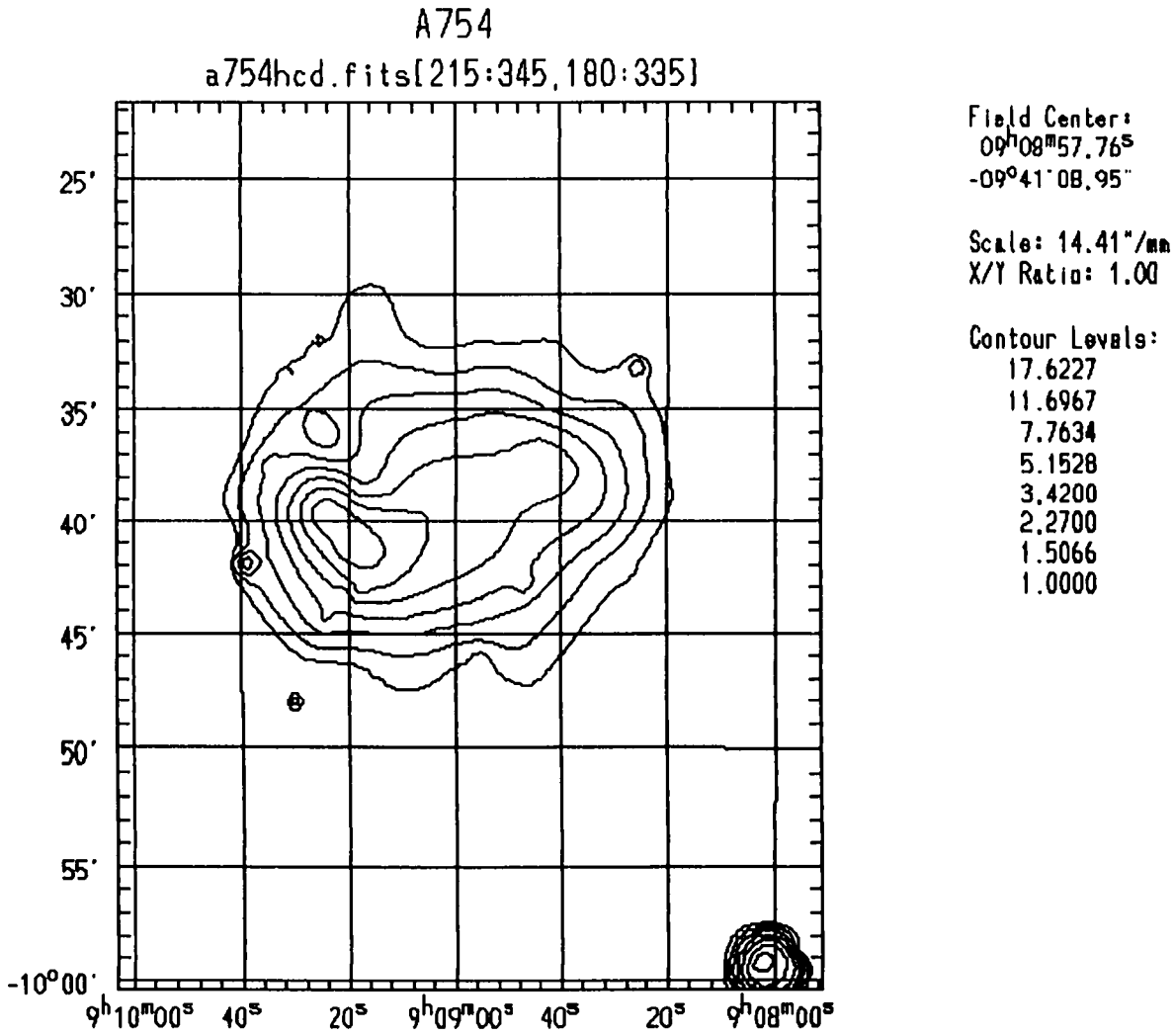

Figure 46. Contour map of Abell 754. Scale is approximately 1.9 Mpc per side. Contour levels are given in counts.

ABELL 754

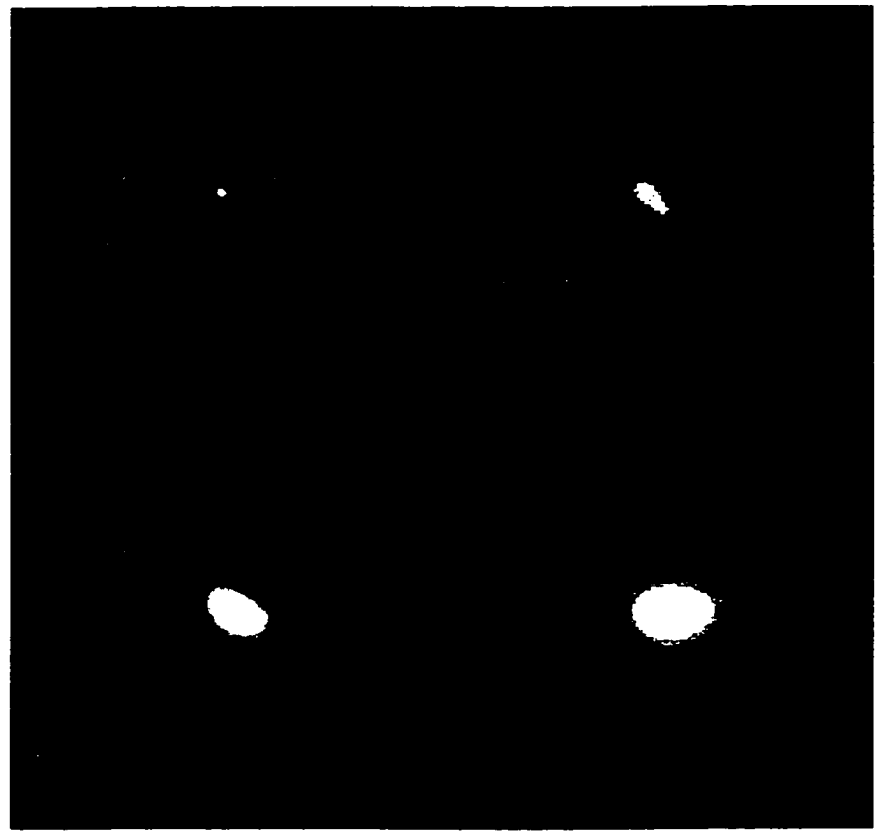

Figure 47. Wavelet transform images for Abell 754. Clockwise from upper left in 2, 3, 4, and 5 pixel scales.

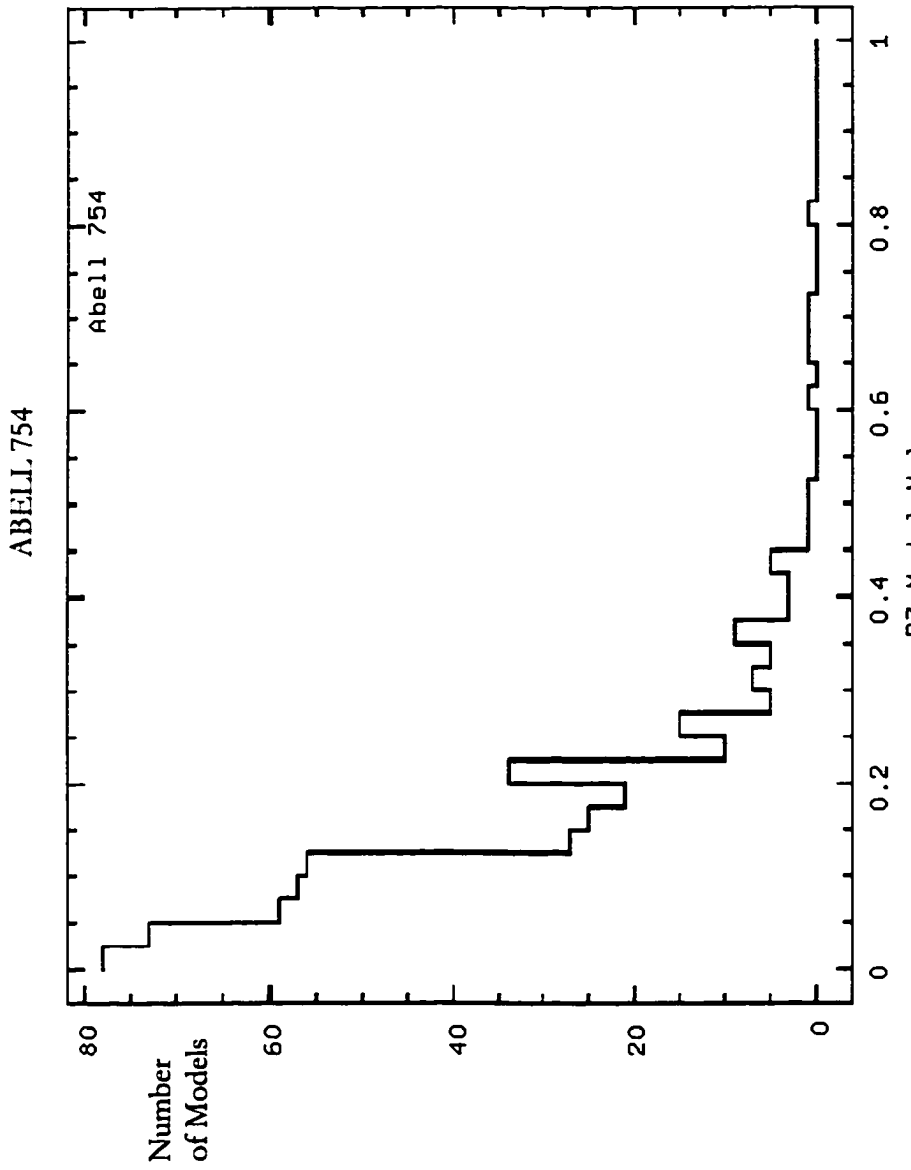

Figure 48. Histogram plots for P_3 moment for models of Abell 754.

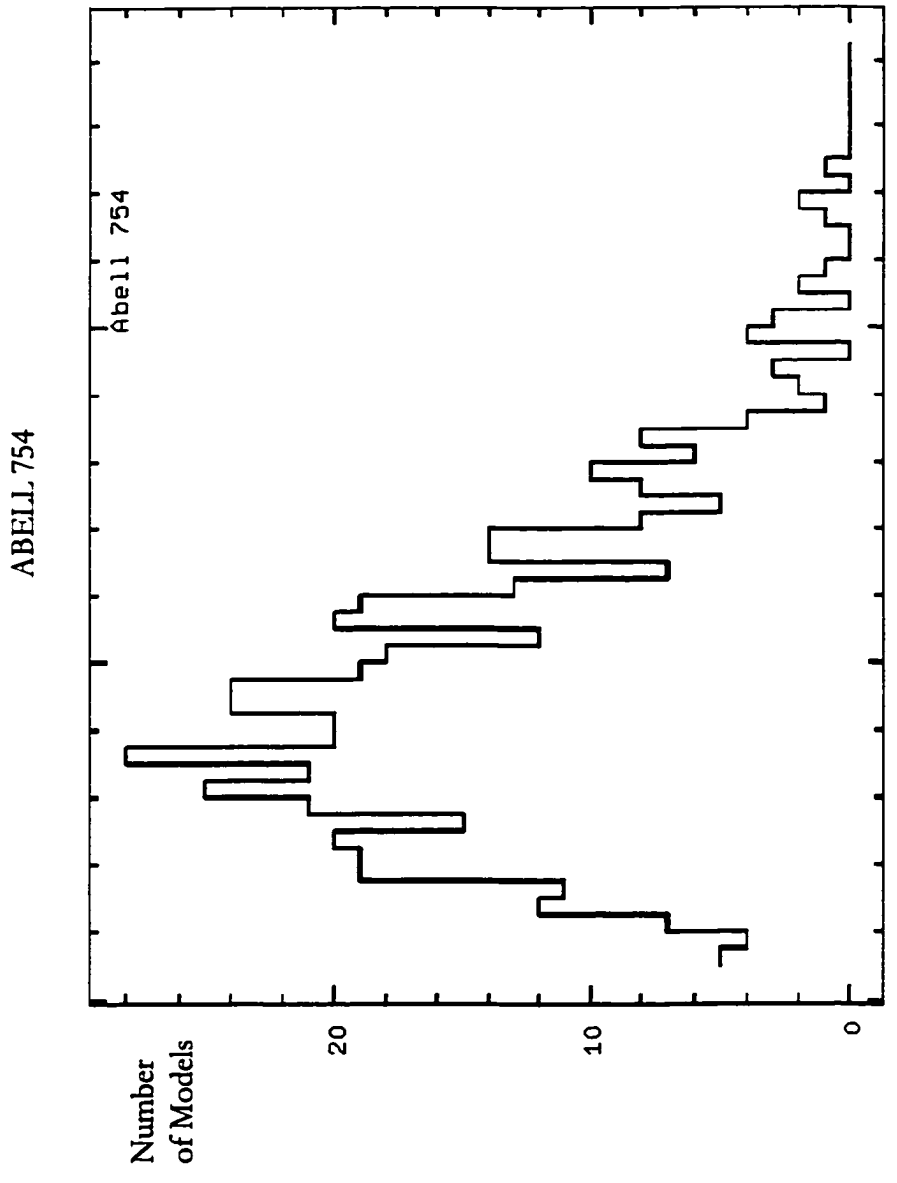

Figure 49. Histogram plots for P_4 moment for models of Abell 754.

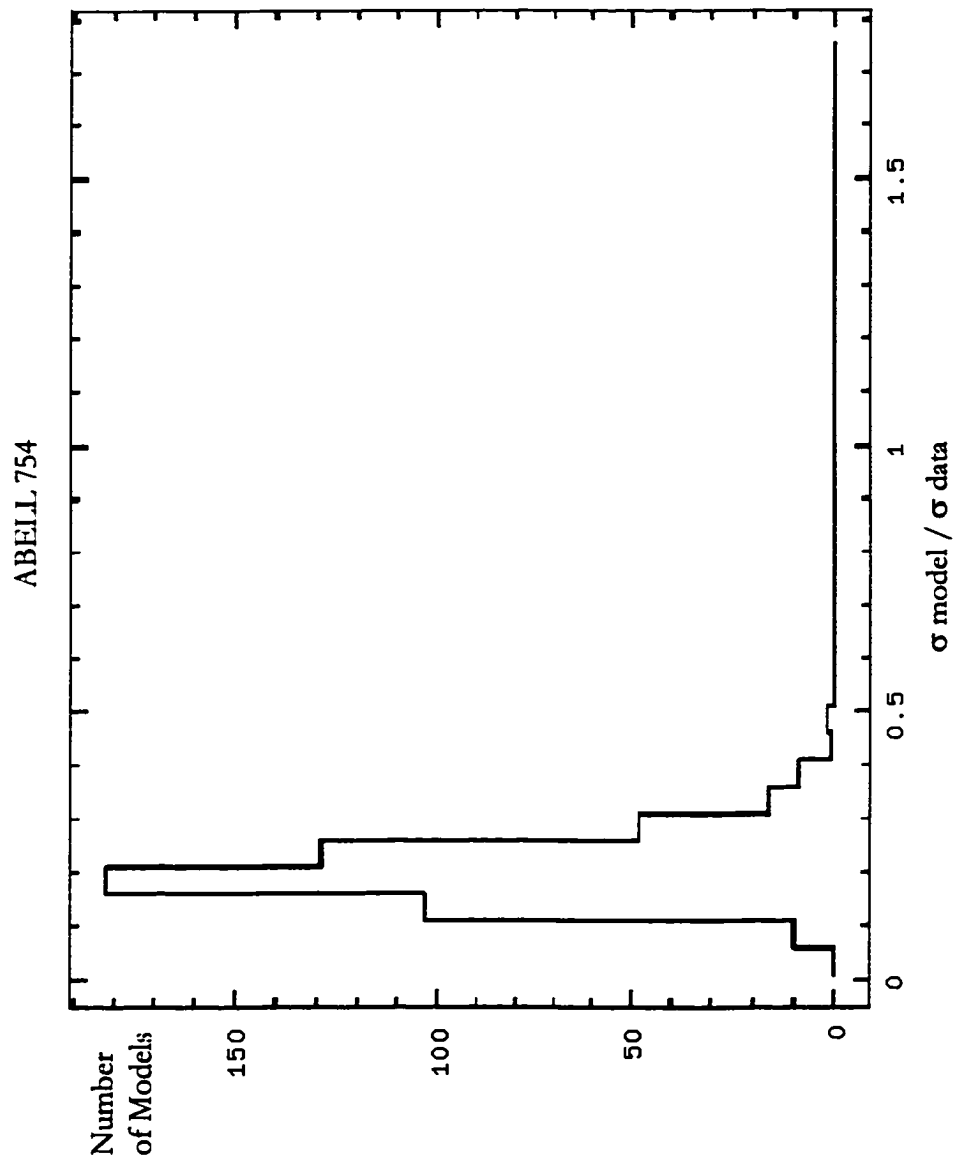

Figure 50. Sigma significance plot for Abell 754 for 'center shift' program.

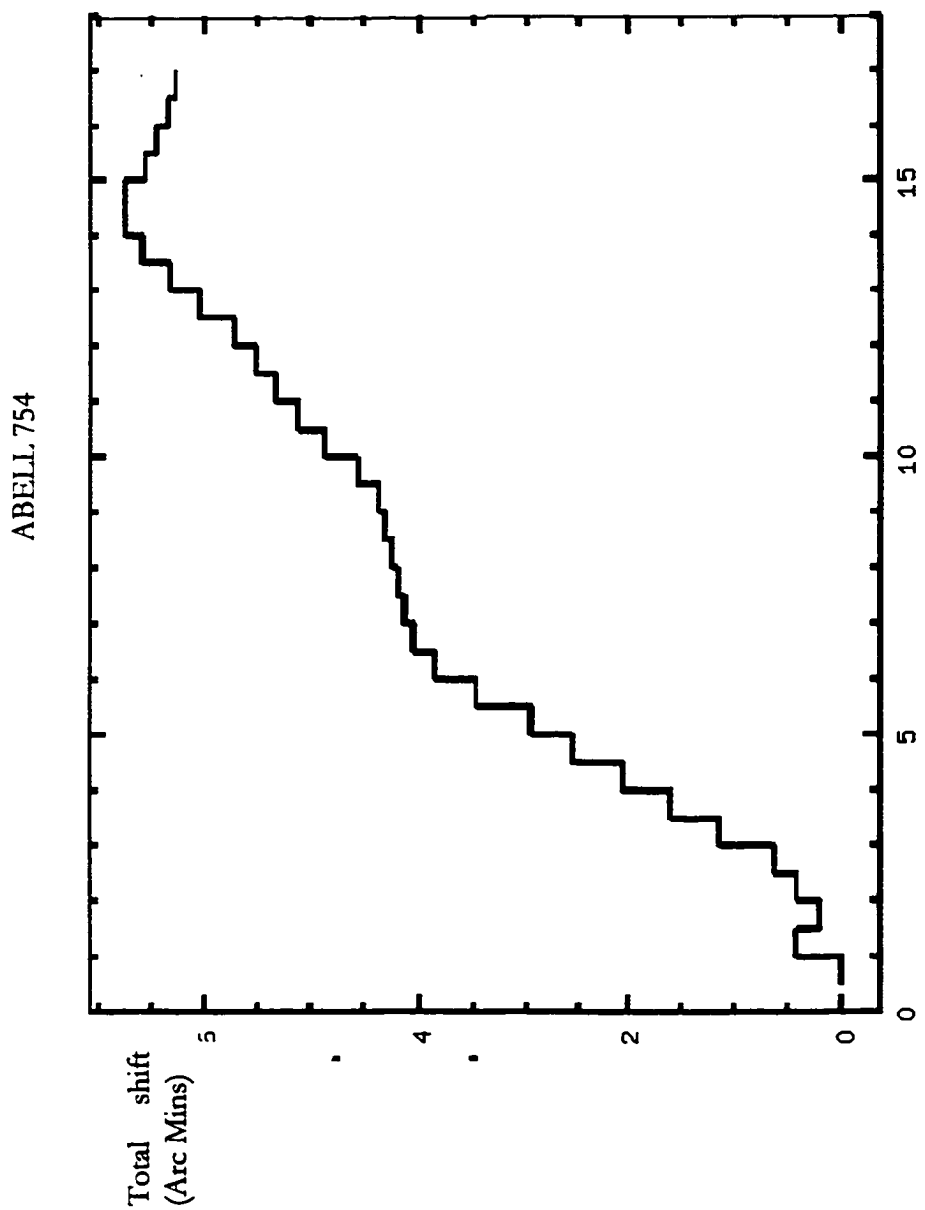

Figure 51. Total shift plot for Abell 754 for 'center shift' program.

ABELL 2052

Figure 52. Cleaned and filtered image of Abell 2052. Scale is approximately 1.0 Mpc per side.

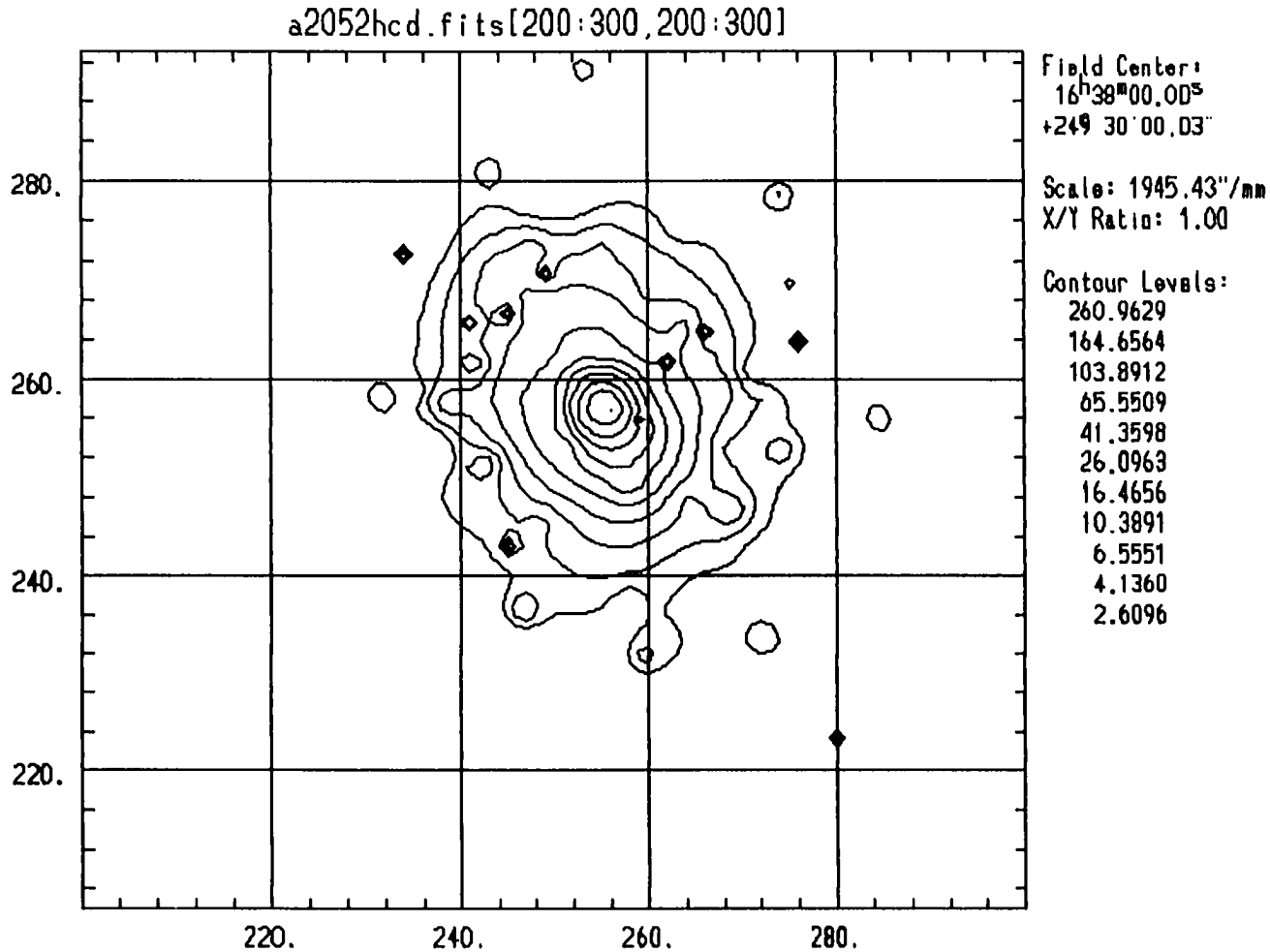

Figure 53. Contour map of Abell 2052. Scale is approximately 1.0 Mpc per side. Contour levels are given in counts.

ABELL 2052

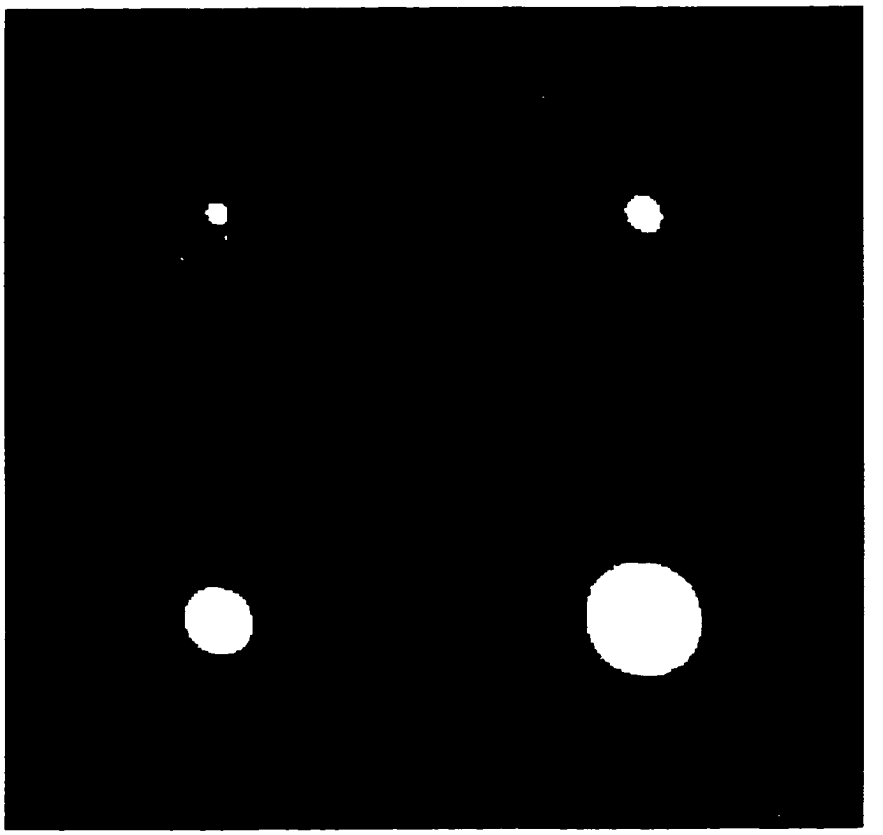

Figure 54. Wavelet transform images for Abell 2052. Clockwise from upper left in 2, 3, 4, and 5 pixel scales.

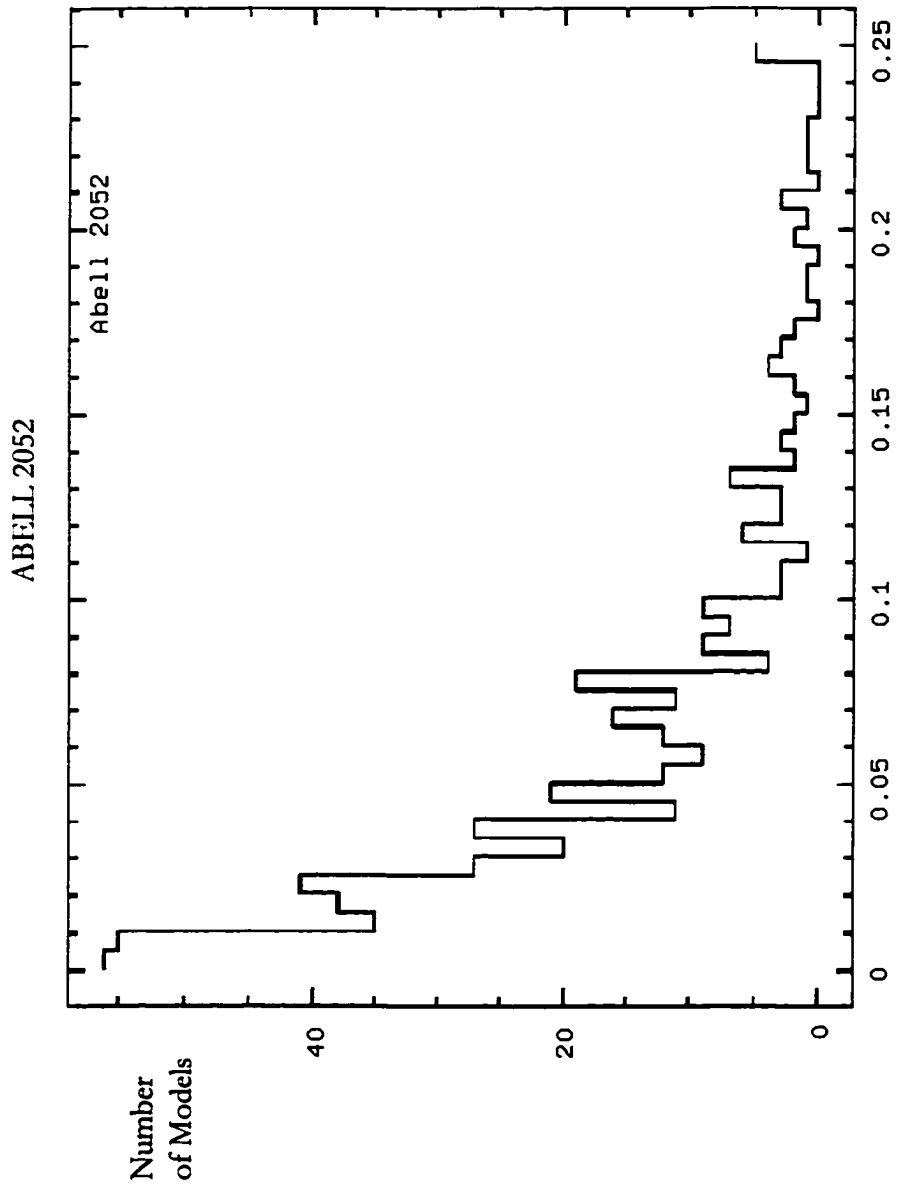

Figure 55. Histogram plots for P_3 moment for models of Abell 2052.

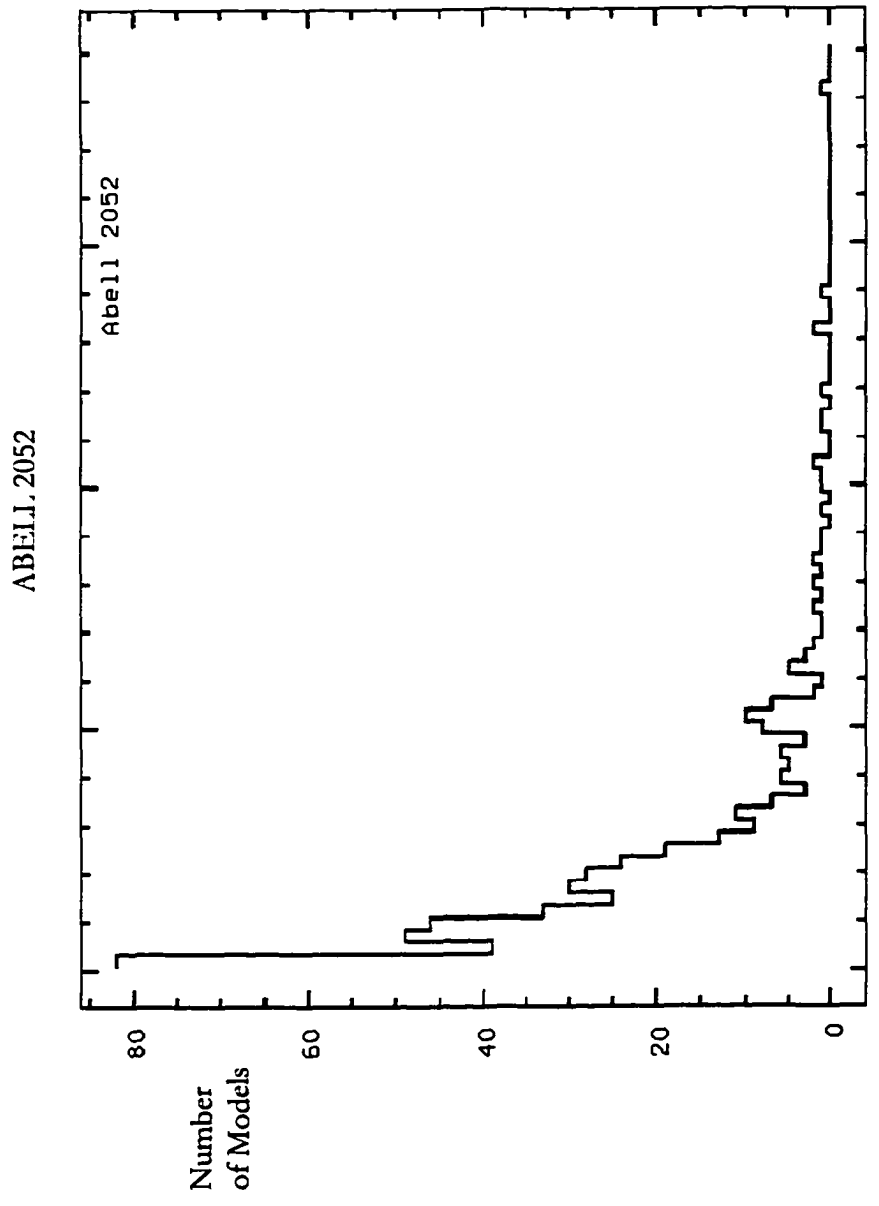

Figure 56. Histogram plots for P_4 moment for models of Abell 2052.

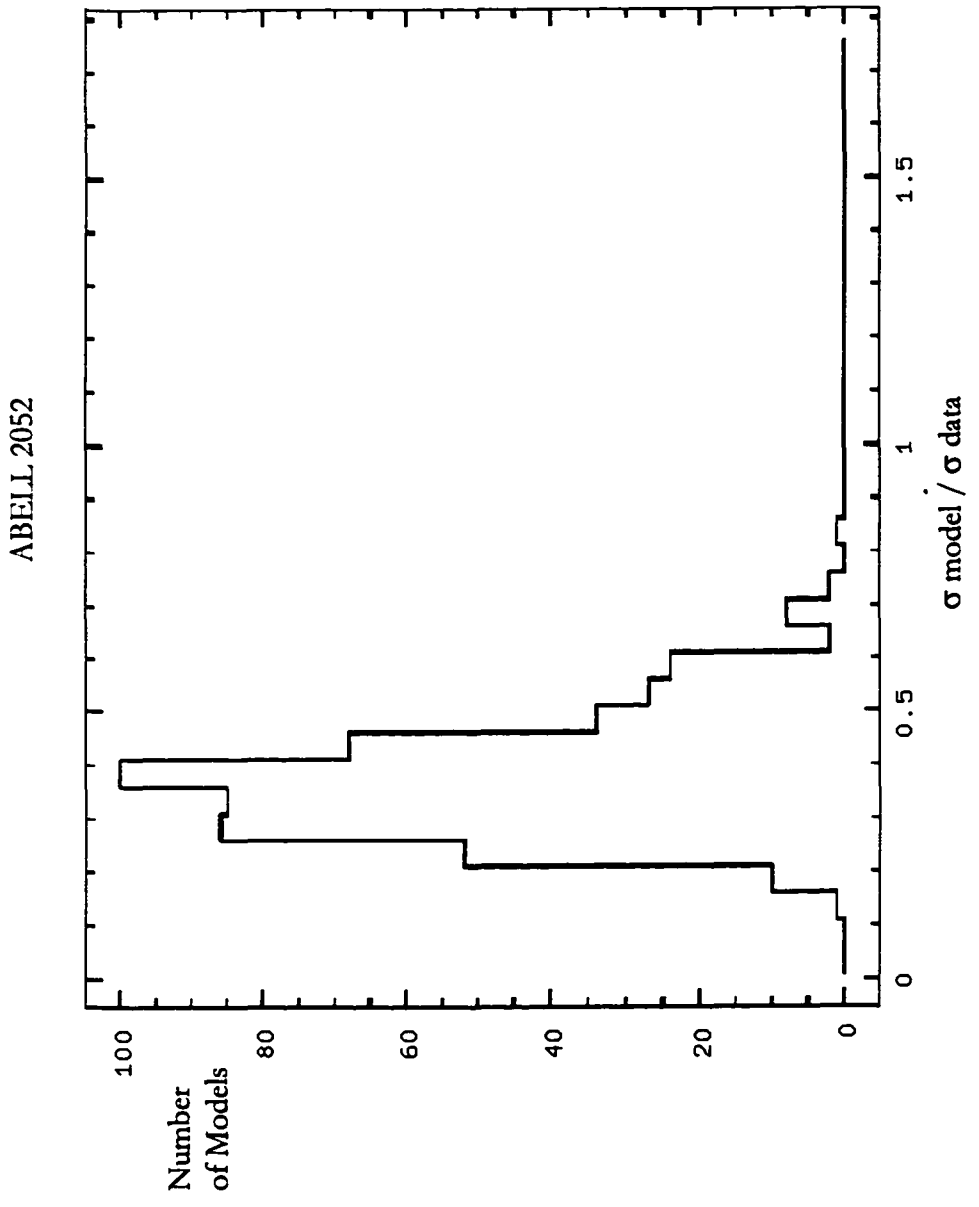

Figure 57. Sigma significance plot for Abell 2052 for 'center shift' program.

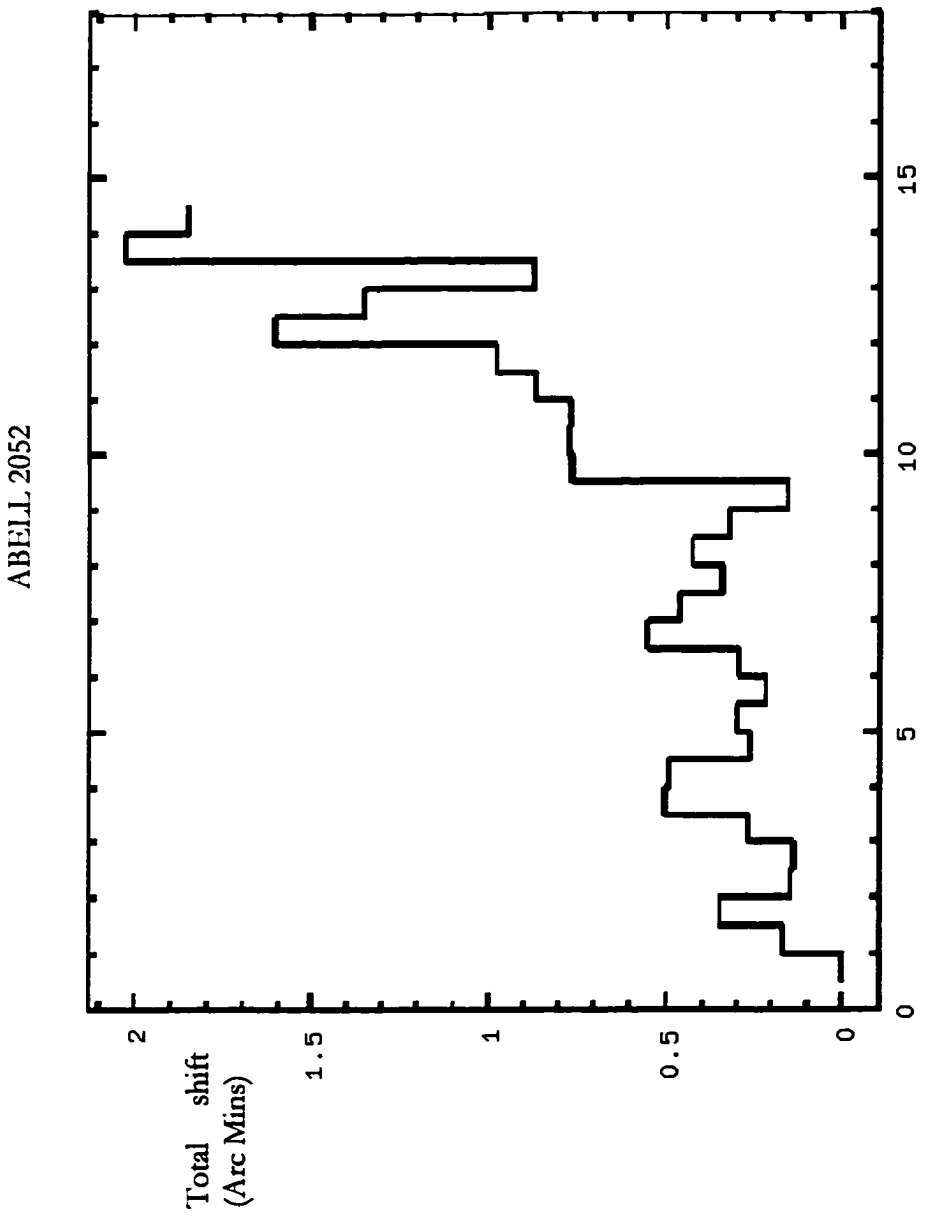

Figure 58. Total shift plot for Abell 2052 for 'center shift' program.

ABELL 2382

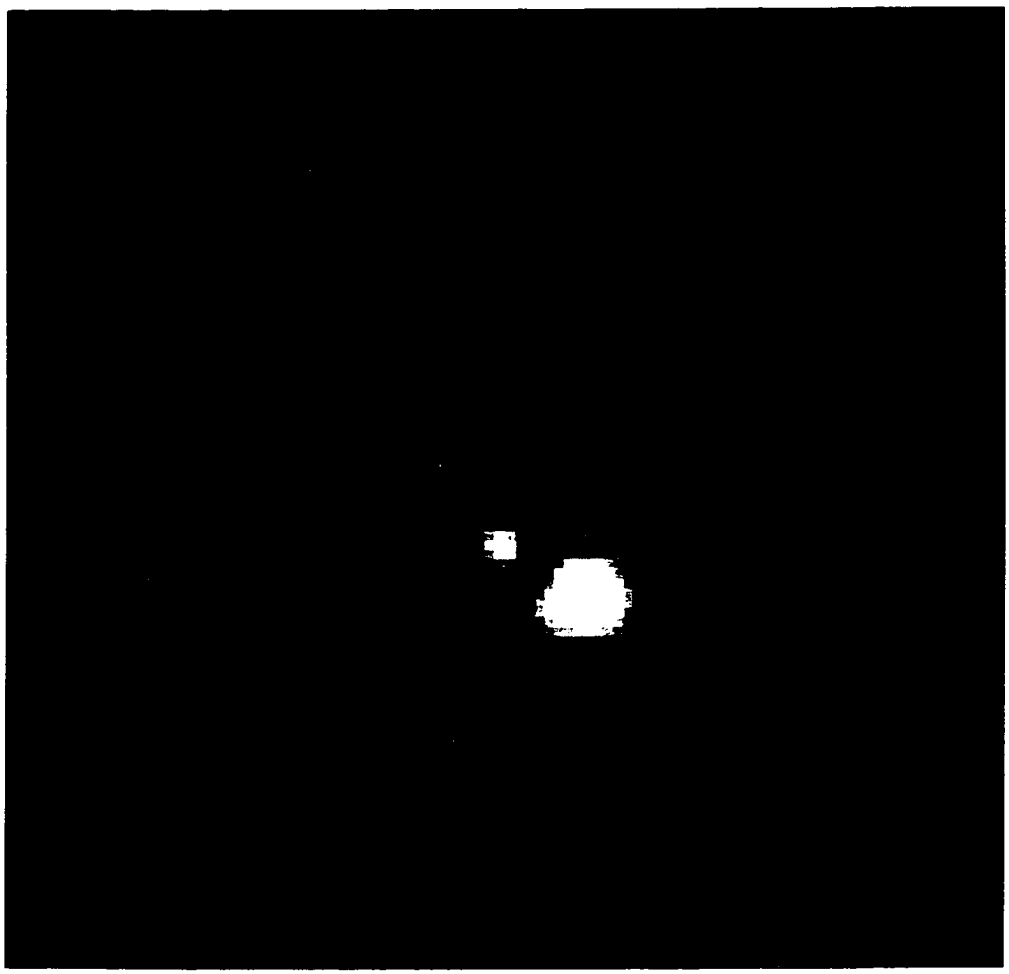

Figure 59. Cleaned and filtered image of Abell 2382. Scale is approximately 1.6 Mpc per side.

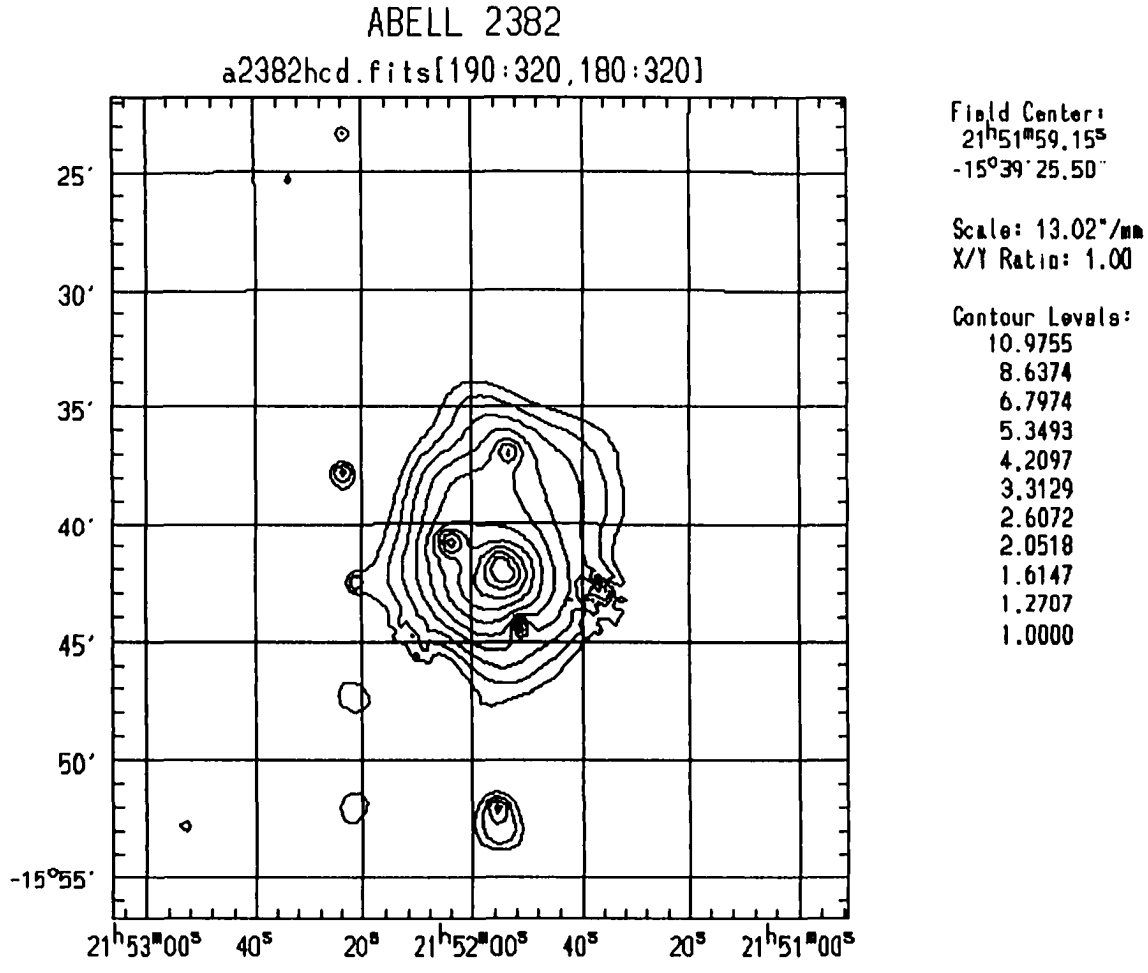

Figure 60. Contour map of Abell 2382. Scale is approximately 1.6 Mpc per side. Contour levels are given in counts.

ABELL 2382

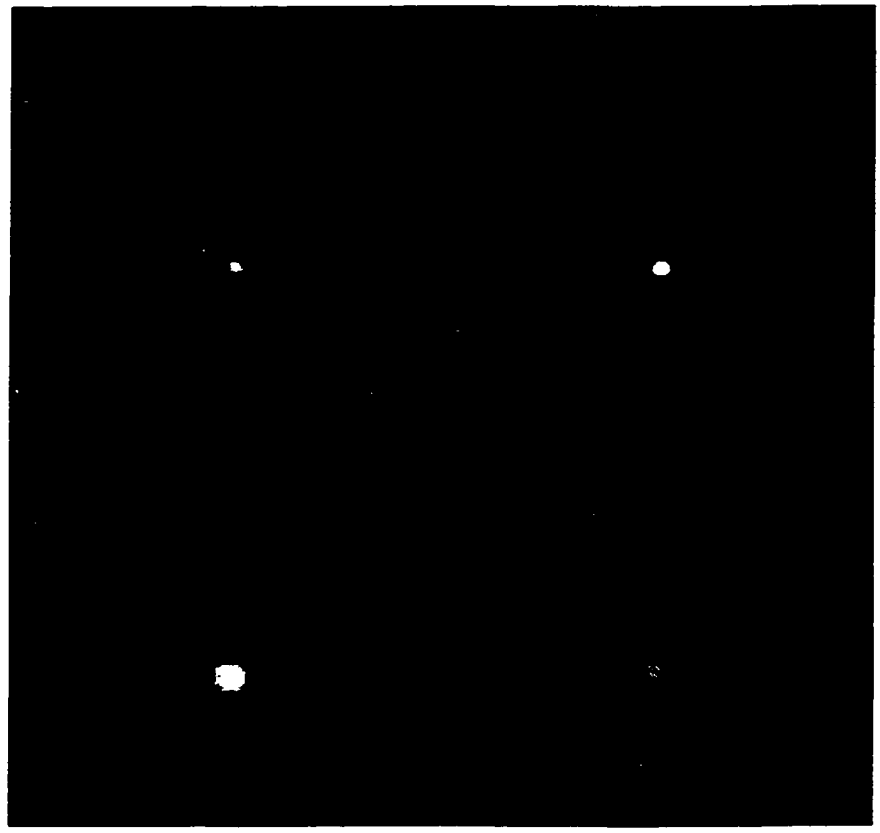

Figure 61. Wavelet transform images for Abell 2382. Clockwise from upper left in 2, 3, 4, and 5 pixel scales.

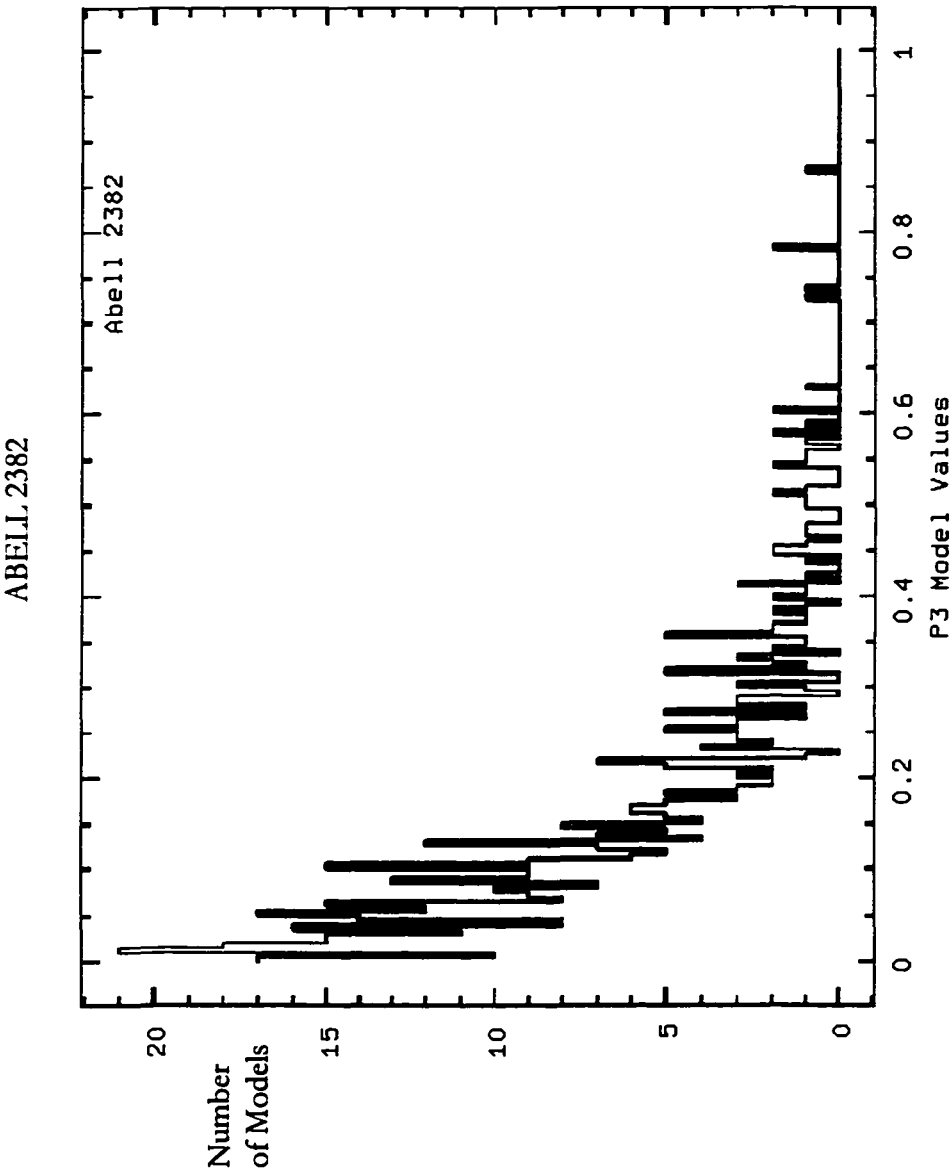

Figure 62. Histogram plots for P_3 moment for models of Abell 2382.

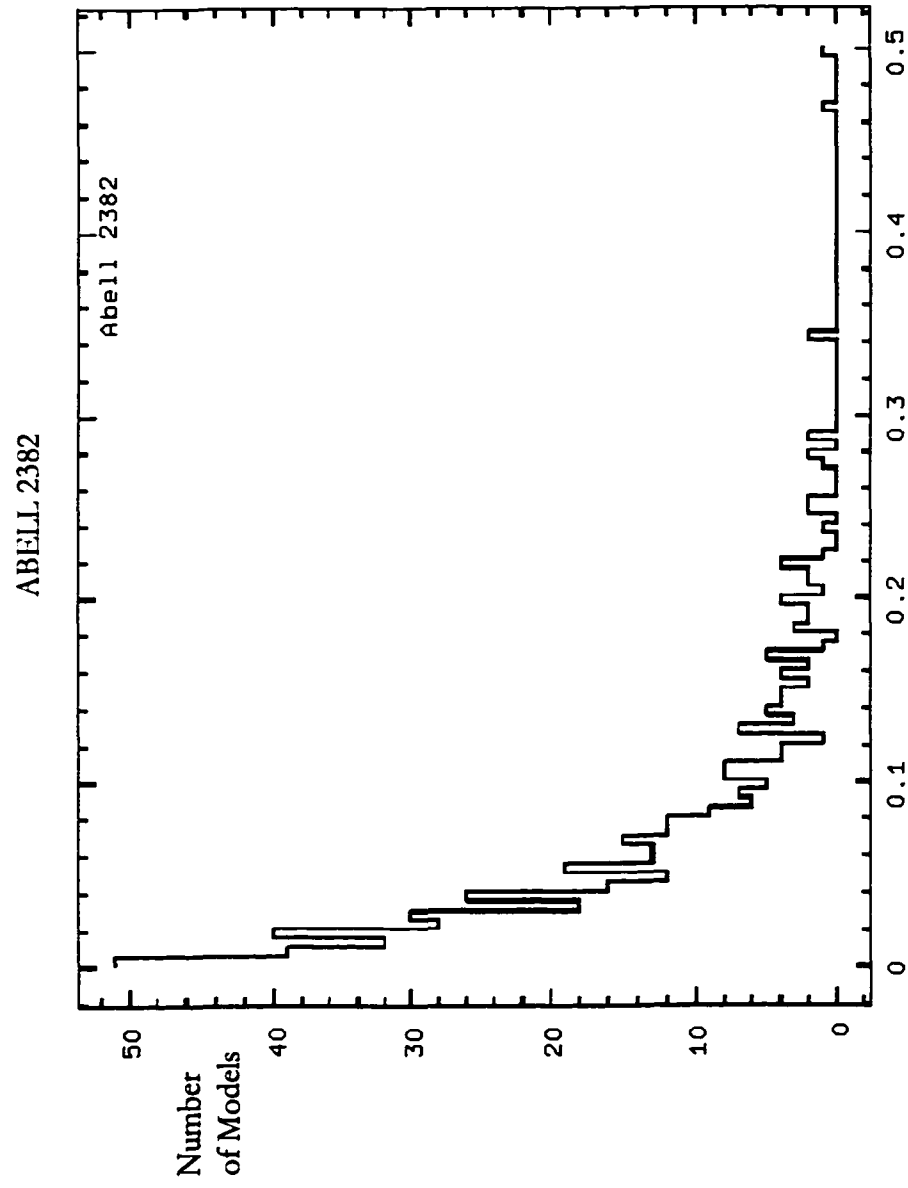

Figure 63. Histogram plots for P_4 moment for models of Abell 2382.

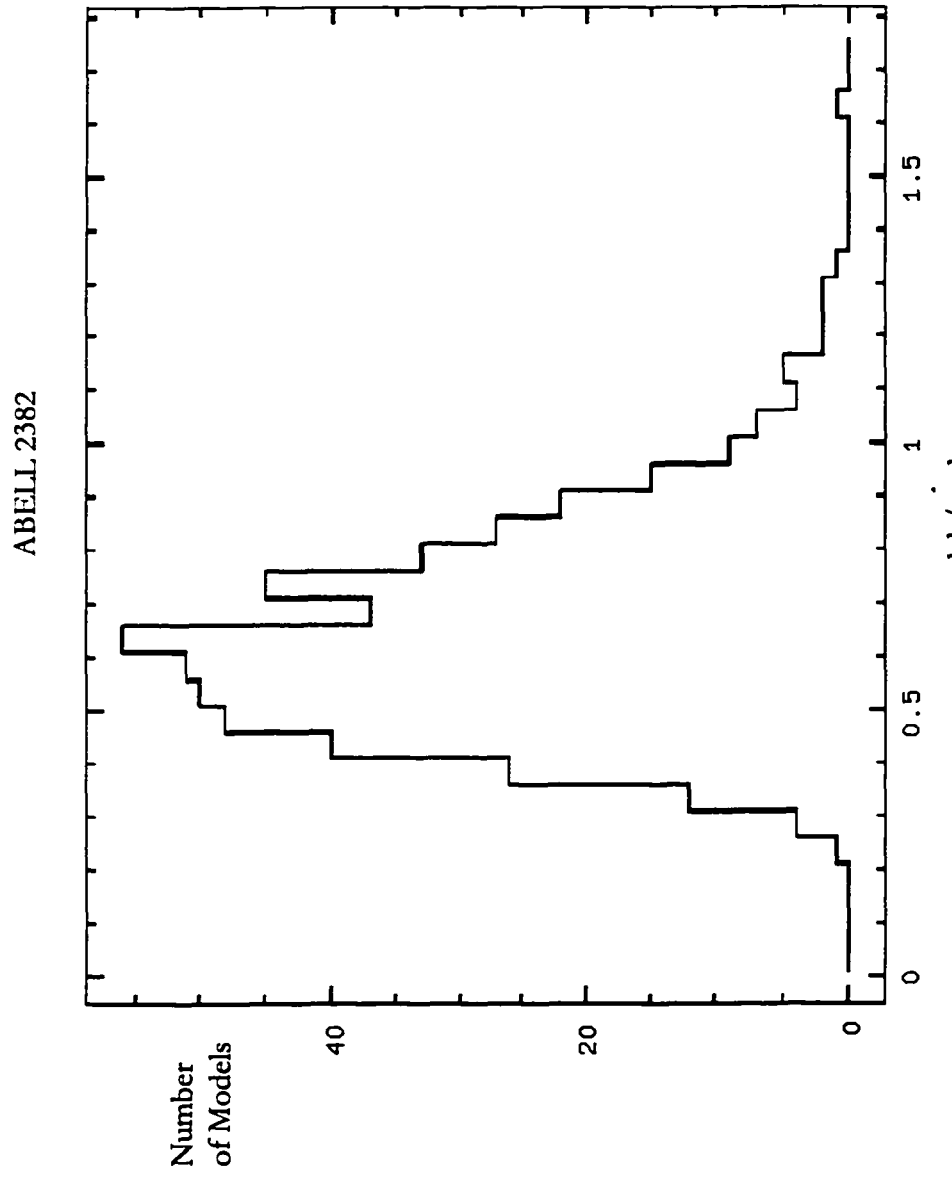

Figure 64. Sigma significance plot for Abell 2382 for 'center shift' program.

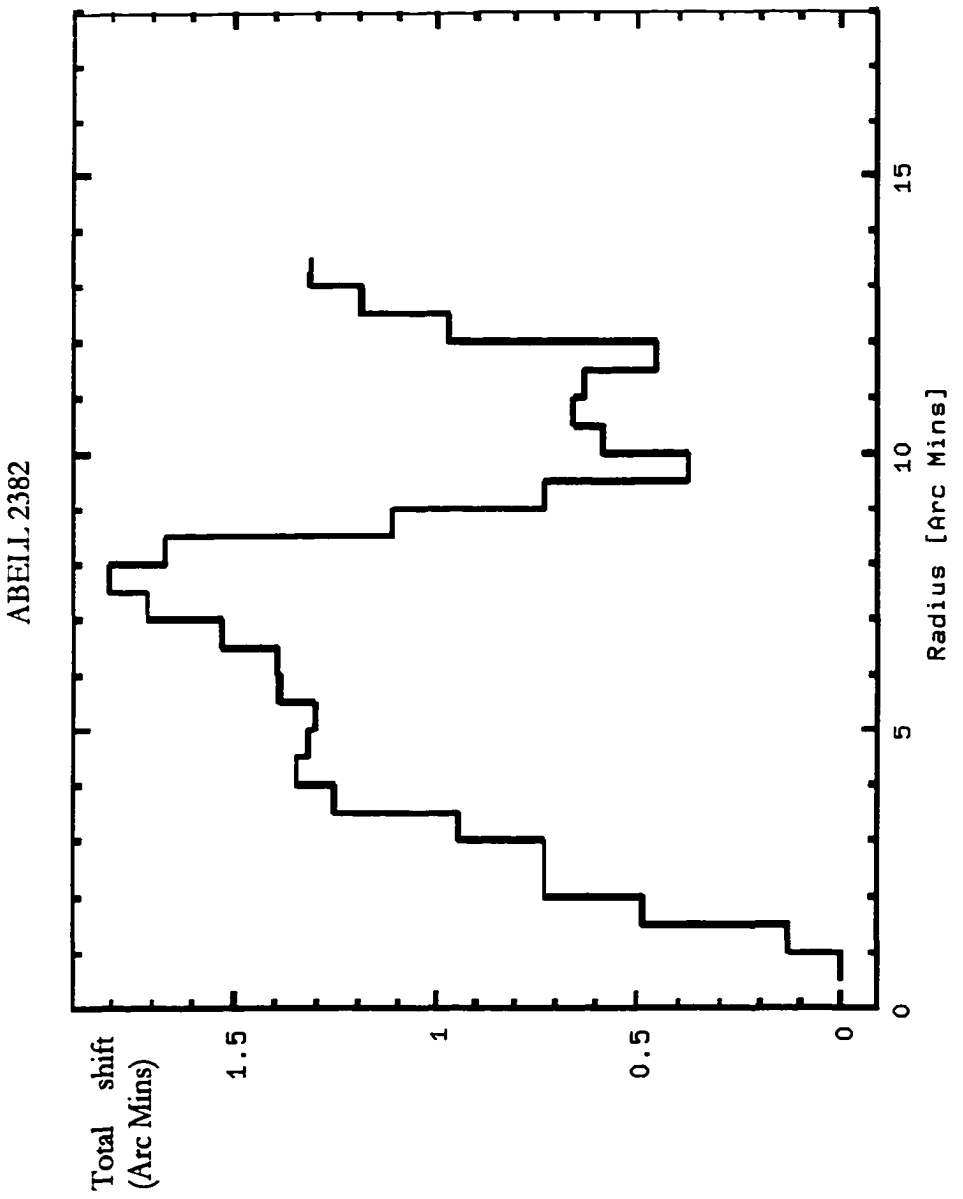

Figure 65. Total shift plot for Abell 2382 for 'center shift' program.

ABELL 2717

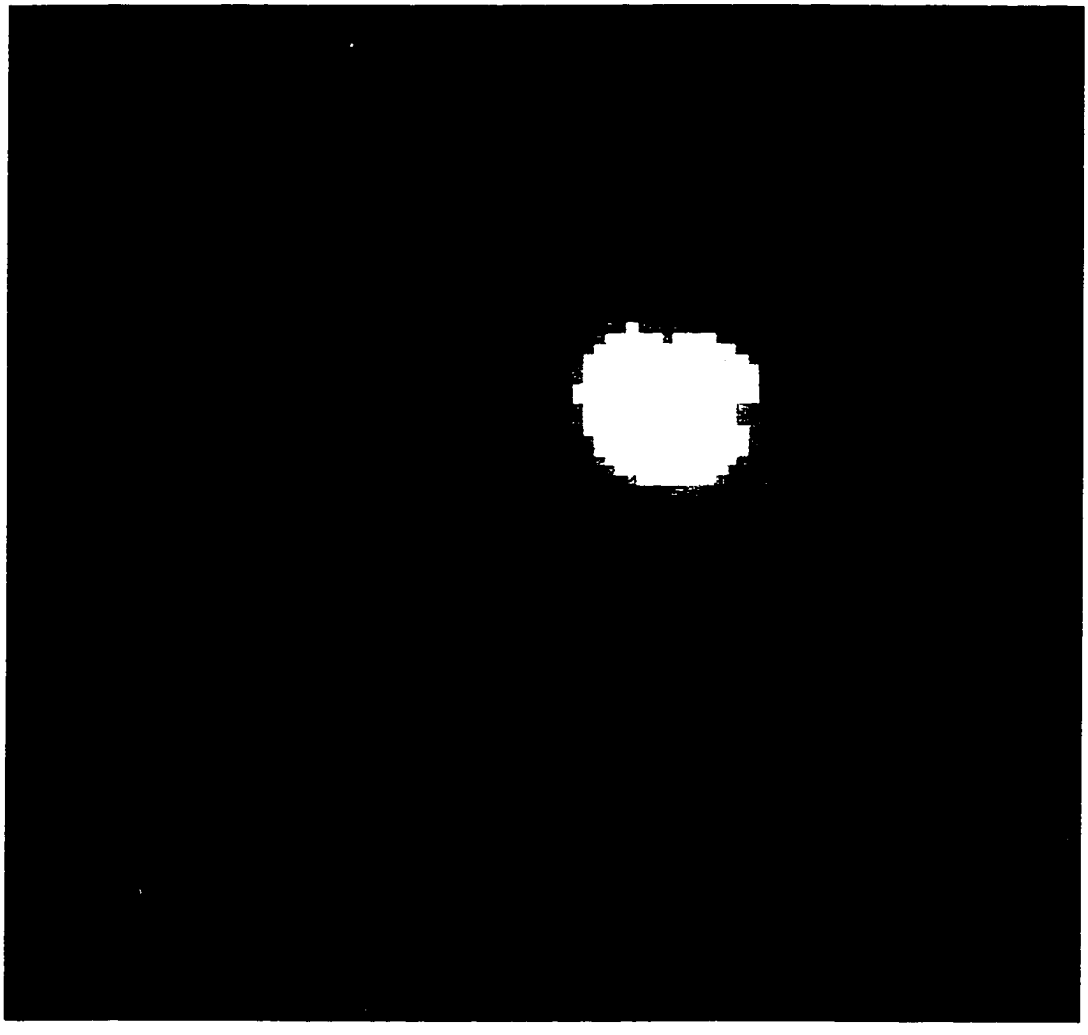

Figure 66. Cleaned and filtered image of Abell 2717. Scale is approximately 1.3 Mpc per side.

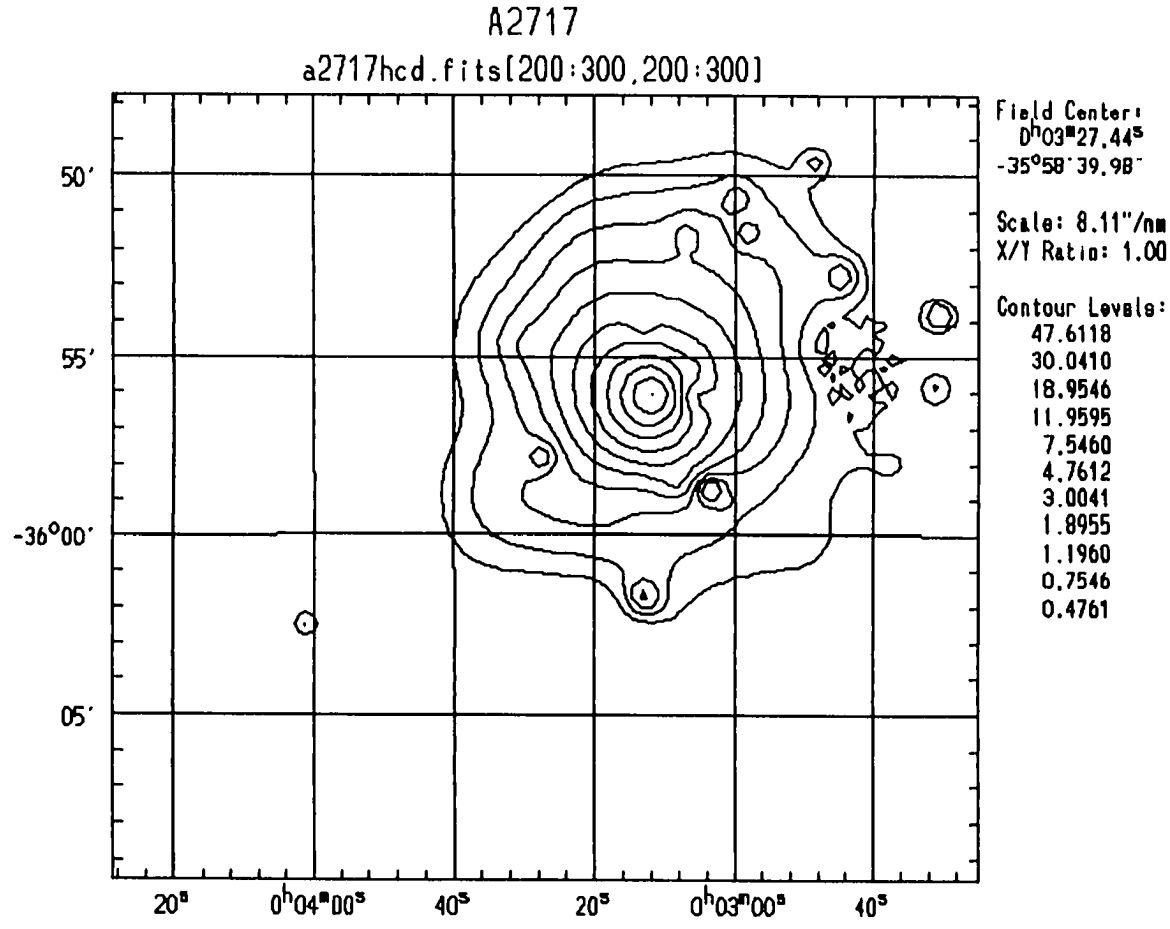

Figure 67. Contour map of Abell 2717. Scale is approximately 1.3 Mpc per side. Contour levels are given in counts.

ABELL 2717

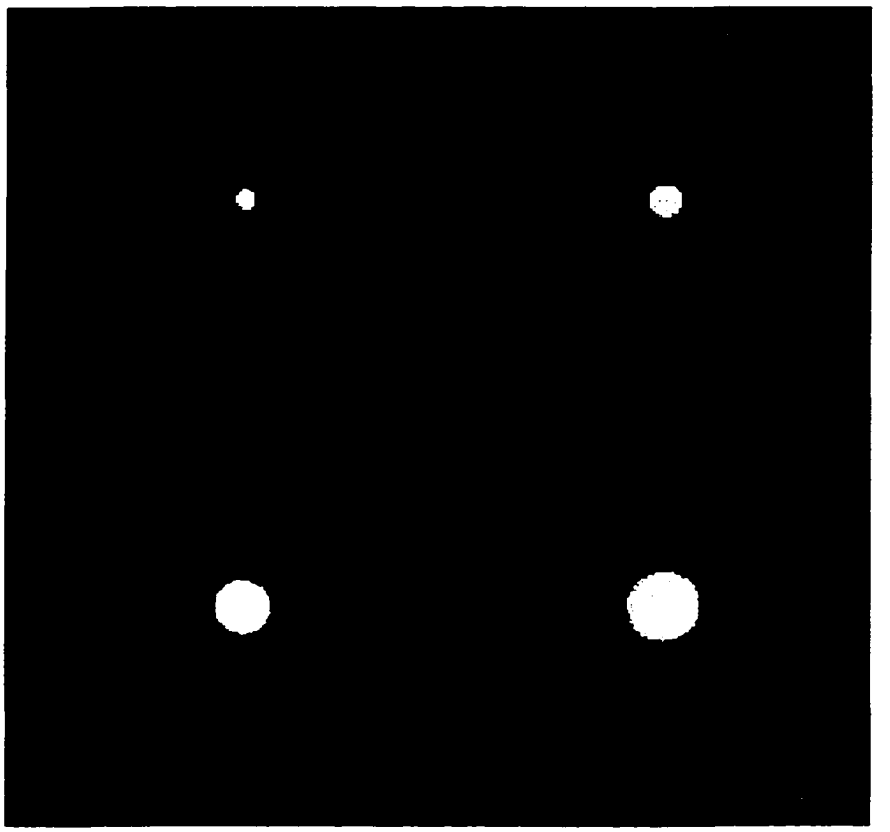

Figure 68. Wavelet transform images for Abell 2717. Clockwise from upper left in 2, 3, 4, and 5 pixel scales.

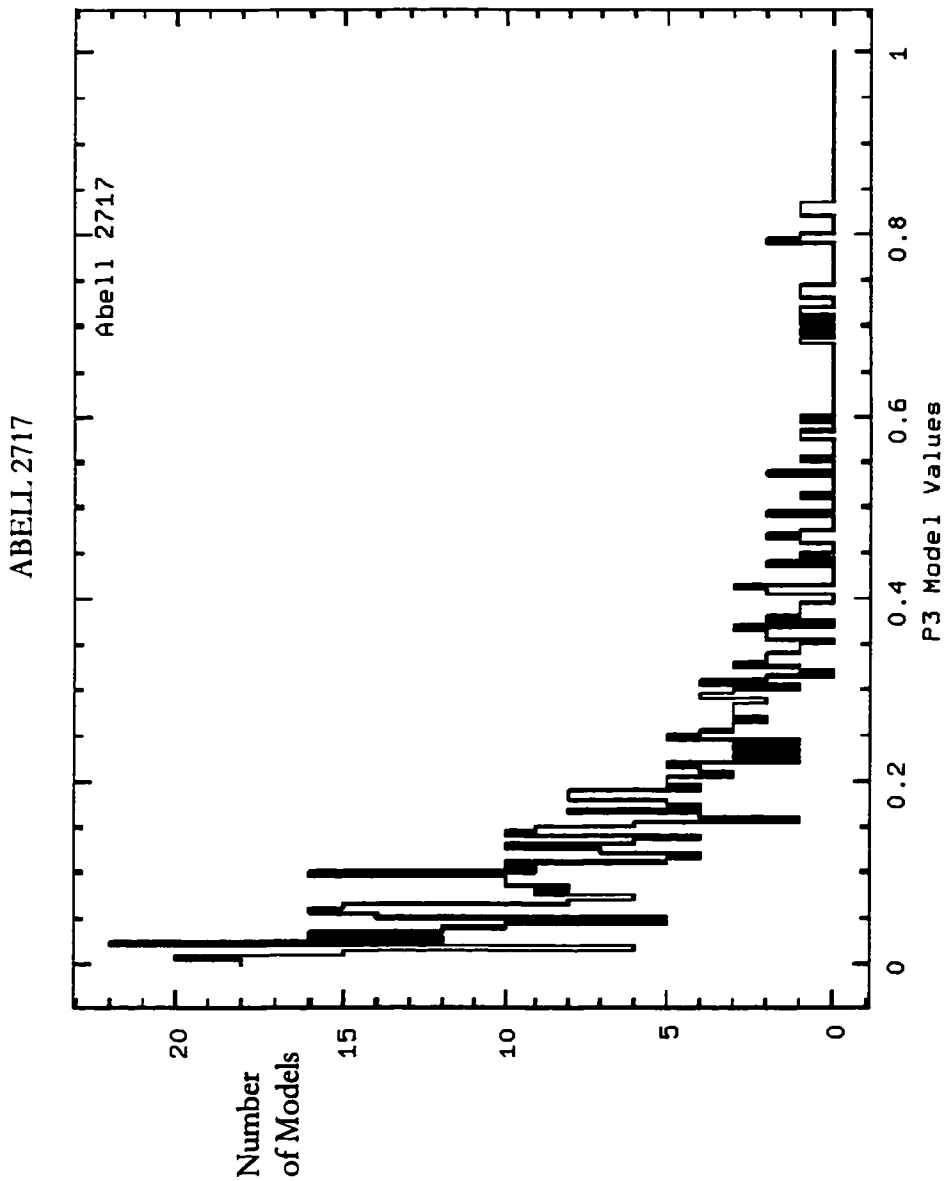

Figure 69. Histogram plots for P_3 moment for models of Abell 2717.

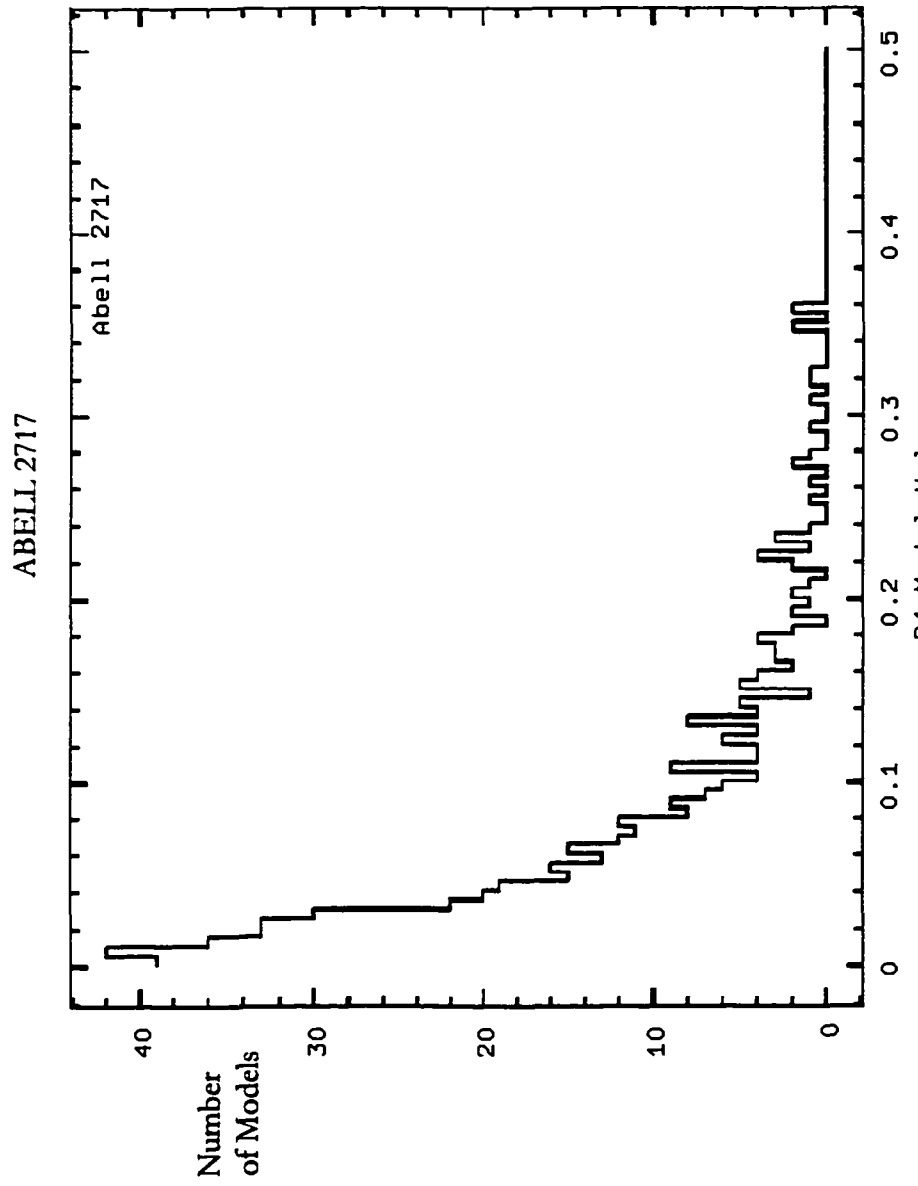

Figure 70. Histogram plots for P_4 moment for models of Abell 2717.

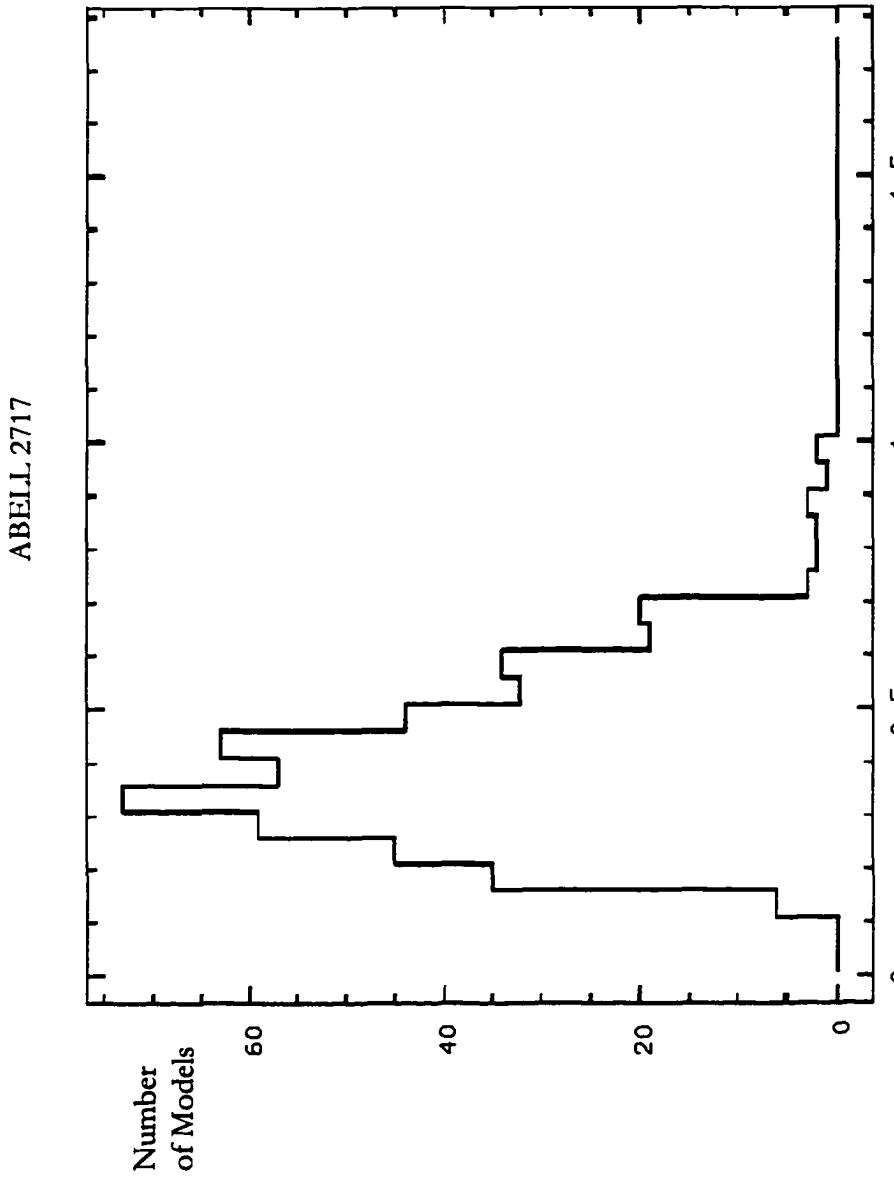

Figure 71. Sigma significance plot for Abell 2717 for 'center shift' program.

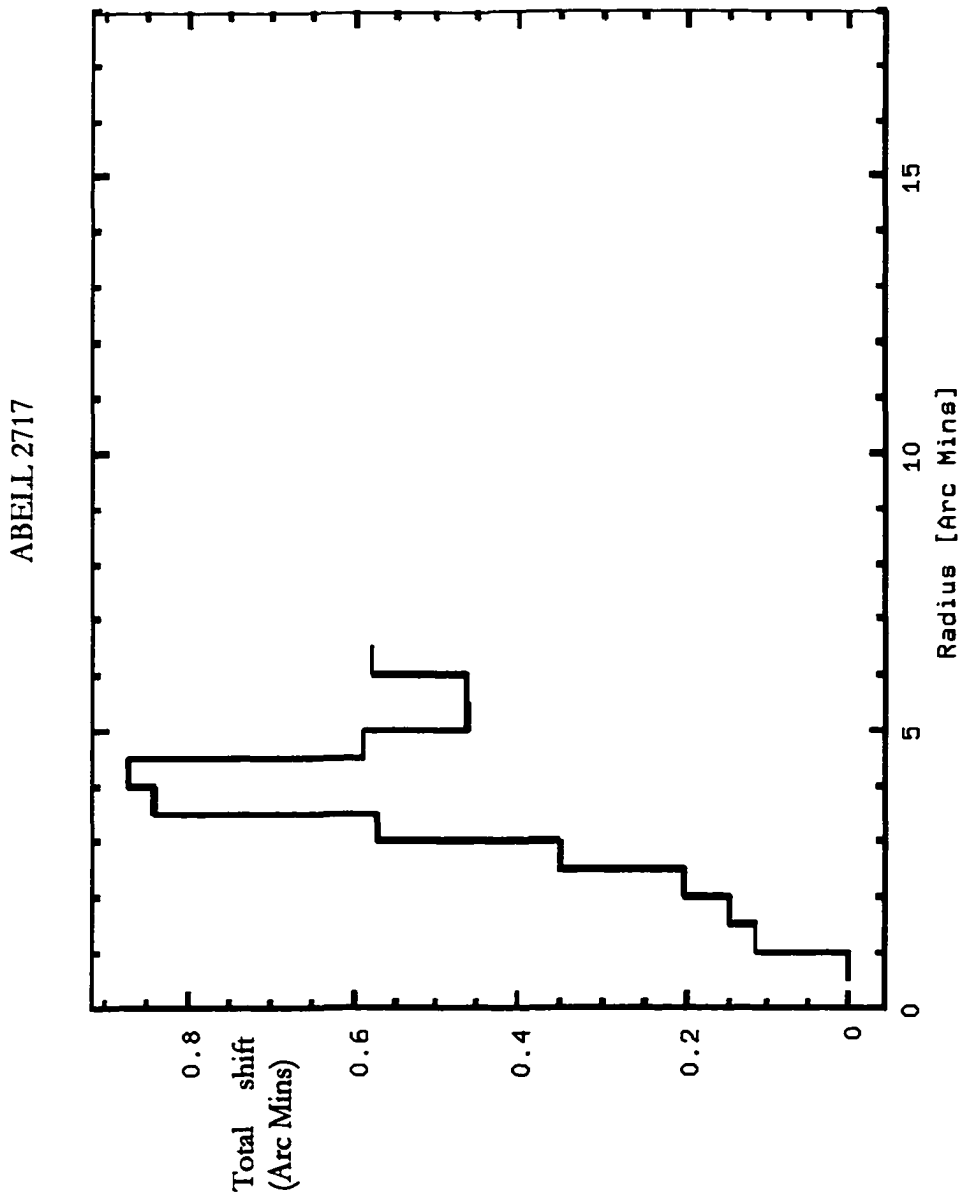

Figure 72. Total shift plot for Abell 2717 for 'center shift' program.

ABELL 2734

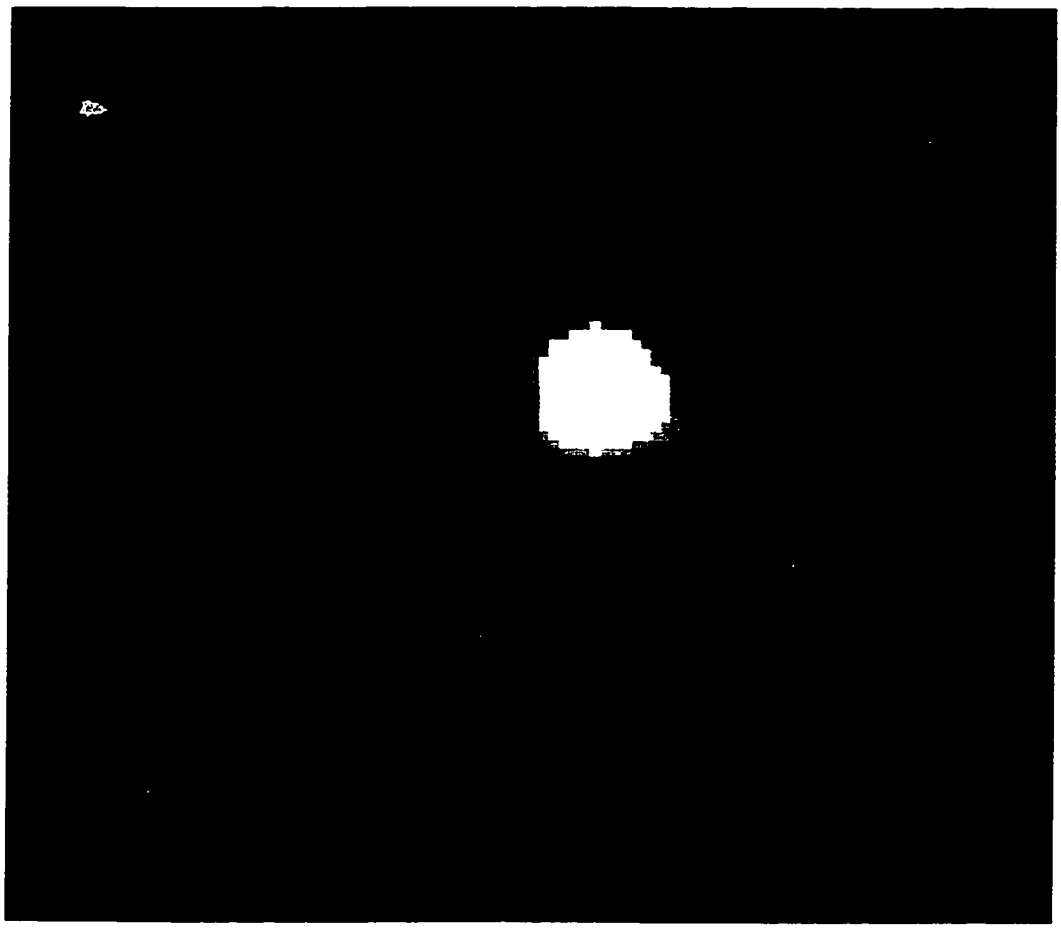

Figure 73. Cleaned and filtered image of Abell 2734. Scale is approximately 1.5 Mpc per side.

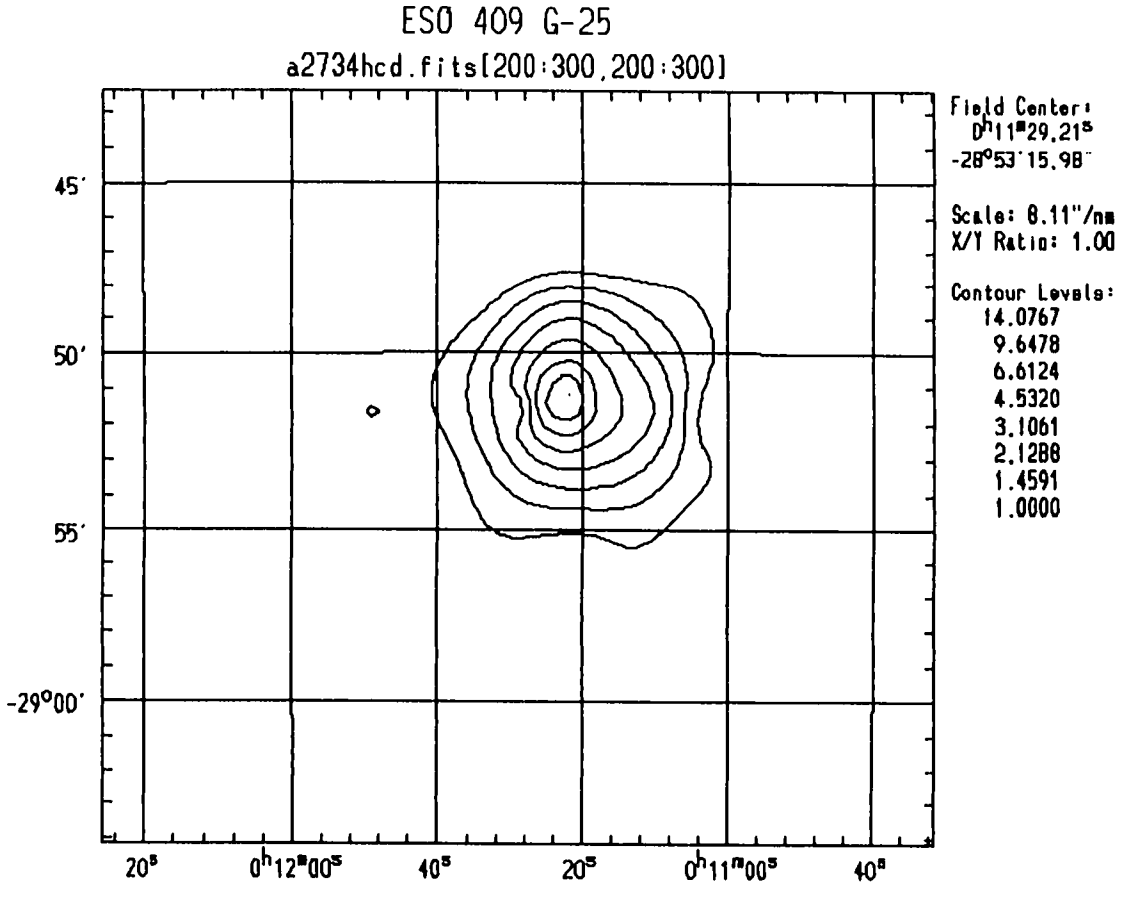

Figure 74. Contour map of Abell 2734. Scale is approximately 1.5 Mpc per side. Contour levels are given in counts.

ABELL 2734

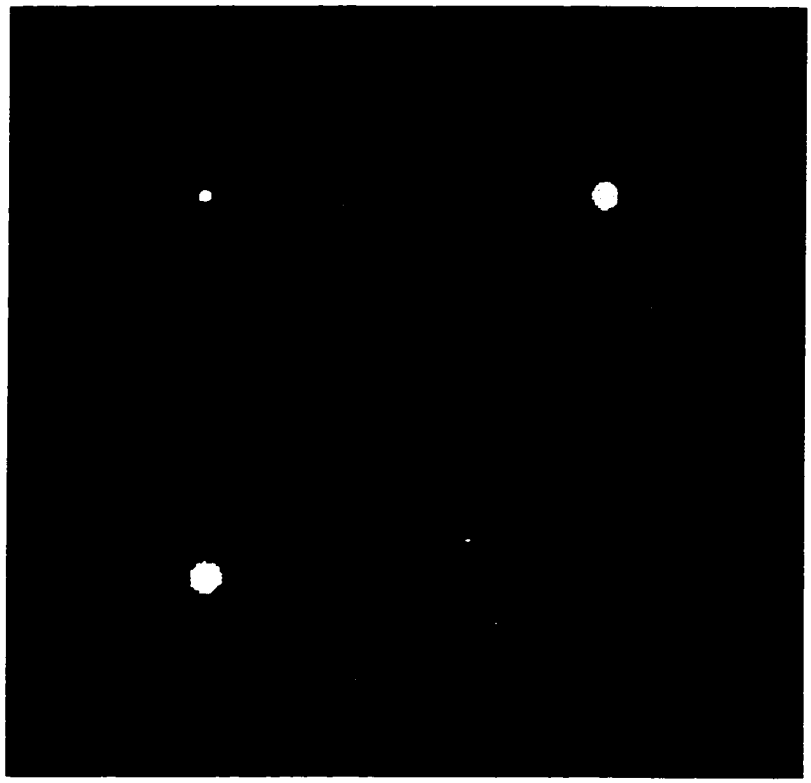

Figure 75. Wavelet transform images for Abell 2734. Clockwise from upper left in 2, 3, 4, and 5 pixel scales.

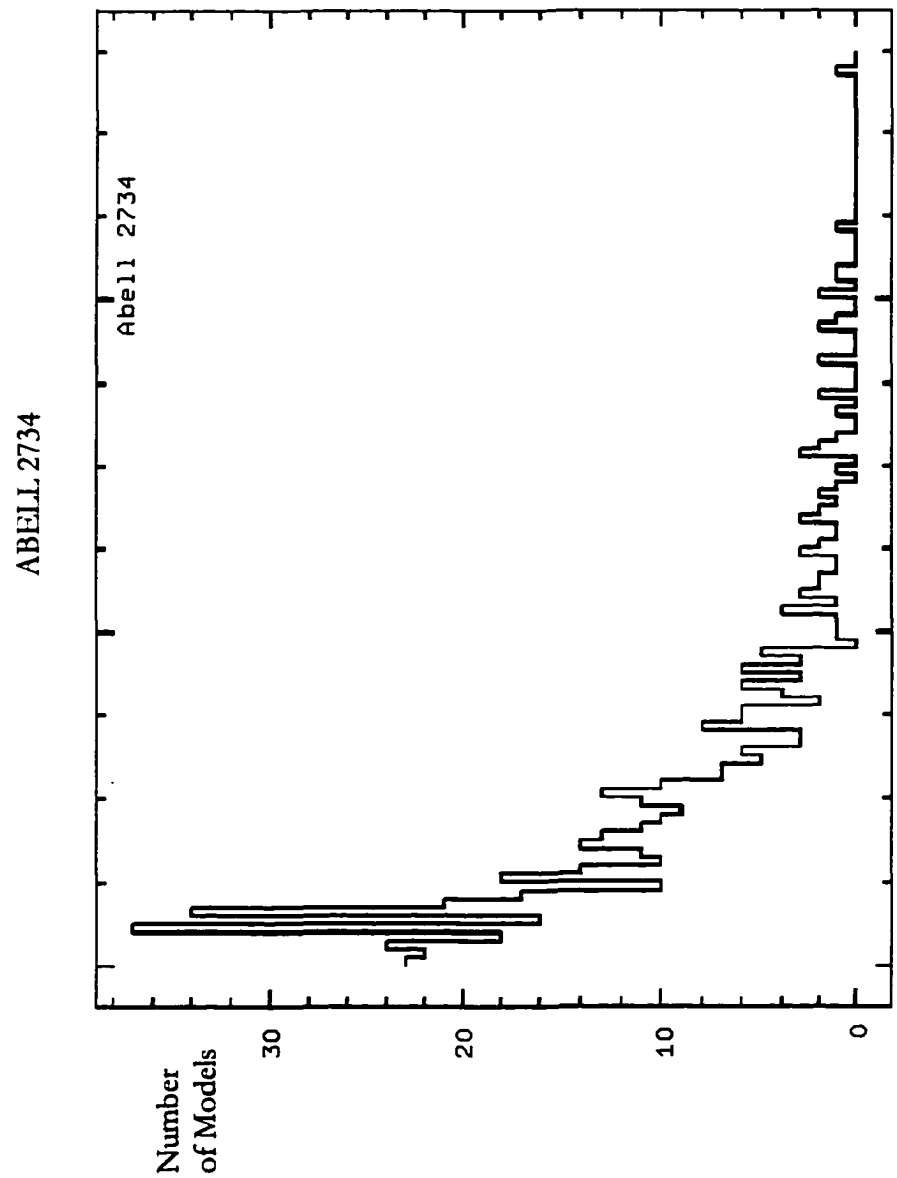

Figure 76. Histogram plots for P_3 moment for models of Abell 2734.

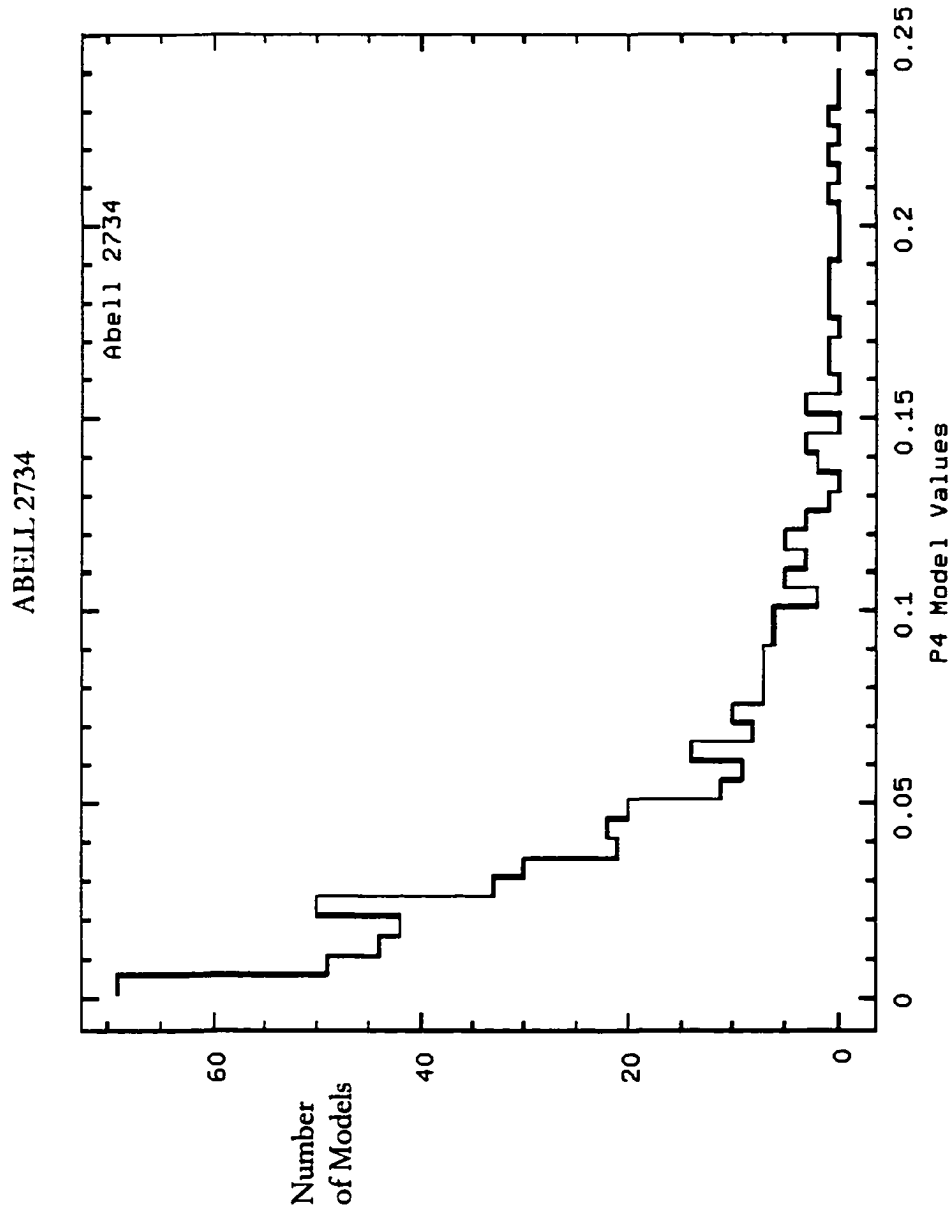

Figure 77. Histogram plots for P_4 moment for models of Abell 2734.

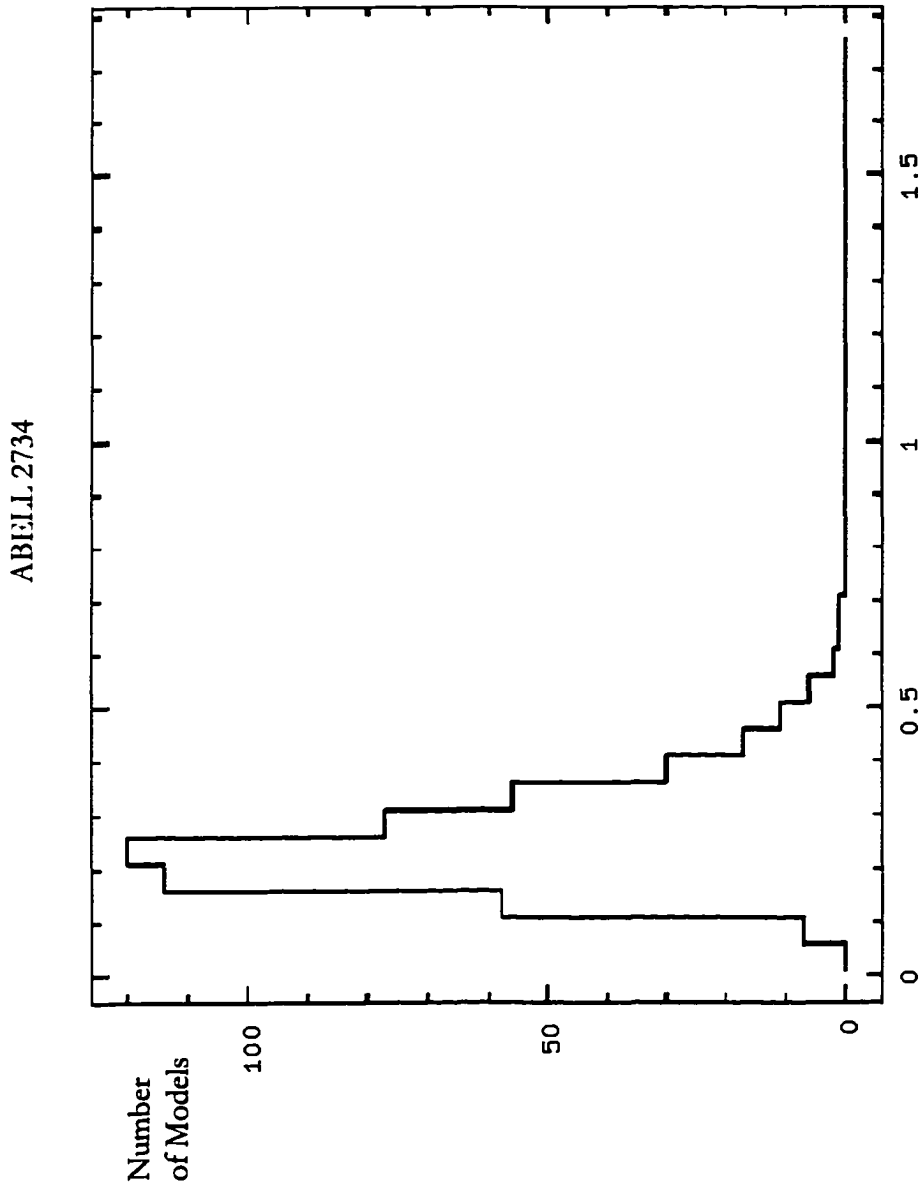

Figure 78. Sigma significance plot for Abell 2734 for 'center shift' program.

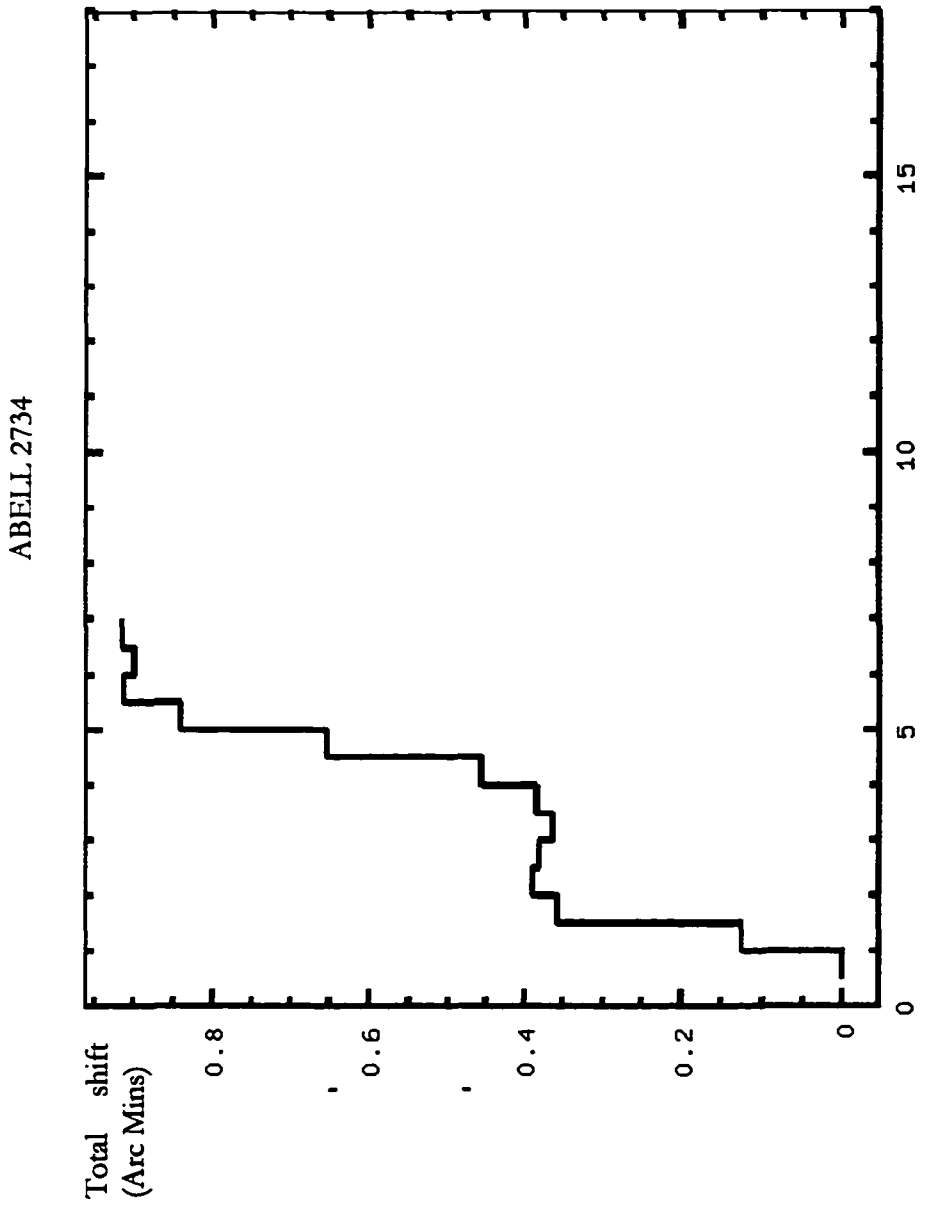

Figure 79. Total shift plot for Abell 2734 for 'center shift' program.

ABELL 3111

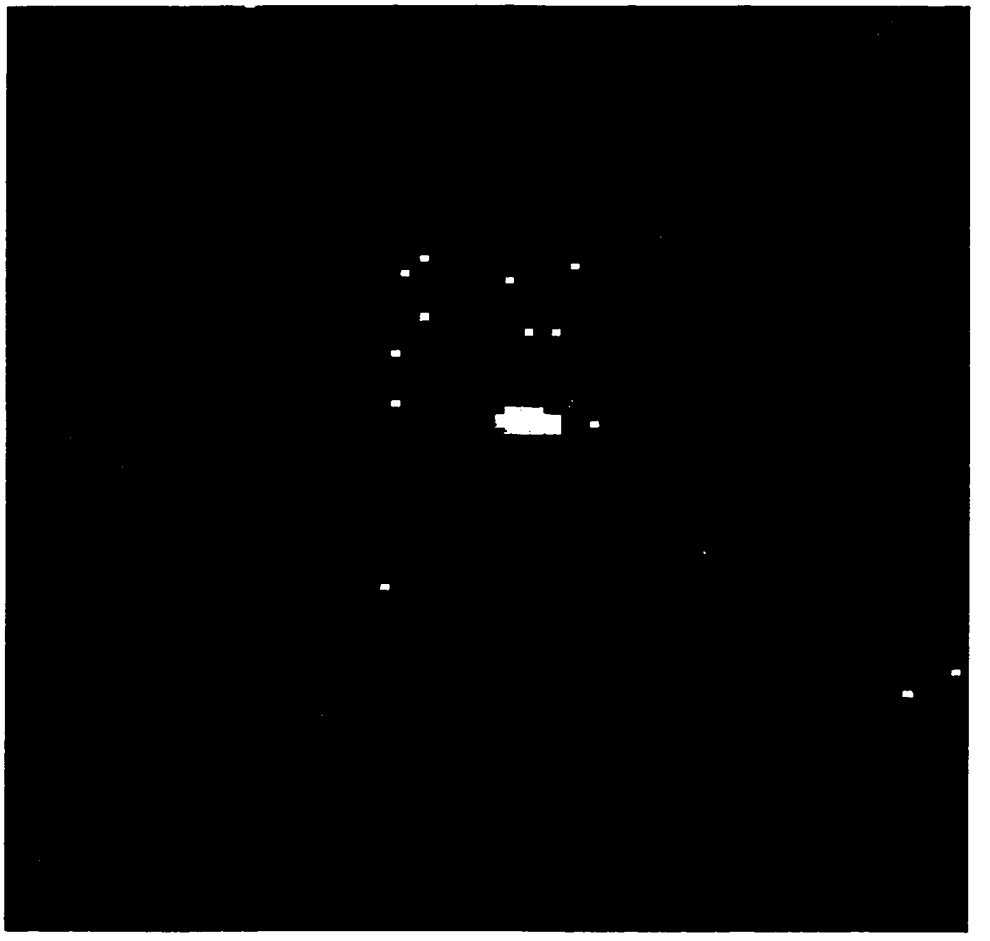

Figure 80. Cleaned and filtered image of Abell 3111. Scale is approximately 1.9 Mpc in X and 2.5 Mpc in Y.

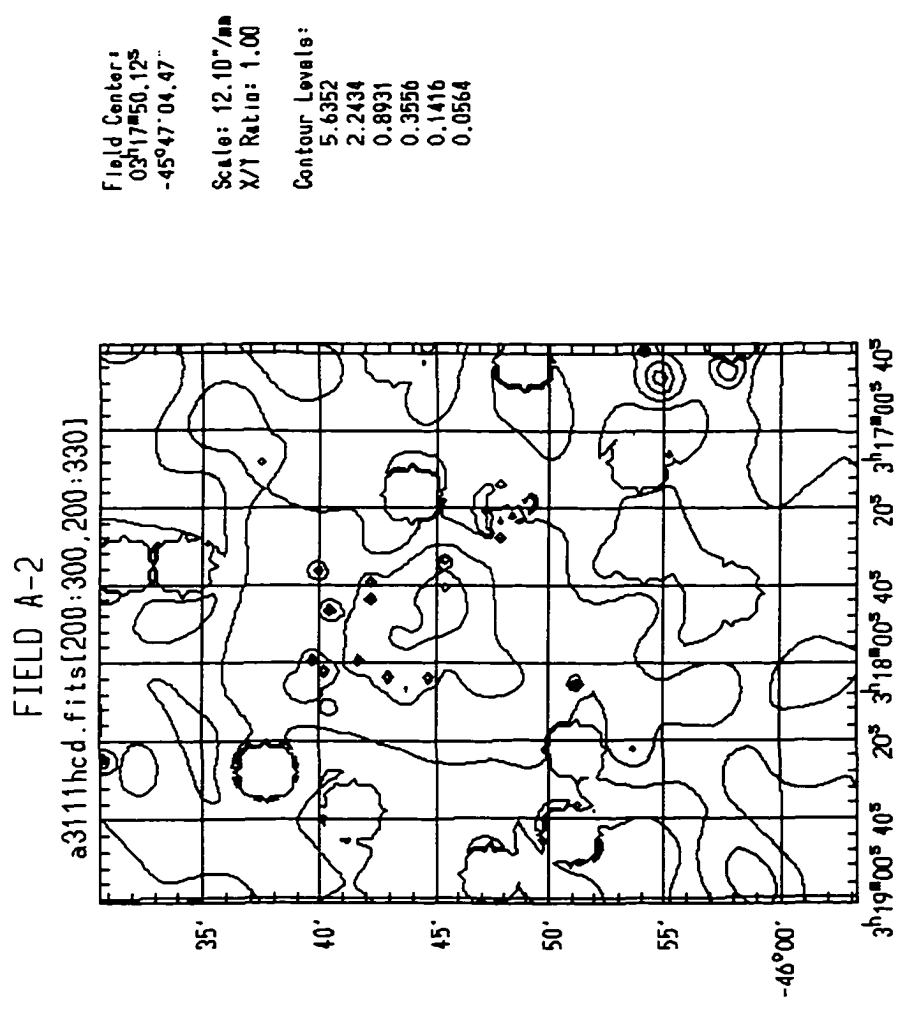

Figure 81. Contour map of Abell 3111. Scale is approximately 1.9 Mpc in X and 2.5 Mpc in Y. Contour levels are given in counts.

ABELL 3111

Figure 82. Wavelet transform images for Abell 3111. Clockwise from upper left in 2, 3, 4, and 5 pixel scales.

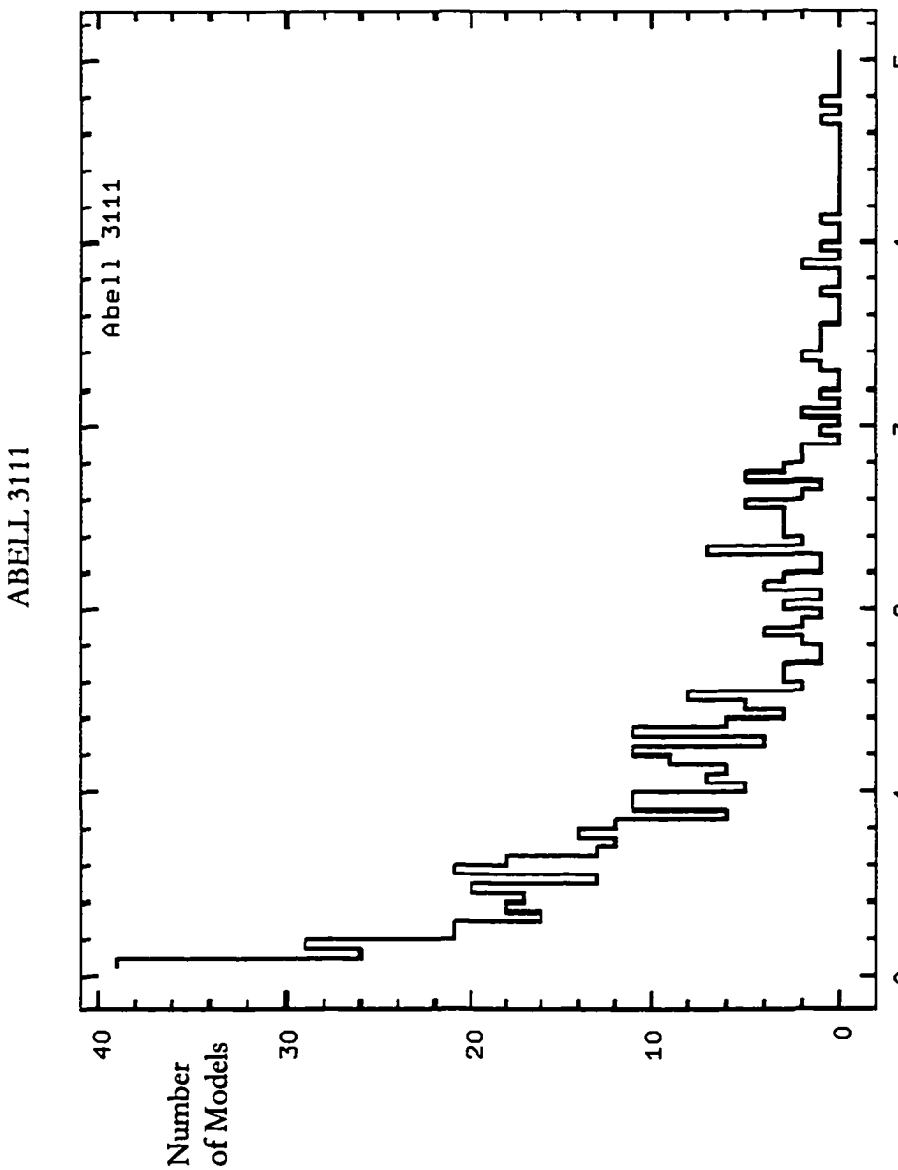

Figure 83. Histogram plots for P_3 moment for models of Abell 3111.

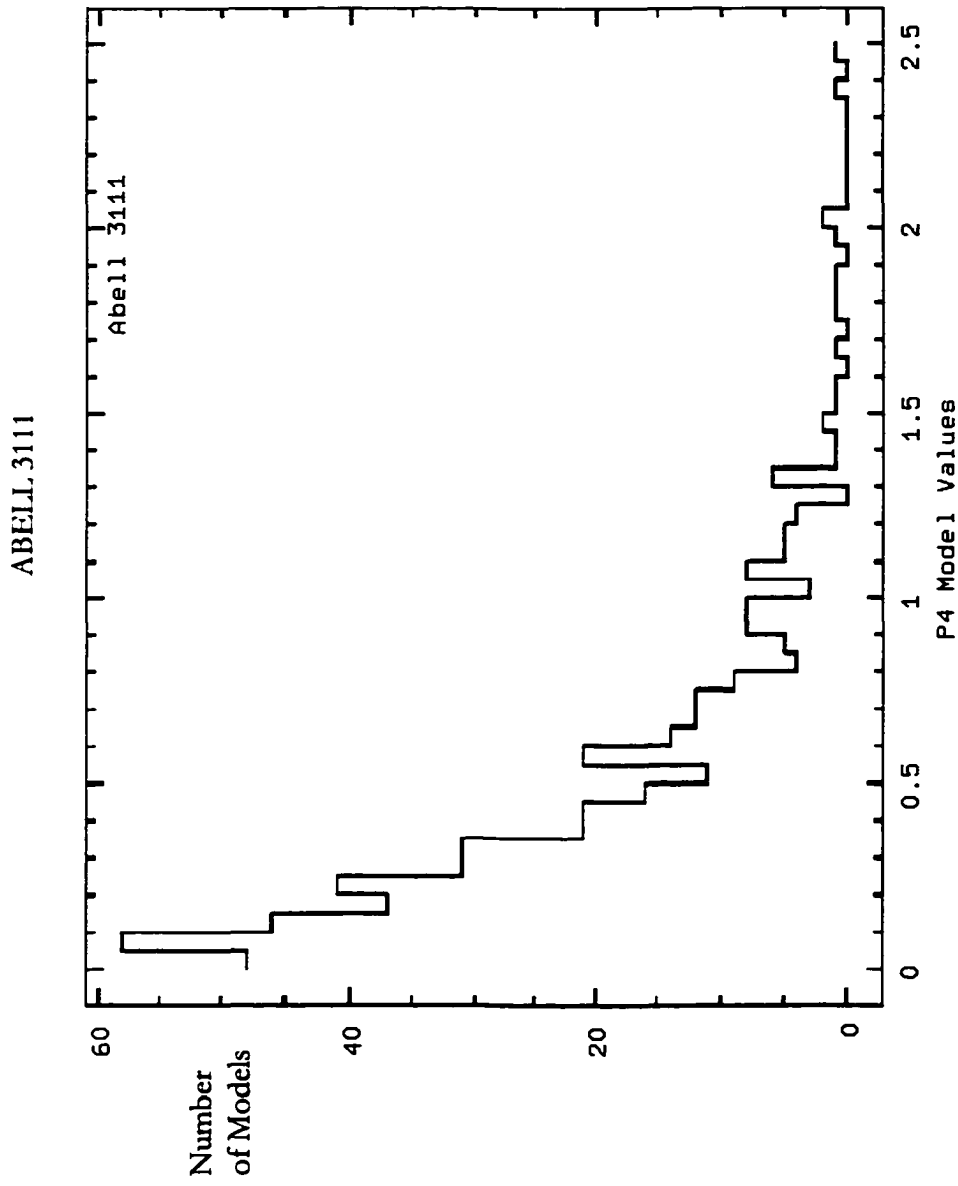

Figure 84. Histogram plots for P_4 moment for models of Abell 3111.

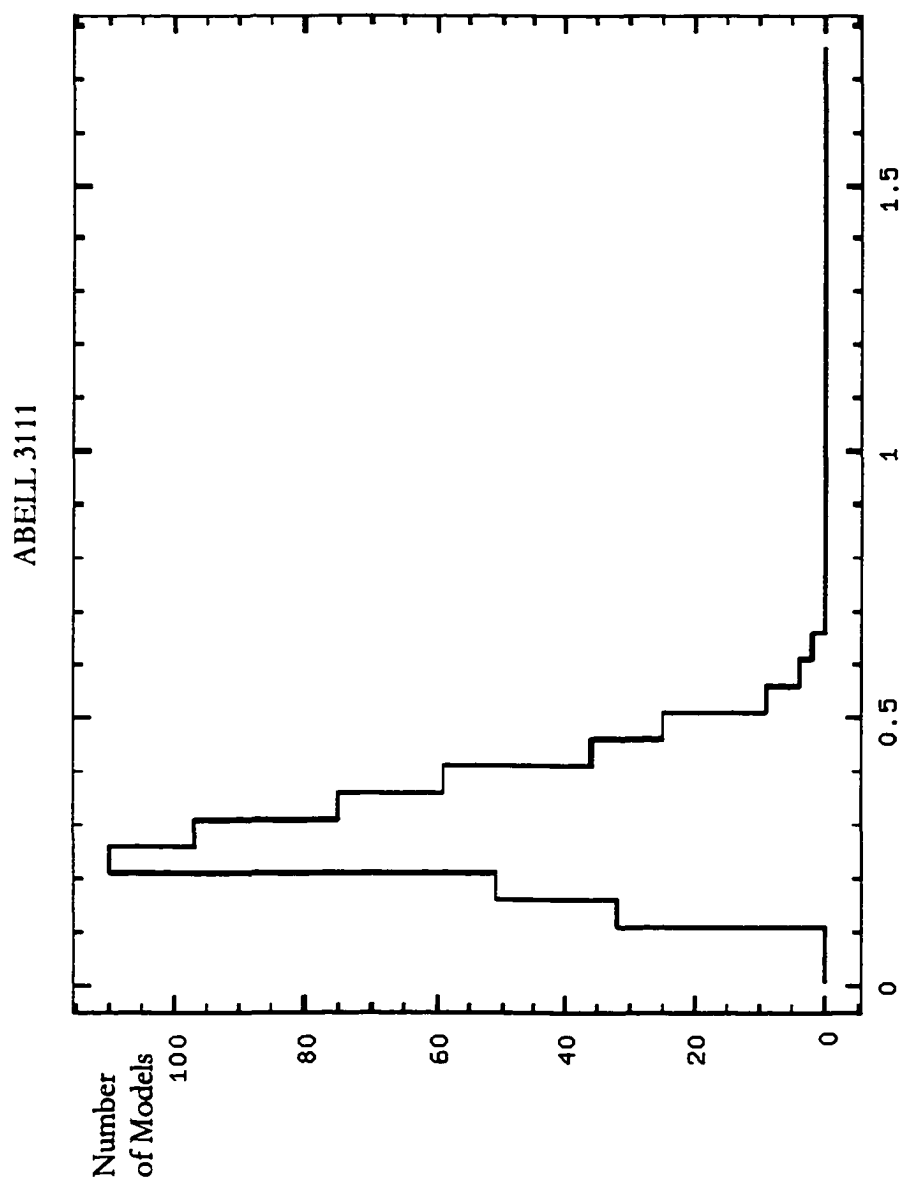

Figure 85. Sigma significance plot for Abell 3111 for 'center shift' program.

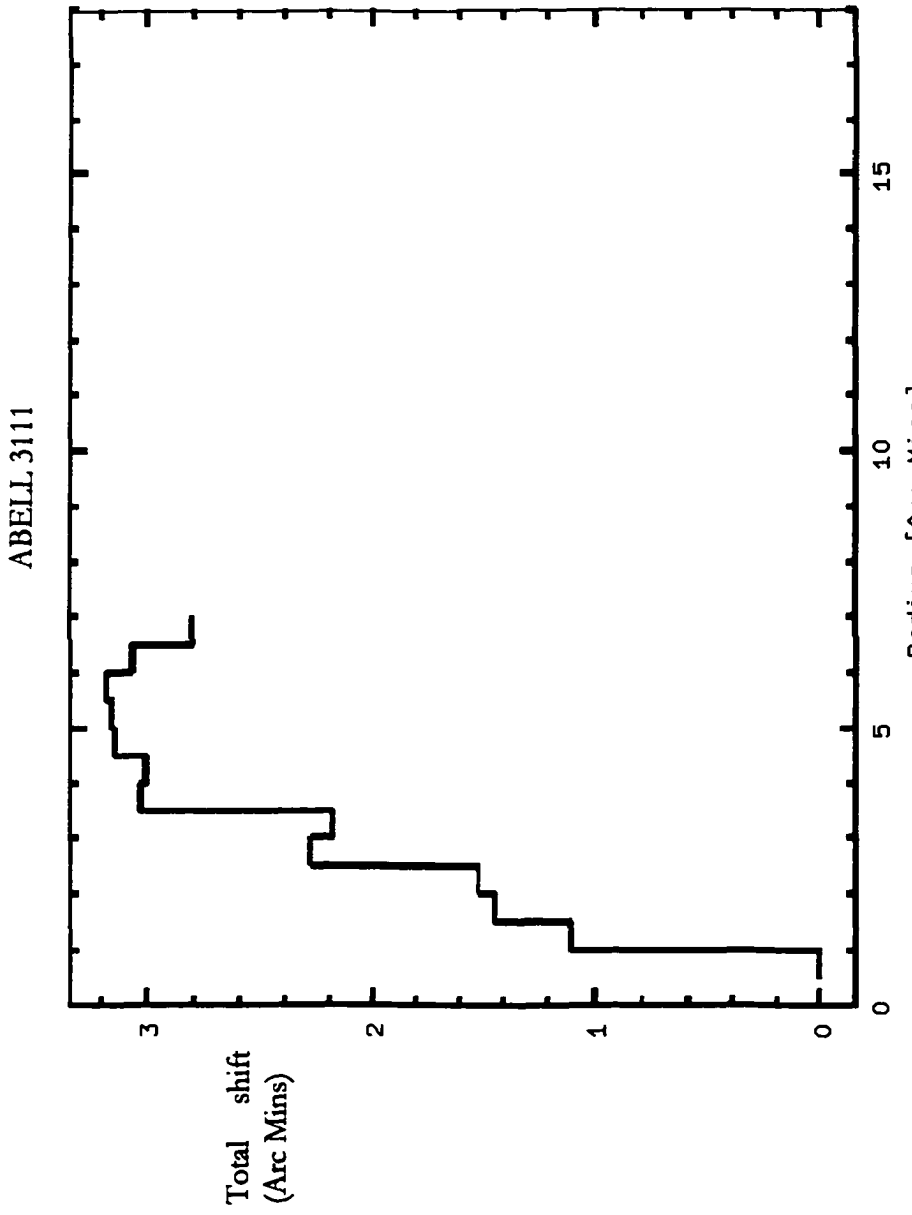

Figure 86. Total shift plot for Abell 3111 for 'center shift' program.

ABELL 3112

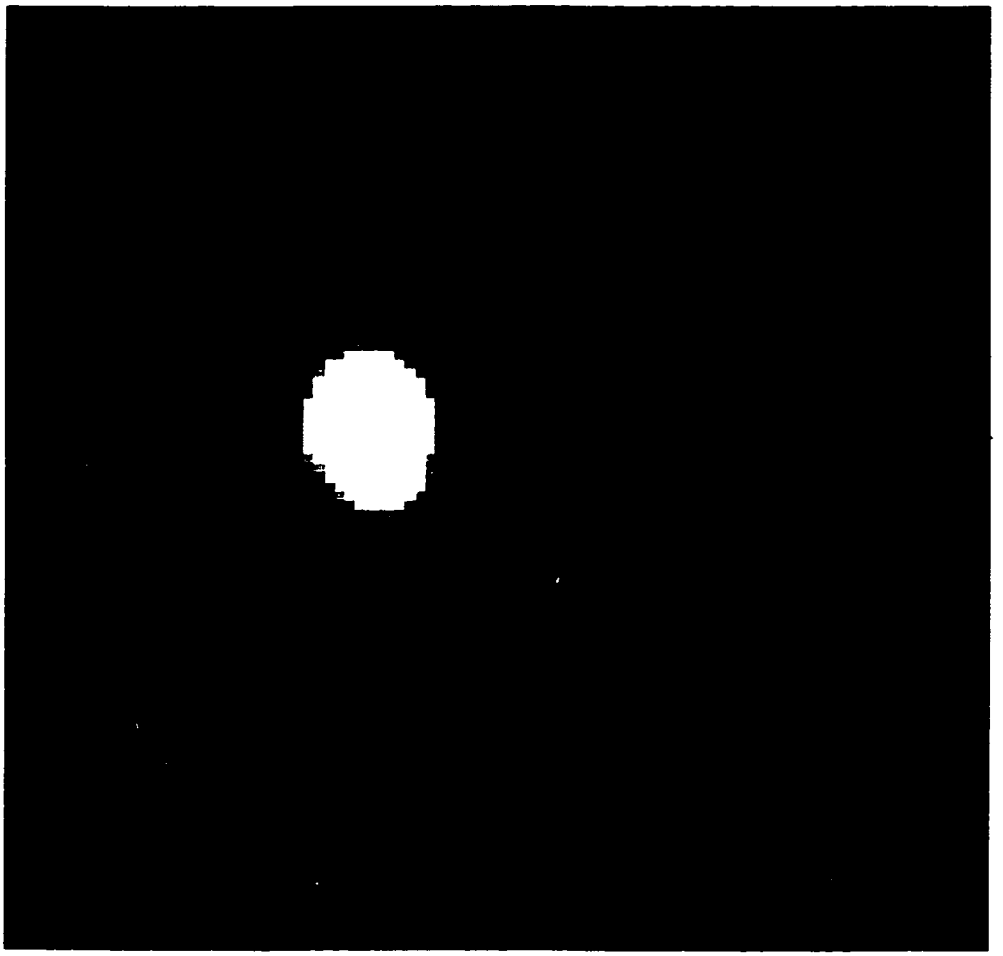

Figure 87. Cleaned and filtered image of Abell 3112. Scale is approximately 1.8 Mpc per side.

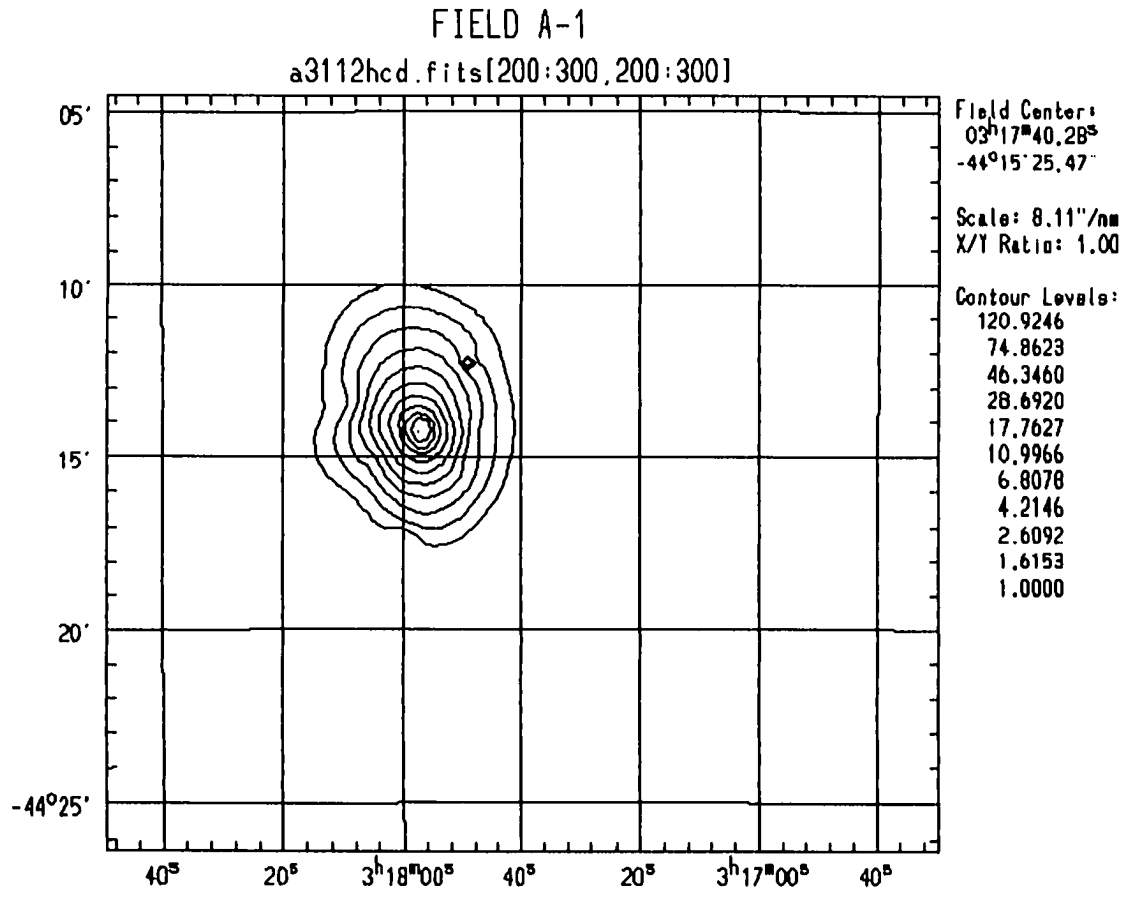

Figure 88. Contour map of Abell 3112. Scale is approximately 1.8 Mpc per side. Contour levels are given in counts.

ABELL 3112

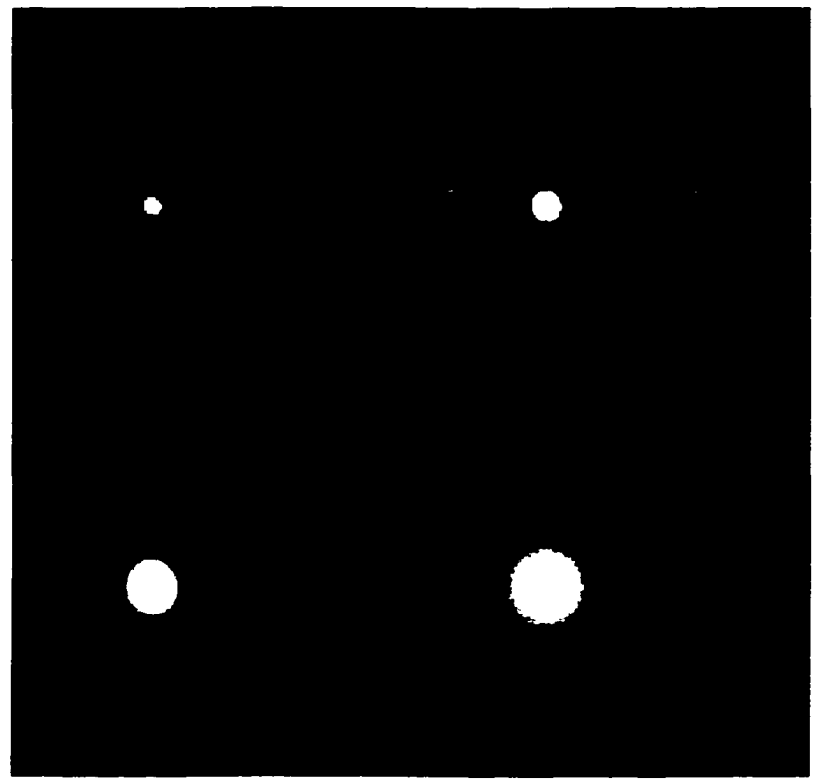

Figure 89. Wavelet transform images for Abell 3112. Clockwise from upper left in 2, 3, 4, and 5 pixel scales.

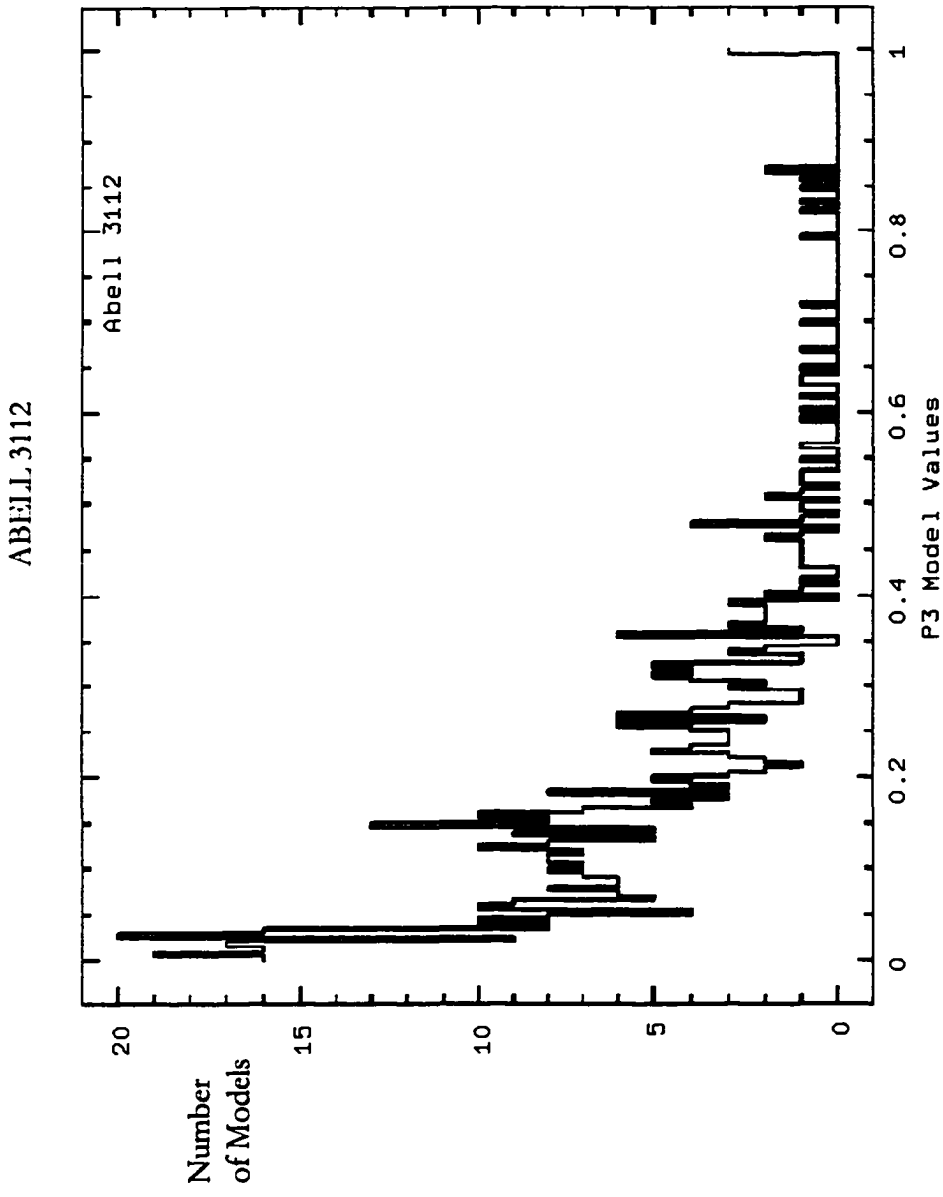

Figure 90. Histogram plots for P_3 moment for models of Abell 3112.

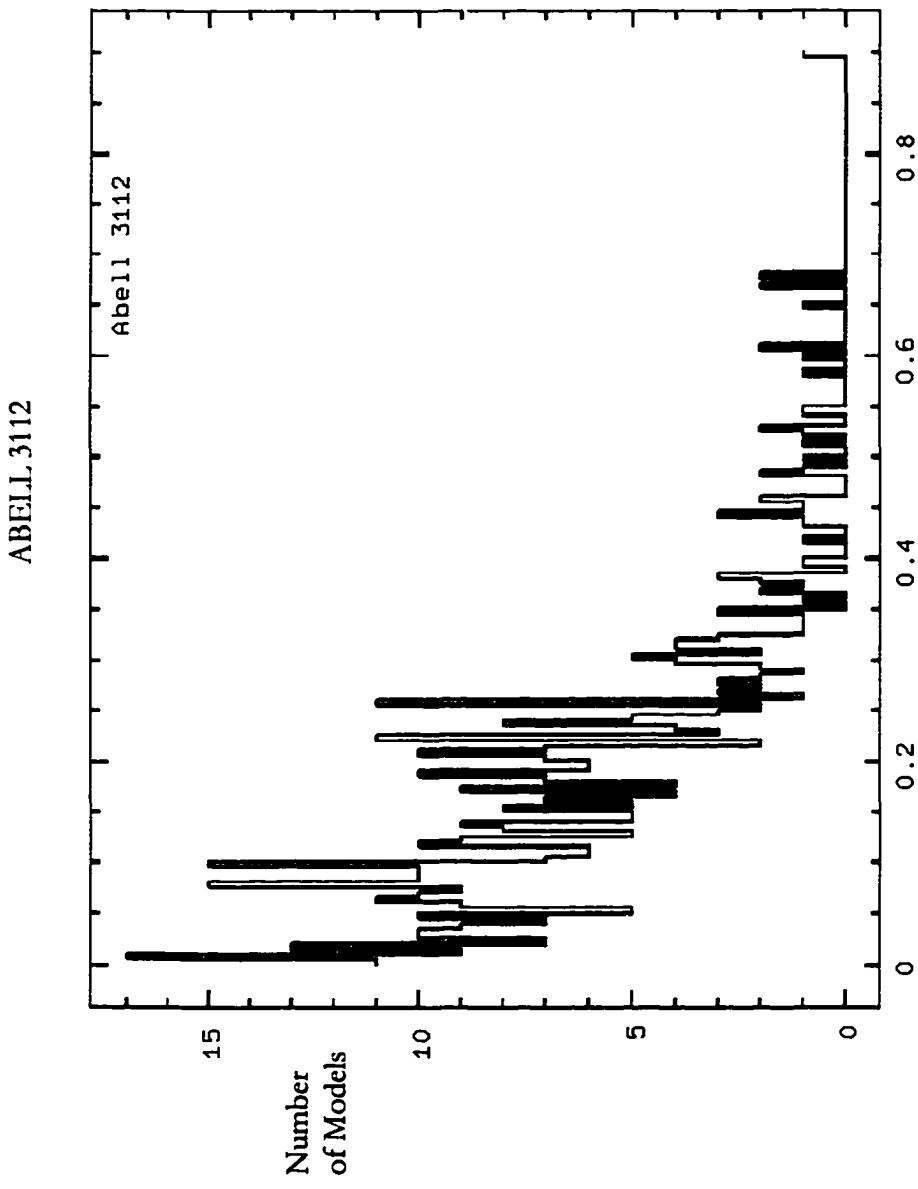

Figure 91. Histogram plots for P_4 moment for models of Abell 3112.

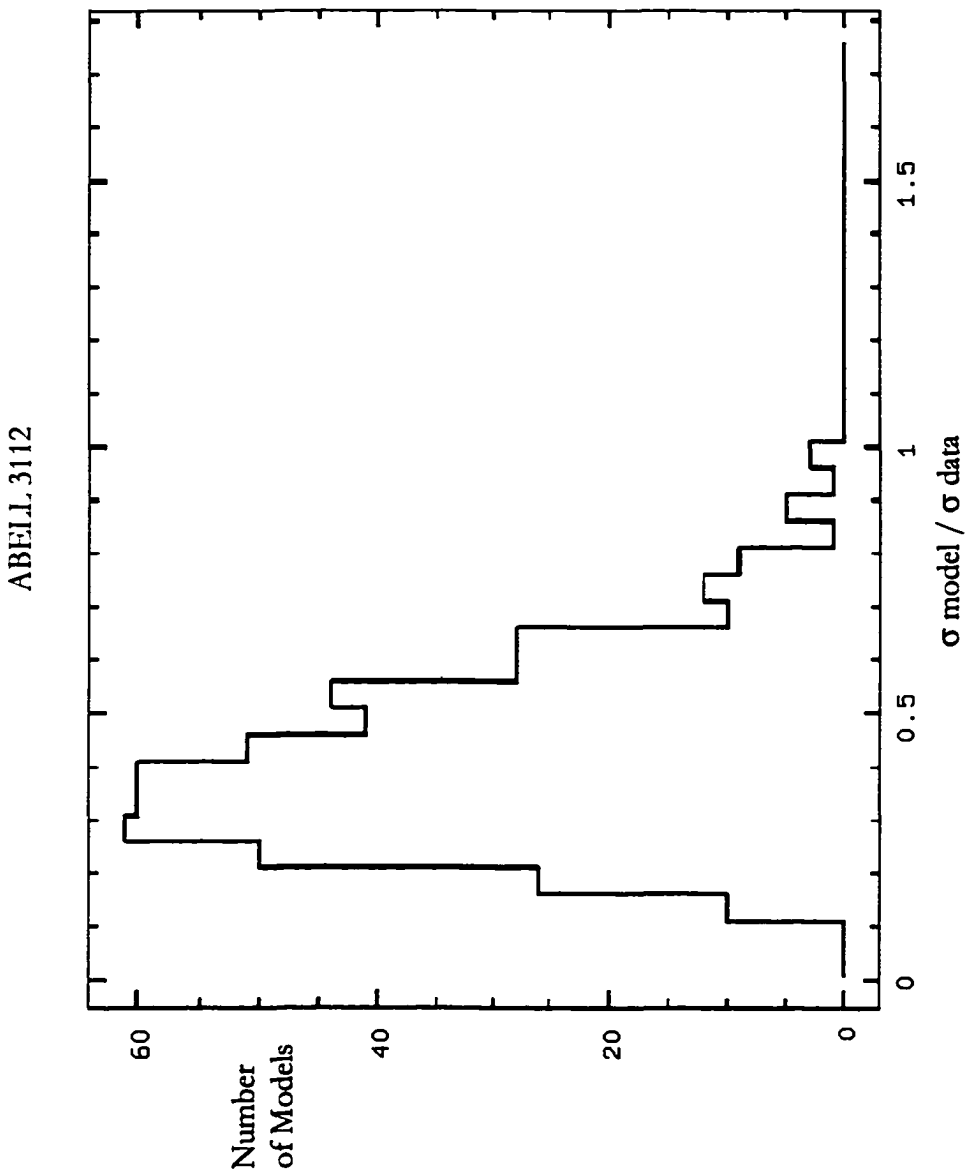

Figure 92. Sigma significance plot for Abell 3112 for 'center shift' program.

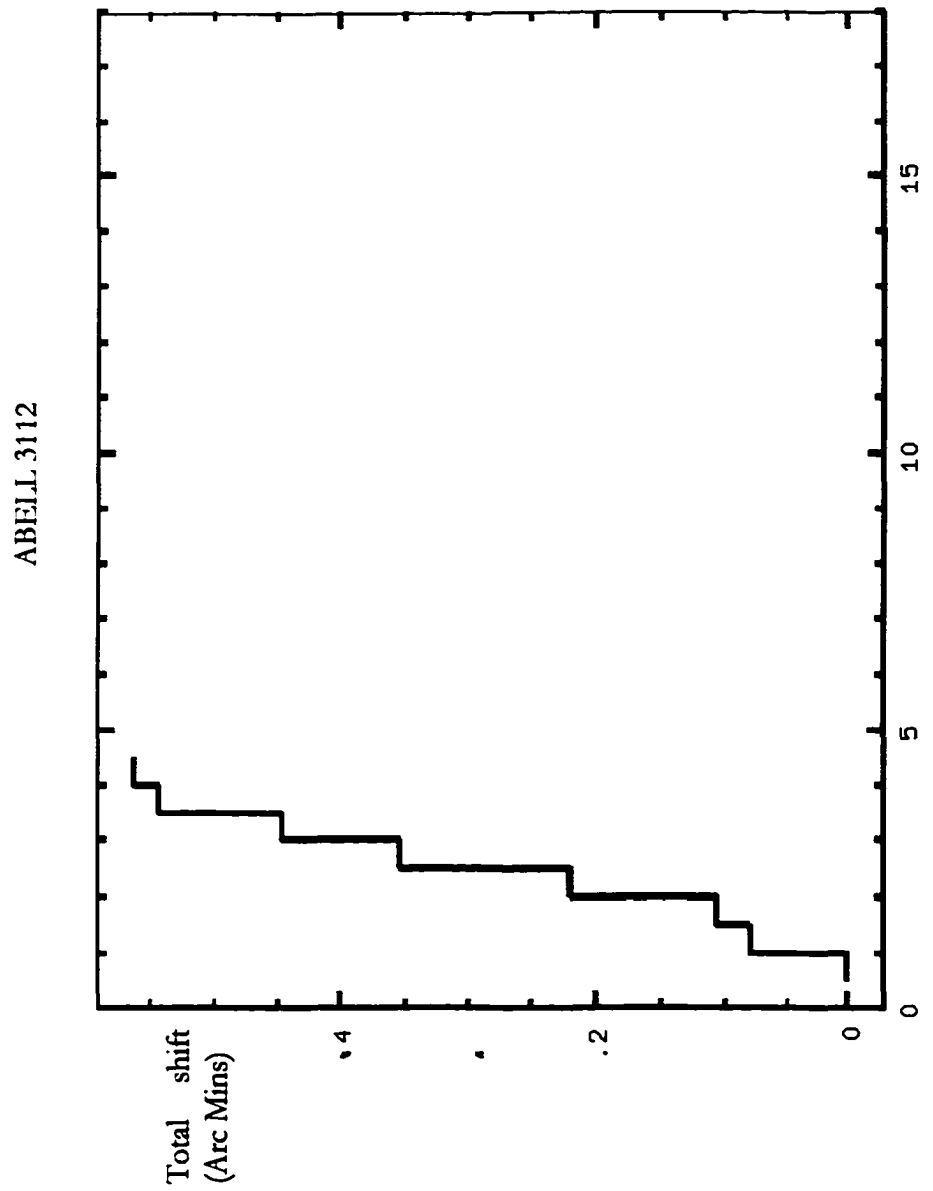

Figure 93. Total shift plot for Abell 3112 for 'center shift' program.

ABELL 3158

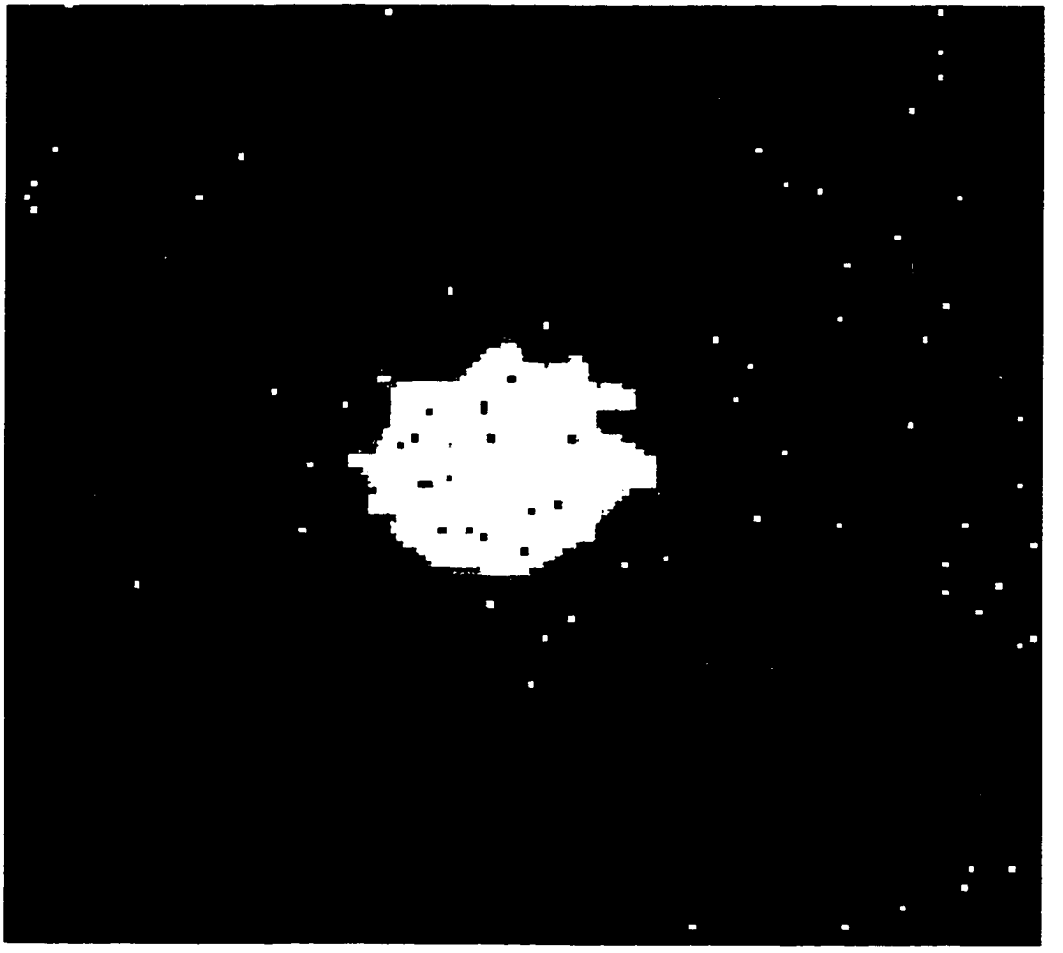

Figure 94. Cleaned and filtered image of Abell 3158. Scale is approximately 1.8 Mpc per side.

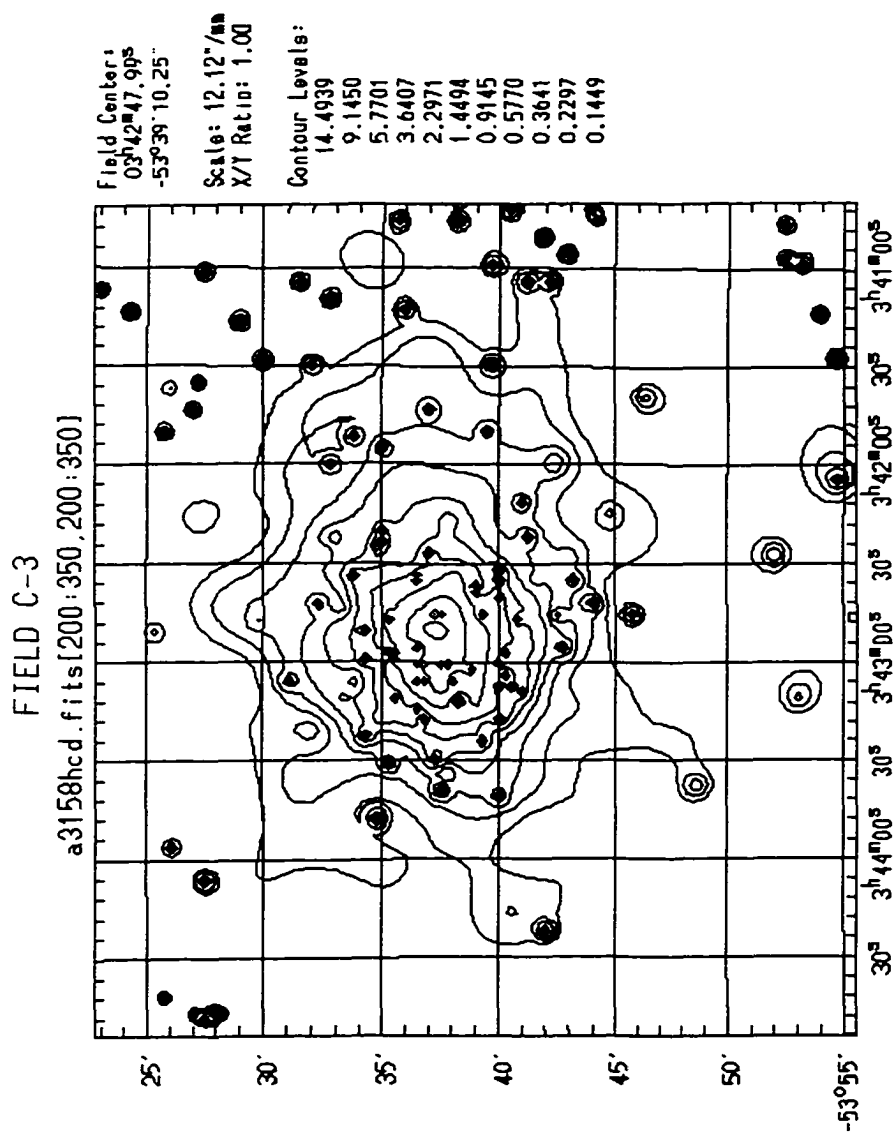

Figure 95. Contour map of Abell 3158. Scale is approximately 1.8 Mpc per side. Contour levels are given in counts.

ABELL 3158

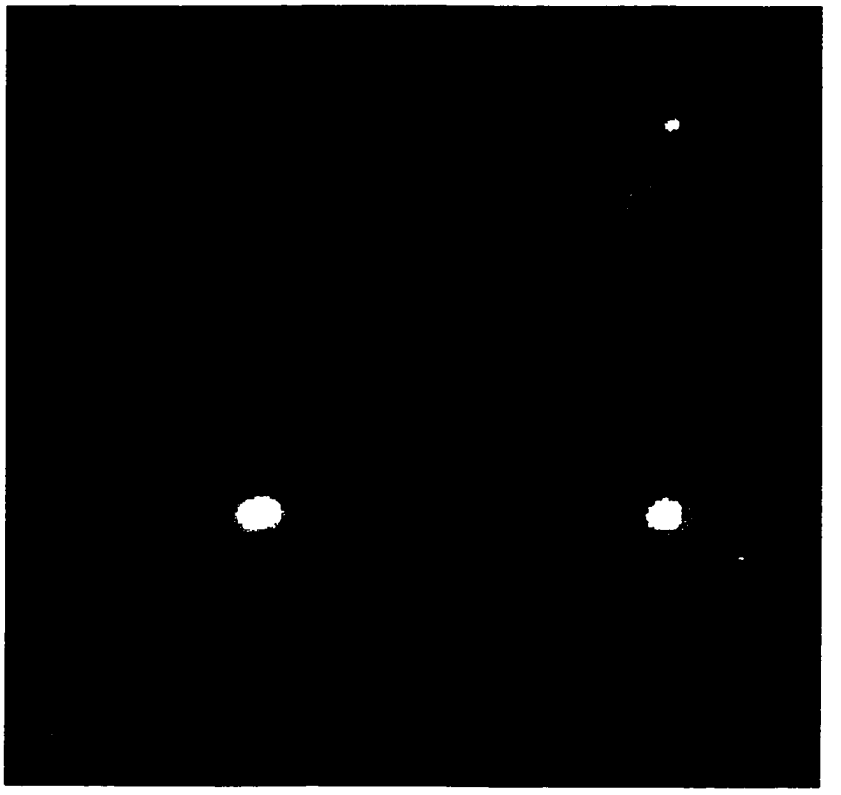

Figure 96. Wavelet transform images for Abell 3158. Clockwise from upper left in 2, 3, 4, and 5 pixel scales.

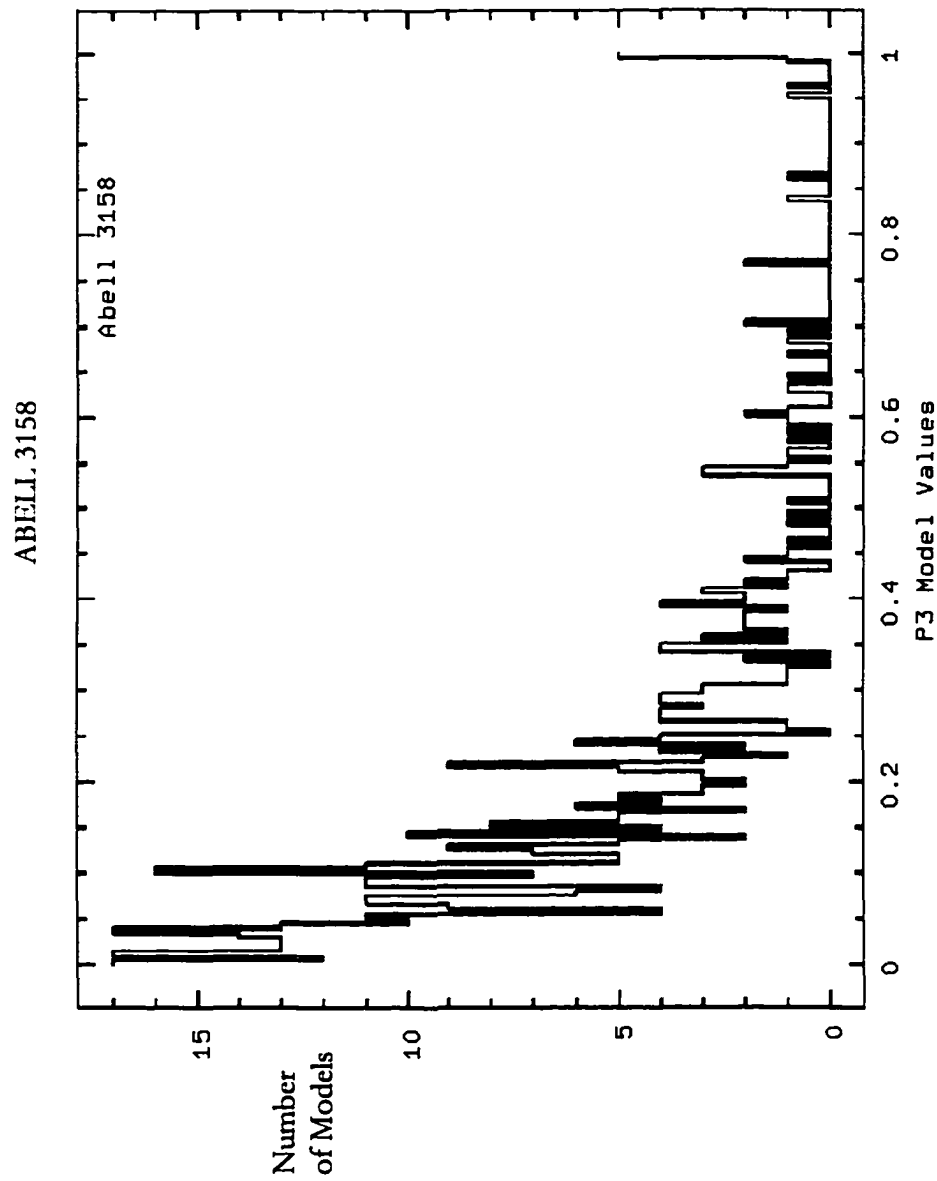

Figure 97. Histogram plots for P_3 moment for models of Abell 3158.

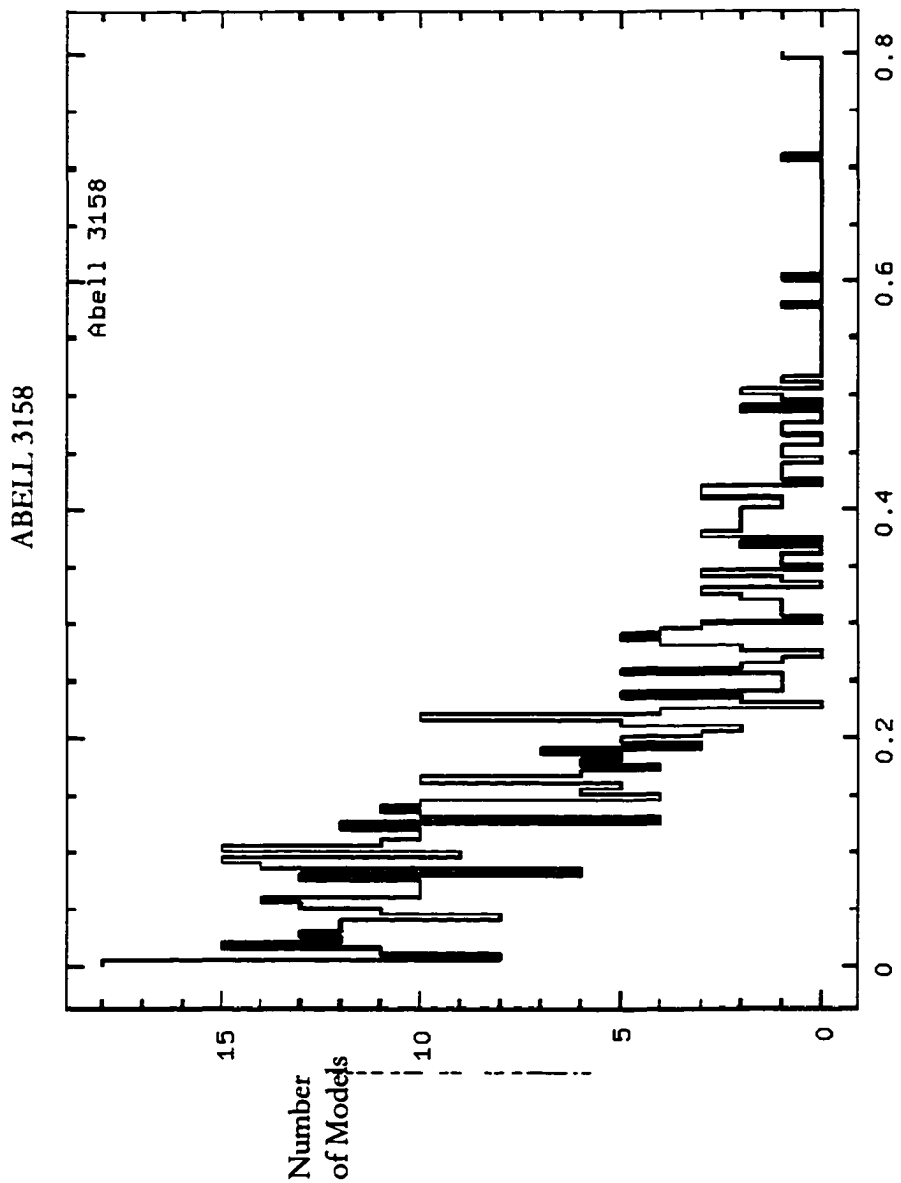

Figure 98. Histogram plots for P_4 moment for models of Abell 3158.

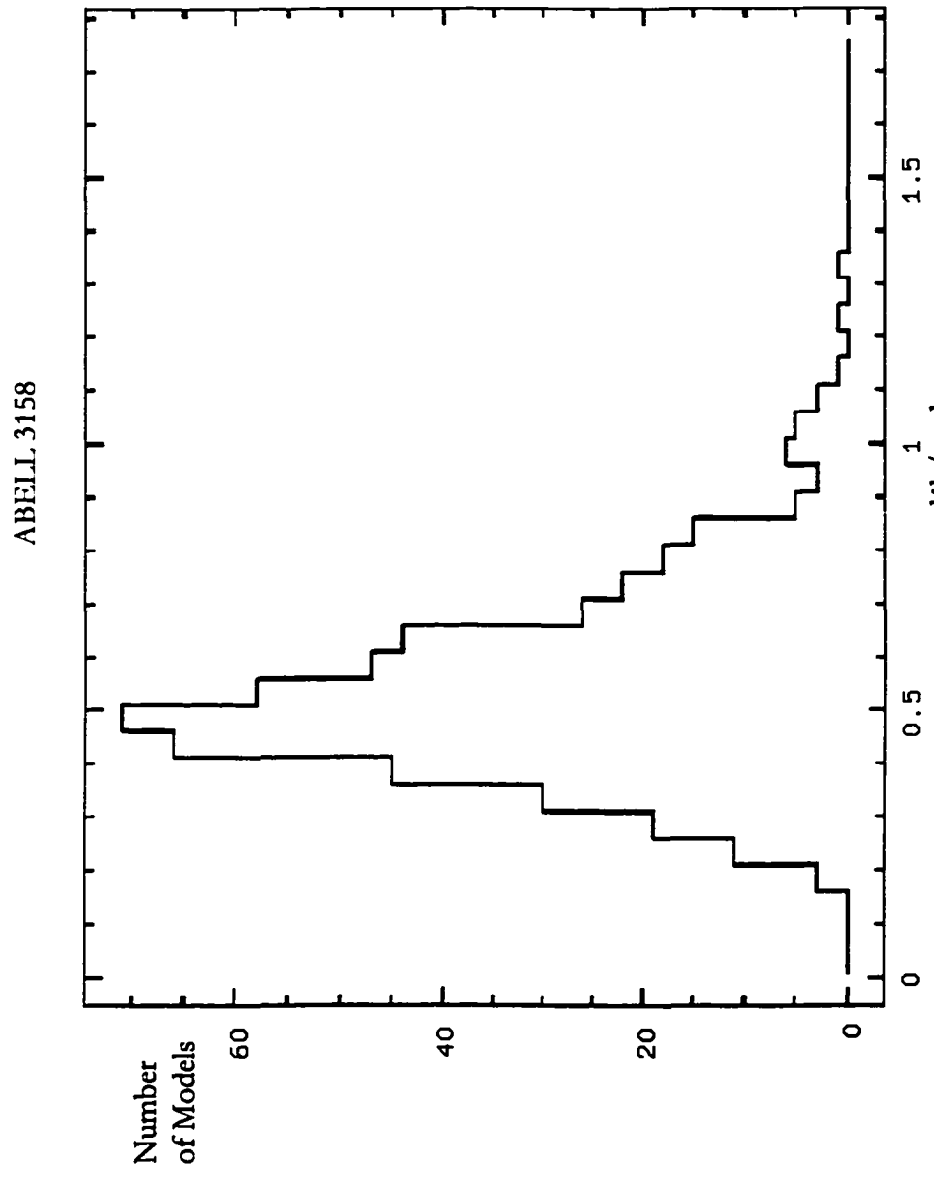

Figure 99. Sigma significance plot for Abell 3158 for 'center shift' program.

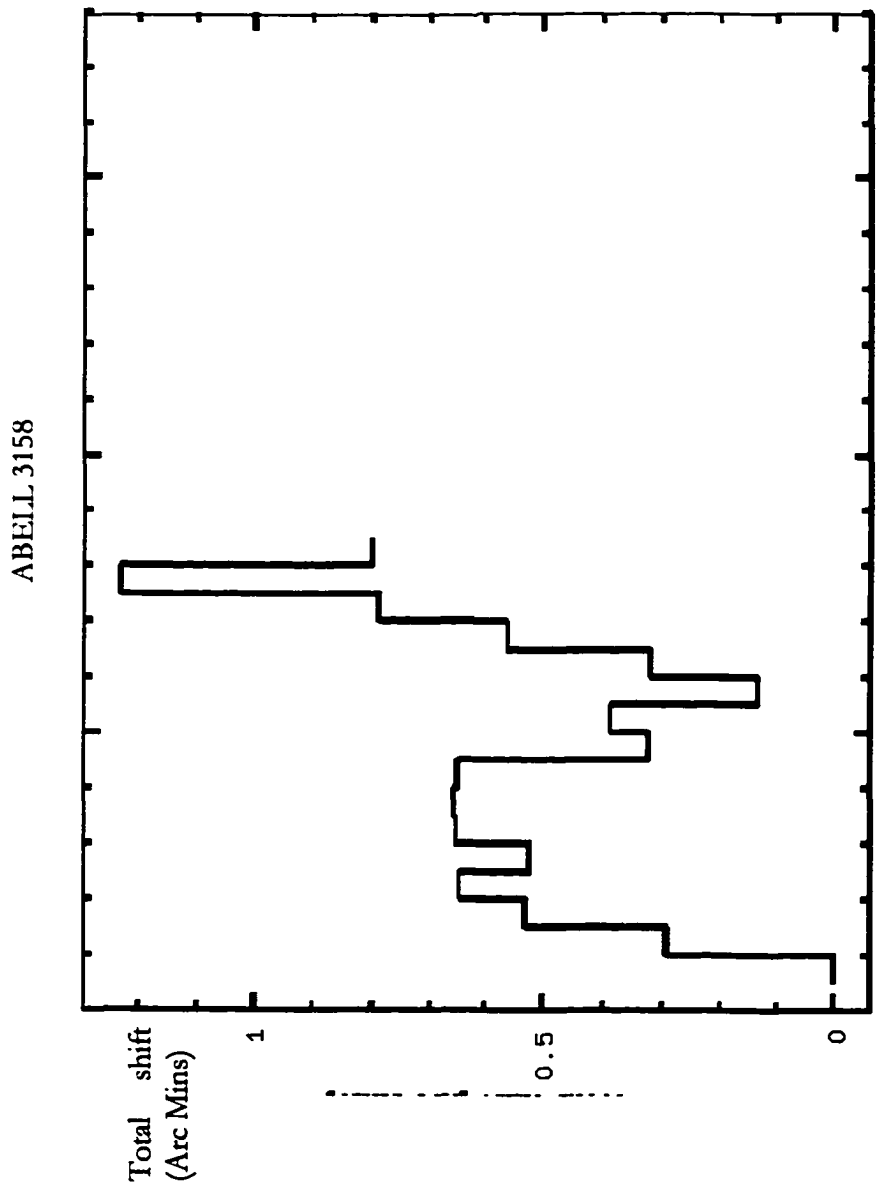

Figure 100. Total shift plot for Abell 3158 for 'center shift' program.

ABELL 3266

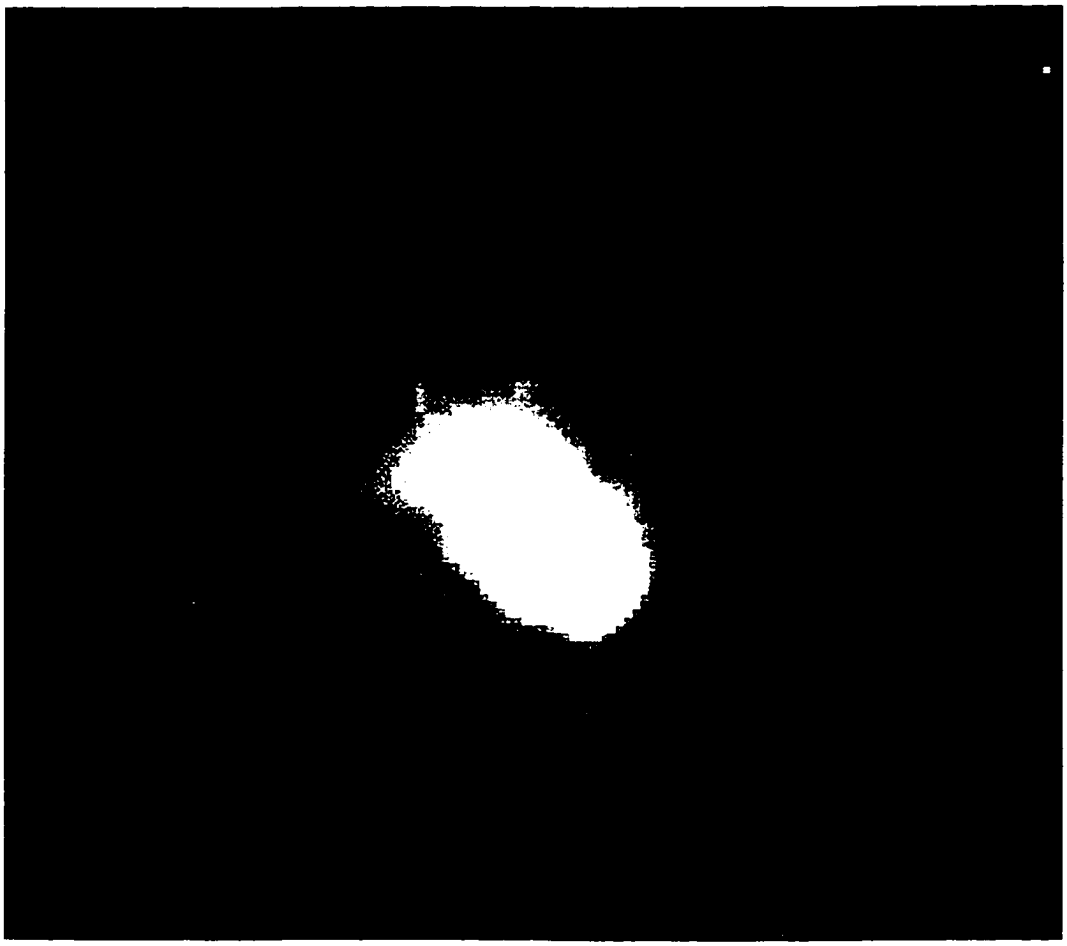

Figure 101. Cleaned and filtered image of Abell 3266. Scale is approximately 1.8 Mpc per side.

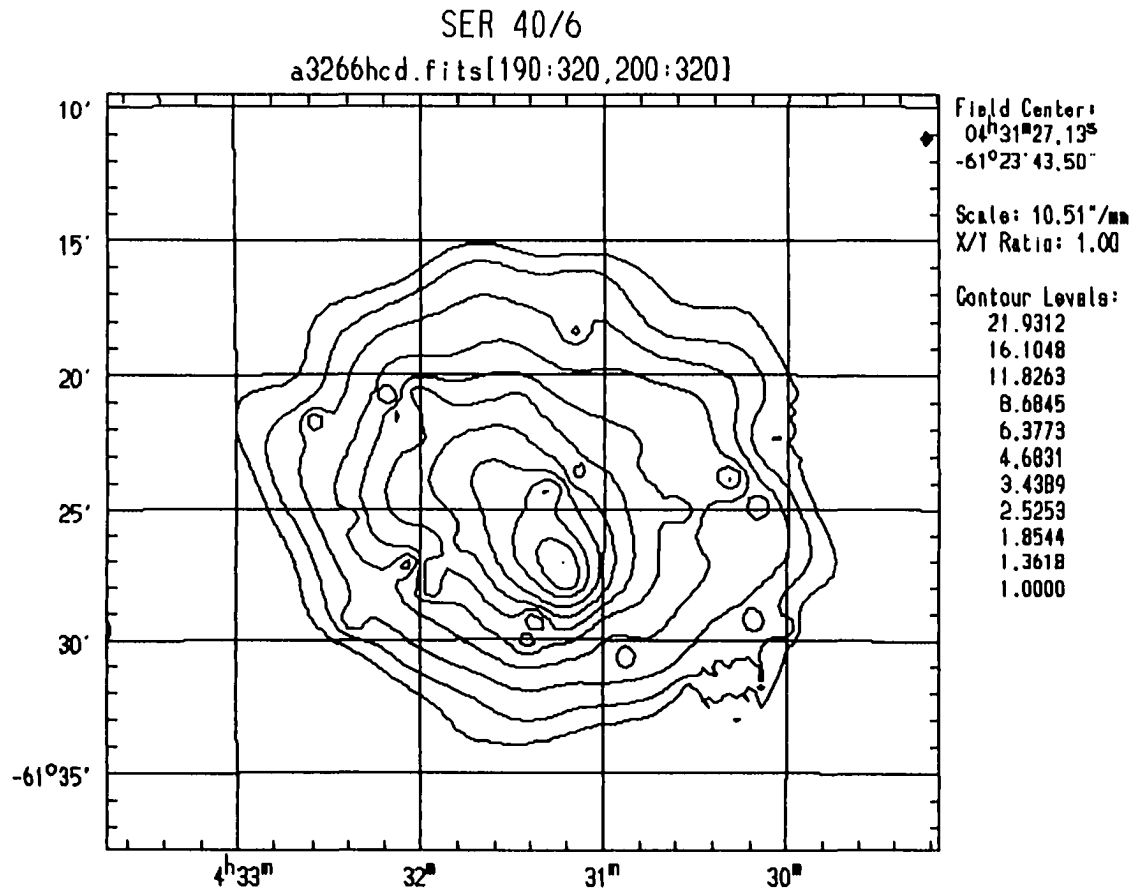

Figure 102. Contour map of Abell 3266. Scale is approximately 1.8 Mpc per side. Contour levels are given in counts.

ABELL 3266

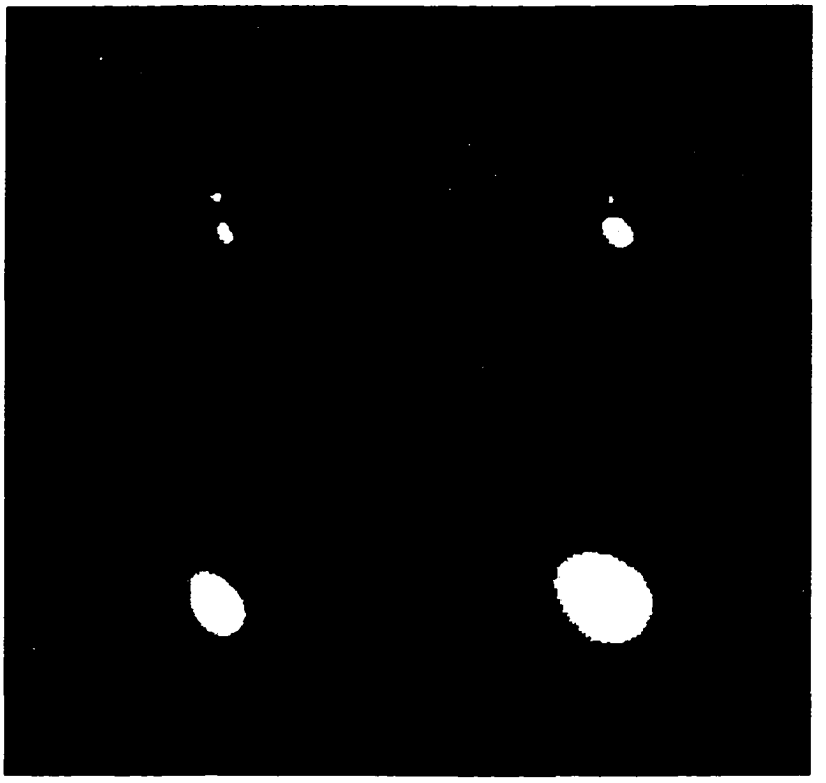

Figure 103. Wavelet transform images for Abell 3266. Clockwise from upper left in 2, 3, 4, and 5 pixel scales.

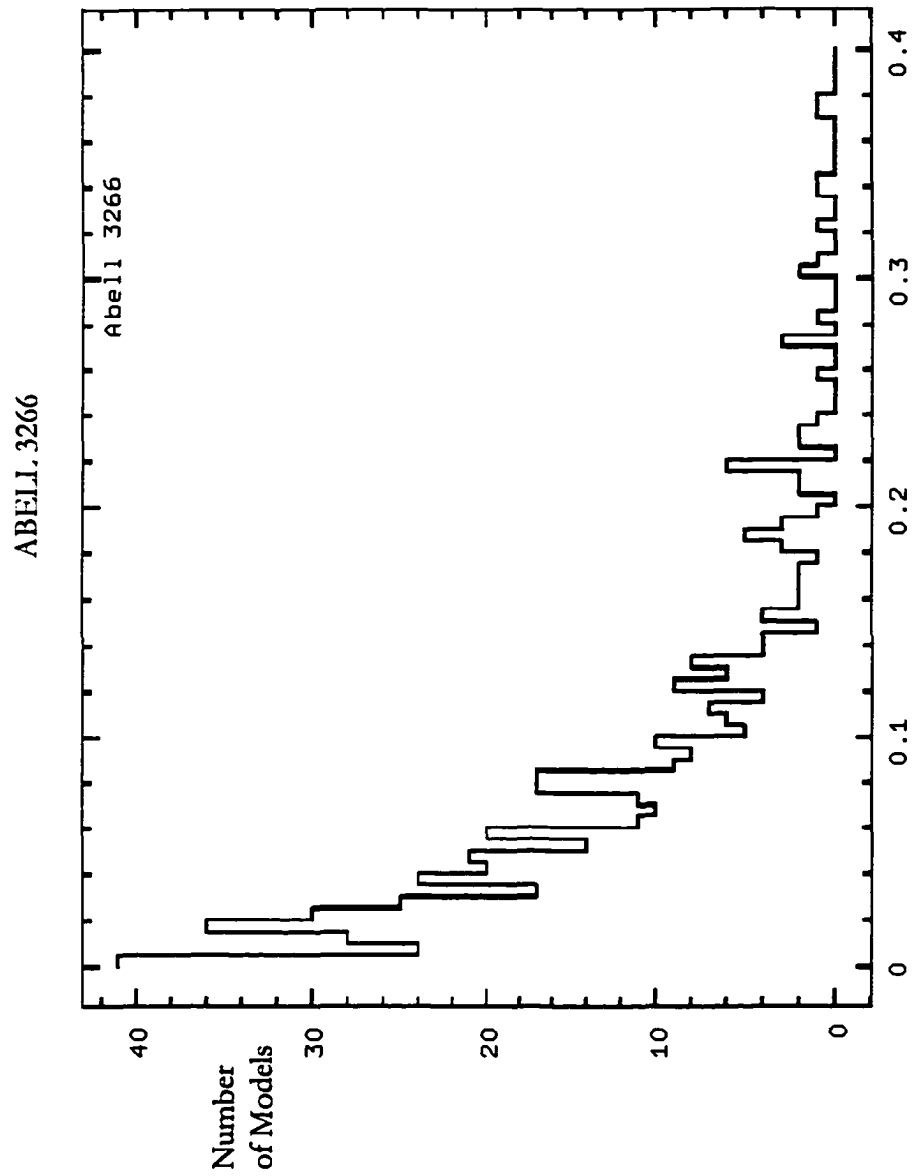

Figure 104. Histogram plots for P_3 moment for models of Abell 3266.

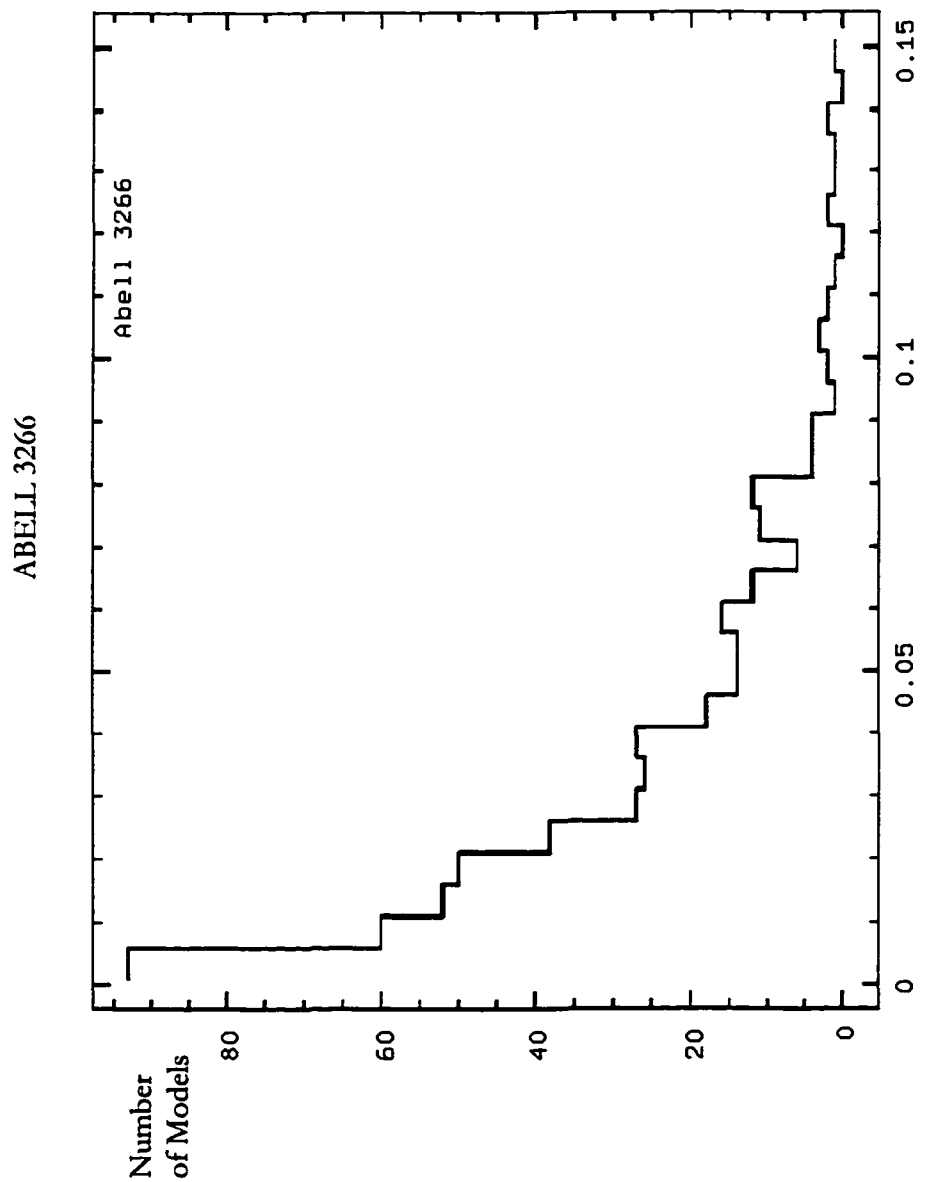

Figure 105. Histogram plots for P_4 moment for models of Abell 3266.

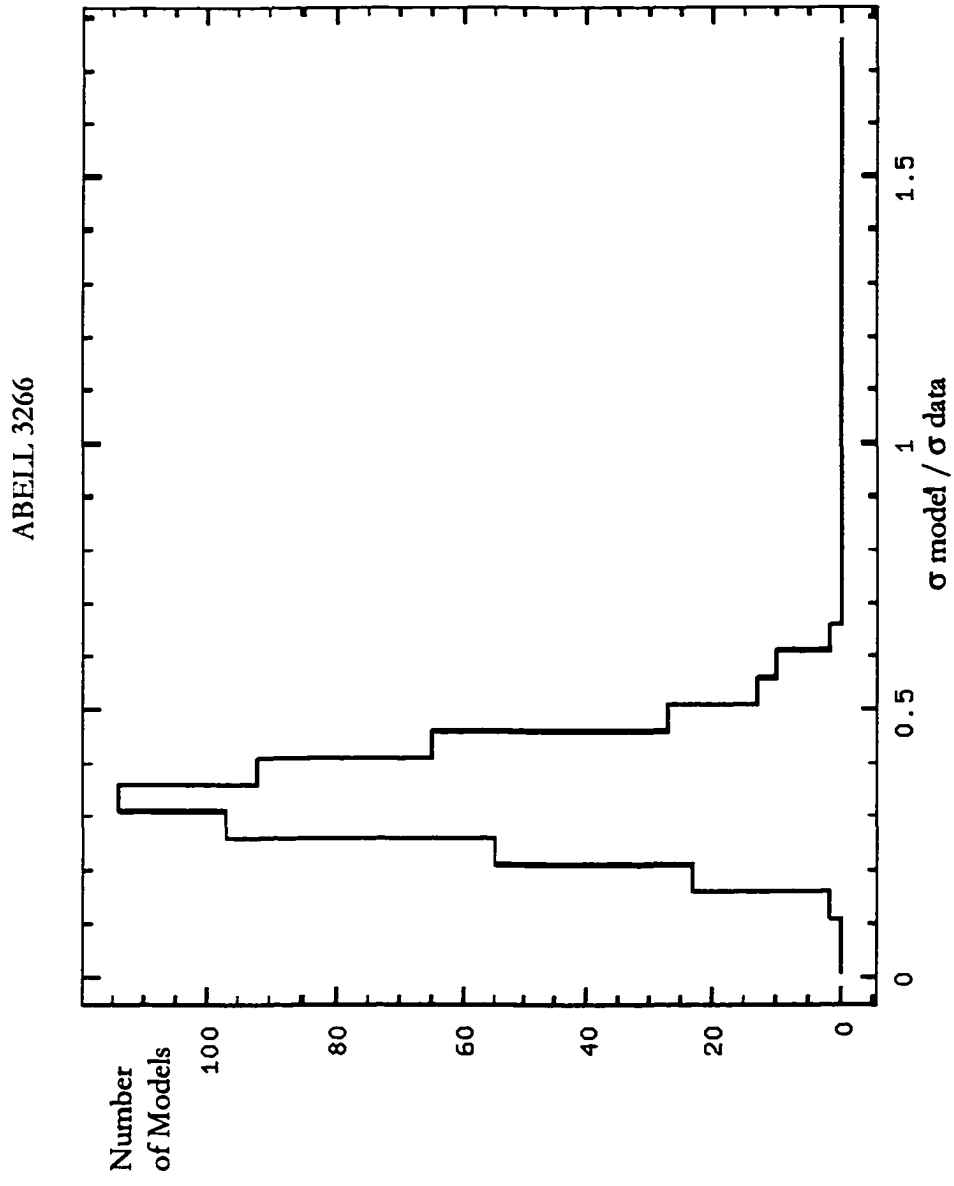

Figure 106. Sigma significance plot for Abell 3266 for 'center shift'

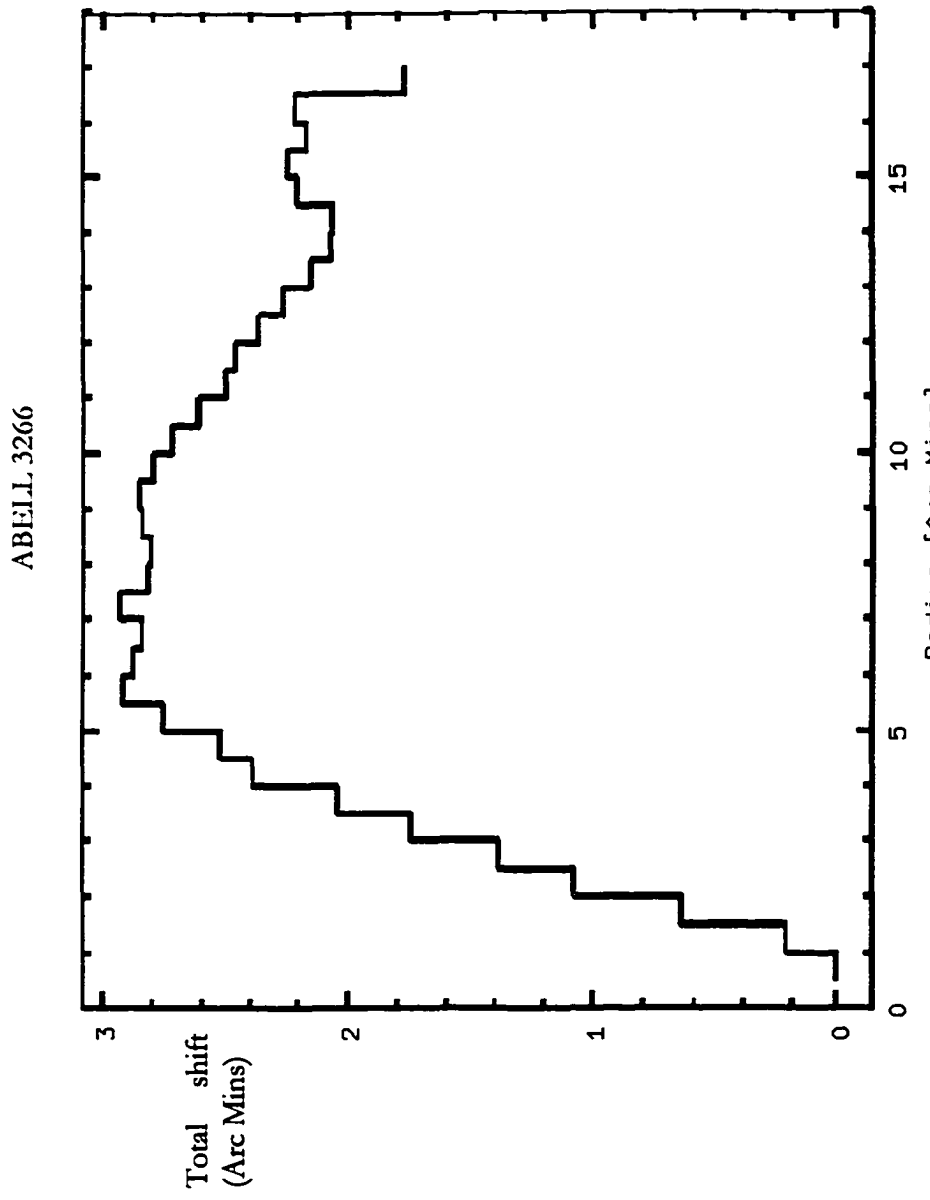

Figure 107. Total shift plot for Abell 3266 for 'center shift' program.

ABELL 3558

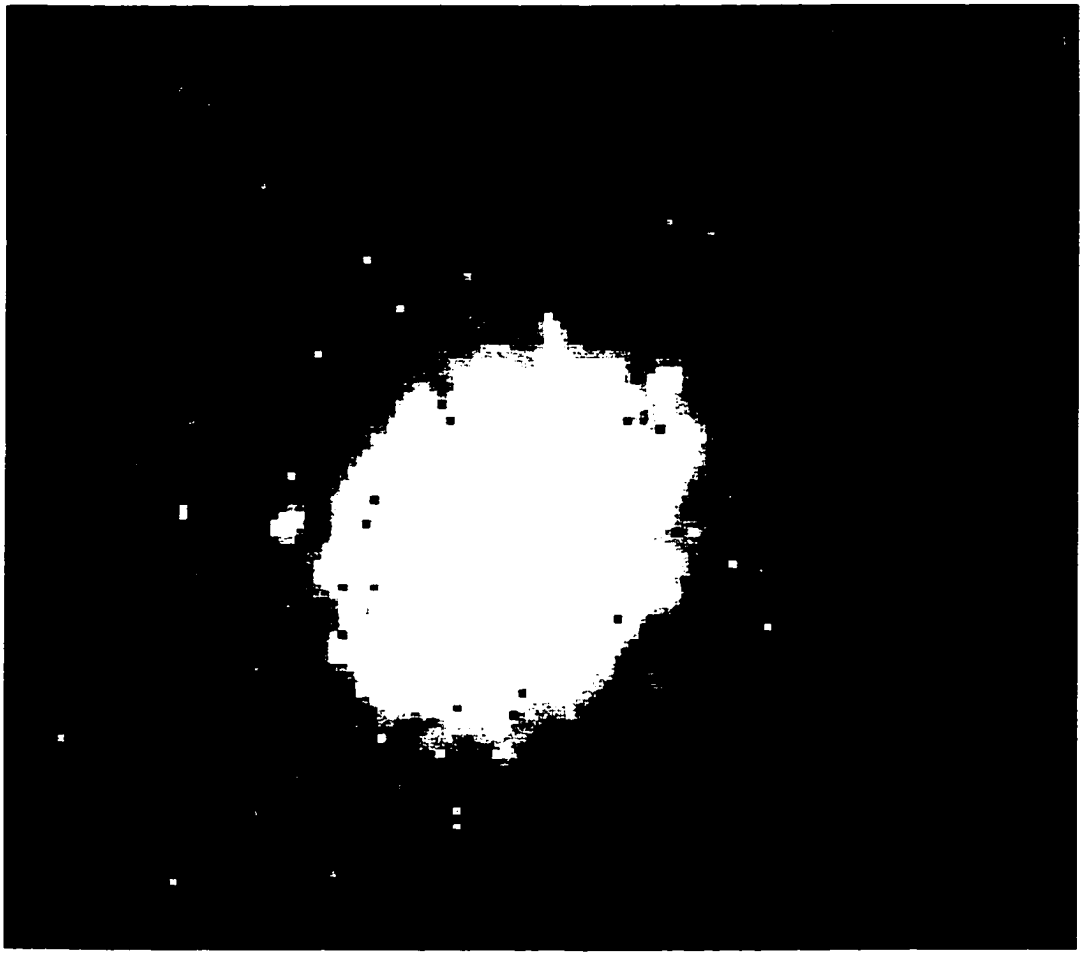

Figure 108. Cleaned and filtered image of Abell 3558. Scale is approximately 1.8 Mpc per side.

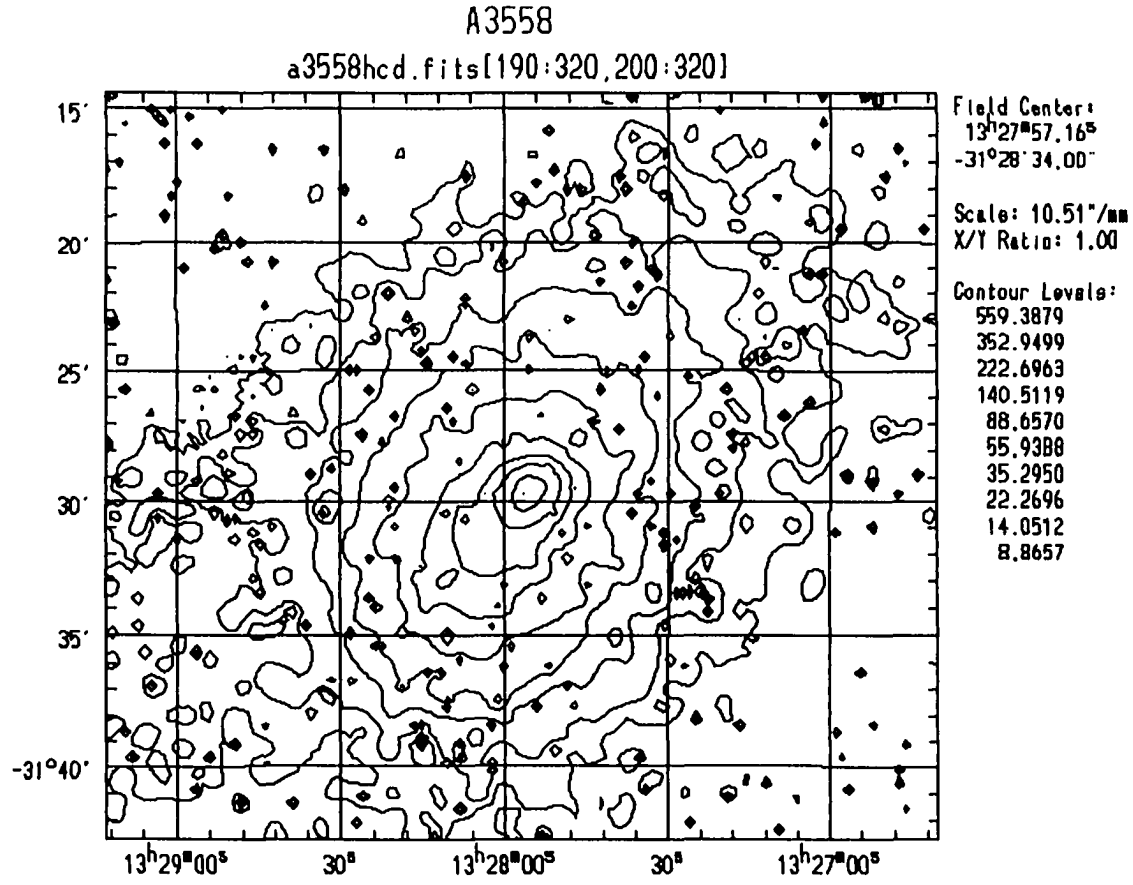

Figure 109. Contour map of Abell 3558. Scale is approximately 1.8 Mpc per side. Contour levels are given in counts.

ABELL 3558

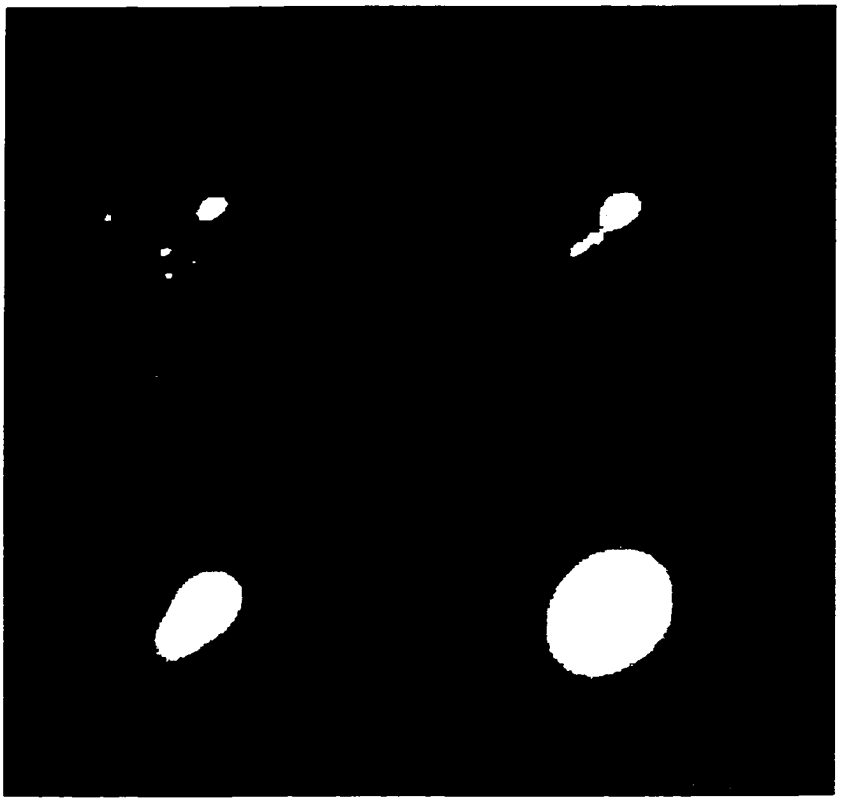

Figure 110. Wavelet transform images for Abell 3558. Clockwise from upper left in 2, 3, 4, and 5 pixel scales.

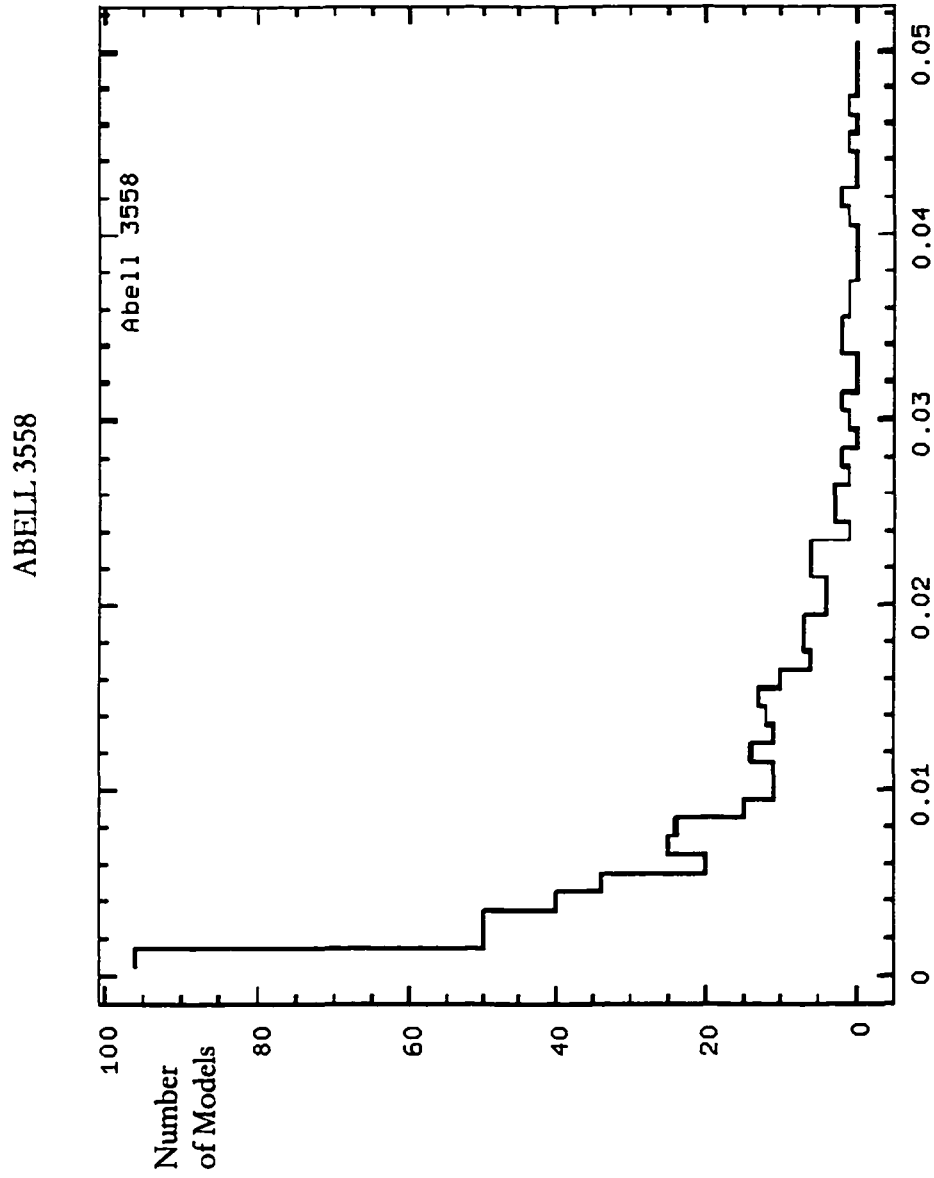

Figure 111. Histogram plots for P_3 moment for models of Abell 3558.

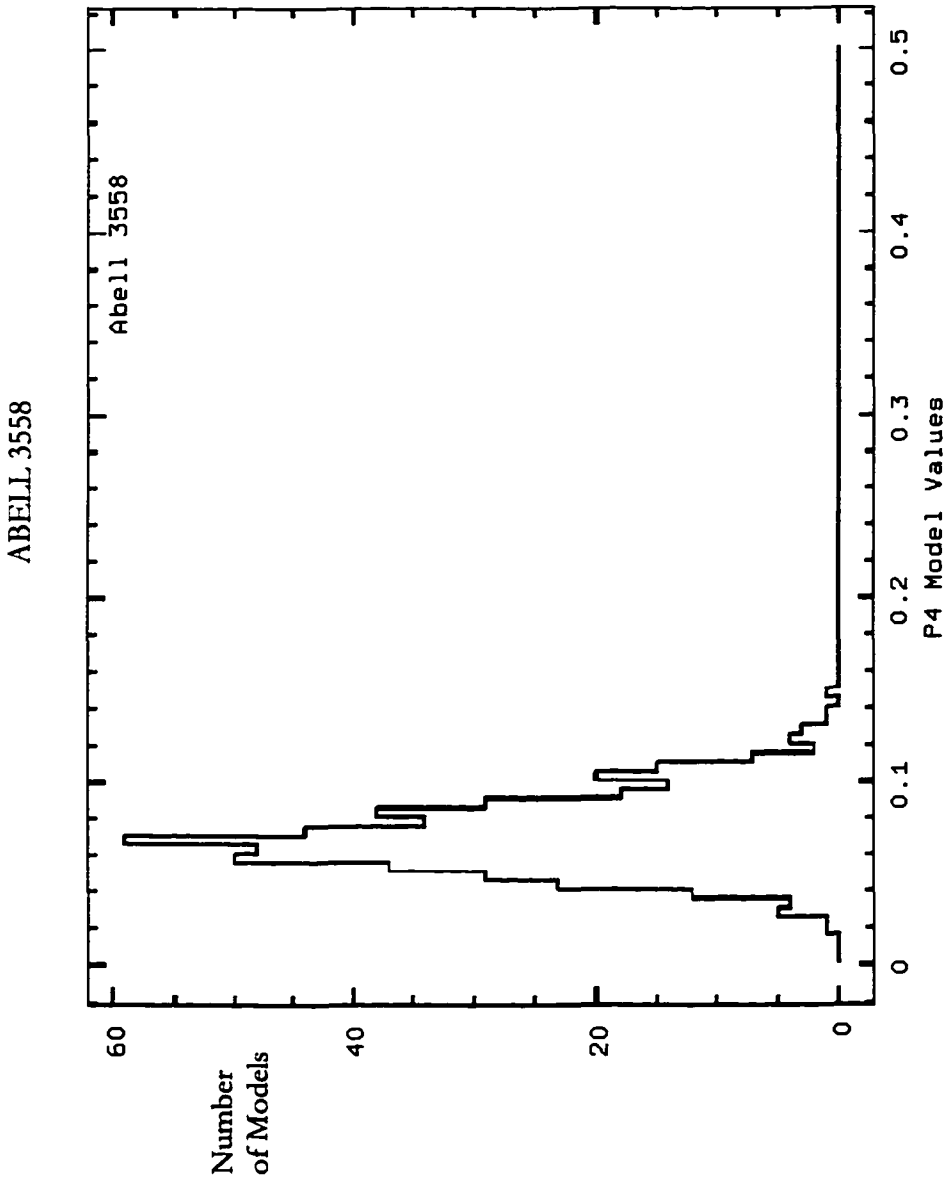

Figure 112. Histogram plots for P_4 moment for models of Abell 3558.

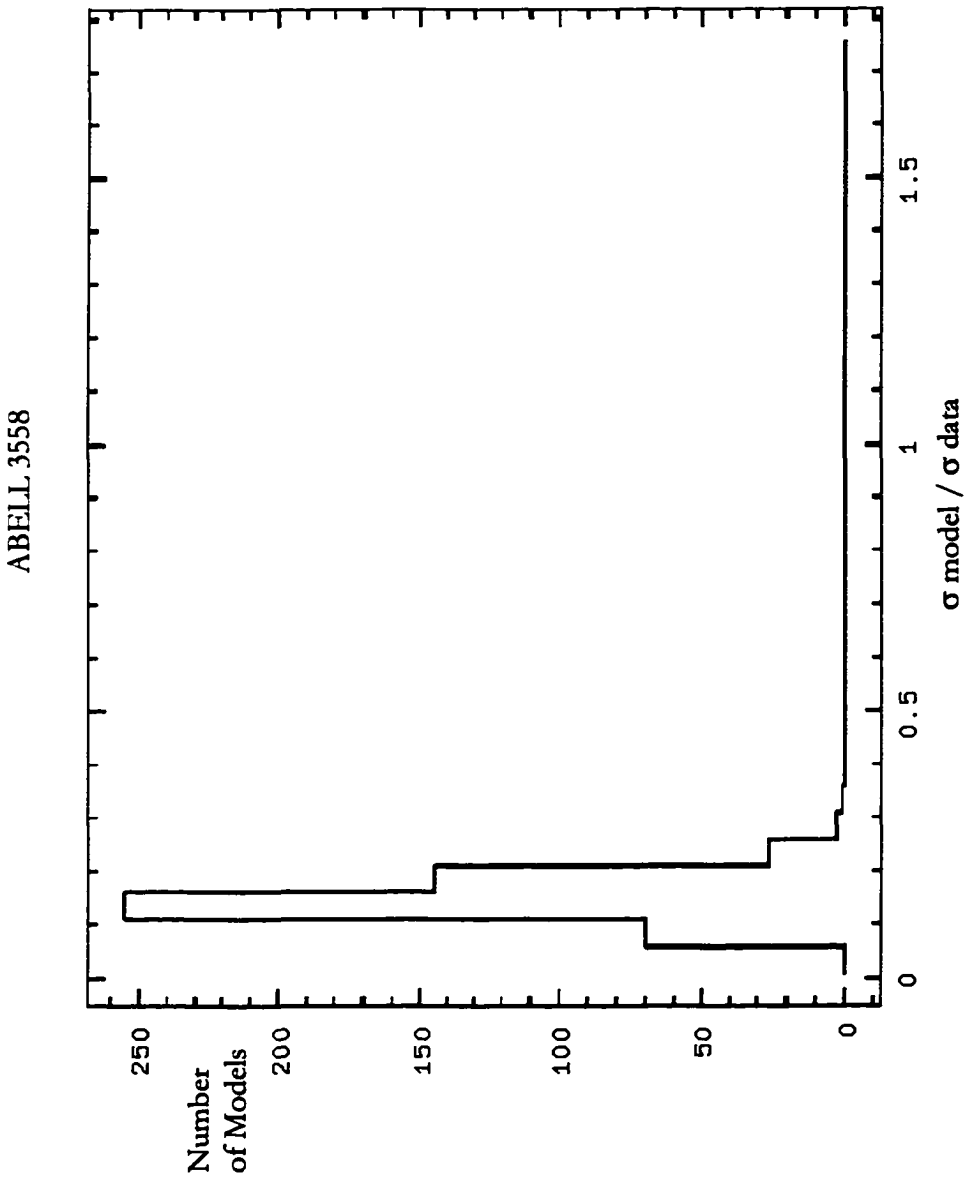

Figure 113. Sigma significance plot for Abell 3558 for 'center shift'

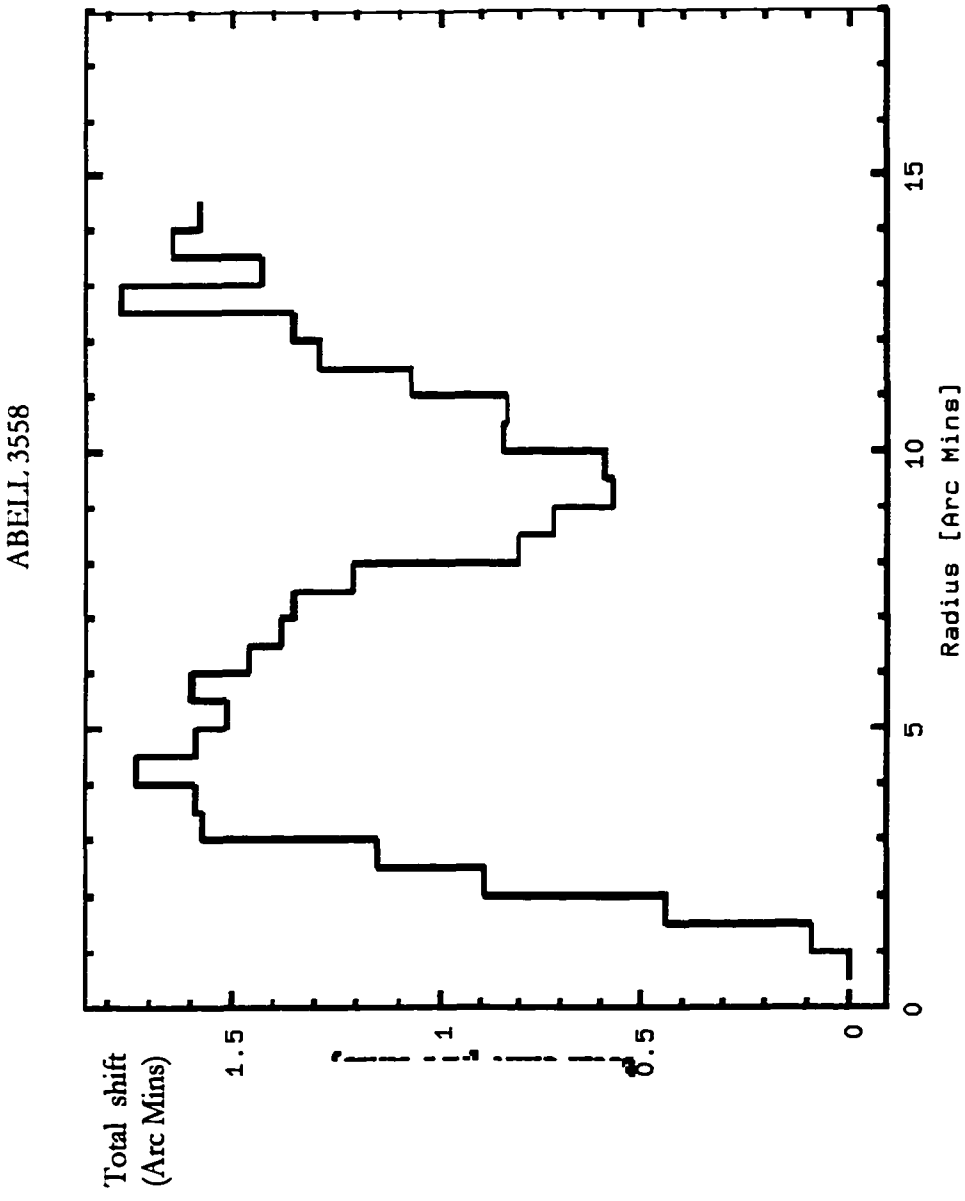

Figure 114. Total shift plot for Abell 3558 for 'center shift' program.

ABELL 3562

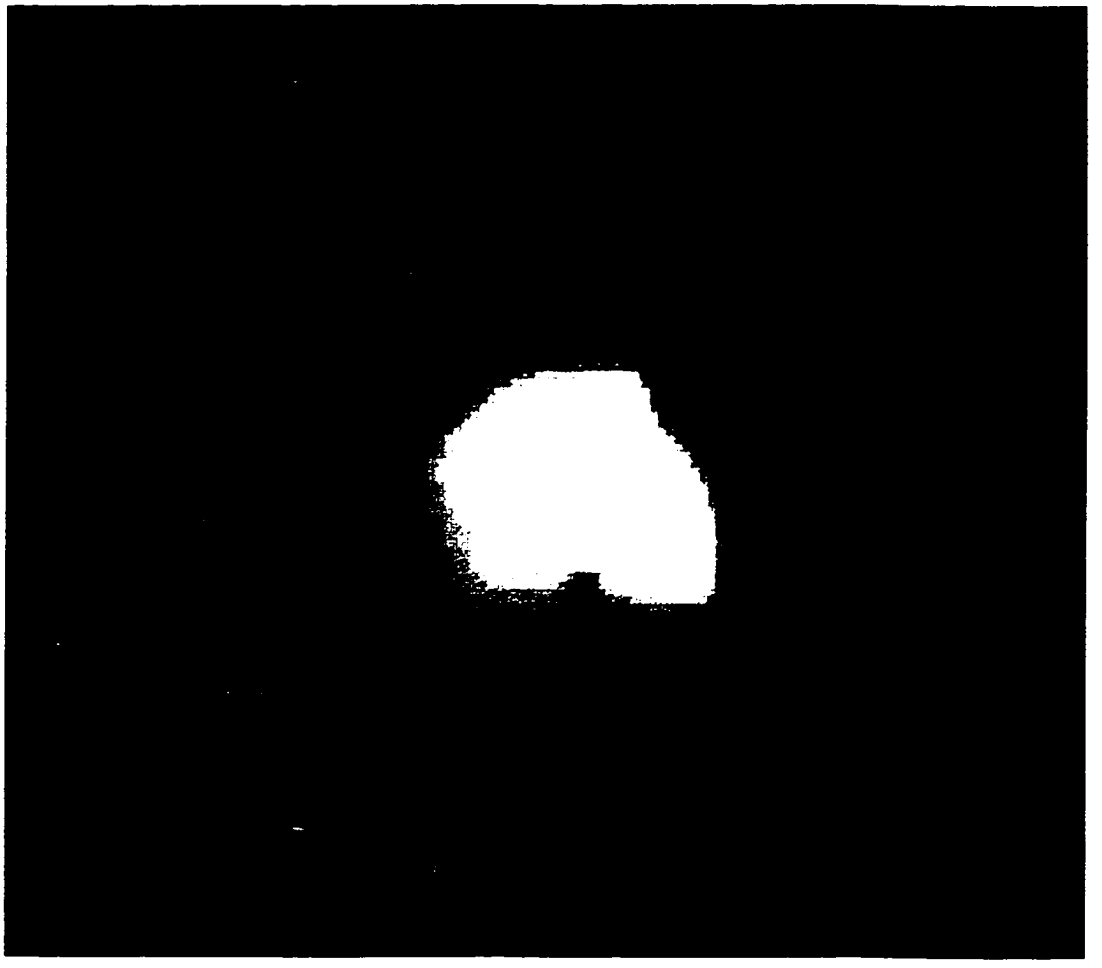

Figure 115. Cleaned and filtered image of Abell 3562. Scale is approximately 1.8 Mpc per side.

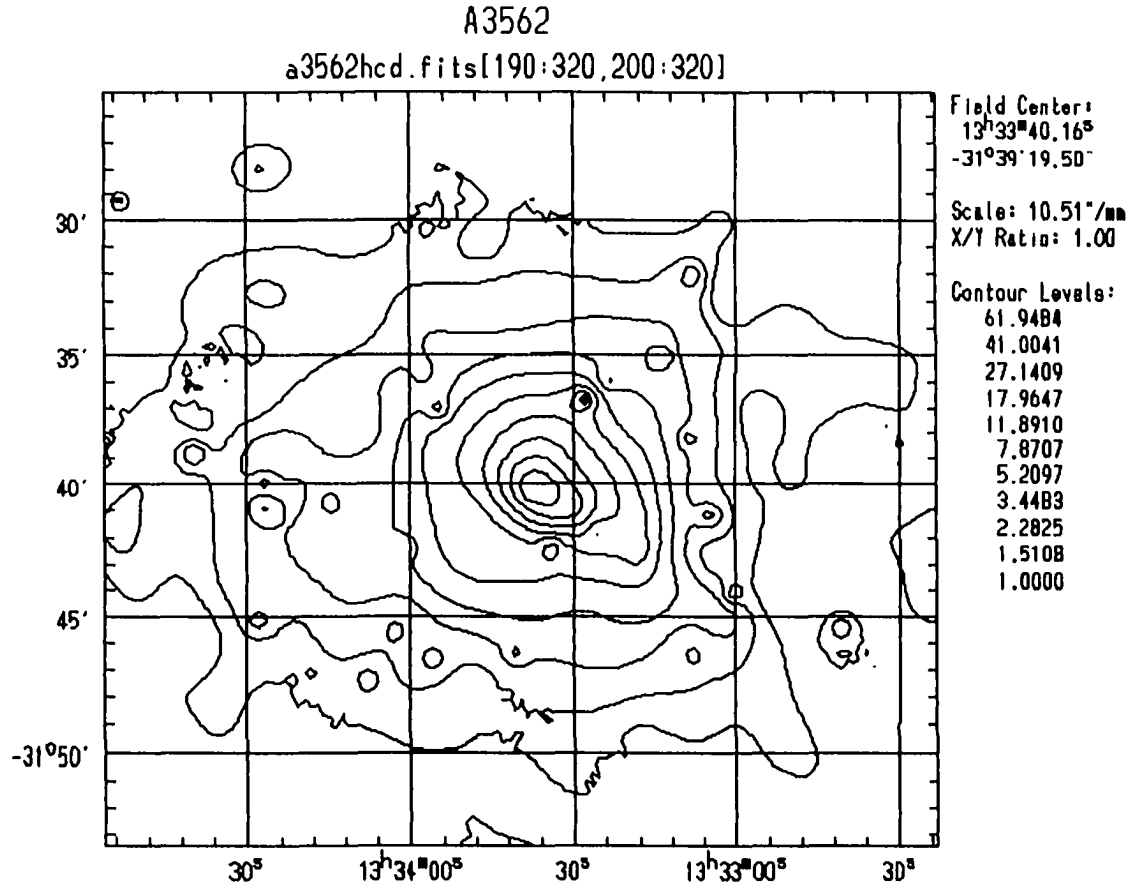

Figure 116. Contour map of Abell 3562. Scale is approximately 1.8 Mpc per side. Contour levels are given in counts.

ABELL 3562

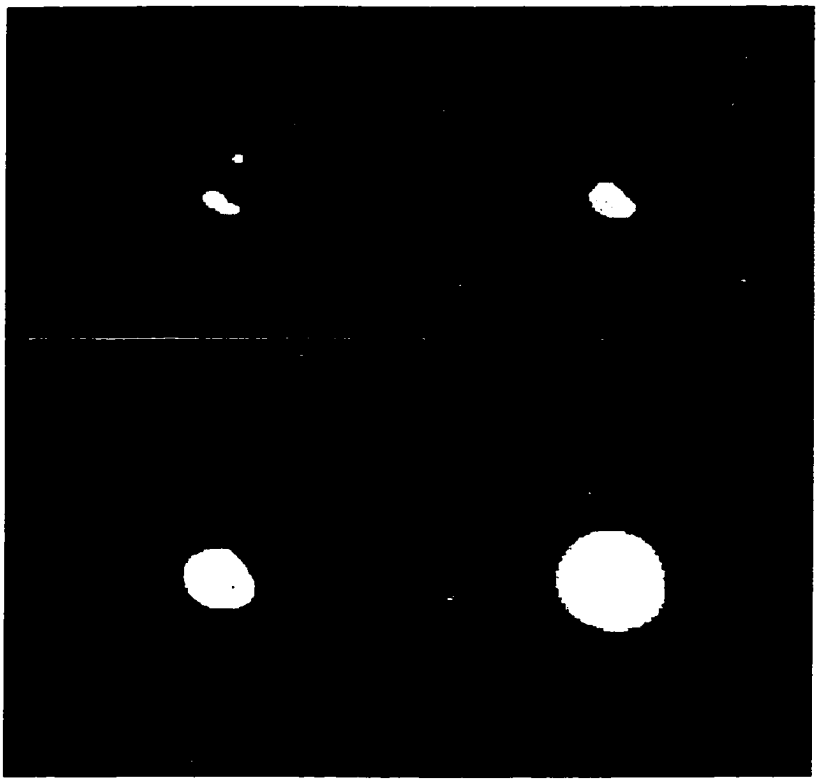

Figure 117. Wavelet transform images for Abell 3562. Clockwise from upper left in 2, 3, 4, and 5 pixel scales.

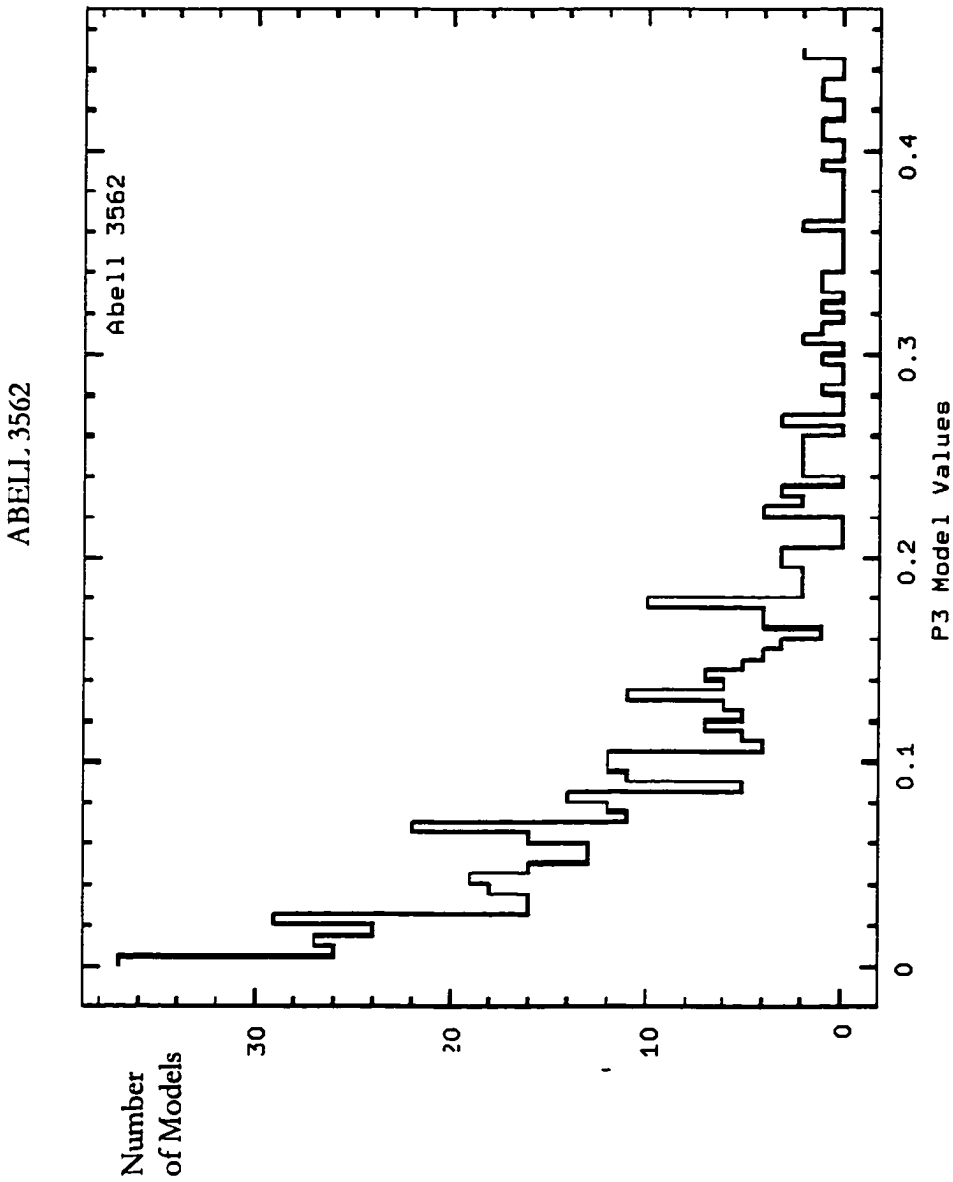

Figure 118. Histogram plots for P_3 moment for models of Abell 3562.

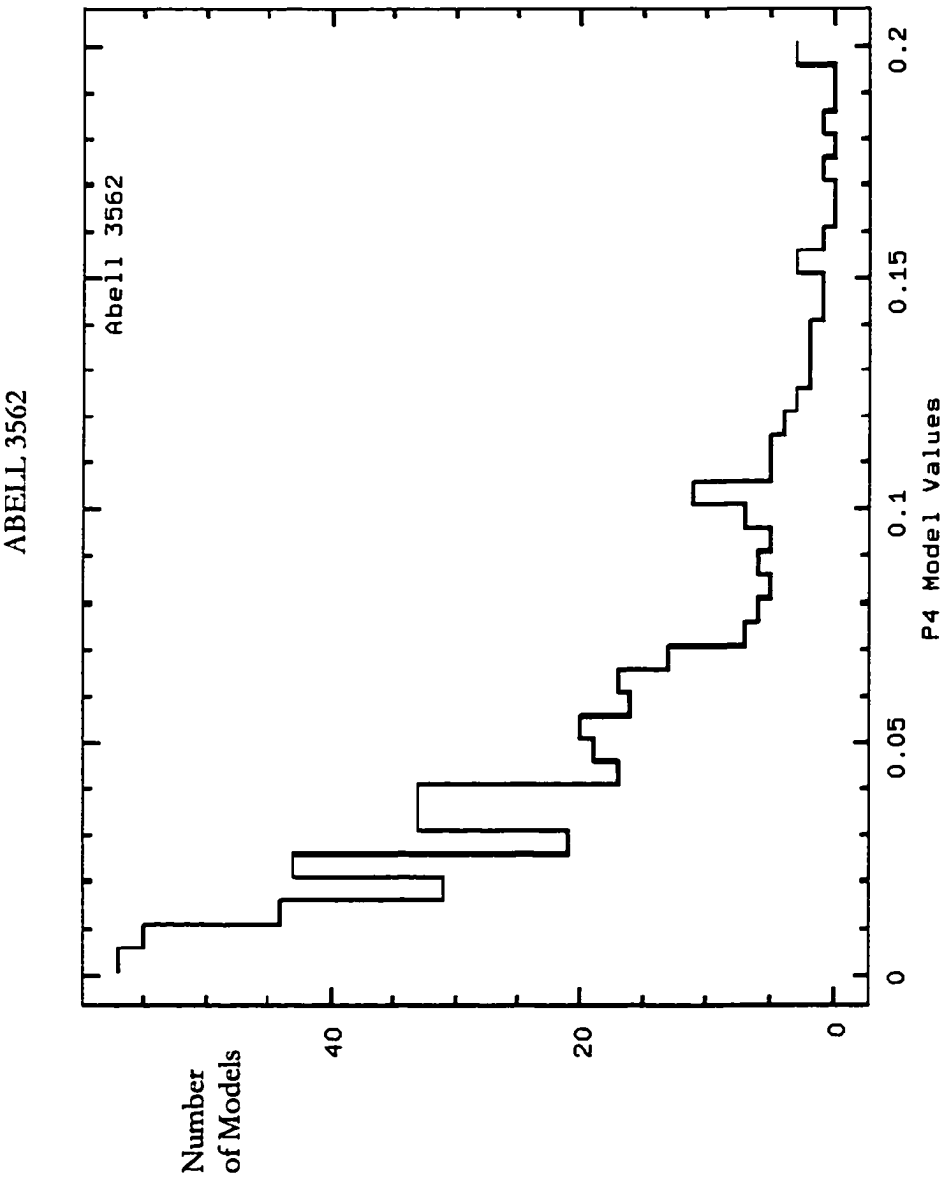

Figure 119. Histogram plots for P_4 moment for models of Abell 3562.

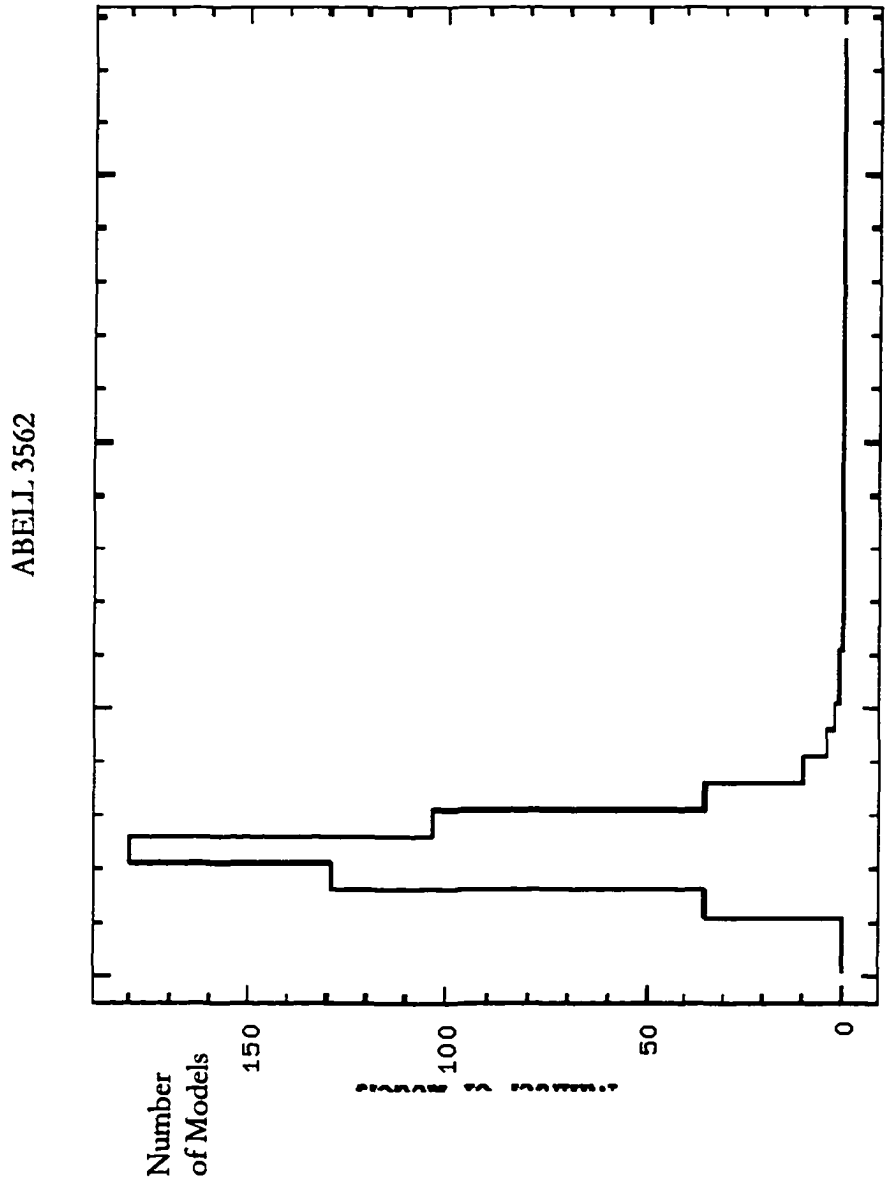

Figure 120. Sigma significance plot for Abell 3562 for 'center shift'

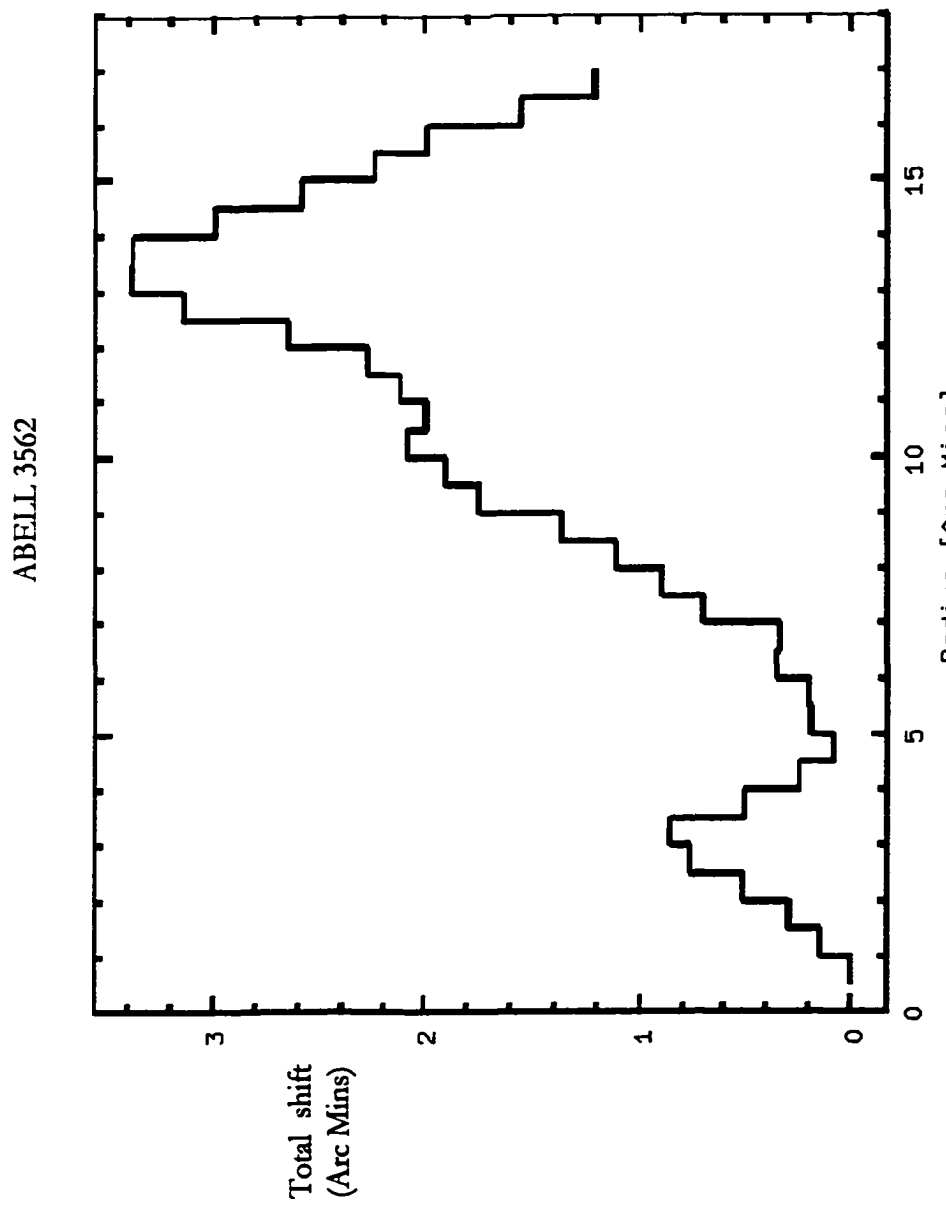

Figure 121. Total shift plot for Abell 3562 for 'center shift' program.

ABELL 3667

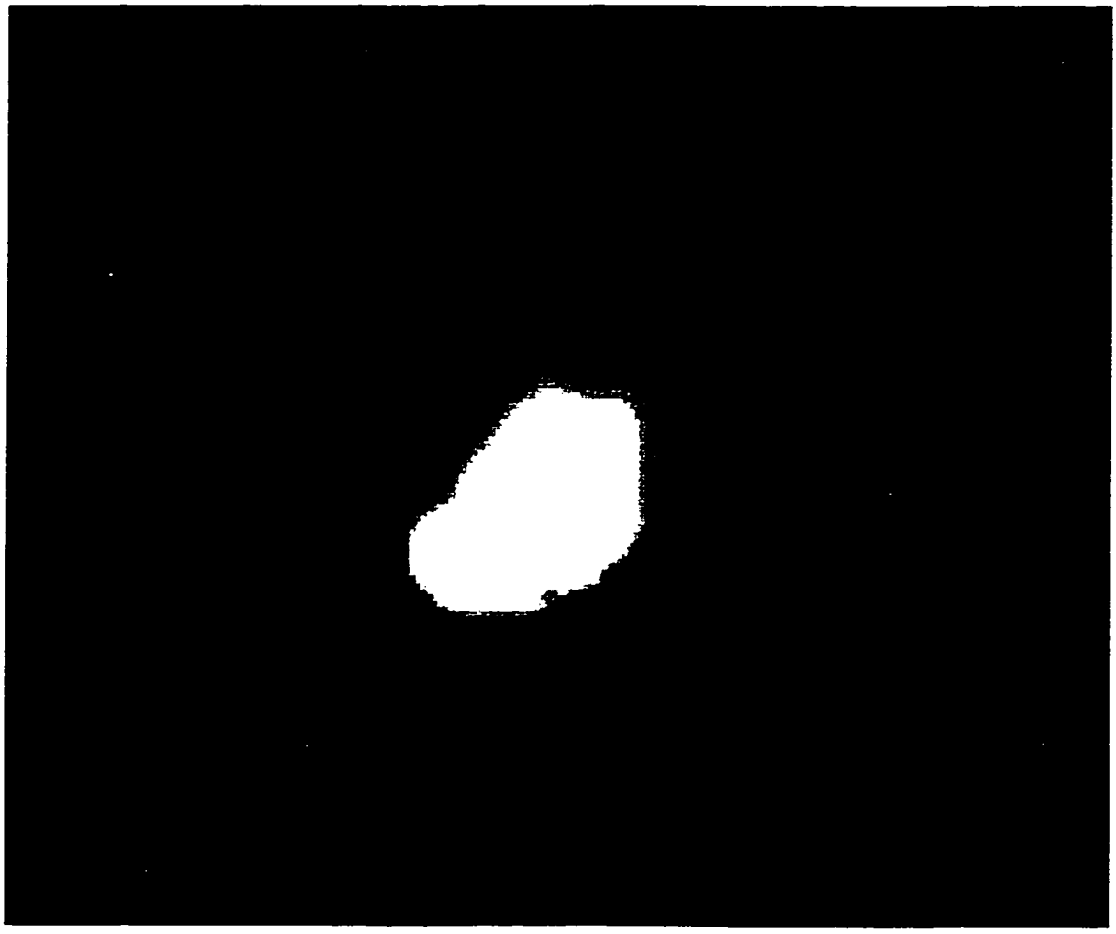

Figure 122. Cleaned and filtered image of Abell 3667. Scale is approximately 1.8 Mpc per side.

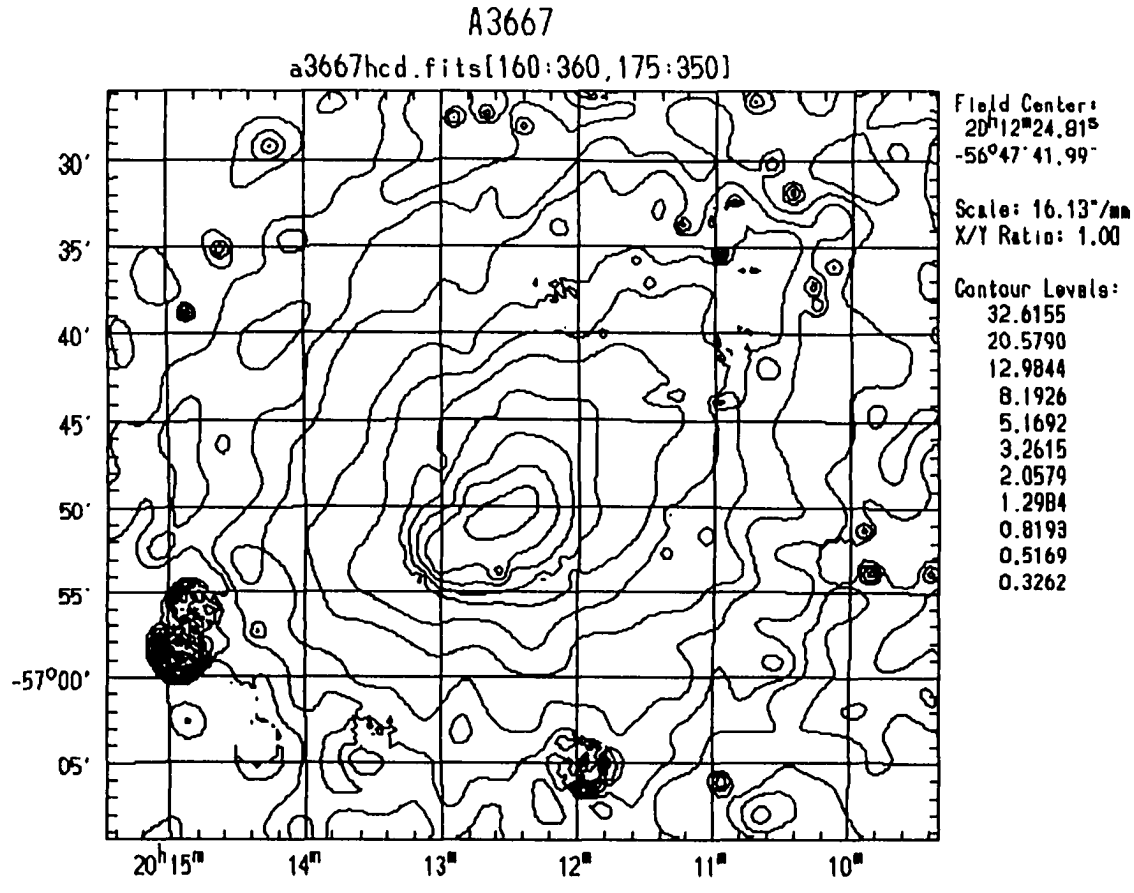

Figure 123. Contour map of Abell 3667. Scale is approximately 1.8 Mpc per side. Contour levels are given in counts.

ABELL 3667

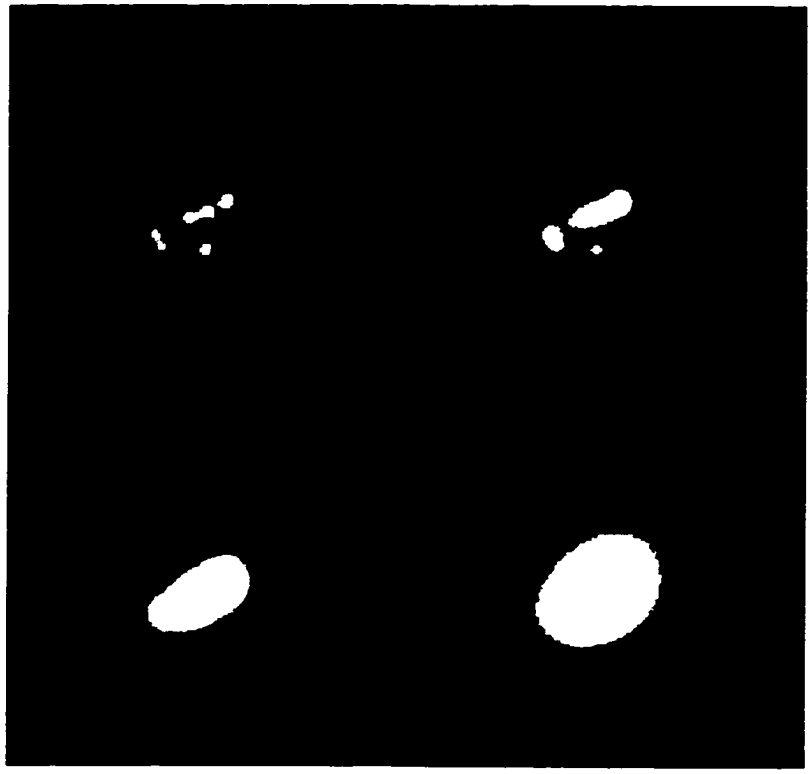

Figure 124. Wavelet transform images for Abell 3667. Clockwise from upper left in 2, 3, 4, and 5 pixel scales.

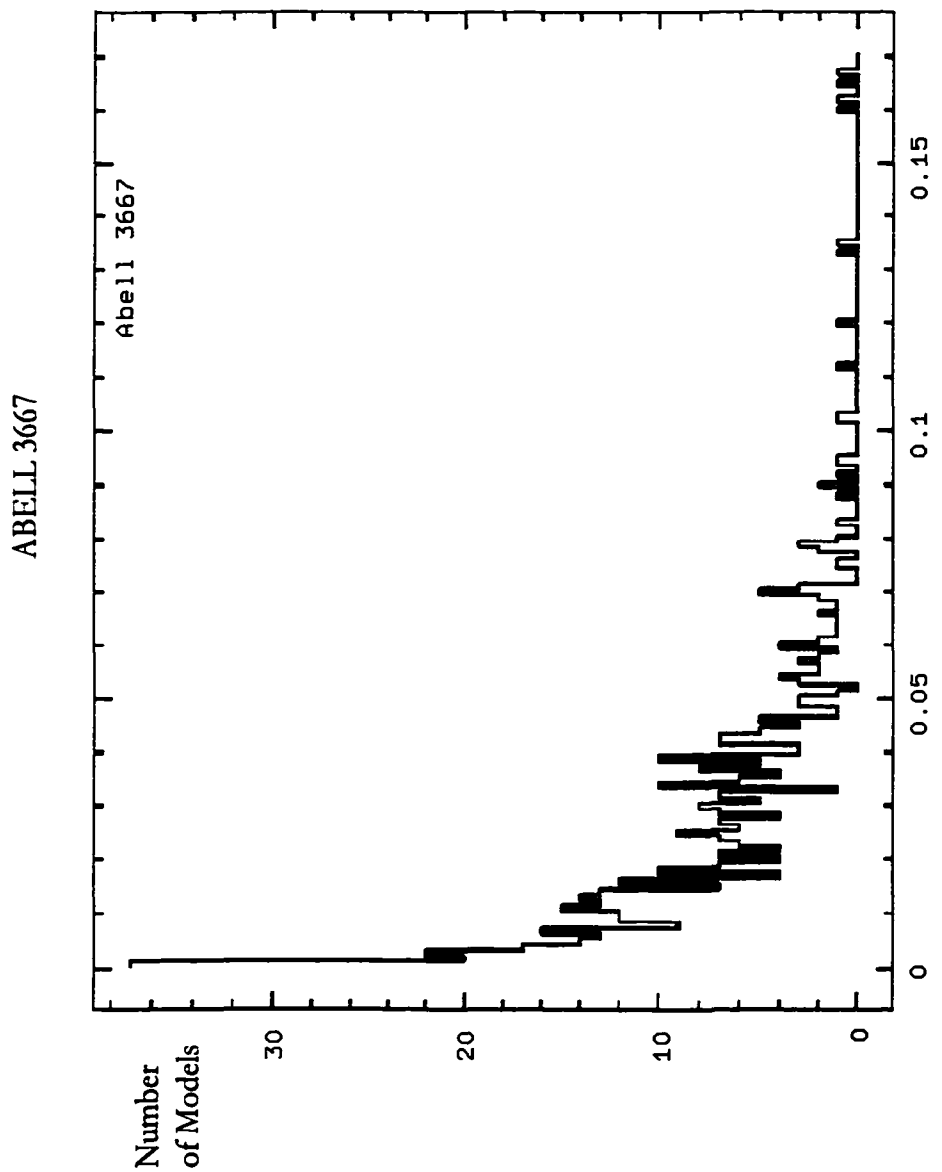

Figure 125. Histogram plots for P_3 moment for models of Abell 3667.

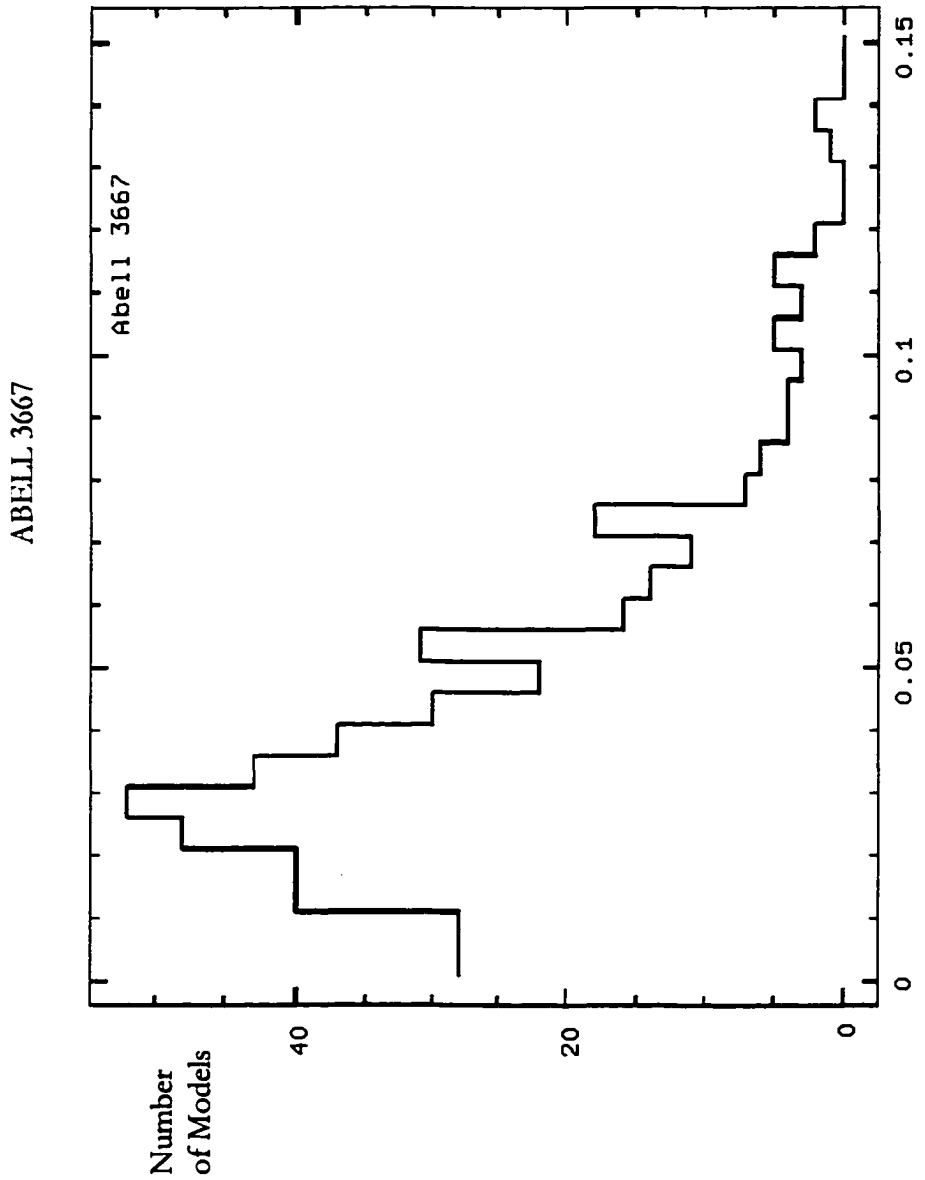

Figure 126. Histogram plots for P_4 moment for models of Abell 3667.

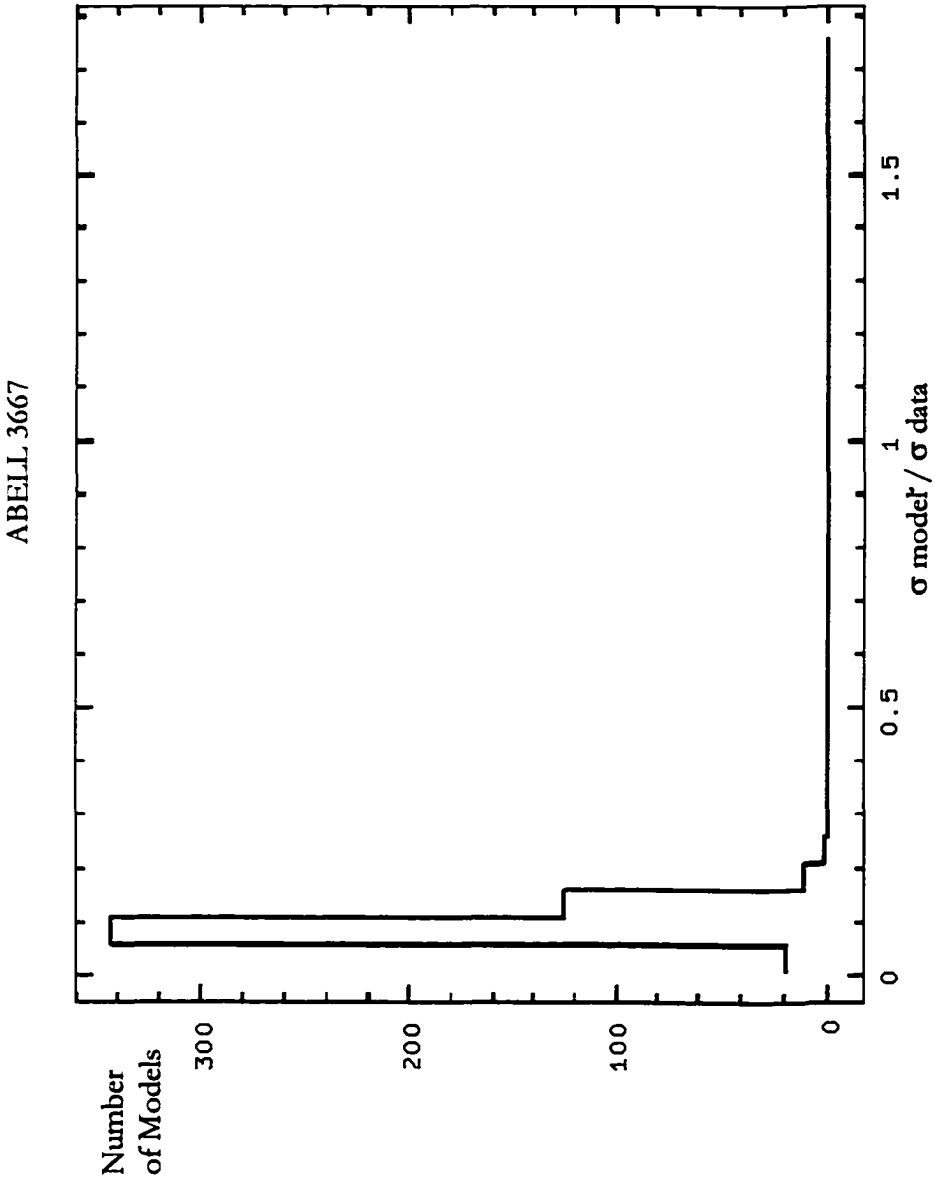

Figure 127. Sigma significance plot for Abell 3667 for 'center shift'

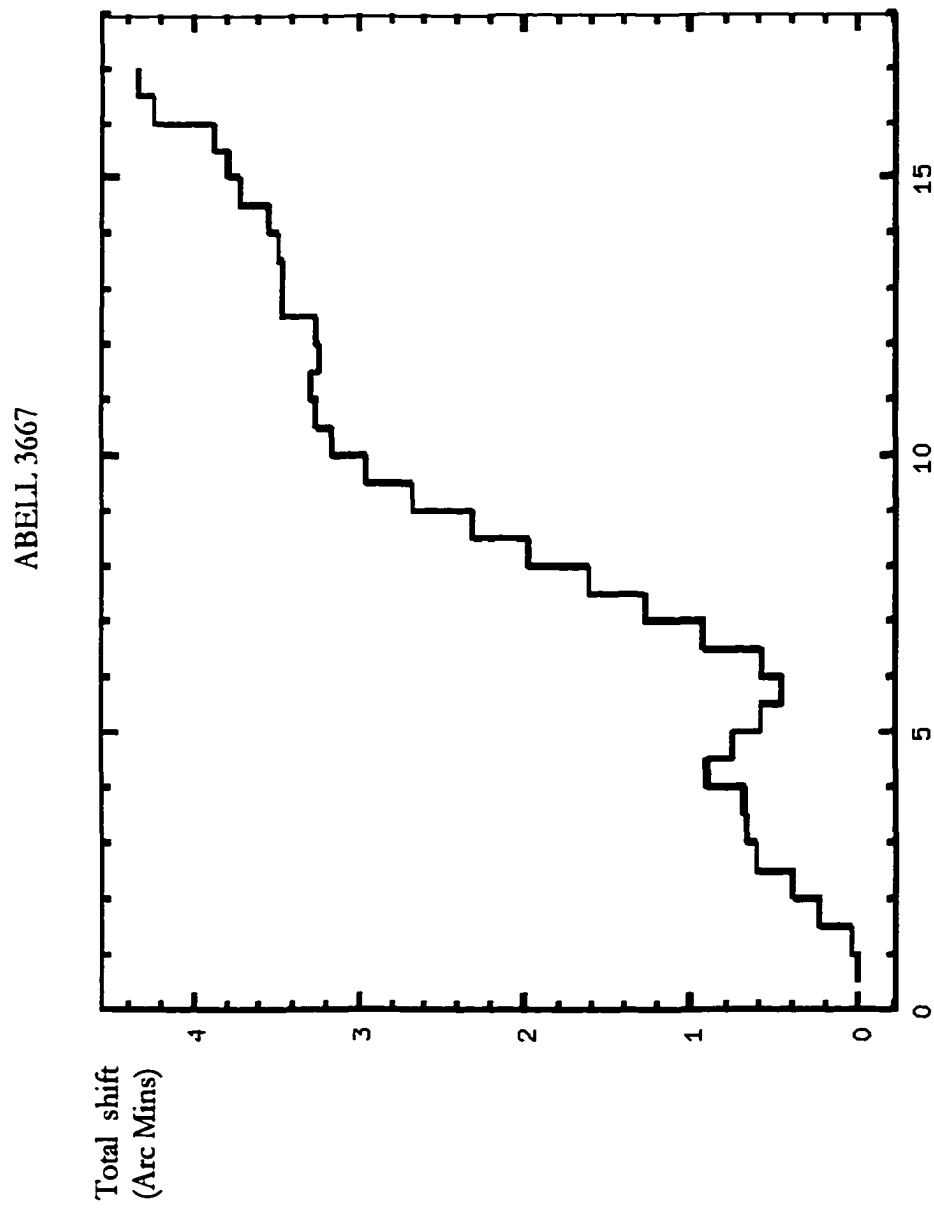

Figure 128. Total shift plot for Abell 3667 for 'center shift' program.

ABELL 3897

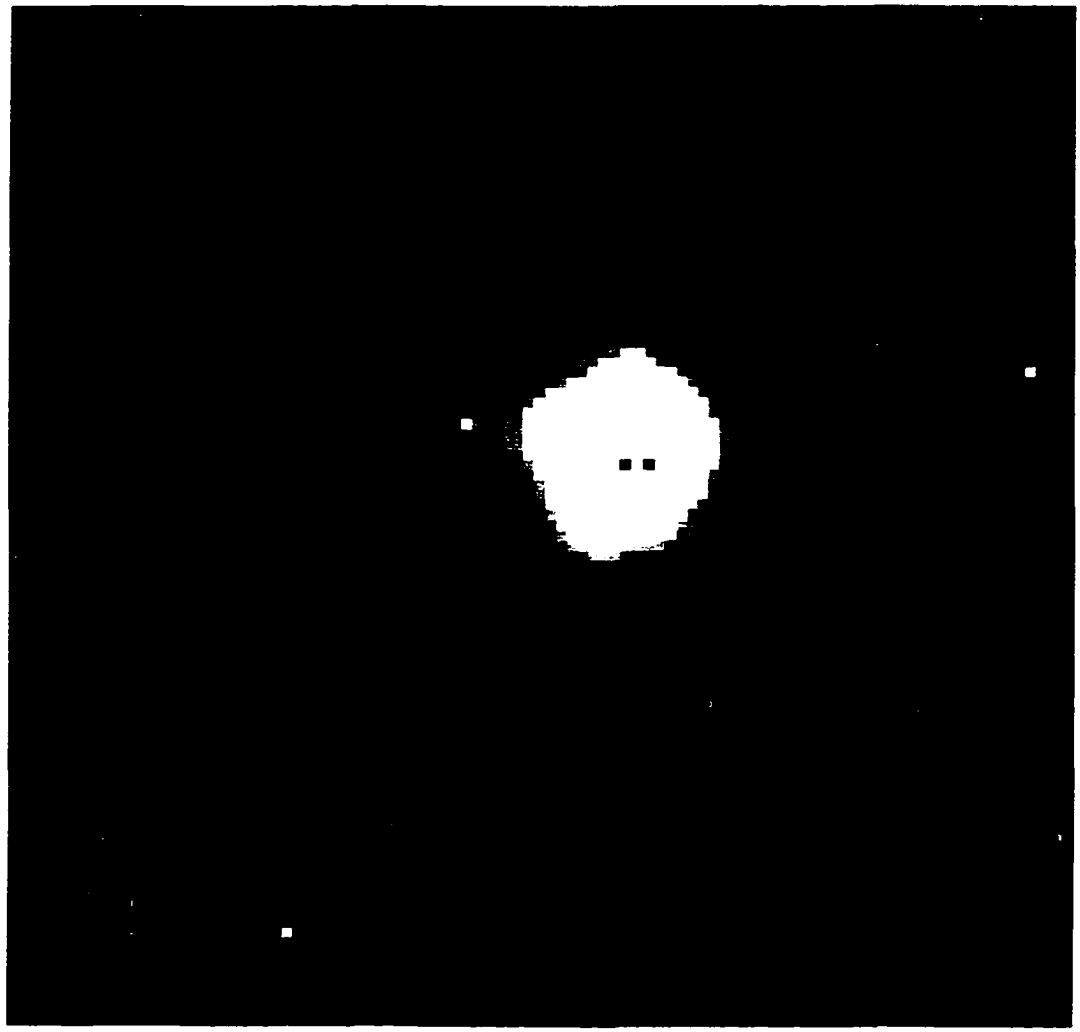

Figure 129. Cleaned and filtered image of Abell 3897. Scale is approximately 1.8 Mpc per side.

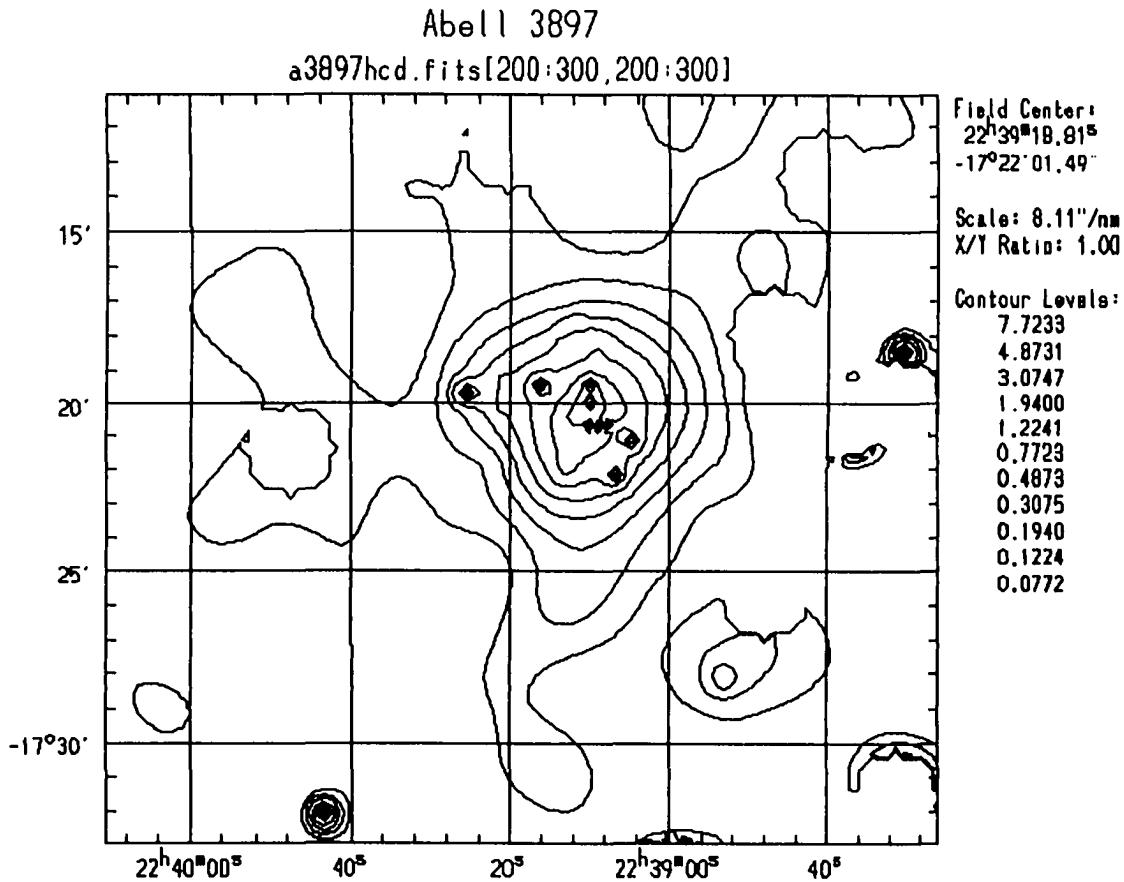

Figure 130. Contour map of Abell 3897. Scale is approximately 1.8 Mpc per side. Contour levels are given in counts.

ABELL 3897

Figure 131. Wavelet transform images for Abell 3897. Clockwise from upper left in 2, 3, 4, and 5 pixel scales.

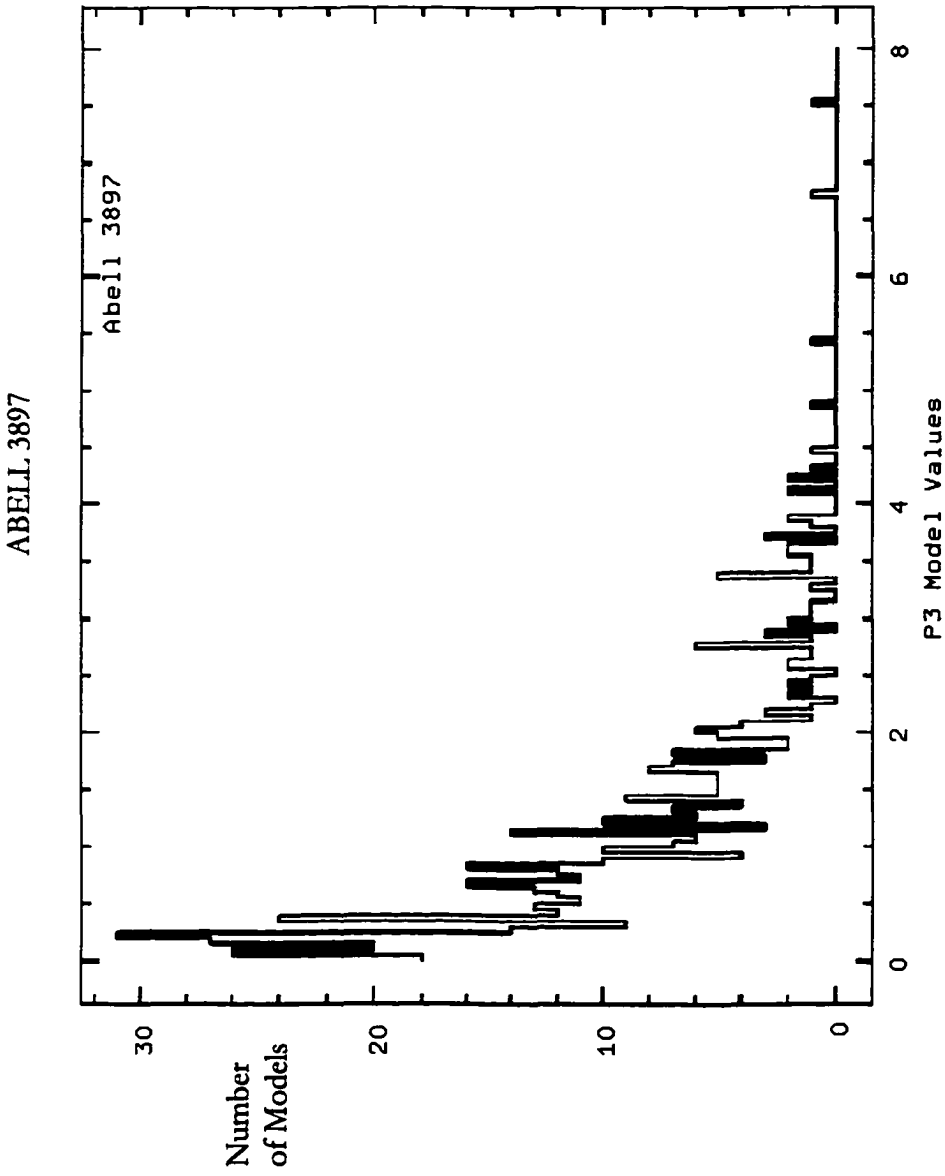

Figure 132. Histogram plots for P_3 moment for models of Abell 3897.

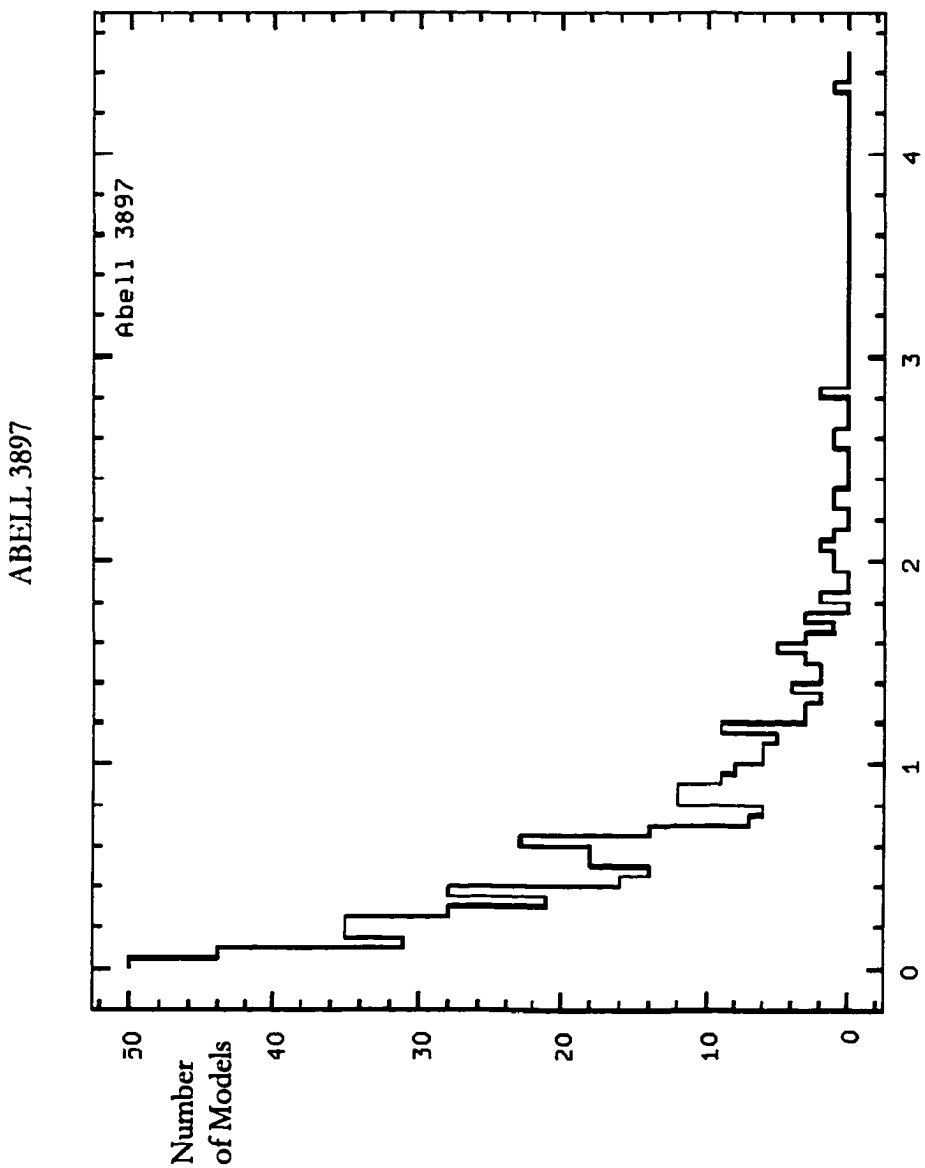

Figure 133. Histogram plots for P_4 moment for models of Abell 3897.

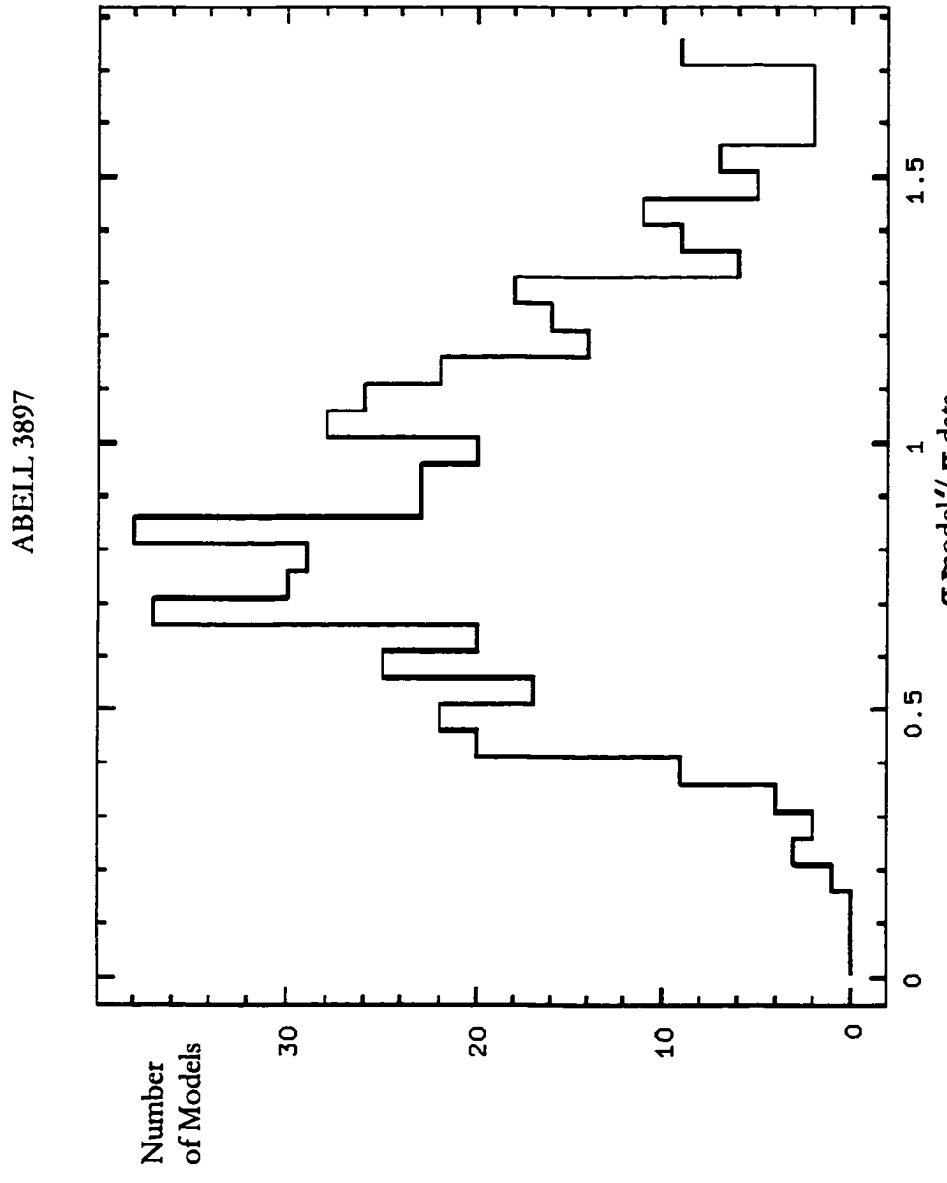

Figure 134. Sigma significance plot for Abell 3897 for 'center shift'

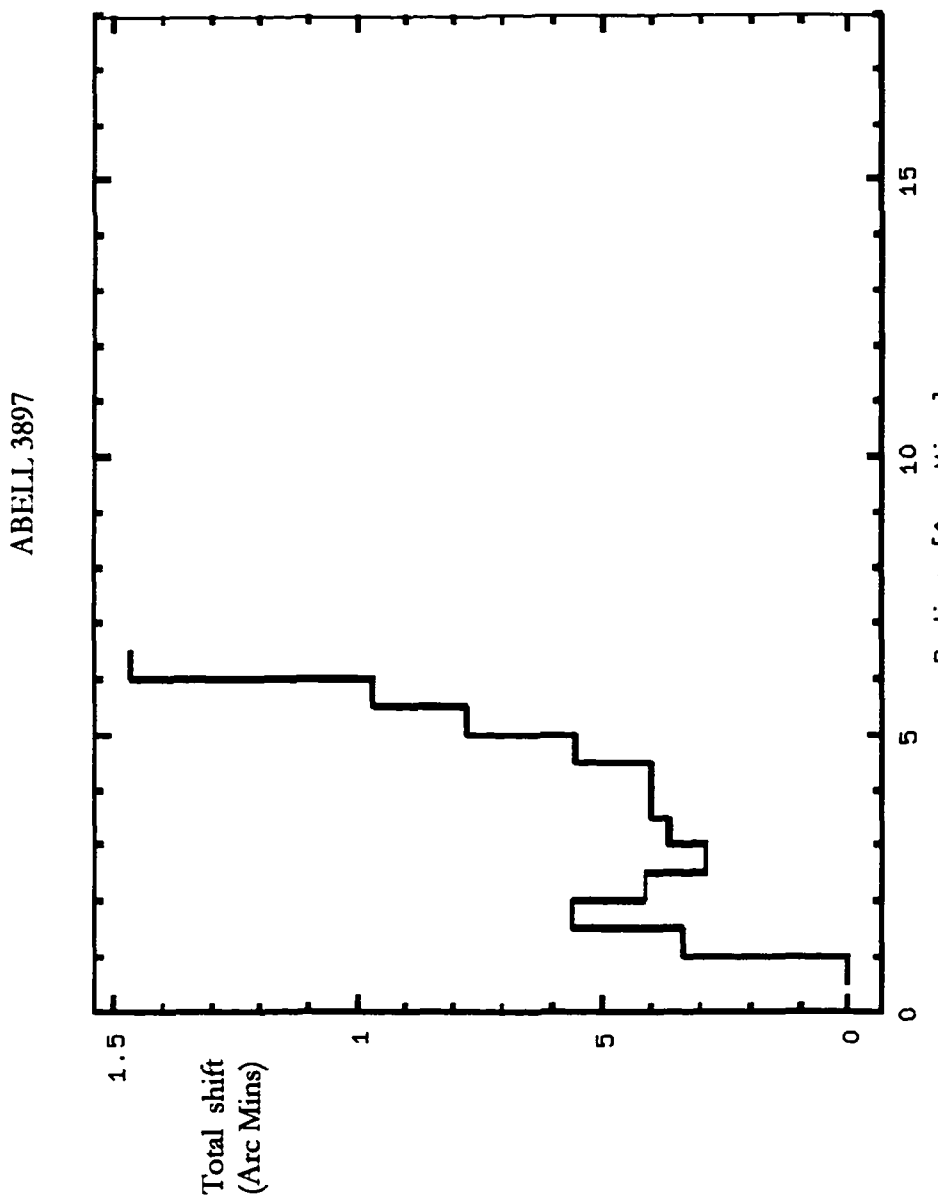

Figure 135. Total shift plot for Abell 3897 for 'center shift' program.

ABELL 4038

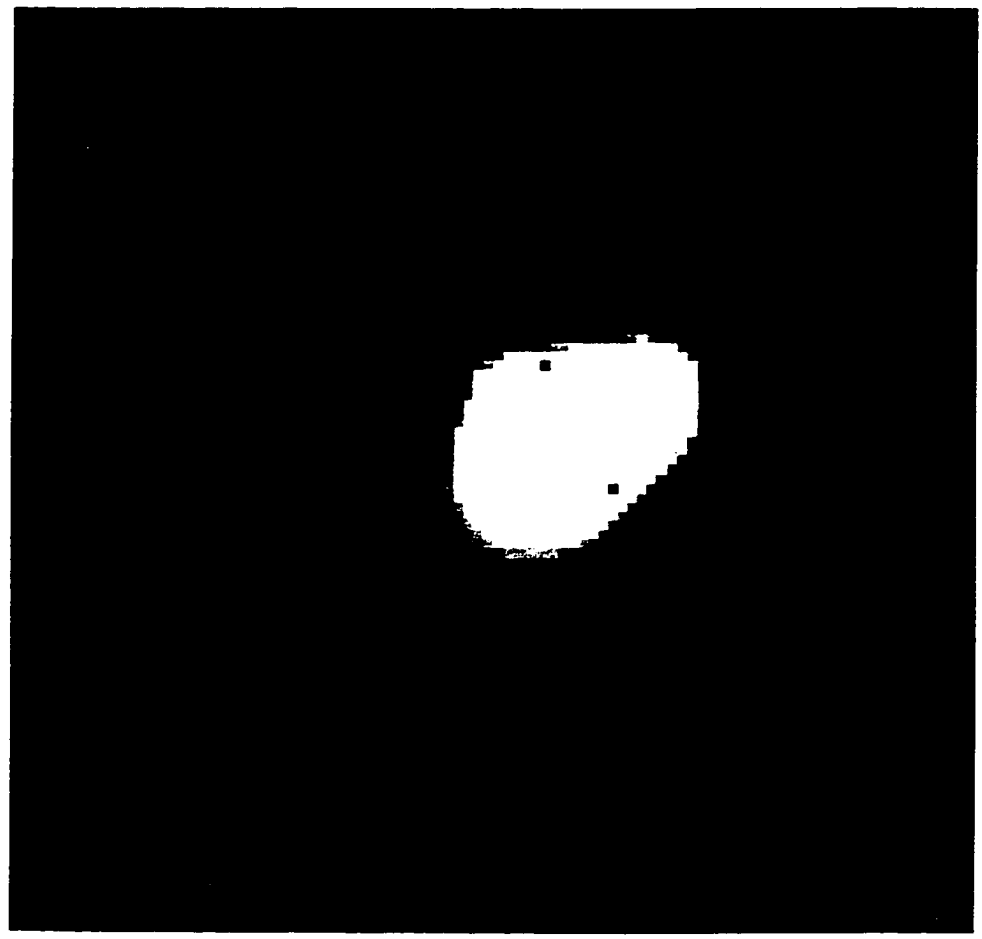

Figure 136. Cleaned and filtered image of Abell 4038. Scale is approximately 1.8 Mpc per side.

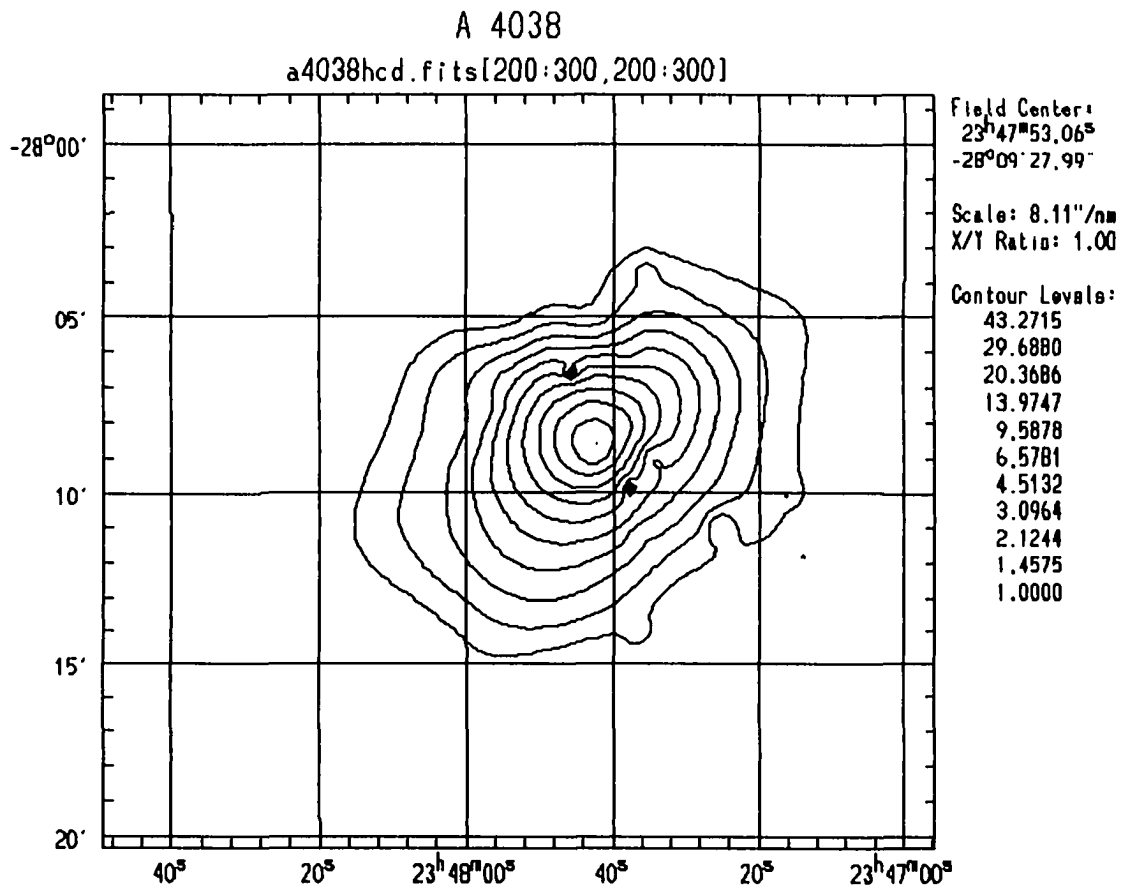

Figure 137. Contour map of Abell 4038. Scale is approximately 1.8 Mpc per side. Contour levels are given in counts.

ABELL 4038

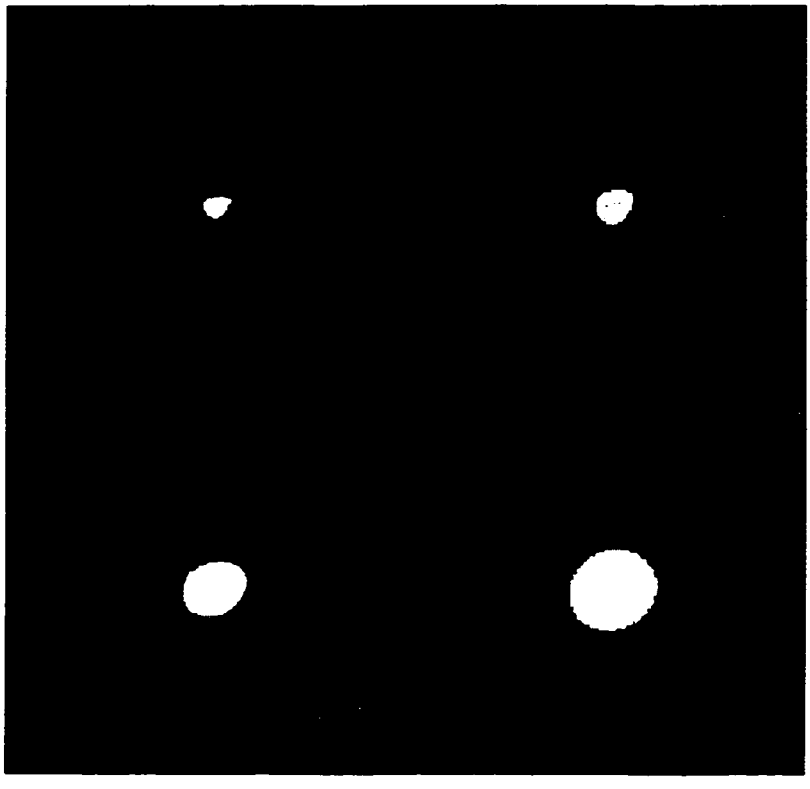

Figure 138. Wavelet transform images for Abell 4038. Clockwise from upper left in 2, 3, 4, and 5 pixel scales.

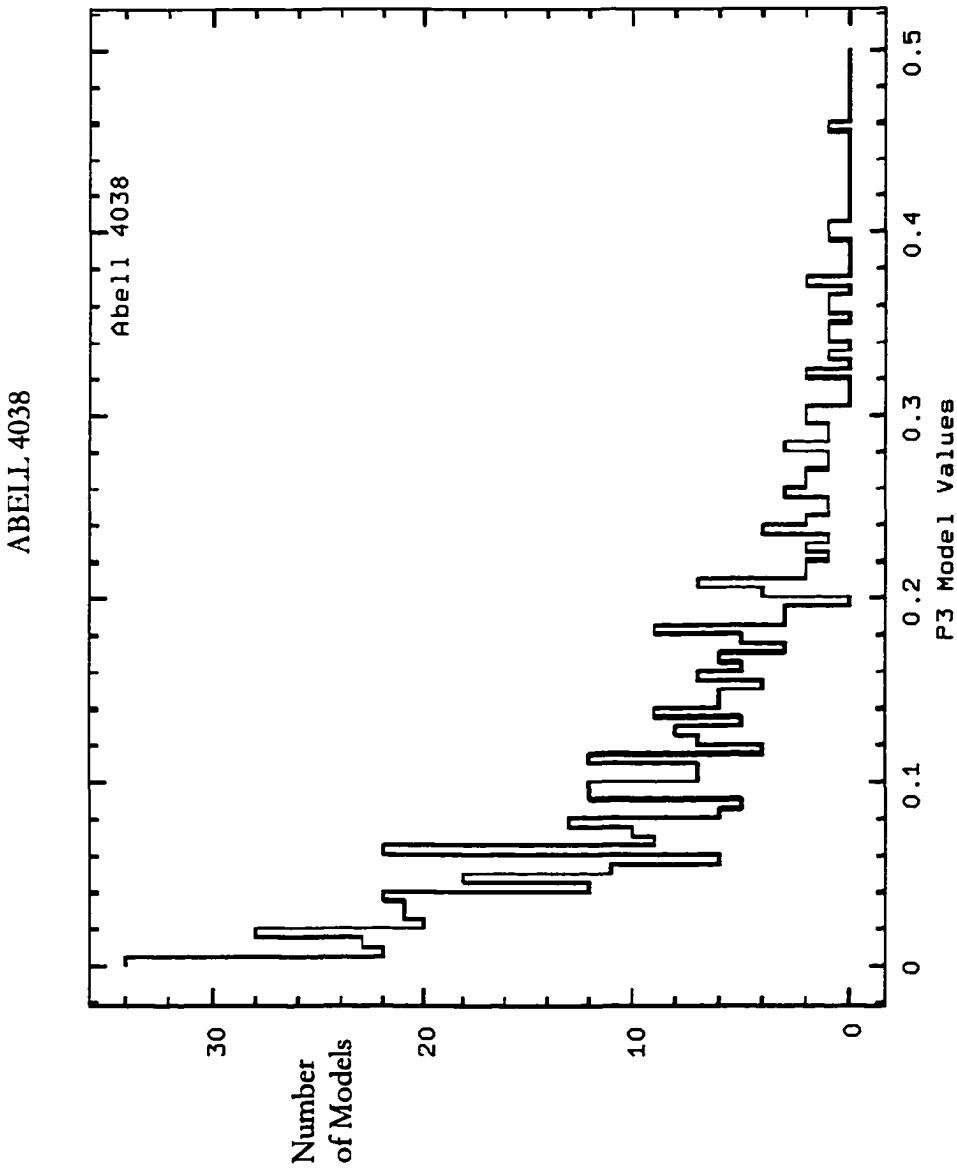

Figure 139. Histogram plots for P_3 moment for models of Abell 4038.

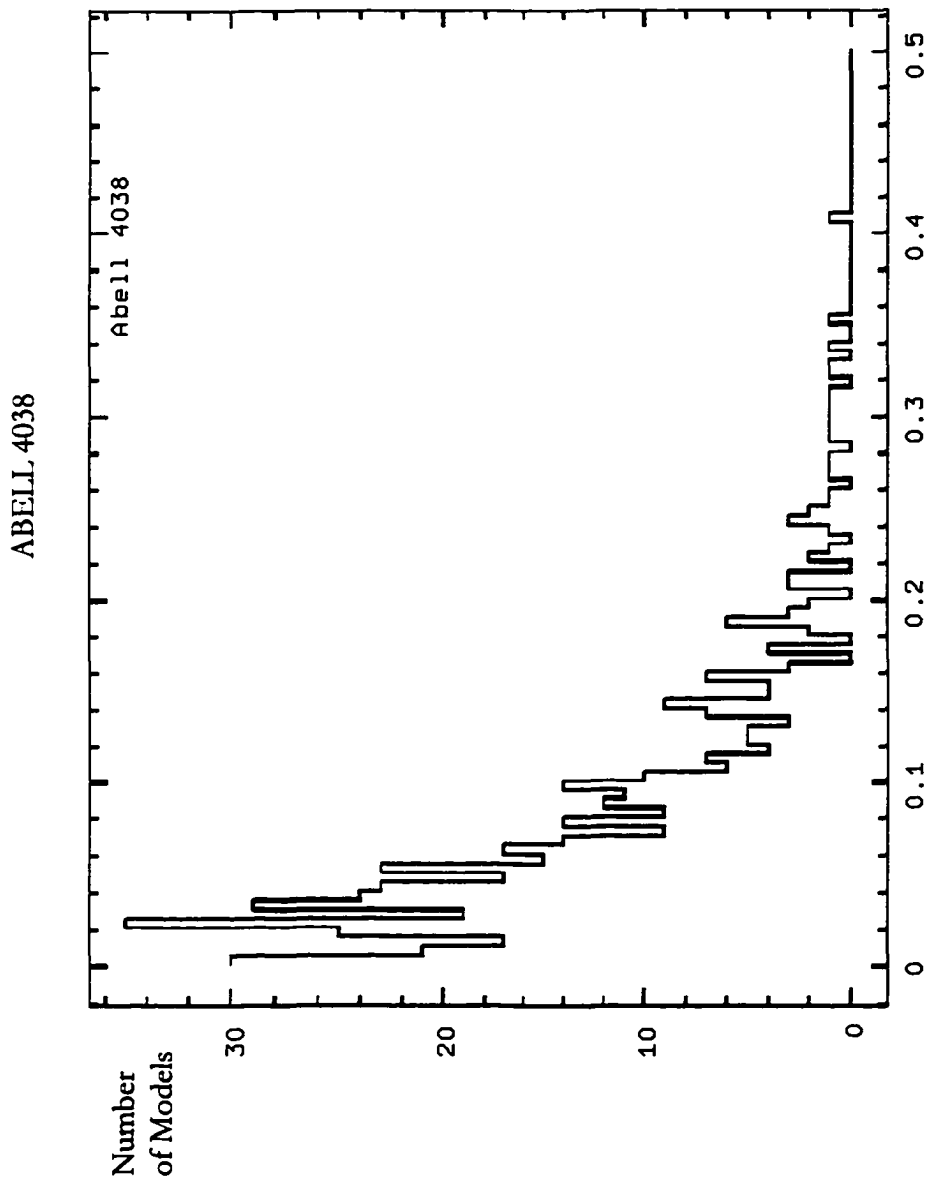

Figure 140. Histogram plots for P_4 moment for models of Abell 4038.

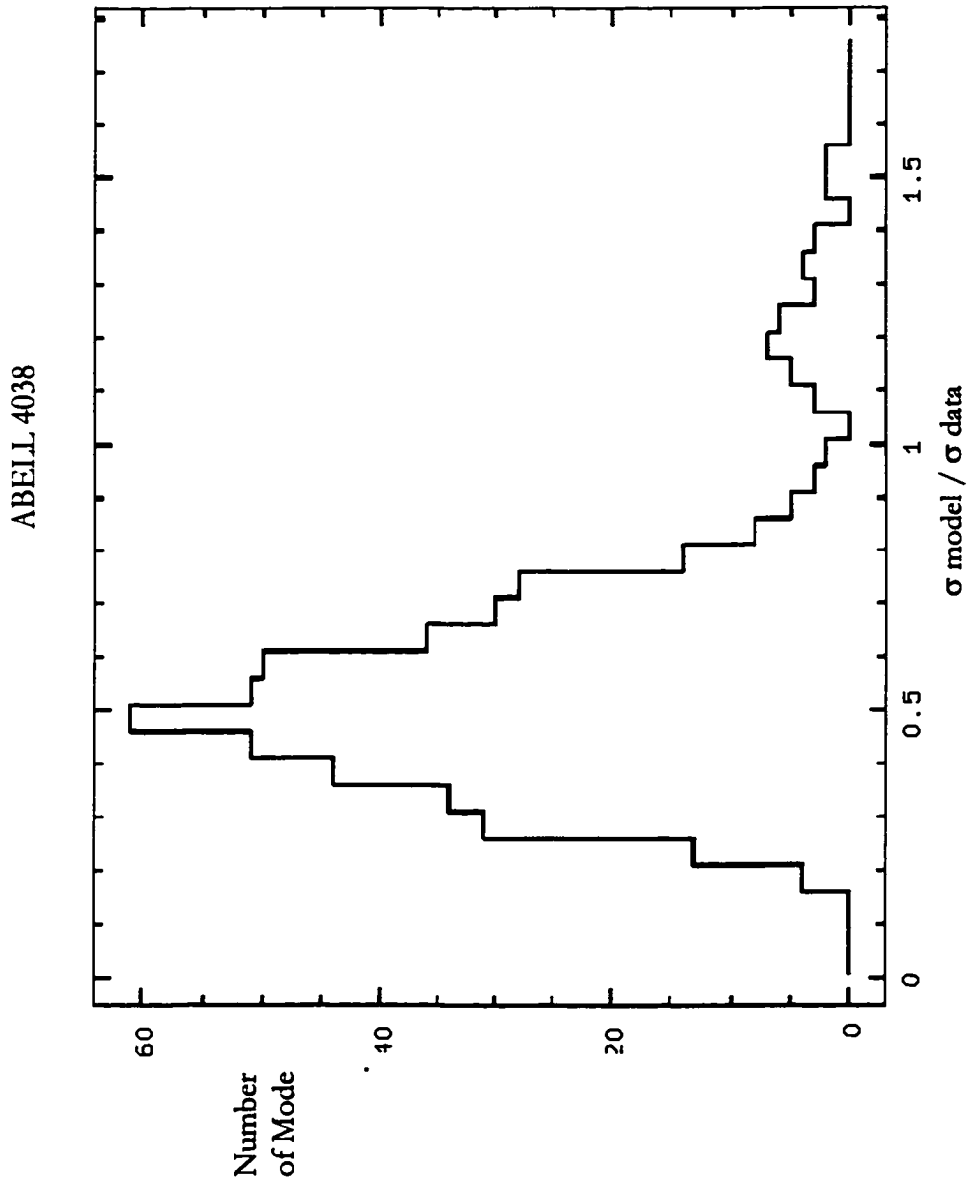

Figure 141. Sigma significance plot for Abell 4038 for 'center shift'

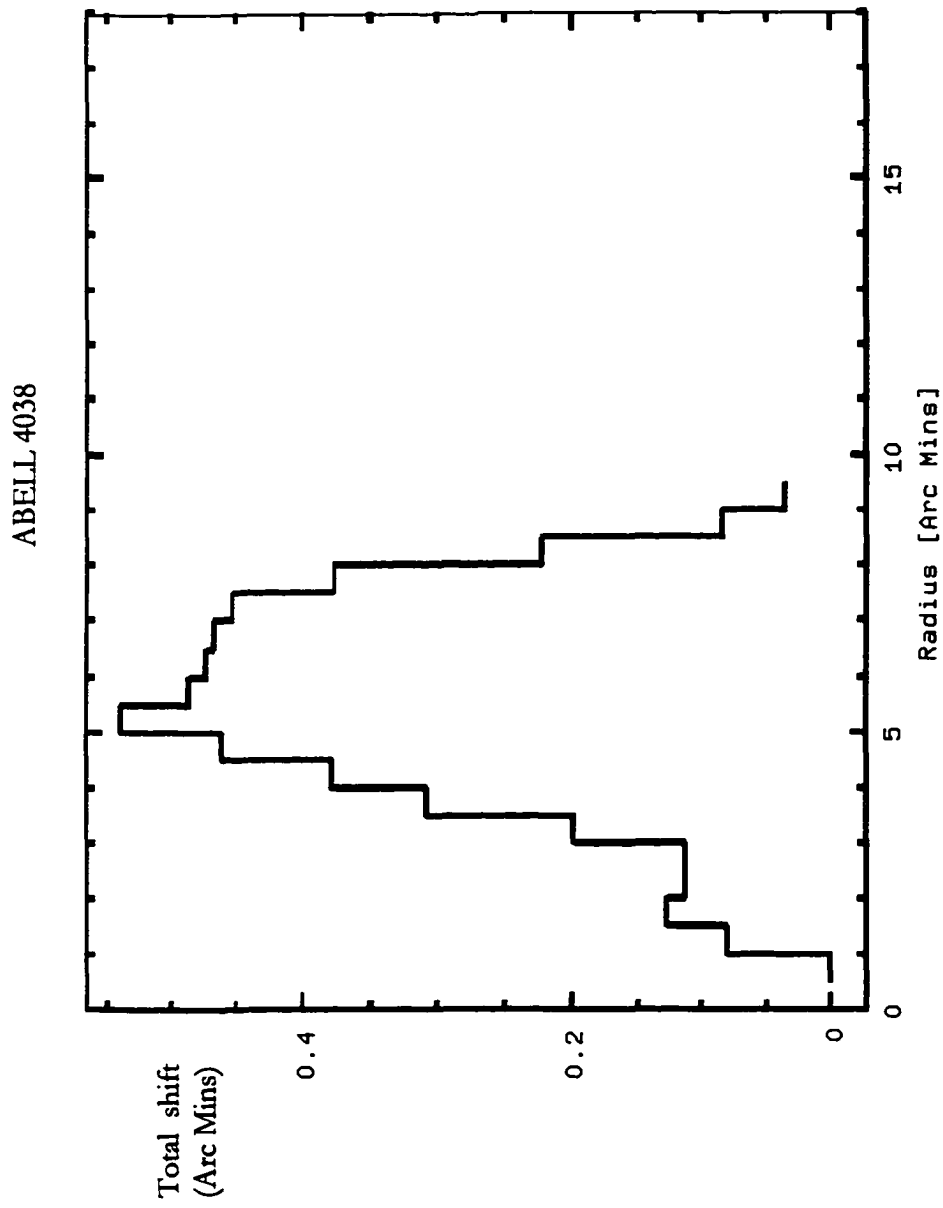

Figure 142. Total shift plot for Abell 4038 for 'center shift' program.

ABELL 4059

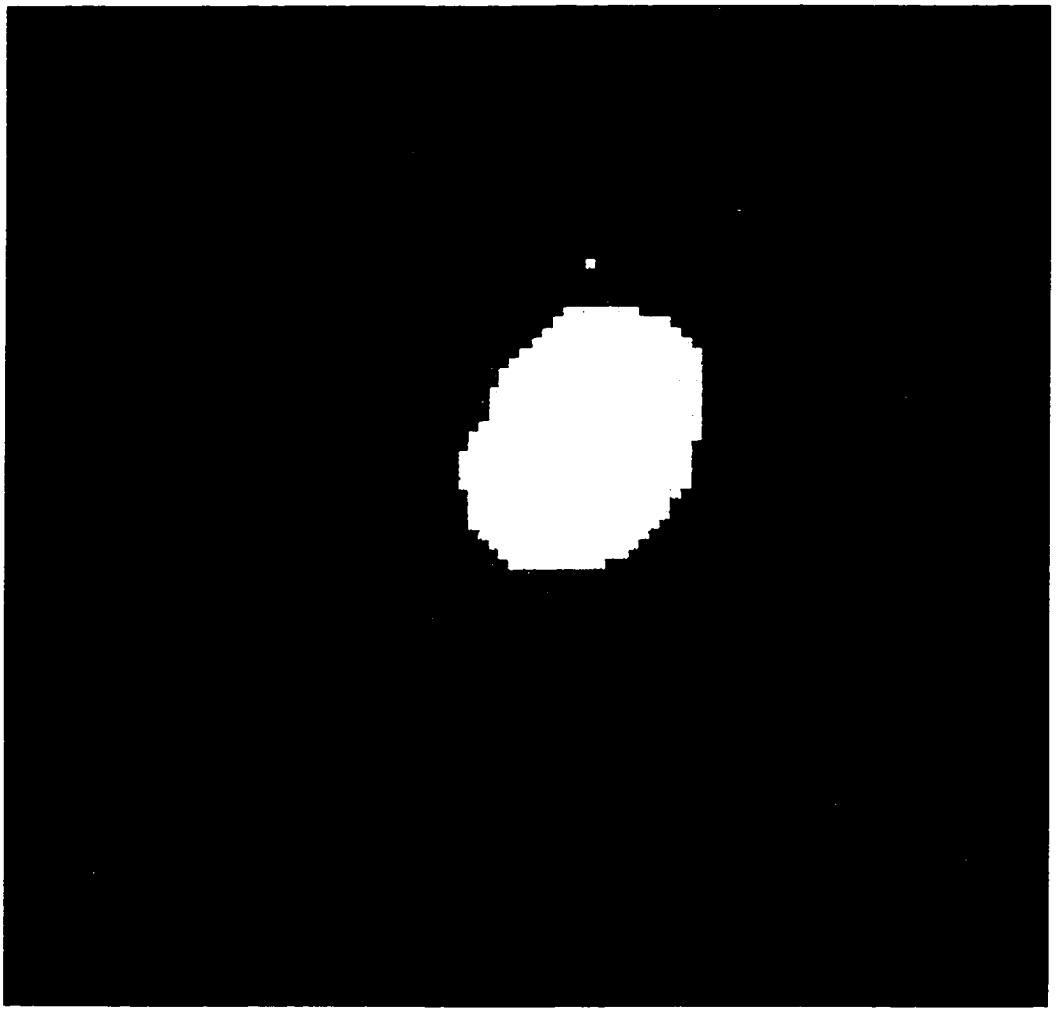

Figure 143. Cleaned and filtered image of Abell 4059. Scale is approximately 1.8 Mpc per side.

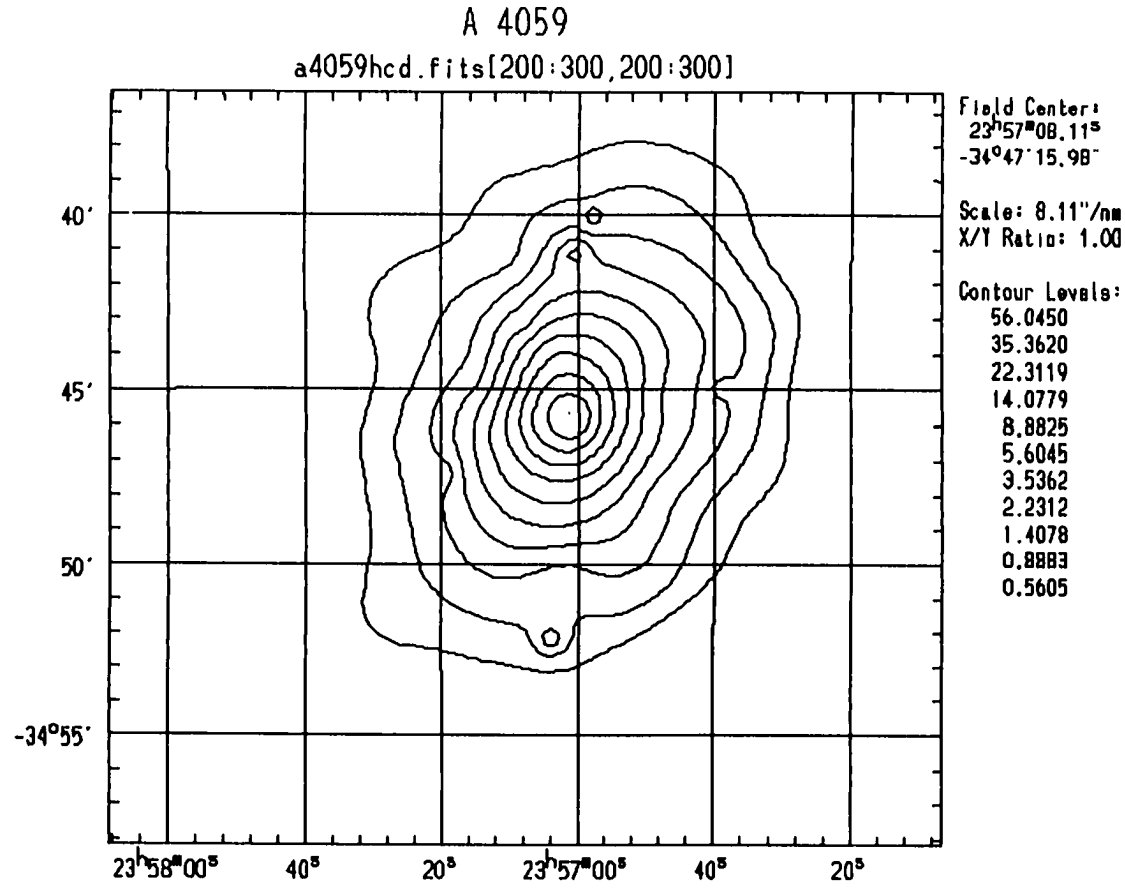

Figure 144. Contour map of Abell 4059. Scale is approximately 1.8 Mpc per side. Contour levels are given in counts.

ABELL 4059

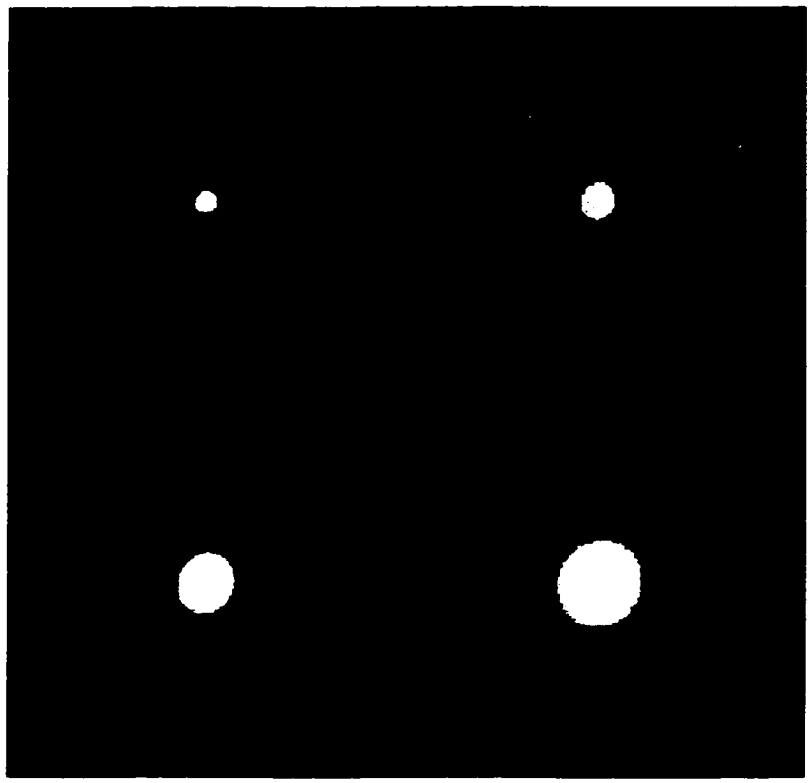

Figure 145. Wavelet transform images for Abell 4059. Clockwise from upper left in 2, 3, 4, and 5 pixel scales.

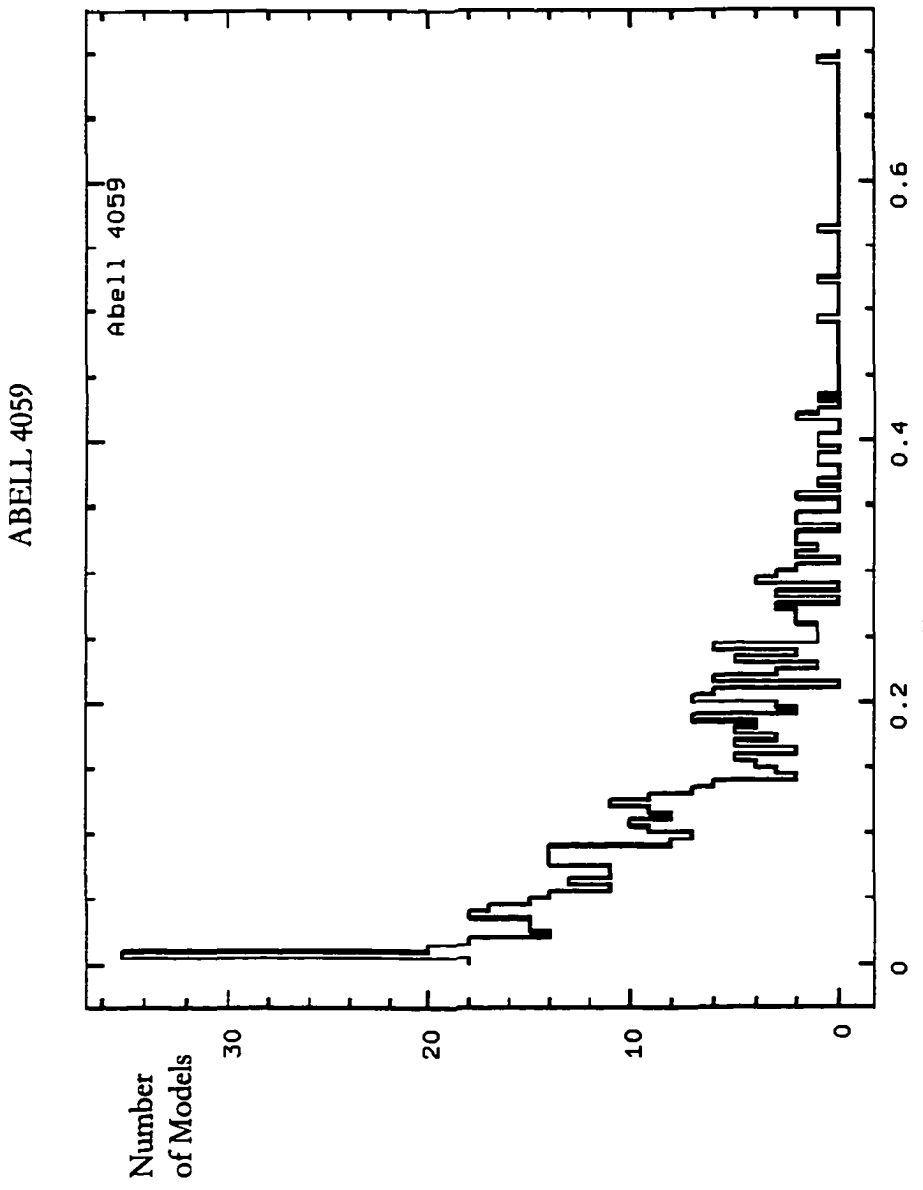

Figure 146. Histogram plots for P_3 moment for models of Abell 4059.

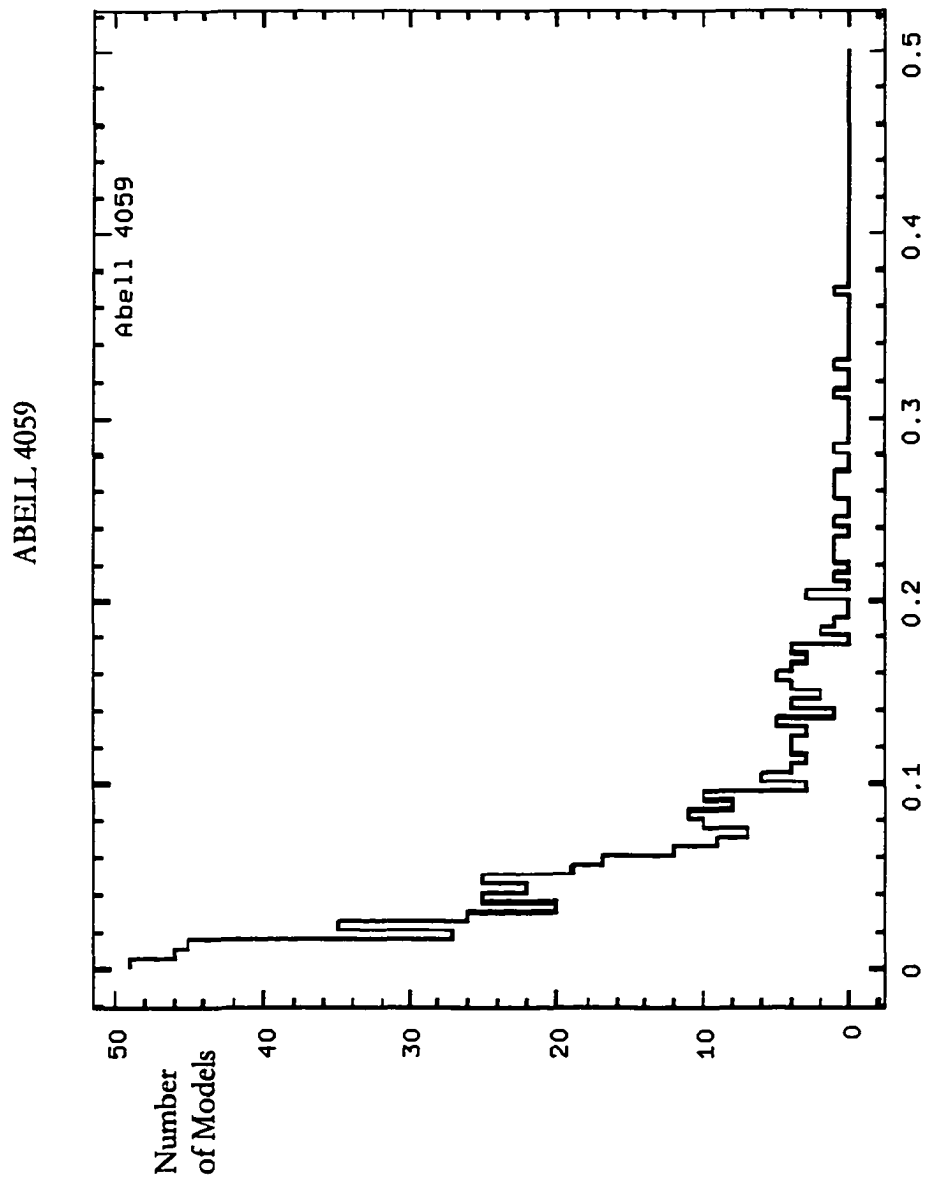

Figure 147. Histogram plots for P_4 moment for models of Abell 4059.

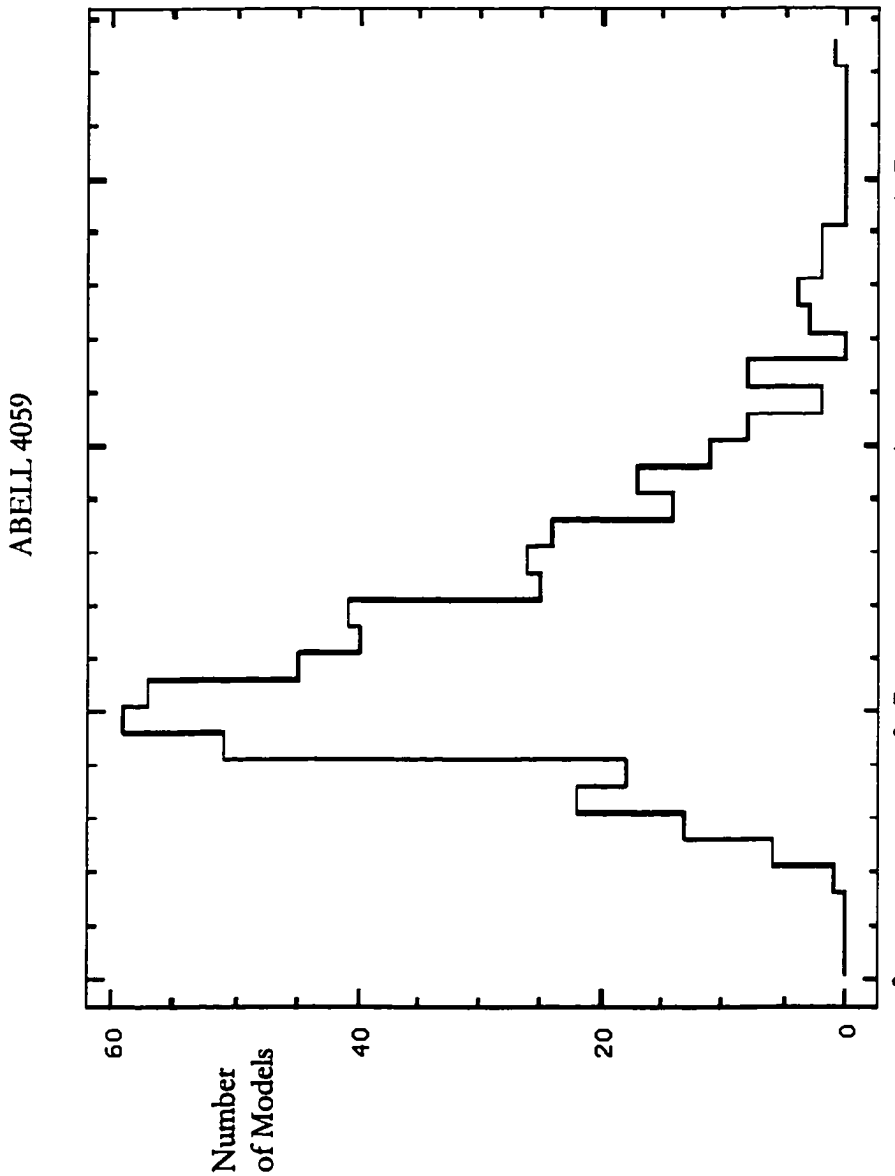

Figure 148. Sigma significance plot for Abell 4059 for 'center shift'

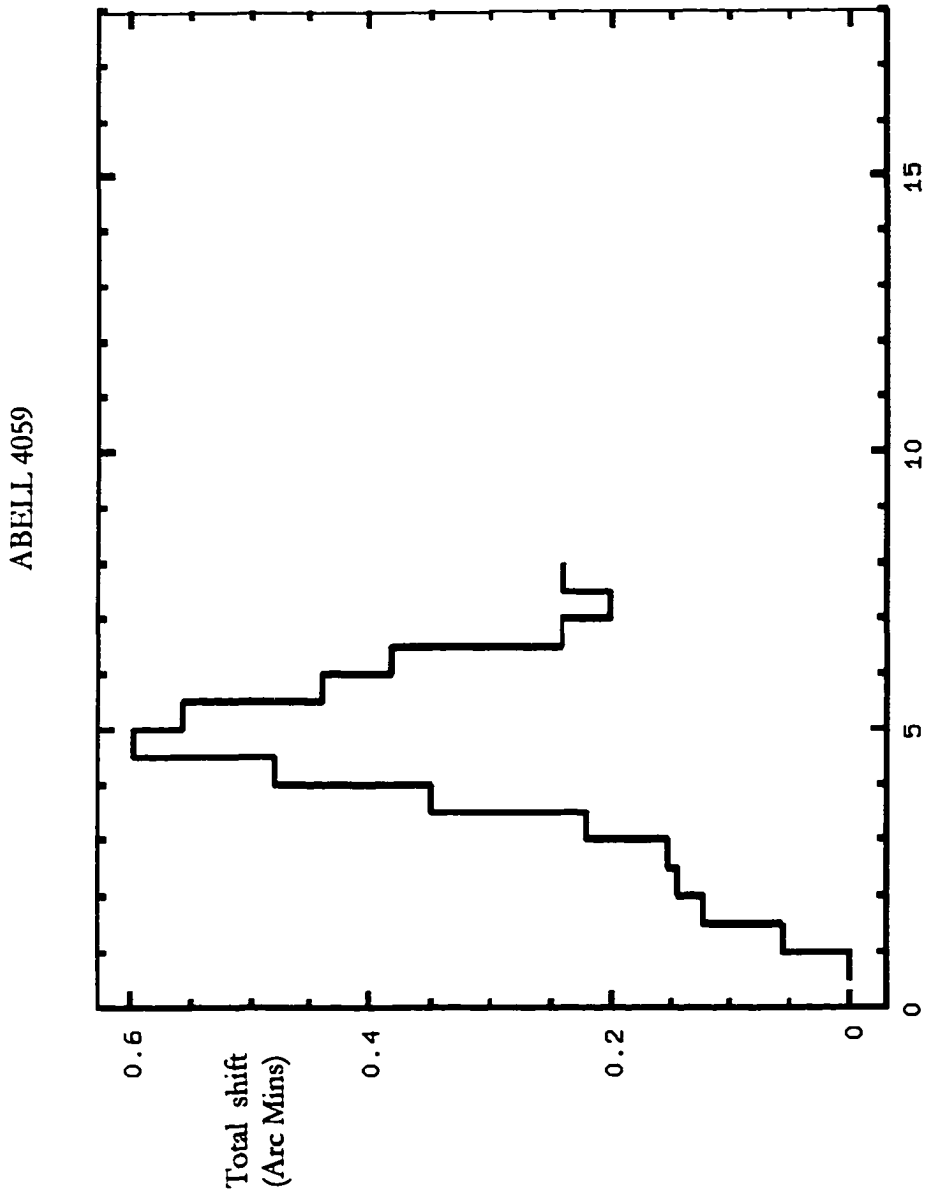

Figure 149. Total shift plot for Abell 4059 for 'center shift' program.

BIBLIOGRAPHY

Abell, George. O., Corwin, Harold, G., Jr., Olowin, Ronald, P., 1989, ApJS, 70, 1A

Bautz, L.P. & Morgan, W. W., 1970, ApJ, 162, 149

Bird, C., 1994, AAS, 185.5304

Buote, D. A. & Tsai, J. C., 1995, ApJ, 452, 522

Buote, D. A. & Tsai, J. C., 1996, ApJ, 458, 27

Dressler, A. & Shectman, S. A., 1988, AJ, 95, 985

Escalera, E., et al, 1994, ApJ, 423, 539

Geller, M. J. & Beers, T. C., 1982, PASP 94, 421

Henriksen, M. J., Mushotzky, R. F., 1986, ApJ, 302, 287

Katgert, P., Mazure, A., Perea, J., et al., 1996, A&A, 310, 8

King, I. R., 1962, A.J., 67, 471

King, I. R., 1966, A.J., 71, 64

Kauffmann, G., & White, S. D. M., 1993, MNRAS, 261, 921

Lacey, C. & Cole, S., 1993, MNRAS, 262, 627

Mazure, A., Katgert, P., den Hartog, R., et al., 1996, A&A, 310, 31

Mohr, J. J., Fabricant, D. G. & Geller, M. J., 1993, ApJ, 413, 492

Mohr, J. J., Fabricant, D. G. & Geller, M. J., 1993, egte.nasa, 285

Pislar, V., Durret, F., Gerbal, D., et al., 1997, A&A, 322, 53

Pownall, H. R., 1997, Ph.D Thesis, University of Leichester

Rhee, G., 1989, Ph.D Thesis, University of Leiden

Rhee, G., Burns, J. B. & Kowalski, M. P., 1994, AJ, 108, 1137

Richstone, D., Loeb, A. & Turner, E. L., 1992, ApJ, 393, 477

Rood, H. J., Sastry, G. N., 1971, PASP, 83, 313

Salvador-Sole, E., Sanroma, M. & Gonzalez-Casado, G., 1993, ApJ, 402, 398

Sarazin, C. L., 1998, Private Communication

Sarazin, C. L., 1988, X-ray Emissions From Clusters of Galaxies (Cambridge University Press)

Starck, J. L., Murtagh, F. & Bijaoui, A., 1995, adass, 4, 279

Starck, J. L., Murtagh, F. & Bijaoui, A., 1995, GM&IP, 57, 420

Struble, M. F. & Rood, H. J., 1984, ApJS, 63, 543

Struble, M. F. & Rood, H. J., 1982, AJ, 87, 7

West, M. J., Jones, C. & Forman, W., 1995, ApJ, 451, 5

VITA

Graduate College
University of Nevada, Las Vegas

Philip L. Rogers, Jr.

Local Address:
2649 Heritage Dr.
Las Vegas, Nevada 89121

Degrees:
Bachelor of Science, Physics, 1993
University of Nevada, Reno

Thesis Title: A Study of X-ray Substructure in Rich Clusters of Galaxies

Thesis Examination Committee:
Chairperson, Dr. George Rhee, Ph.D.
Committee Member, Dr. Lon Spight, Ph.D.
Committee Member, Dr. Donna Weistrop, Ph.D.
Committee Member, Dr. Stephen Lepp, Ph.D.
Graduate Faculty Representative, Dr. Jean Cline, Ph.D.

IMAGE EVALUATION
TEST TARGET (QA-3)

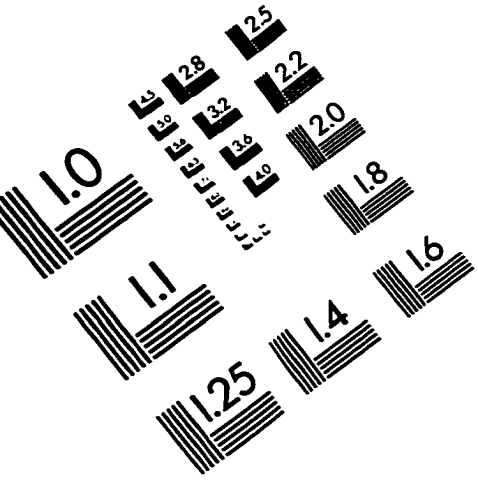

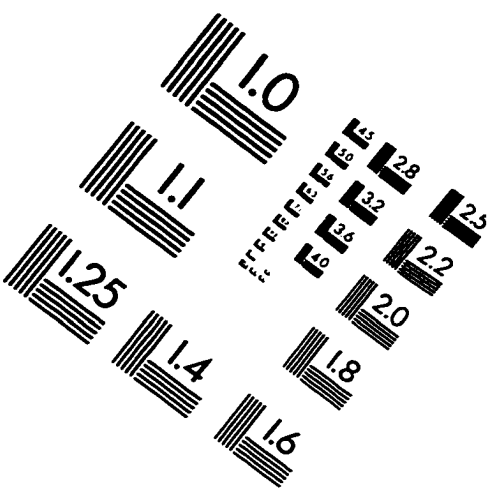

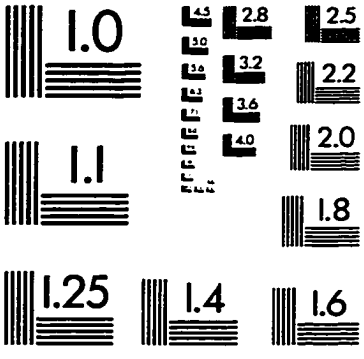

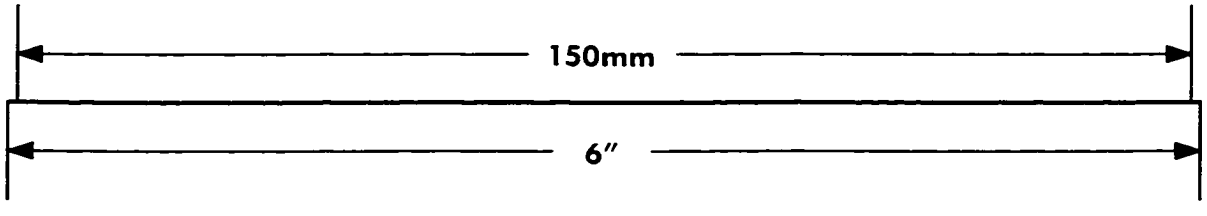

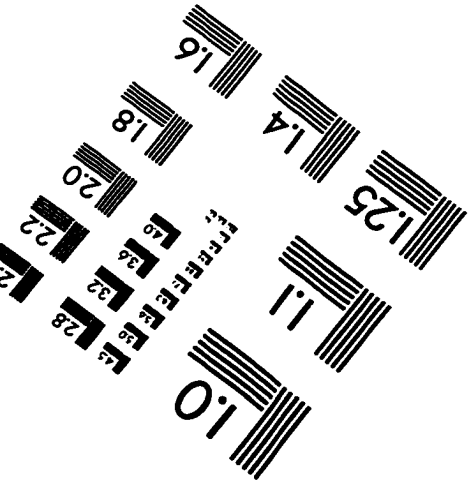

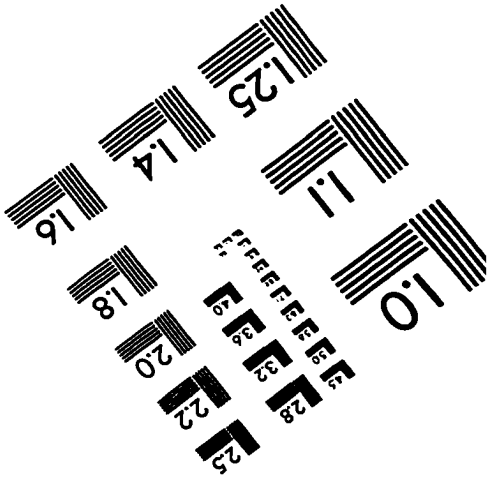

APPLIED IMAGE, Inc
1653 East Main Street
Rochester, NY 14609 USA
Phone: 716/482-0300
Fax: 716/288-5989